

# **TAILORED SURFACE-ENHANCED RAMAN SUBSTRATES FOR SENSITIVE, ECONOMICAL, AND REUSABLE CONTAMINANT DETECTION**

**Doctoral Thesis**

**by**

**"Heena Sammi"**

**(2018MSZ0003)**



**DEPARTMENT OF METALLURGICAL AND  
MATERIALS ENGINEERING  
INDIAN INSTITUTE OF TECHNOLOGY ROPAR  
March, 2024**

# **TAILORED SURFACE-ENHANCED RAMAN SUBSTRATES FOR SENSITIVE, ECONOMICAL, AND REUSABLE CONTAMINANT DETECTION**

A Thesis Submitted

In Partial Fulfilment of the Requirements  
for the Degree of

**DOCTOR OF PHILOSOPHY**

by

**“Heena Sammi”  
(2018MSZ0003)**



DEPARTMENT OF METALLURGICAL AND  
MATERIALS ENGINEERING  
**INDIAN INSTITUTE OF TECHNOLOGY ROPAR**

**March, 2024**

Heena Sammi: *Tailored Surface-Enhanced Raman  
Substrates for Sensitive, Economical, and Reusable  
Contaminant Detection*

Copyright © 2024, Indian Institute of Technology Ropar

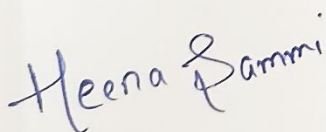
All Rights Reserved

Dedicated  
To  
GOD, Mentors, and My Family



### Declaration of Originality

I, Heena Sammi, hereby declare that the work which is being presented in the thesis entitled “Tailored Surface-Enhanced Raman Substrates for Sensitive, Economical, and Reusable Contaminant Detection” has been solely authored by me. It presents the result of my own independent investigation/research conducted during the time period from January 2019 to January 2024 of Ph.D thesis submission under the supervision of Dr. Neha Sardana (Assistant Professor, Ph.D.) and Dr. Rajesh V. Nair (Associate Professor, Ph.D.). To the best of my knowledge, it is an original work, both in terms of research content and narrative, and has not been submitted or accepted elsewhere, in part or in full, for the award of any degree, diploma, fellowship, associateship, or similar title of any university or institution. Further, due credit has been attributed to the relevant state-of-the-art and collaborations with appropriate citations and acknowledgments, in line with established ethical norms and practices. I also declare that any idea/data/fact/source stated in my thesis has not been fabricated/ falsified/ misrepresented. All the principles of academic honesty and integrity have been followed. I fully understand that if the thesis is found to be unoriginal, fabricated, or plagiarized, the Institute reserves the right to withdraw the thesis from its archive and revoke the associated Degree conferred. Additionally, the Institute also reserves the right to appraise all concerned sections of society of the matter for their information and necessary action (if any). If accepted, I hereby consent for my thesis to be available online in the Institute’s Open Access repository, inter-library loan, and the title & abstract to be made available to outside organizations.



Signature

Heena Sammi

2018MSZ0003

Program: PhD

Department: Metallurgical and Materials Engineering

Indian Institute of Technology Ropar

Rupnagar, Punjab 140001

Date: 20.03.24.

## **Acknowledgements**

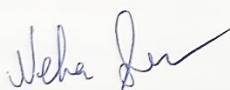
At first, I would like to express my sincere gratitude to my supervisor Dr. Neha Sardana for her thoughtful guidance, motivation, and continuous support throughout the journey. It is an honour to have you as a research advisor. Thank you so much for hiring me in your group. I would like to sincerely thank my co-supervisor Dr. Rajesh V. Nair for his valuable guidance, efforts, and time he has spent in encouraging and supporting me during this time period. I would like to thank lab group members (past and present) for all their help. I would like to express my gratitude to all of the committee members: Dr. Ravi Mohan Prasad (chairperson), Dr. Pratik Ray, Prof. Narinder Singh, and Dr. Kailash C. Jena, for their time and insightful comments that helped me to improve the content of this dissertation.

I am also very grateful to the staff members of CRF facility of IIT Ropar (operators of SEM, FE-SEM, Raman, and AFM instruments) for their kind assistance during characterization. I would also like to extend my sincere thanks to the Department of Chemistry and all the staff members of Chemistry, Metallurgical and Materials Engineering departments who gave me access to the laboratory and research facilities. Without their precious support, it would not have been possible to conduct this research. I would also like to gratefully acknowledge IIT Ropar for PhD—Fellowship, which helped me to become financially strong.

Finally, I would like to thank all my family members who consistently encouraged and helped me to accomplish this advanced degree. Without their support, I would not be able to finish my dissertation. Special thanks to God who gave me strength and blessings throughout the journey.

### Certificate

This is to certify that the thesis entitled “**Tailored Surface-Enhanced Raman Substrates for Sensitive, Economical, and Reusable Contaminant Detection**” submitted by **Heena Sammi (2018MSZ0003)**, a student in the Department of Metallurgical and Materials Engineering, Indian Institute of Technology Ropar, India, for the award of the degree of **Doctor of Philosophy** has been carried out under our supervision and this work has not been submitted elsewhere for the award of any type of degree.



Signature of the Supervisor (s)  
Neha Sardana  
Department of Metallurgical and Materials  
Engineering  
Indian Institute of Technology Ropar Rupnagar,  
Punjab 140001

Date: 20/03/2024



Signature of the Supervisor (s)  
Rajesh V. Nair  
Department of Physics  
Indian Institute of Technology Ropar  
Rupnagar,  
Punjab 140001

Date: 20.3.24

## Summary

The facile methods (dealloying and nanotexturing) have been used for the fabrication of rigid as well as flexible SERS substrates. Both methods are reproducible, cost-effective, and scalable, as well as able to fabricate the substrate with minimum equipment facilities and environmental conditions. The rigid substrate such as Nanoporous gold (NP-Au) has been fabricated by the dealloying method. The prepared substrate is able to enhance the signal up to  $\sim 10$  fold without any kind of modifications on its surface, and the reason for the enhancement is the generation of local field creation around the nanoligments as well as the hot spot formation between adjacent ligaments, which leads to the strengthening of the signals. The substrate has shown good sensing capability by detecting the  $10^{-9}$  M concentration of R6G (organic pollutant) and Urea (fertilizer). Furthermore, the substrate has demonstrated only a  $\sim 50$  % reduction in SERS signal intensity even after storage for  $\sim 2$  years; this property shows the good durability of the prepared substrate. The rigid substrates has certain disadvantages such as these substrates are difficult to apply on curved surfaces (apple, tomato, etc.) in order to collect the residues of molecules, hence non-destructive detection is not possible by using these substrates. This factor limits its use for onsite contaminant detection. Whereas this problem can be overcome by using flexible SERS substrates that can adjust on any kind of surfaces and also show good adhesion property on attachment to the surface. Therefore, a flexible substrate has been fabricated to overcome this problem as well as for real-world sensing of contaminants. It has been prepared by using a Rose petal as a template, PDMS as an elastomer, and a nanotexturing approach is used to create the inverted texture of rose. The prepared flexible substrate is also able to sense lower concentrations ( $10^{-9}$  M) of R6G and urea, as well as able to enhance the signal up to 23-fold of urea in comparison to Si. The enhancement in signals arises here due to the generation of a local field around the NPs and the plasmonic coupling between the adjacent NPs. The substrate shows good stability ability even after storage for  $\sim 4$  months. In order to check the effectiveness and flexibility of substrate for real-world application, urea fertilizer residues have been collected over the tomato surface via the paste and peel-off approach.

Furthermore, both substrates are reusable by applying a simple drop-casting approach. This property is beneficial because it can help to reduce the fabrication cost and pollution after disposal of the single-used substrate and also save the researcher's time, which is required for the fabrication of similar morphology substrates.

## Abstract

Raman spectroscopy is an effective characterization technique for the detection of a wide range of analytes due to its potential to provide figure-print spectra of a variety of molecules by detecting the inelastic scattering of incident photons with very low signal-to-noise ratio. Structured plasmonic substrates which enhance the weak Raman signal is a solution to increase Raman signal via reducing noise, which is known as surface-enhanced Raman spectroscopy (SERS). From the past few decades, researchers have fabricated many of SERS substrates that show good enhancement factor, are highly sensitive towards trace level detection, and are also stable for months. But what about other parameters like flexibility, reusability, and degradation? Based on the literature reports, very few studies are based on the substrate's homogeneity and reproducibility, although there are rare reports available on the substrate's reusability. Majority of the literature has focused on the fabrication of SERS substrates based on solid substrates. These substrates are advantageous for various sensing applications. However, with these substrates, the molecules can be detected easily from the planar or flat objects, whereas on non-planar objects such as banana, mango, etc., the detection is quite complex. Hence, non-destructive such as on-field: pathogens, fertilizer, and trace chemical detection is difficult. Therefore, a flexible SERS substrate that can adjust on any kind of surface to detect the molecules is in great demand.

In the current work, both solid as well as flexible SERS substrates have been fabricated by the facile and reproducible method. The solid substrate has been prepared by a cost-effective dealloying method for a varied time-period to determine which dealloying time shows the highest enhancement in the signal. The final networked structure of Nanoporous gold (NP-Au) shows excellent SERS activity. On the other hand, the flexible substrate has been prepared by replicating the pattern of red rose petals by using a polymer to make the patterned substrate. The nanocasting approach has been used to create the inverted texture of rose, and then the textured substrate is made SERS active by the deposition of pre-synthesized Au NPs via a self-assembly approach. After fabrication, the effectiveness of both substrates has been tested by detecting the Raman active molecule such as R6G (organic contaminant) and further, from a real-world application point of view, these substrates have also been used for the detection of urea (fertilizer). The highlighted point about the substrates is that these are reusable by applying a simple washing method and show good sensing capability by detecting urea molecules in the nanomolar range.

Keywords: Surface-enhanced Raman scattering; Dealloying; Flexible; Rhodamine 6G; Sensing.

## **List of Publications from Thesis**

### **Journal**

1. Heena Sammi, Rajesh V. Nair, and Neha Sardana\* (2023), Reusable SERS substrate based on interconnected metal network structure, *Materials Chemistry and Physics*, 293, 126894.
2. Heena Sammi and Neha Sardana\* (2023) Reusable, Flexible, Facile, and Economical SERS substrates based on rose petal replicas for pesticide detection, *Sensors, and Actuators: A. Physical*, 362, 2023, 114638.
3. Heena Sammi, Rajesh V. Nair, and Neha Sardana\*, Fabrication of SERS Substrates by Laser Restructuring of Interconnected Au Nanostructures for Urea detection, *Optical Materials*, Accepted.

### **Conference Proceeding**

1. Heena Sammi, Rajesh V. Nair, and Neha Sardana\* (2021), Recent advances in nanoporous AAO based substrates for surface-enhanced Raman scattering, *Materials Today: Proceedings*, 41, 843–850.

## **Contents**

<b>Chapter 1: Overview of research work.....</b>	<b>1</b>
<b>1.    Introduction .....</b>	<b>1</b>
1.1        Research gaps .....	2
1.2        Motivation .....	3
1.3        Objectives .....	3
1.4        Scope .....	4
1.5        Thesis outline.....	5
<b>Chapter 2: Literature review .....</b>	<b>7</b>
<b>2.1    Introduction to Raman scattering.....</b>	<b>7</b>
2.1.1        Principle.....	7
2.1.2        Energy level diagram explanation .....	7
2.1.3        Mechanism of Raman spectroscopy/Mathematical explanation .....	8
2.1.4        Instrumentation.....	10
2.1.5        Sample preparation methods .....	11
2.1.6        Applications of Raman spectroscopy .....	12
2.1.7        Limitations of Raman spectroscopy and solution to overcome.....	15
<b>2.2    Surface-enhanced Raman scattering (SERS) .....</b>	<b>15</b>
2.2.1        Introduction .....	15
2.2.2        Background.....	16
2.2.3        SERS enhancement mechanism .....	16
2.2.4        Materials for SERS substrate.....	19
2.2.5        Factors affecting SERS performance .....	19
2.2.6        Fabrication methods for SERS .....	20
2.2.7        Applications of Surface-enhanced Raman scattering substrates .....	25
2.2.8        Limitations of Surface-enhanced Raman scattering .....	26
2.2.9        SERS substrates based on rigid substrates .....	27
2.2.10        SERS substrate based on flexible substrate .....	43
<b>Chapter 3: Techniques used for the SERS substrate's characterization.....</b>	<b>50</b>
<b>3.1    Techniques based on topography measurement .....</b>	<b>50</b>
3.1.1        Field-Emission scanning electron microscopy (FESEM) .....	50
3.1.2        Atomic force microscopy (AFM) .....	51
<b>3.2    Techniques based on optical properties measurement .....</b>	<b>51</b>
3.2.1        UV-visible (UV-Vis) .....	51
3.2.2        Photoluminescence (PL).....	51



3.2.3	Dynamic light scattering (DLS) .....	52
3.2.4	Raman spectroscopy .....	52
<b>Chapter 4. Rigid SERS substrates for urea detection .....</b>		<b>54</b>
<b><i>Part 4.1: Rigid SERS substrate fabrication .....</i></b>		<b>54</b>
4.1.1	<i>Introduction .....</i>	54
4.1.2	<i>Materials and Methods.....</i>	55
4.1.2.1	Materials .....	55
4.1.2.2	Fabrication methods .....	56
4.1.3	<i>Result and Discussion .....</i>	58
4.1.3.1	Absorption peak determination .....	58
4.1.4	SERS effectiveness testing of NP-Au .....	60
4.1.5	Morphology examination .....	65
4.1.6	Composition determination .....	69
4.1.7	SERS parameter determination .....	71
<i>Conclusion of part 4.1.....</i>		74
<b><i>Part 4.2: Tuning the structure of NP-Au substrate by Raman spectrometer ‘Argon’ ion laser to improve SERS performance. ....</i></b>		<b>75</b>
4.2.1	<i>Introduction.....</i>	75
4.2.2	<i>Materials and Methods.....</i>	76
4.2.2.1	Materials .....	76
4.2.2.2	Morphology tuning approach of NP-Au substrate .....	76
4.2.2.3	Instrumentation.....	76
4.2.3	<i>Result and Discussion .....</i>	77
4.2.3.1	Laser power-dependent SERS intensities of NP-Au .....	77
4.2.3.2	Morphological characterization.....	80
4.2.3.3	SERS parameters examination .....	86
<i>Conclusion of part 4.2.....</i>		92
<b><i>Part 4.3: Testing of NP-Au substrate for urea detection .....</i></b>		<b>93</b>
<b>4.3.1</b>	<b>Introduction.....</b>	<b>93</b>
4.3.2	<i>NP-Au sensor fabrication.....</i>	94
4.3.3	<i>NP-Au sensor testing for urea detection .....</i>	94
<i>Conclusions of part 4.3 .....</i>		96
<b>Chapter 5. Flexible SERS substrate for urea detection.....</b>		<b>97</b>
5.1	<i>Introduction .....</i>	97
5.2	<i>Material and Methods .....</i>	98

5.2.1	Materials .....	98
5.2.2	Fabrication processes.....	99
5.2.3	SERS Substrate characterization .....	101
5.3	<i>Results and Discussion</i> .....	101
5.3.1	Absorption spectra determination.....	101
5.3.2	Morphological Identification of flexible substrates.....	102
5.3.3	SERS performance determination .....	106
	<i>Conclusion of chapter 5</i> .....	113
	<b>Chapter 6. Summary and future perspectives .....</b>	<b>116</b>
6.1	<i>Summary</i> .....	116
	Klarite .....	117
	Au thin film on Si nanopyramids.....	117
	Klarite™ 302 SERS substrates .....	117
	<b>RAM-SERS-AU-5 SERS Substrates .....</b>	<b>117</b>
	<b>SERStrate .....</b>	<b>117</b>
6.2	<i>Future perspectives</i> .....	117
	<b>References .....</b>	<b>119</b>

## ***List of Figures***

### Chapter 1.

<b>Figure 1. 1.</b> Schematic illustration represents (a) Normal Raman Spectroscopy and (b) Surface Enhanced Raman Spectroscopy. ....	1
---	---

### Chapter 2.

<b>Figure 2. 1.</b> Schematic of the Rayleigh and Raman scattering process. ....	8
<b>Figure 2. 2.</b> Schematic representation of Raman Spectroscopy Set-up. ....	11
<b>Figure 2. 3.</b> Raman Spectrophotometer (a) bench top for lab scale and (b) handheld for on-site molecules detection. ....	11
<b>Figure 2. 4.</b> Raman spectra of few-layer graphene. ....	13
<b>Figure 2. 5.</b> Raman spectra of various biomolecules. ....	14
<b>Figure 2. 6.</b> Left-hand side image shows when an electric field (green) is applied, the surface electrons (light pink) of the metal nanoparticles start oscillating. The right-hand side image shows the generation of a local electric field around the nanoparticles. ....	17
<b>Figure 2. 7.</b> A schematic illustration of a “hot spot”, is a gap between the nanoparticle dimer and the change in SERS enhancement factor is observed with respect to the particle distance. ....	18
<b>Figure 2. 8.</b> Schematic representation of the various factors which influence the SERS signal performance. ....	20
<b>Figure 2. 9.</b> The key requirement of SERS substrate is described in this graphic. ....	27
<b>Figure 2. 10.</b> Pictorial representation of nano-porous substrate formation from alloy. ....	29
<b>Figure 2. 11.</b> represents a step-by-step pore formation mechanism in an Ag-Au alloy (Au (orange) and Ag (grey)). The fig ‘a’ demonstrates the removal of Ag atoms from the terrace and the vacancy generation, which later converted into Au clusters by substantial diffusion as can be seen from fig ‘b’. As the dissolution processed from layer-to-layer, coarsening of Au atoms occurs, which lead to the formation of hills like structure first (fig. d) and then the structure changes to islands with time (fig. e). At the end, the entire surface is made up of pores and islands of Au atoms (fig. f). ....	30

<b>Figure 2. 12.</b> Morphological and cross-sectional view of NP-Au substrates show coarsening of ligaments and pores upon continued immersion in acid for varied time period.....	31
<b>Figure 2. 13.</b> Schematic representation of NP-Au template formation by dynamic hydrogen bubble route using square wave potential pulse voltammetry approach. ....	34
<b>Figure 2. 14.</b> UV–vis absorption spectra of NP-Au with different pore sizes. ....	38
<b>Figure 2. 15.</b> Right-hand side is the morphological view of NP-Au dealloyed for different time period (a) 5 min; (b) 48 h; sample (b) was further annealed for 2 h at varied temperature range (c) 200 °C; (d) 400°C; (e) 500°C; (f) 600°C; (g) represents intensities of $10^{-7}$ M R6G at $1650\text{ cm}^{-1}$ at 514.5 nm laser and $10^{-5}$ M CV at $1175\text{ cm}^{-1}$ at 632.8 nm laser.....	39
<b>Figure 2. 16.</b> Aptamer-modified NP-Au-based SERS sensor. (a) SEM; (b) TEM image of NP-Au. (c) Schematic illustration of protocol used for the sensing of $\text{Hg}^{2+}$ via the substrate; (d) represents the increase in concentration of $\text{Hg}^{2+}$ ions lead to the drop in the intensity of Cy5 tag.....	41
<b>Figure 2. 17.</b> AFM image of (a) dealloyed NP-Au; (b) nano-cones on the NP-Au after 90 minutes of plating; and (c) nano-cones on the NP-Au after 180 minutes of plating; (d) SERS spectra of R6G onto NP-Au (blue colour), NC1@NP-Au (green colour), and NC2@NP-Au (pink colour).....	42
<b>Figure 2. 18.</b> Schematic representation of the fabrication process for h-paper-based surface-enhanced Raman scattering (SERS) sensor. (a) SEM image of the Au NPs@GO coated h-paper substrate. SERS spectra of varied concentration of (b) R6G and (c) urea onto h-paper substrate. ....	45
<b>Figure 2. 19.</b> Schematic representation of the substrate fabrication process. Below the SERS spectra is shown for the varied concentrations of thiram measured using the prepared substrate on different fruits (a) apple, (b) pear, and (c) grape.....	46
<b>Figure 2. 20.</b> Schematic demonstration of the fabrication of SERS tape; SEM images of (A) adhesive tape and (B) Au NPs decorated adhesive tape (C) SERS spectra of parathion-methyl peel off from the surfaces of (a) apples, (b) oranges, (c) cucumbers, (d) green vegetables using SERS tape. ....	47

**Figure 2. 21.** Schematic demonstration of the substrate fabrication process. The SEM images of (a) Ag nanorod arrays on Si wafer and (b) Ag nanorods embedded in PDMS film. (c) SERS spectra of different concentration of thiram pesticide extracted from apple peel.....48

**Figure 2. 22.** Photographic pictures representing the Ag NPs aggregation and R6G accumulation on the one area of rose petal. SEM images (A) upper surface (B) lower surface of rose petal after absorption of R6G. SERS spectra of varied concentration of R6G (c) lower surface of Rose Petal.....49

#### Chapter 4.

**Figure 4. 1.** Schematic representation of step-by-step fabrication of NP-Au from an alloy leaf by the chemical dealloying method .....57

**Figure 4. 2.** Pictorial representation of the fabrication of NP-Au as a SERS sensor.....58

**Figure 4. 3.** (A) Absorption and emission spectrum of ethanolic solution of R6G and (B) absorption spectrum of NP-Au substrates dealloyed for different time.....59

**Figure 4. 4.** Raman spectra of R6G adsorption on different substrates recorded at 10 mW laser power (a) bare Si substrate; (b) SERS substrate (NP–Au coated on Si); (c) Raman spectrum of SERS substrate without adsorption of R6G molecule. Right-hand side is the enlarging view of (b) and (c) spectrum clearly indicating that the bare SERS substrate does not show its own peaks.....61

**Figure 4. 5.** Raman spectrum of R6G adsorbed on substrates corresponding to 0.1 mW laser power (a) bare Si substrate; (b) SERS substrate; (c) Raman spectrum of SERS substrate without adsorption of R6G molecule. ....62

**Figure 4. 6.** SERS spectrum of  $10^{-3}$  M R6G on the samples dealloyed for different time....63

**Figure 4. 7.** Intensities of the characteristic peaks of R6G measured from fig. 4.6.....64

**Figure 4. 8.** FESEM images of (a) Au<sub>50</sub>Ag<sub>50</sub> alloy leaf, (b) S<sub>6</sub> and (c) S<sub>9</sub> samples. The magnification of all the shown images is 75k.....65

**Figure 4. 9.** AFM analysis of Alloy leaf (a) represents the 2D image and (a') shows the 3D view of surface. The size of both image is  $3\ \mu\text{m} \times 3\ \mu\text{m}$ . The height scales are shown in the right side of 2D image. ....67

<b>Figure 4. 10.</b> AFM analysis of dealloyed samples such as (b) and (b') represents the sample dealloyed for 30 minutes and (c) and (c') represents the sample dealloyed for 45 minutes. The surface morphology shifts from a nonuniform substrate to uniformly nano-structured surface with dealloying. The left-hand side is the 2D view and the Right-hand side is the 3D view of the substrate. The size of each image is $3\ \mu\text{m} \times 3\ \mu\text{m}$ . The height scales are shown in the right side of 2D image. ....	68
<b>Figure 4. 11.</b> EDS spectra (a) commercial alloy, (b)-(n) dealloyed samples and (o) the composition variance of Au and Ag with respect to samples. ....	70
<b>Figure 4. 12.</b> SERS spectrum of $10^{-3}$ M R6G obtained at seven areas selected randomly on the same NP-Au substrate (A) $S_6$ and (B) $S_9$ . ....	71
<b>Figure 4. 13.</b> (a) Reusability test, spectra (a') (c') (e') (g') (i') related to $S_6$ sample and (b') (d') (f') (h') (j') related to R6G adsorbed on $S_6$ sample; (b) Histogram shows variation in the intensities of the characteristic peaks of R6G after four cycles.....	73
<b>Figure 4. 14.</b> Pictorial illustration of the NP-Au treatment process via different laser power of Raman system.....	77
<b>Figure 4. 15.</b> (a) SERS spectra of R6G on NP-Au excited with different laser power (0.01, 0.1, 1, 3.2, 5, and 10 mW); (b) Relationship between the intensity of the $611\ \text{cm}^{-1}$ peaks under a varied laser power (black line) and fitted with a polynomial fitting (red line). The exposure time for each spectrum was 2s. The signals collected at each power is represented in different colours; (c) Comparison SERS spectrum of R6G adsorbed on different substrates (laser treated NP-Au (green), untreated NP-Au (red) and Si (black)) recorded at lower laser power (0.1 mW). ....	79
<b>Figure 4. 16.</b> Microstructure revelation of the (a) alloy; (b) NP-Au; NP-Au incident with varied laser power (c) 0.1 mW; (d) 1 mW; (e) 3.2 mW and (f) 10 mW. The different shapes of pores such as open, diffused as well as interconnected is observed in the samples exposed with different power. The interconnected pores are represented by the yellow circle and the red circle is used to depict diffused pores. All the shown images are at the same magnification (120 K); the single scale bar shown in the fig. corresponds to 400 nm applied to each image. ....	82
<b>Figure 4. 17.</b> AFM analysis of alloy leaf (a) 2D image, (a') 3D image; and laser untreated sample (b) 2D image, (b') 3D image. The size of each image corresponds to $1.5 \times 1.5\ \mu\text{m}$ . The height scales are demonstrated in the right side 2D.....	84

**Figure 4. 18.** AFM analysis of laser treated sample (c, d, e, and f). The left-hand side shows the 2D view and the right-hand side represents the 3D view of the samples. The size of each image corresponds to  $1.5 \times 1.5 \mu\text{m}$ . The height scales are demonstrated in the right side of the 2D....85

**Figure 4. 19.** The plots (g) and (h) corresponds to the roughness and height of the structures. ....86

**Figure 4. 20.** (a) SERS spectra of R6G at a concentration range from  $10^{-3}$  M to  $10^{-11}$  M on NP-Au. The blank is the spectrum of NP-Au; (b) The calibration curve produced by logarithmic linear trend between the  $611 \text{ cm}^{-1}$  peak intensity and the R6G concentration (the x-axis is expressed in logarithmic scale and y axis is not converted to logarithmic scale for the readers better understanding); (c) Enlarged view of  $10^{-11}$  M R6G concentration on NP-Au.....87

**Figure 4. 21.** (a) Raman spectra of the  $10^{-9}$  M R6G measured from seven random spots; (b) The intensity variation of  $611 \text{ cm}^{-1}$  peak obtained from spectra (a).....89

**Figure 4. 22.** (a) SERS spectra of the freshly prepared NP-Au and after 2 years storage of the same substrate; (b) Histogram represents the reduced intensity value of the stored sample with respect to the fresh sample. .... 90

**Figure 4. 23.** FESEM images of NP-Au (a) freshly prepared; (b) '2' years stored sample. The stored sample is consisting larger and interconnected pores due to multiple time laser treatment. The figure (a') and (b') represents the composition analysis of freshly and stored NP-Au samples. .... 91

**Figure 4. 1.** XPS analysis of NP-Au (blue spectra corresponds to fresh sample of NP-Au and red spectra corresponds to NP-Au sample stored for two years).

**Figure 4. 25.** Raman spectrum of  $10^{-3}$  M urea on NP-Au and on Si substrate. .... 95

**Figure 4. 26** (a) Raman spectra of urea under different concentrations. (b) The calibration curve of the intensity vs different concentrations of urea. The x-axis is converted to a logarithmic scale and the y-axis is mentioned as it (intensity counts) for better understanding of the reader. .... 96

## Chapter 5.

**Figure 5. 1.** Schematic representation of the fabrication process to create inverse replicas of the rose petal by using PDMS..... 99

<b>Figure 5. 2.</b> A step-by-step pictorial illustration of the process for the deposition of Au NPs onto the APTMS functionalized Rose replicated substrate. The purple colour dotted lines show the enlarged view of the region, representing the presence of functional groups and bond formation between the molecules.....	
	100
<b>Figure 5. 3.</b> Absorption spectra of (a) Au NPs suspension in water; self-assembled Au NPs onto (b) unstructured and (c) structured substrate.....	102
<b>Figure 5. 4.</b> Optical image of the replicated structured PDMS prepared from the rose. The scale bar corresponds to 4 $\mu\text{m}$ .....	103
<b>Figure 5. 5.</b> SEM images of (a)-(d) prior to Au decoration, (a) natural rose petal; (b) magnified view of the single rose petal; (c) negative structured PDMS replica of rose petal; (d) magnified image of the single replicated structure.....	104
<b>Figure 5. 6.</b> (A) Histogram represents the NPs size distribution measured from DLS spectra. (B) FESEM observations of Au NPs.....	104
<b>Figure 5. 7.</b> Images (e) and (f) are the FESEM images represents the post -Au decoration onto PDMS replica of rose petal (e) and flat PDMS (f), correspondingly (g) and (h) are the magnified view of image (e) and (f) respectively. Figure (g'), (g'') and (g''') are the images captured from different areas of a single pore.....	105
<b>Figure 5. 8.</b> SERS spectra of R6G on the different substrates- Si Substrate (black line); NPs decorated onto the unstructured/flat flexible (red line) as well as onto the structured flexible (blue line).....	106
<b>Figure 5. 9.</b> SERS spectra of R6G on different substrates, clearly represents the intensity counts of structured substrate is higher than the unstructured and Si substrate.....	107
<b>Figure 5. 10.</b> SERS spectrum of $10^{-3}$ M urea on different substrates- Si substrate (black line), NPs assembled onto structured (red line) and unstructured (blue line) substrate.....	108
<b>Figure 5. 11.</b> SERS spectra of urea on different substrates clearly represent structured substrate is able to enhance the signal compared to the unstructured and flat substrate.....	109



<b>Figure 5. 12</b> (a) Raman spectra of urea under different concentrations. (b) The calibration curve of the intensity vs different concentrations of urea. The x-axis is converted to a logarithmic scale and the y-axis is mentioned as it (intensity counts) for better understanding.....	110
<b>Figure 5. 13.</b> Detection of $10^{-13}$ M urea concentration on the structured substrate.....	110
<b>Figure 5. 14.</b> (a) Represents the washing method to reuse the substrate; (b) reusability test spectra of urea absorbed on substrate after (a') '1' day and (c') '120' days and (b') corresponds to washed substrate; (c) histogram shows variation in the intensities of the characteristic peak of urea of the 120 days old sample with respect to one-day old sample.....	111
<b>Figure 5. 15.</b> Pictorial representation of procedure used for detecting urea on the Tomato surface.....	112
<b>Figure 5. 16.</b> SERS spectra of substrate contaminated with urea residues directly peeled from the tomato surface. ....	113

### *List of Tables*

<b>Table 4. 1.</b> Conversion of R6G characteristic peaks from wavenumber to wavelength. ....	59
<b>Table 4. 2.</b> Representation of substrate names with abbreviations .....	63
<b>Table 4. 3.</b> Calculation of SERS EF for the S <sub>6</sub> & S <sub>9</sub> samples. ....	65
<b>Table 4. 4.</b> Represents the statistical parameters of the samples such as surface area, roughness, and height of the structures. ....	69
<b>Table 4. 5.</b> RSD values of samples S <sub>6</sub> & S <sub>9</sub> corresponds to the characteristic peaks of the R6G .....	71
<b>Table 4. 6.</b> represents the material which is required for the fabrication (alloy leaf, HNO <sub>3</sub> , glass slides, two beakers (one for HNO <sub>3</sub> and other for DI water) with cost. ....	74
<b>Table 4. 7.</b> SERS enhancement factor calculation corresponding to different laser power. In the formula, I <sub>n</sub> represents the intensity counts related to 0.1, 1, 3.2, 5 and 10 mW power and I <sub>0.01</sub> corresponds to counts of 0.01 mW. ....	79
<b>Table 4. 8.</b> Representation of substrate names with abbreviations .....	83
<b>Table 4. 9.</b> Represents the concentration values obtained after inserting the slope, intercept, and intensities values collected from spectrum. ....	88
<b>Table 4. 10.</b> RSD values of substrate corresponds to the characteristic peaks of the R6G. ....	89
<b>Table 4. 11.</b> XPS spectral data represents the compositional variation of fresh and stored NP-Au substrate. ....	92

**Table 4. 12.** demonstrates the fabrication material with cost which is required for second substrate (a rose petal as a template, PDMS as a surface texturing agent, Silicon substrate, H<sub>2</sub>O<sub>2</sub>, and HF).....113

**Table 4. 13:** Cost comparison with company made substrates.....117

## Nomenclature

APTMS	3-Aminopropyl triethoxysilane
AFM	Atomic force microscope
CM	Chemical enhancement mechanism
$C_{\text{normal}}$	Concentration of molecule on bare (silicon) substrate
$C_{\text{SERS}}$	Concentration of molecule on SERS Substrate
D.I	Deionized water
$\mu$	Dipole moment
DLS	Dynamic light scattering
EDS	Energy dispersive X-ray spectroscopy
EM	Electromagnetic enhancement mechanism
E	Electric field
EBL	Electron-beam lithography
EF	Enhancement factor
FESEM	Field-Emission scanning electron microscopy
FIB	Focused-ion beam lithography
'h'	Planks constant
$\nu_0$	Incident frequency
$I_{\text{normal}}$	Intensities of detected molecule on bare (silicon) substrate
$I_{\text{SERS}}$	Intensities of detected molecule on SERS substrate
LOD	Limit of detection
LSPR	Localized surface plasmon resonance
NP	Nanoparticles
NA	Numerical aperture
NP-Au	Nanoporous gold
NSL	Nanosphere lithography
PL	Photoluminescence
PDMS	Polydimethylsiloxane
$\alpha$	Polarizability
RSD	Relative standard deviation
R6G	Rhodamine 6G
$\nu_m$	Scattered frequency

Si	Silicon
SERS	Surface-enhanced Raman scattering
SPR	Surface plasmon resonance
UV-Vis	Ultraviolet - visible
$\lambda$	Wavelength
$\lambda_{\text{exc}}$	Wavelength of excitation source
$\lambda_{\text{max}}$	Wavelength of maximum absorption

## Chapter 1: Overview of research work

### 1. Introduction

Raman spectroscopy is an effective characterization technique for the detection of wide range of analytes due to its potential to provide figure-print spectra of variety of molecules by detecting the inelastic scattering of incident photons [1]. However, its use is limited due to the small scattering cross-section typically in the range of  $10^{-29}\text{cm}^2/\text{molecule}$  that results in a very low signal-to-noise ratio. This precludes in a wide range of applications in sensing of many molecules and chemicals [2]. This drawback can be overcome by the use of structured metallic substrates which enhances the weak Raman signal by several orders of magnitude. Here, a molecule is located in a close proximity to the plasmonic substrate [3] and then excited with a suitable wavelength as shown in fig 1.1. This modified technique is known as the surface-enhanced Raman spectroscopy (SERS), which is a highly sensitive and selective spectroscopy technique. It has applications in many areas such as the bioimaging, forensic science, cell characterization, food, and environmental analysis [4], [5]. Even after decade long research on SERS based systems, the mechanism behind the SERS process is debatable. It has been shown that an increase in Raman signal intensity is due to the strong electromagnetic fields produced by localized surface plasmon resonance on the rough metallic substrate [5]. The enhancement of electromagnetic field is usually observed at nanogaps between metal nanostructures known as the hot spots [6]. The major concern for the practical applications using SERS is the requirement of hot spots at precise spatial locations over the SERS substrate which depends on the shape, size, and the surrounding environment.

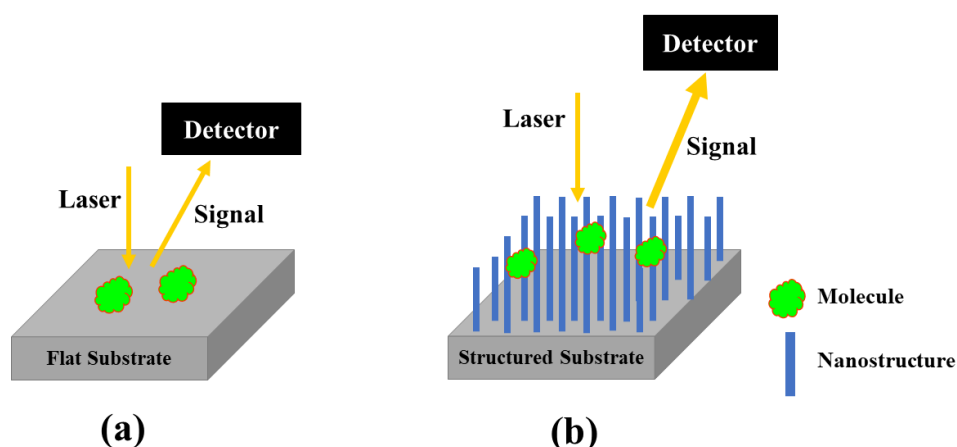


**Figure 1.1.** Schematic illustration represents (a) Normal Raman Spectroscopy and (b) Surface Enhanced Raman Spectroscopy.

Various materials such as metals (Ag, Au, Cu, Al, Pd, Pt, Co, Fe, Ru,), non-metals (C, Graphene, Graphene Oxide), semimetals ( $\text{Mo}_2\text{C}$ , MXene) and transition metal dichalcogenides ( $\text{MoS}_2$ ) have been used to make SERS substrate [7], [8]. Among these materials, Ag and Au are extensively used due to their excellent plasmonic properties compared to others and also their localized surface

resonance lies in the visible and near-infrared wavelength range, where most Raman measurements occur [9], [10]. Furthermore, in comparison to Ag; Au is preferred to make SERS substrate due to its ultrahigh chemical stability, which can prevent the reduction in signal intensity due to oxidation [11].

In SERS field, for strong signal enhancement, the structural morphology of SERS substrates matters most [12]. The fabrication methods such as chemical etching, self-assembly, spin-coating, sputtering, electron beam, focused ion beam, nanoimprint lithography, and photolithography etc., is widely used for the random and periodic arrangement of nanostructures onto the substrates [12], [13]. Although substrates prepared by these methods is able to show strong enhancement, but along with that the optimized conditions and specific expensive setups are essential for many of these techniques [14].

Although SERS has developed as a potential tool for biological and chemical sensing, still it has certain limitations as like other techniques. Glass slides and Silicon substrates are the two most common base substrates used for the formation of SERS active layers [15]. Whereas, these base substrates are brittle and rigid and cannot be applied onto curved surfaces (requires pre-treatment steps) as well as show poor adhesion property upon attachment to the surface. From the past few years, efforts have been initiated to fabricate flexible SERS substrates. Flexible substrates have advantages over rigid substrates as they can be wrapped onto irregular surfaces (fruit, suitcase, table, bag etc.,) and can be cut into different sizes and shapes as per the application demand, also non-invasive and in-situ detection is possible [16].

### *1.1 Research gaps*

From the past few decades, researchers have fabricated many of SERS substrates; that show good enhancement factor, are highly sensitive towards the trace level detection, and are also stable for months [3]. But what about other parameters like flexibility, reusability, and degradation? Based on the literature reports very few studies are based on the substrate's homogeneity and reproducibility, although there are rare reports available on the substrate's reusability. As per today's era point of view, the recycling/reusability of substrates is an important and beneficial factor for society. The disposal of the substrate after a single use increases the fabrication cost and the pollution caused by the use of chemicals [16]. On the other hand, most of the literature has focused on the fabrication of SERS substrates based on solid substrates such as silicon, glass, quartz, and alumina. These substrates are advantageous for various sensing applications. However, with these substrates, the detection of molecules only on planar or flat objects is possible, whereas on non-planer, uneven, and on curved objects: non-destructive detection is difficult [4]. This factor limits its use for real-world sensing applications such as on-field pesticides, fertilizers, pathogens, and trace chemical detection. Therefore, a flexible SERS substrate which can adjust on any kind of

surface (irregular as well as on planer surface) to detect the unknown molecules is in great need [17].

## 1.2 Motivation

With the increasingly widespread use of pesticides and fertilizers in agriculture, food safety has become a major concern in today's era. Pesticides and fertilizers are widely used to increase the crop production and to protect the crops from various kinds of insects, fungi, weeds, and other pests [24]. On the other hand, their wrong and excessive use is toxic to humans and can cause acute and chronic health issues. Therefore, to prevent humans from the adverse effects of pesticides and fertilizers, WHO has recommended a maximum permissible limit for each pesticide and fertilizer, beyond that limit these are considered toxic [25].

There are various methods to detect pesticides/fertilizer in food products such as gas chromatography-mass spectrometry, high-performance liquid chromatography, and liquid chromatography-mass spectrometry. These are effective and accurate, but rather than that the sample preparation is difficult, time-consuming, and lower limit detection is not possible [26]. Additionally, the non-destructive detection is also not possible by using these methods.

As compared to the existing and currently used methods, Surface Enhanced Raman Scattering (SERS) is suitable and well fits the above-mentioned characteristics due to its simplicity, fast nature, and ability to detect lower concentration of contaminants such as pathogens, pesticides, fertilizers, and environmental pollutants. Furthermore, by using flexible substrates the non-destructive detection is also possible.

In the current work, both solid as well flexible SERS substrates have been fabricated by the facile and reproducible method. After fabrication, the effectiveness of both substrates has been tested by detecting the Raman active molecule such as R6G (organic contaminant) and further, for real-world application point of view, these substrates have also been used for the detection of the urea (fertilizer).

## 1.3 Objectives

Development of reusable, stable, cost-effective, uniform, and sensitive SERS substrates (rigid and flexible) for lower limit of detection for contaminants (LOD).

### 1.3.1 Rigid substrate

1. Fabrication of substrate by dealloying method (facile/reproducible/cost-effective).
2. Spectroscopic, morphological, and compositional analysis of the substrate by UV-visible, Raman spectrometer, FE-SEM, and EDS spectroscopy.
3. Optimization of experimental conditions (dealloying time) and instrumental parameters (laser power, acquisition time, and accumulation time etc.) for better SERS performance.



4. SERS parameters examination such as effectiveness testing, sensitivity, uniformity, reusability, and stability.
5. Testing of the substrate for contaminant detection via the drop-casting method for real-world application purposes.

### 1.3.2 *Flexible substrate*

1. Fabrication of structured substrate by nanotexturing approach (facile/reproducible/cost-effective).
2. Spectroscopic and morphological analysis of the prepared substrate by UV-visible, Raman spectrometer, Dynamic light scattering, optical microscope, and FE-SEM.
3. Optimization of experimental conditions (surface modification process and Au nanoparticle immersion duration etc.) and instrumental parameters (laser power, acquisition time, and accumulation time etc.) for better SERS performance.
4. SERS parameters examination such as effectiveness testing, sensitivity, uniformity, reusability, and stability.
5. Testing of the substrate for contaminant detection via paste and peel-off approach for real-world application purposes.

## 1.4 *Scope*

- The substrates are reusable by applying a simple drop-casting method. This point is beneficial and currently in demand in SERS field. This property can help to reduce the fabrication cost as well as pollution which generally occurs due to the use of chemicals for the preparation of new substrates and after disposal of the single-used substrate. Furthermore, the reusability saves researcher's time which is required for the fabrication of similar morphology substrates.
- The flexible structured substrates prepared from natural artifacts (butterfly, cicada wing, plant leaves such as lotus, rose petals, taro, and rice) can open a new door in the field of facile, rapid, economical, and bulk-scale synthesis of substrates as compared to lithography, sputtering, molecular beam epitaxy-based techniques which are highly dependent on the specialized equipment's facility and environmental conditions.
- These substrates can also be used for the detection of other contaminants such as pathogens (bacteria and viruses, etc.), environmental pollutants (heavy metals {As, Pb, and Cd, etc.}), narcotics (cocaine, heroin, morphine, and codeine, etc.) and can also be used to identify other food contaminants (pesticides {chlorpyrifos, methyl parathion, and thiram which are commonly used to kill pests and protect the crop from fungal diseases}, insecticides, herbicides, and fertilizers). Most importantly, the prepared flexible substrates can be used for the onsite detection (real-world application) of contaminants, etc. and can also be used for other

applications such as optoelectronic (photoelectric properties) and biomedical (capture and release of tumor cells) instead of SERS.

## 1.5 Thesis outline

*Chapter 1:* Briefly discusses about Raman spectroscopy, Surface Enhanced Raman Spectroscopy (SERS) and the advantages, disadvantages, applications, and challenges associated with them. A brief literature review regarding the materials and fabrication methods used for SERS substrate preparation and then an overview has been given on the types of SERS substrates (rigid and flexible substrate) used. Based on the study we have explored research gaps as well as challenges associated with the field, accordingly, the objective of the thesis has been decided.

*Chapter 2:* Detailed literature survey is discussed on earlier mentioned topics such as Raman spectroscopy (principle, energy level diagram, mechanism of Raman spectroscopy/mathematical explanation, instrumentation, sample preparation methods, applications of Raman spectroscopy, limitations of Raman spectroscopy and solution to overcome), Surface-enhanced Raman spectroscopy (introduction, background, enhancement mechanism, materials and fabrication methods used, factor affecting SERS performance, applications and limitations of SERS) and further, the chapter is divided into two subsections- one section discusses the state-of-art based on solid SERS substrate and the other discusses about the flexible SERS substrates.

*Chapter 3:* Discusses about the techniques used for the characterization of substrates. This chapter is divided into two subsections. In one part, the techniques which provides information about topology is discussed (FESEM, AFM) and in the other part techniques used to examine the optical properties of the substrates are discussed (UV-visible, PL, DLS, and Raman Spectroscopy).

*Chapter 4:* This chapter discusses the fabrication of rigid SERS substrates and their use for contaminant detection for real-world application purposes. The chapter is divided into three parts. In the first part: the methodology, materials used for the fabrication, and results such as absorption peak determination, morphology and composition examination, and SERS parameters (effectiveness testing, enhancement factor determination, uniformity, and reusability) are discussed. The next part is based on the determination of the effect of laser power variation onto the substrate morphology as well as onto the SERS performance. In the third part, substrate effectiveness towards fertilizer detection is examined, and a conclusion is given at the end of each part.

*Chapter 5:* Discusses about the fabrication of flexible substrate for fertilizer detection via paste and peel-off approach. This chapter includes methodology and materials used for the fabrication of flexible substrate, then discusses about the results (absorption peak determination, SERS Parameters {effectiveness testing, enhancement factor determination, sensitivity, uniformity,

reusability, stability, and testing for urea detection}, morphological examination) and at least provides conclusion of the work.

*Chapter 6:* Includes the overall summary of the present research work and provides a perspective for future studies.

## ***Chapter 2: Literature review***

### ***2.1 Introduction to Raman scattering***

Raman scattering is the inelastic scattering of a photon. It was predicted theoretically by an Australian physicist Adolf Smekal in 1923 and later experimentally observed by Indian physicists C.V. Raman and K. S. Krishnan in 1928 [18] and the effect was observed using a very simple optical set-up, i.e., sunlight as an illumination source, colour filters, telescope, and viewer's eye as a detector [19]. Professor Raman for this discovery was awarded with the Nobel Prize in 1930 in physics. Initially, the phenomenon was beneficial only to measure highly concentrated pure organic solvents, and its effect was observable with eyes. Whereas, the effect was weaker for diluted solutions. Due to that, the applications of Raman spectroscopy were delayed for several years until the invention of the laser and other effective optical components such as holographic gratings, notch and neutral density filters, high throughput monochromators, photomultiplier tubes, and charge-coupled devices [20]. As a result, it is now possible to detect lower concentrations of molecules even in the nanomolar range, which was nearly impossible just a few years ago.

#### ***2.1.1 Principle***

When a monochromatic beam interacts with an atom or molecule, both elastic and inelastic scattering occurs. Most of the scattered radiation is of same energy as the incident photons known as elastic or Rayleigh scattering, whereas a small fraction of radiation (1 out of 10 million photons) is scattered with a different energy than the incident radiation called inelastic/Raman scattering [21]. In Raman scattering, due to light-molecule interaction, the molecule either loses or gains energy from the photon. If it gained energy from the photon then that scattering is known as Stoke scattering, and if it loses the energy and provided to photon then that scattering is known as anti-Stoke scattering. This energy difference corresponds to the rotational and vibrational modes of the molecules and provides the Raman spectra which help to determine the atomic orientation and bonding within a system [22]. Moreover, vibrational information is specific to chemical bonds, symmetry of the molecules, and the electronic environment. Therefore, Raman spectroscopy provides a “fingerprint” which enables the qualitative determination of individual molecules. The energy level diagram for Rayleigh, Stokes, and Antistokes scattering is represented in fig. 2.1.

#### ***2.1.2 Energy level diagram explanation***

Let us consider that the incident photon energy is  $h\nu_0$ , the ground state is represented as  $E_0$  and the energy difference between the ground and vibrational state is  $h\nu_m$  as shown in fig. 2.1. The term  $h(\nu_0 - \nu_m)$  indicates Stokes scattering and  $h(\nu_0 + \nu_m)$  represents anti-Stokes scattering. The Raman shifts are represented in terms of wavenumber using the standard unit of  $\text{cm}^{-1}$ . When a photon ( $h\nu_0$ ) from a high-intensity laser is incident on the molecule, the molecule is excited to a virtual state (not a stable energy level). From this virtual state, the relaxation of a molecule is

different [23]. If the molecule relaxes to the same energy level and scatters a photon of same frequency ( $h\nu_0$ ) as the incident photon then this scattering is known as Rayleigh scattering. Whereas, when the molecule relaxes to different vibrational states either lower or higher vibrational state and scatters a photon of different energy then this scattering is known as Raman scattering. As discussed, Raman scattering is described by two scattering mechanisms. One is Stokes scattering and the other is anti-Stokes scattering. In Stokes scattering, a molecule relaxes to a lower vibrational energy state from its beginning state and scatters a photon of lower frequency ( $h(\nu_0 - \nu_m)$ ). In anti-Stokes, a molecule relaxes to a higher vibrational energy state than its excitation state and emits a photon of higher energy ( $h(\nu_0 + \nu_m)$ ) than the incident photon. From fig. 2.1. it can be seen that in the case of anti-Stokes scattering, the molecule is already in the excited state before excitation. The peak intensity of the Stokes lines is higher than the anti-Stokes, therefore anti-Stokes lines are difficult to detect because they merge in Stokes lines.

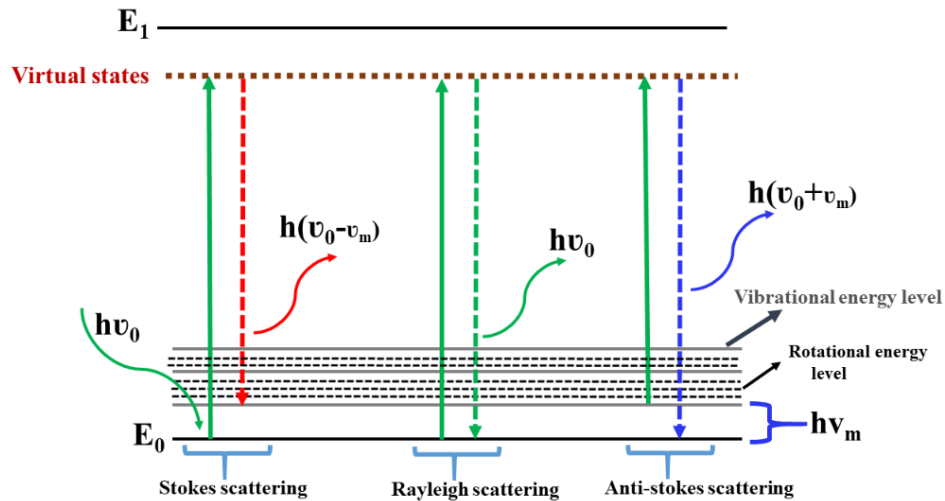


**Figure 2.1.** Schematic of the Rayleigh and Raman scattering process.

### 2.1.3 Mechanism of Raman spectroscopy/Mathematical explanation

To obtain the Raman spectrum of a sample, a change in polarizability during molecular vibration is a necessary condition. When a molecule is placed in an oscillating electric field 'E', nuclei and electrons are displaced from their positions. As a result, the dipole moment is induced inside the molecule; this dipole moment is known as induced dipole moment and is represented by the term ' $\mu_i$ '. If 'E' is the strength of applied electric field and  $\mu_i$  is the magnitude of induced dipole moment [24], then the magnitude of the induced dipole moment is proportional to the strength of the applied field and is given by the following equation.

$$\mu_i = \alpha E \quad (\text{eq. 2.1})$$

Where  $\alpha$  is the polarizability of the molecule and is associated with the dipole moment  $\mu_i$ . The

amount of displacement of the electron cloud surrounding a molecule is determined by polarizability. The change in  $\mu_i$  parameter leads to Raman scattering; therefore, the Raman signal intensity is the square of the  $\mu_i$  [25]. The polarizability shows the intrinsic characteristic of the molecule and is affected by the electronic structure and the type of chemical bond.

$$I_{Raman} \propto \alpha^2 E^2 \quad (eq. 2.2)$$

The electric field strength of an electromagnetic wave of frequency ‘ $\nu$ ’ is represented as

$$E = E_0 \cos 2\pi\nu t \quad (eq. 2.3)$$

Where  $E_0$  is the amplitude of the electromagnetic wave. Substituting the value of Equation (2.3) into (2.1)

$$\mu = \alpha E_0 \cos 2\pi\nu t \quad (eq. 2.4)$$

Equation (2.4) represents when electromagnetic radiation of frequency ‘ $\nu$ ’ is incident onto a molecule, it induces a molecular dipole moment which resonates with the same frequency. However, the small displacement of the molecule from its equilibrium position (i.e., molecular vibration) causes the change in polarizability factor and is determined by

$$\alpha = \alpha_0 + (r - r_{eq}) \frac{\partial \alpha}{\partial r} \quad (eq. 2.5)$$

where  $\alpha_0$  is the equilibrium polarizability, and  $r$  and  $r_{eq}$  are the bond lengths at equilibrium position and at any instant, respectively. If a molecule executes simple harmonic motion, the displacement can be expressed as

$$(r - r_{eq}) = r_{max} \cos 2\pi\nu_i t \quad (eq. 2.6)$$

where  $r_{max}$  is the maximum separation distance between atoms and  $\nu_i$  is the vibrational frequency of a molecule relative to its equilibrium position. Combining equations (2.5) and (2.6) gives

$$\alpha = \alpha_0 + r_{max} \cos 2\pi\nu_i t \left( \frac{\partial \alpha}{\partial r} \right) \quad (eq. 2.7)$$

Substituting equation (2.7) into equation (2.4)

$$\mu = \left\{ \alpha_0 + r_{max} \cos 2\pi\nu_i t \left( \frac{\partial \alpha}{\partial r} \right) \right\} E_0 \cos 2\pi\nu t \quad (eq. 2.8)$$

$$\mu = \alpha_0 E_0 \cos 2\pi\nu t + E_0 r_{max} \left( \frac{\partial \alpha}{\partial r} \right) \cos 2\pi\nu t \cos 2\pi\nu_i t \quad (eq. 2.9)$$

Multiply and divide the 2<sup>nd</sup> term of right-hand side of equation (2.9) with ‘2’ gives

$$\begin{aligned} \mu = & \alpha_0 E_0 \cos 2\pi\nu t + \frac{E_0}{2} r_{max} \left( \frac{\partial \alpha}{\partial r} \right) \cos[2\pi(\nu + \nu_i)]t + \\ & \frac{E_0}{2} r_{max} \left( \frac{\partial \alpha}{\partial r} \right) \cos[2\pi(\nu - \nu_i)]t \end{aligned} \quad (eq. 2.10)$$

$$(\therefore 2 \cos A \cos B = \cos (A+B) \cos (A-B))$$

The first term in equation (2.10) corresponds to Rayleigh scattering; here the scattered frequency is similar to the excitation frequency  $\nu$ . The second and third terms represents the anti-Stokes ( $\nu + \nu_j$ ) and Stokes ( $\nu - \nu_j$ ) scattering, where the scattered frequency has been altered by the vibrational frequency of the bond.

#### 2.1.4 Instrumentation

In Raman spectrometer, the sample is illuminated with monochromatic light and the scattered signal is collected by an objective lens. The instrument schematic is represented in fig 2.2. It consists of following components: a laser as an excitation source to illuminate the sample with monochromatic light, a neutral density filter, optical lenses (objectives, mirrors), holographic notch filter, and a detector to collect the scattered light [26]. As discussed, the intensity of scattered radiation is very weak, therefore an extremely intense source of radiation such as a laser is required. The commonly used lasers in Raman spectrometer are Argon ion (~ 488/514 nm), Krypton ion (~ 532/647.1 nm), Helium:Neon (~ 633 nm), Diode lasers (~ 785/830 nm), and Nd:YAG (1064 nm) [27]. All these lasers have attracted significant attention in the Surface-enhanced Raman scattering field due to their ability to excite the localized surface plasmons of the metallic nanostructures [28].

In some cases, the use of a high-power laser can cause strong fluorescence emission and decomposition of the sample. In order to reduce these effects or to get an effective Raman signal, a neutral density filter is used. It decreases the intensity of the laser, which helps to reduce the fluorescence and sample decomposition. Then the light passes through the dichroic filter. It functions like a beam splitter. It reflects the incident light, directs it towards the sample and simultaneously allows the transmission of the emitted light from the sample. The light is then falls onto the notch filter. The emitted light contains three kinds of scattering signals: Rayleigh, Stokes, and anti-Stokes. This filter is used to remove Rayleigh scattering (laser line) and then the remaining light which consists of Stokes and anti-Stokes signals, is sent to a spectrophotometer. The spectrophotometer involves different optical elements such as a slit, holographic grating (dispersing element), and CCD detector. After passing through the notch filter, the signal passed through a thin slit (which controls the amount of light that enters the spectrometer) and strikes onto the grating, which split the light into various colours. The light is captured by a CCD detector, hence resulting in a Raman spectrum.

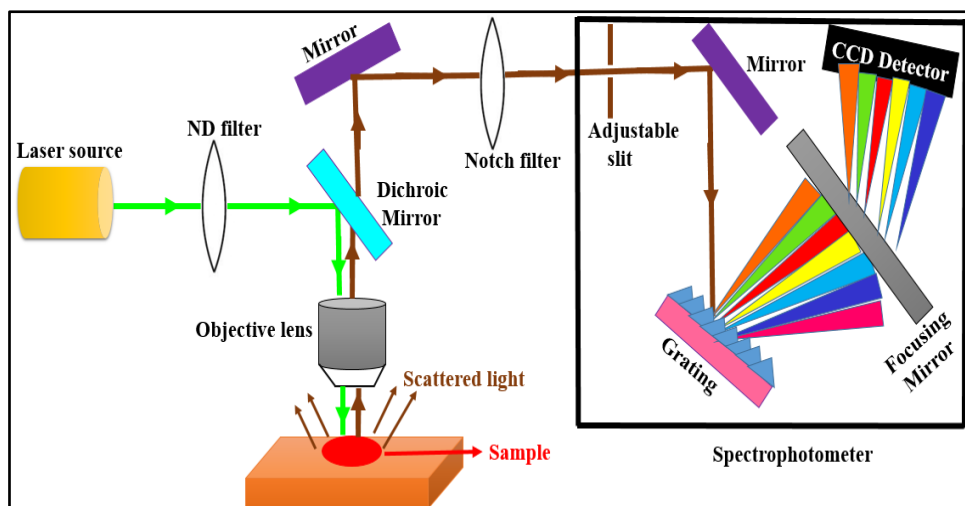


**Figure 2.2.** Schematic representation of Raman Spectroscopy Set-up [26].

As per the application point of view, Raman spectrophotometer is categorized into two types: one is bench-top, which is generally used in laboratories and the other is hand-held or portable spectrophotometer used for onsite molecule detection [29]. The basic principle is same for both cases and these systems vary in terms of an instrument's versatility, size, and the cost of its components. In portable spectrophotometers, more compact components are used. The pictorial representation of both systems is shown in fig 2.3.

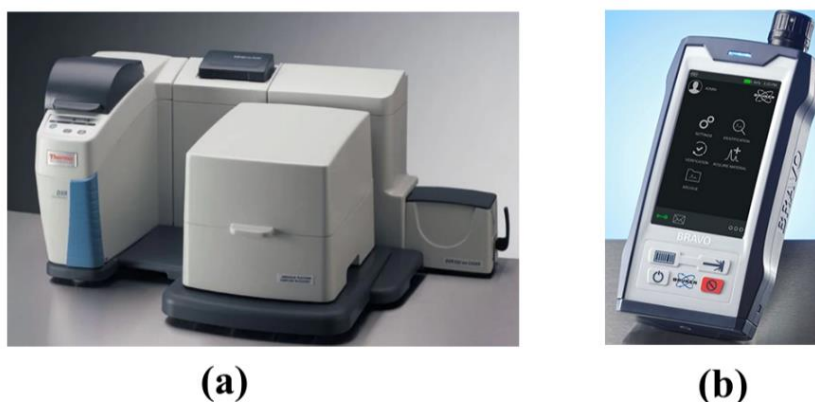


**Figure 2.3.** Raman Spectrophotometer (a) bench top for lab scale and (b) handheld for on-site molecules detection [29].

### 2.1.5 Sample preparation methods

Raman spectroscopy has benefits in numerous research areas. This technique does not require any specific sample preparation method, unlike other chemical analysis techniques. It is a non-destructive and non-invasive technique; hence no contact with the sample is required at all [30]. In this technique, there is a need to just illuminate the sample with a particular laser and then the scattered photons are collected. The most beneficial property of this spectrometer is that the direct analysis of packed products (glass bottles, plastics, and blister packs) can be performed



without disturbing their sealings. For the analysis of liquid samples, two approaches are used. One is the use of a glass cuvette to hold the sample and the other is a drop-casting method. In the second method, variety of molecules such as dyes, pesticides, fertilizers, biomolecules, and environmental containments can be drop-casted onto a solid substrate (silicon/glass). The advantage of this technique over IR is that the aqueous samples can be easily measured; this point is beneficial for the determination of biological, inorganic, and water pollutant samples. The Raman spectrum of water is weak in the fingerprint region, while it shows high absorption in the IR region. In the case of solid samples, there is a need to grind the powder to make it finer. Then the powder is placed onto the substrate and pressed with a clean glass slide to make its surface smooth. Gas samples are also analysed by using this spectroscopy, a specific cuvette which consists of a cylindrical glass tube with mirrors on both ends is used.

#### 2.1.6 *Applications of Raman spectroscopy*

Since its invention from 1928, Raman spectroscopy has been acknowledged as a very useful analytical technique. It is able to provide information which is difficult to obtain with other analytical methods. Due to the invention of laser in 1960, detectors, and filtration methods, Raman spectroscopy has become a preferred tool for chemical and biological applications. It can be used for the quantitative and qualitative determination of organic, inorganic, and biological samples. The Raman spectrum shows well-resolved spectral bands that correspond to the unique fingerprint of the molecule and are used for qualitative analysis. The most beneficial application of it is that advanced carbonaceous materials such as graphene, carbon nanotubes (CNT), and amorphous carbon have been extensively studied with Raman spectroscopy [31].

In the case of CNTs, it helps to reveal the distinctive features of single-walled, double-walled, and multi-walled CNTs. Every CNT has a distinct Raman active mode, known as a radial breathing mode (RMB) at around 100 and 200  $\text{cm}^{-1}$ . This spectroscopy extensively helps to determine the structure of graphene whether it is single-layer, bilayer, tri-layer, or multilayer graphene [32].

Graphene is a 2D material, where  $\text{sp}^2$  hybridized carbon atoms are arranged in hexagonal networks and each carbon atom is covalently bonded to the other carbon atom. The defect-free single-layer graphene shows two characteristic bands named as G ( $\sim$  at 1582  $\text{cm}^{-1}$ ) and 2D ( $\sim$  at 2700  $\text{cm}^{-1}$ ) bands represented in fig 2.4. The full-width half maximum of the 2D band provides information about the number of graphene layers [33]. The increase in intensity of the band and the broadness of the 2D band confirm the increment of graphene layers.

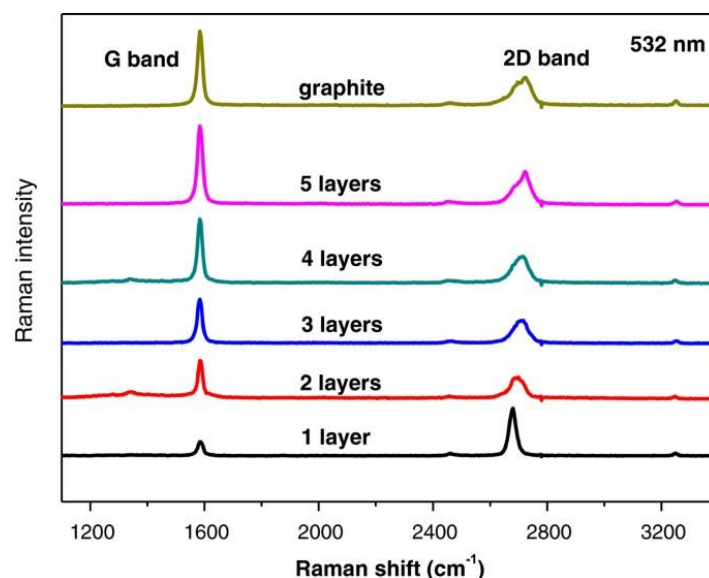


**Figure 2.4.** Raman spectra of few-layer graphene [33].

Amorphous carbon has attracted a lot of attention from the past few years due to its diverse properties, which enable it to be used in a variety of areas like textile, plastic, and healthcare industries [34]. The Raman spectrum of the amorphous carbon shows a G-band (at around  $1510\text{ cm}^{-1}$ ) and a D-band (at around  $1350\text{ cm}^{-1}$ ). By analysing the width of the G-band, the degree of disorder in the sample is measured: the higher the width, the more is disorder.

In the area of cultural property diagnostics, Raman spectroscopy has also attracted great interest. It has been used to determine the degradation and ageing of various paints, artefacts, and statues. It is also able to recognize the composition of the pigments used [35].

As discussed, this spectroscopy has advantage to analyse the biological samples because water does not interfere with the results. Pathological abnormalities such as cancer, inflammation, and infection cause structural and chemical changes, which can be detected during Raman measurements. These changes are very specific and unique, corresponding to the fingerprints of the pathological samples. This fingerprint provides information about the variety of diseases, such as gastrointestinal disorders, brain cancer, dental disease, etc. [36]. This technique has been used to identify different types of biomolecules. Biological materials such as tissue, cells, etc. are composed of different compositions of a variety of biomolecules. Therefore, it is essential to understand the properties and structure of each biomolecule. Each of these molecules has a unique chemical identity. Therefore, these molecules formed a signature Raman spectrum. The Raman spectra of some biomolecules such as bovine serum albumin (BSA), calf-thymus DNA, lipids (cholesterol), and carbohydrates (glucose) is represented in fig. 2.5.

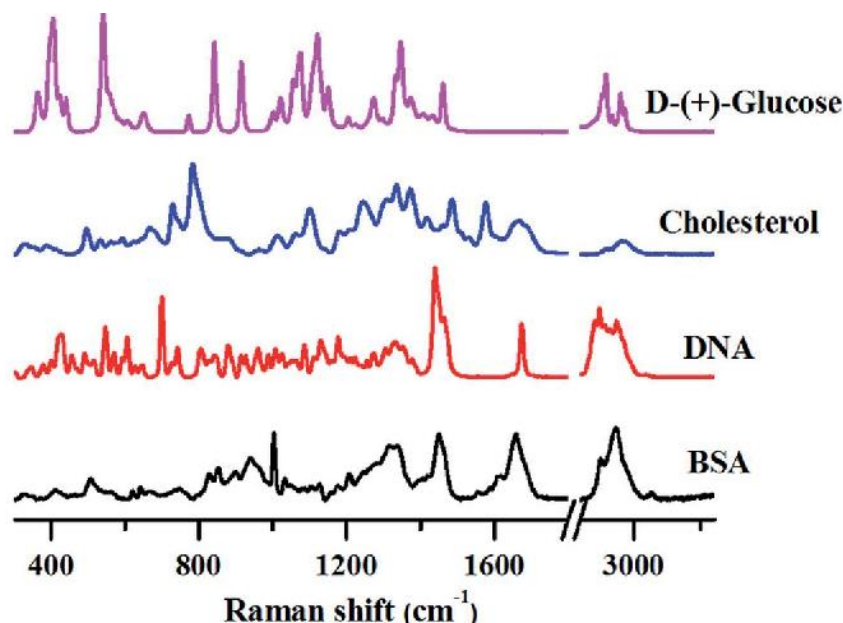


**Figure 2.5.** Raman spectra of various biomolecules [36].

Food and agricultural products are important for life and are also essential for the world economy. Due to the increasing demand of safe, sustainable, and high-quality agricultural and food products, researchers have paid much more attention to these factors from the past few years. Various techniques such as calorimetry, fluorimetry, gas chromatography-mass spectrometry (GC-MS), high-performance liquid chromatography (HPLC), liquid chromatography-mass spectrometry (LC-MS), conductometry, and ion-sensitive field-effective transistors is used for the characterization of these products. These are powerful techniques for composition determination and component quantification, but these methods are time-consuming, require sample preparation (extraction of chemicals), and to operate as well as for the analysis of results an experienced person is needed [37]. Hence, non-destructive and on-field detection is not possible by using these techniques. All these barriers have been overcome by using Raman spectroscopy due to its unique features such as sample preparation is not required at all. This characteristic makes the non-destructive or non-invasive detection possible. The applications of Raman spectroscopy have been explored for the testing of many food and agricultural products such as vegetables, fruits, meat, dairy products, crops, oils, beverages, and coffee[38]. Furthermore, due to the advancement in Raman spectroscopy instrumentation, on-site detection of organic contaminants such as pesticide and fertilizer residues on fruit and vegetable surfaces has been done by using a portable Raman spectrometer.

The use of drugs is one of the biggest problems faced by our society, its use is linked to health problems, violence, and crime. Drugs are generally mixed with other substances and cutting agents to hide their existence from the authorities and to increase the dealer's profit. Techniques such as GC-MS, Fourier transform infrared, UV-visible spectroscopy, and X-ray diffraction are

commonly used to identify these. The problem with these techniques is that on-field detection is not possible due to their bulky size, and the measurement/analysis of results take time. In those areas, Raman spectroscopy has shown the greatest advantage for the detection and distribution of ingredients present in an unknown tablet, powder, pill, or liquid[39].

### 2.1.7 *Limitations of Raman spectroscopy and solution to overcome*

With the distinctive advantages, this technique also faced certain limitations. One is the weak Raman effect and the second is strong fluorescent background noise from the detected molecules when excited with the monochromatic light. The strong background often suppresses the Raman signals of the molecule and as a result, a broad spectrum is observed which is of no use. To overcome this problem, a variety of nanostructured plasmonic substrates and lasers of different wavelengths have been used to remove or minimize the background noise. As discussed, Raman scattered signal is very weak and due to that, it is difficult to detect a lower concentration as well as small volume of samples using Raman spectroscopy.

From the past few decades, a variety of advanced Raman spectroscopy techniques (Resonance Raman spectroscopy, tip-enhanced Raman spectroscopy, Surface-enhanced Raman Spectroscopy, coherent anti-Stokes Raman spectroscopy, etc.) have been developed to enhance its detection ability [40]. But as compared to all the techniques Surface-enhanced Raman spectroscopy has attracted significant attention due to its simplicity. Here the enhancement in the Raman signal is due to the adsorption of molecules onto the nanostructured substrate [41]. In Raman spectroscopy, the molecule is adsorbed onto a flat substrate (glass, silicon, etc.), whereas in Surface-enhanced Raman spectroscopy (SERS) the molecule is adsorbed onto the ordered and disordered metallic structured substrates. SERS is a powerful, highly sensitive, and specific technique; with this technique single-molecule detection is also possible [24], [42]. The detailed explanation of SERS is mentioned in Section 2.2.

## 2.2 *Surface-enhanced Raman scattering (SERS)*

### 2.2.1 *Introduction*

SERS is all about the enhancement of the weak Raman signals of molecules by plasmonic nanostructures by several orders of magnitude. Although Raman spectroscopy is an effective technique for the detection of a variety of molecules, but its use is limited due to the small scattering cross-section of the molecule ( $\sim 10^{-30}$  cm<sup>2</sup>/molecule). The detection of a molecule is not able to provide any meaningful information. Sometimes the high fluorescence from the molecule overwhelms the Raman signals. To achieve high sensitivity as well as to quench fluorescence, it is necessary to use SERS substrates which are able to enhance the Raman signal [43]. The enhancement of signal depends on the size, shape, and interparticle spacing of the nanostructures [44]. The maximum enhancement in the signal is observed in the metallic (Ag,

Au, Cu, and Al) nanostructures with a size smaller or comparable to the wavelength of incident light.

### 2.2.2 *Background*

The SERS phenomenon was first reported by Fleischmann et al. in 1974, the group of researchers noticed an extremely enhanced Raman signal of pyridine molecule which was adsorbed onto roughened silver electrode surface [45]. The reason behind the enhancement has been attributed to the increased surface area caused by the roughness of the silver electrode, which provides more adsorption sites to the molecule for adsorption. However, this simple hypothesis raised a lot of questions. Later in 1977, two independent research groups Jeanmarie and Van Duyne, Albrecht and Creighton reported that the enhancement in Raman signal could not be explained alone by the effect of an increased surface area, instead that other mechanisms also exist [46], [47]. In the early days of SERS, several enhancement mechanisms were introduced; however, only two are widely accepted, i.e., Chemical Enhancement (CE) and Electromagnetic Enhancement (EE) mechanisms. CE (Albrecht) depends on the charge transfer complex formation between the molecule and plasmonic nanostructure, and it is able to enhance the signal by about 2-3 orders of magnitude [30],[48]. Whereas EE is based on the generation of localized surface plasmons (LSPs) when oscillations of free electron density is in resonance with the incident electromagnetic field and it can enhance the signal by ten or more orders of magnitude (Jeanmarie). Later in the 1990s, a colloidal solution of Ag was used for the detection of a fluorescent rhodamine 6G (R6G) molecule [49]. This system showed an enormous enhancement of the order of  $\sim 10^{14}$  and was also able to recognize even a single molecule of R6G. This research made a strong impact on the SERS field and helped the readers to understand the fundamentals of SERS.

### 2.2.3 *SERS enhancement mechanism*

As discussed earlier, enhancement in SERS is mainly due to electromagnetic and chemical enhancement mechanism.

#### 2.2.3.1 *Electromagnetic enhancement mechanism (EM)*

Jeanmaire and Van Duyne first proposed the electromagnetic phenomenon of the SERS effect, which is responsible for the enhancement in Raman signal. This phenomenon depends totally on the roughness present on the substrate surfaces and does not depend on the detected molecule. The mechanism is based on the optical properties of nanostructured plasmonic materials and the main optical property of these materials is localized surface plasmon resonance (LSPR) [50]. LSPR is a phenomenon which occurs when light interacts with the metallic nanostructure (the size of the nanostructure is smaller than the wavelength of incident light) as represented in fig. 2.6. As the electric field is applied to the metal nanostructures, the

conduction electrons start oscillating together leads to the formation of surface plasmons (SPs). The beneficial property of these SPs is that, when the plasmon oscillation frequency is in resonance with the incident light frequency, a local field is created around the nanoparticles. The enhancement in local field depends on the size, shape, and interparticle spacing between the nanostructured materials. When the molecule is adsorbed near this local field, it feels a huge enhanced electromagnetic field and correspondingly emits a highly enhanced Raman signal. The plasmons are of two types: 1) propagating and 2) non-propagating [51]. Propagating SPs are also known as surface plasmon polaritons (SPPs) and are generally represented as a surface wave that is bound to metal-dielectric interfaces and generated onto a planar metallic thin film ( $\sim 10\text{-}200$  nm in thickness). Localized surface plasmon polariton (LSPP) is the standard term used for non-propagating surface plasmons. LSPPs are a type of surface plasmon which are confined to and localized around nanostructures (whose sizes typically fall in the range of  $10\text{--}200$  nm) when incident with excitation light.

In literature, the surface plasmon resonance (SPR) term is popular when the plasmons are excited onto the planar metallic films, and the localized surface plasmon resonance (LSPR) term is commonly used when plasmons are excited onto the nanometric-sized structures. The latter one is responsible for the signal enhancement due to EM mechanism. The EM mechanism is dominant mechanism. Most of the SERS enhancement is due to the EM mechanism and it has the ability to enhance the signal by ten or more orders of magnitude.

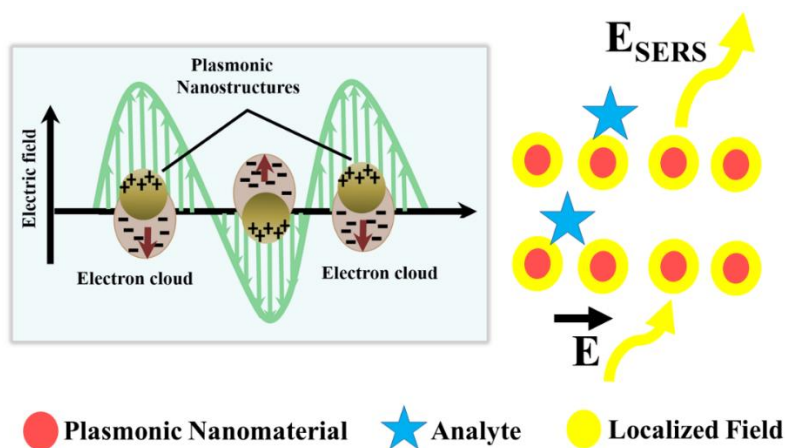


**Figure 2.6.** Left-hand side image shows that when an electric field (green) is applied, the surface electrons (light pink) of the metal nanoparticles start oscillating. The right-hand side image shows the generation of a local electric field around the nanoparticles.

The other way to optimally enhance the SERS signal is the creation of nanogaps ( $\leq 10$  nm) between the nanostructures. These regions are popular by the name of Hot spots. Here the plasmons of adjacent nanostructures are coupled together and due to that a highly enhanced field is generated [52]. Consequently, when the molecule is present in this area, it feels a huge

enhanced electromagnetic field and correspondingly emits a highly enhanced Raman signal. Hot spots can also be generated between NP aggregates or at the sharp edges or tips of individual NPs. The enhancement due to this is highly dependent on the distance between the gaps as shown in fig. 2.7. Such as when the gap size is 2 nm, the enhancement factor is  $10^8$ . When the gap is increasing, the enhancement factor is decreasing respectively. By using a substrate with more nanoregions, it is possible to detect single molecules and make the system more sensitive.

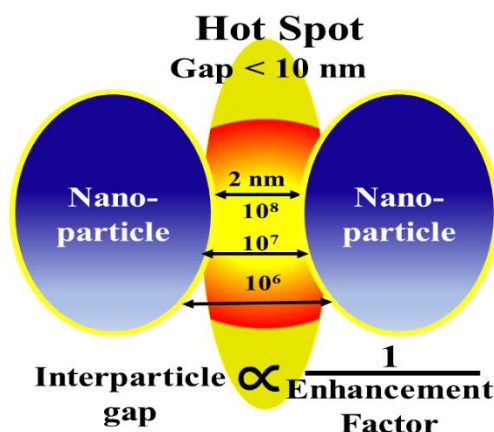


**Figure 2.7.** A schematic illustration of a “hot spot”, is a gap between the nanoparticle dimer and the change in SERS enhancement factor is observed with respect to the particle distance.

#### 2.2.3.2 Chemical enhancement mechanism (CM)

The enhancement in Raman signal due to CM mechanism was introduced firstly by Albrecht and Creighton. The enhancement effect arises due to the chemical interaction between the molecule and the substrate surface and furthermore, it is probe-dependent. The mechanism is also named as charge transfer mechanism; it involves the photoinduced transfer of an electron from the metal's fermi level to an unoccupied molecular orbital of the molecule (LUMO) through indirect coupling [53]. For better signal enhancement, the laser wavelength should be in resonance with the metal-molecule complex. The transfer of energy to the metal causes quenching of the molecule's fluorescence. The contribution of this mechanism in enhancement is relatively less; it is able to enhance the signal only up to  $\sim 10^2$  orders of magnitude. Materials such as semiconductors (Si, GaAs, etc.,) and 2D materials (graphene, MoS<sub>2</sub>, etc.,) show the enhancement due to CM mechanism.

#### 2.2.3.3 SERS enhancement factor calculation

Since the invention of SERS, the magnitude of signal amplification has always been a main focus in this research area, as it provides a clear indication of how effectively SERS performs in comparison to conventional Raman spectroscopy. To measure it, researchers have come up

with a way to figure out the effectiveness of SERS (one of the important SERS parameters) by calculating the enhancement factor (EF) [54]. The enhancement factor is mentioned in eq. 2.11.

$$EF = \frac{(I_{SERS} \cdot C_{Normal})}{(I_{Normal} \cdot C_{SERS})} \quad (eq. 2.11)$$

Where  $I_{SERS}$  and  $I_{Normal}$  correspond to Raman intensity of the molecule on SERS and standard Raman substrate respectively.  $C_{SERS}$  and  $C_{Normal}$  correspond to the molar concentration of molecules on SERS and standard Raman respectively. The important thing is that for the calculation of EF, all the instrumental parameters should be same such as objective lens, laser power, acquisition time, accumulation time, and so forth.

#### 2.2.4 *Materials for SERS substrate*

The maximum enhancement in the signal is observed in the metallic (Ag, Au, Cu, and Al) nanostructures as compared to others [55]. Among them, Ag shows the highest enhancement, because of its excellent plasmonic properties. However, Ag is readily oxidized due to its chemically unstable nature; therefore, Au is widely preferred for the fabrication of SERS substrates (due to its chemically stable as well as biocompatible nature, and also their plasmon resonance frequencies lie in the visible region like Ag) [56], [57]. Therefore, the selection of suitable material is necessary in order to make an effective SERS substrate with good enhancement and better stability. Other materials such as platinum (Pt), gallium (Ga), titanium (Ti), palladium (Pd), indium (In), rhodium (Rh), bismuth (Bi), and ruthenium (Ru), etc. show plasmonic resonance in the ultraviolet region [43].

#### 2.2.5 *Factors affecting SERS performance*

Besides the selection of material, the shape, size, and interparticle spacing between the nanostructures also play an important role in SERS enhancement. From the past few years, researchers have investigated the effect of various parameters on the SERS signal enhancement [58]. It has been stated that substrate parameters such as material, geometry, interparticle spacing and instrumental parameters such as excitation wavelength, pump power, and exposure time affect the SERS performance are mentioned in fig. 2.8. Some of the parameters are discussed below.

**2.2.5.1 *Effect of size:*** The enhancement in signal depends on the optimum size of the nanostructures [59]. If the particles are too small, the light scattering properties decrease which is necessary for the SERS signal enhancement. With the increase in particle size, the SERS effect increases as the electron number increases. When the particle size is about the same as the wavelength of the incident light, the particles are excited to nonradiative modes. This makes the SERS effect weaker.



**2.2.5.2 Effect of shape:** Nanoparticles of different shapes can be formed by adding a variety of capping agents during the synthesis procedure. These can be stars, triangles, cubes, rods, spheres, and of other shapes [60]. However, to get maximum SERS enhancement, it is important to select a proper shape. Depending on the nanoparticle's shape, a wide variety of plasmon resonances can be observed. For example, in the case of star and triangle-shaped nanoparticles, an increase in the localized electromagnetic field is observed from the end of the edges.

**2.2.5.3 Effect of interparticle spacing:** The other thing for maximum SERS enhancement is the interparticle spacing between the nanostructures, which should be less than or equal to 10 nm [61]. And also, the distance between the detected molecule and substrate should be within (1-30) nm.

**2.2.5.4 Effect of excitation wavelength:** The enhancement in SERS signal is highly dependent on the excitation wavelength. The excitation wavelength should be able to generate the LSPR phenomena in the substrate and should be in resonance with the detected molecule. This wavelength can be determined by measuring the absorption spectrum of the substrate as well as the molecule [62]. The selection of the laser wavelength should be close to  $\lambda_{\max}$  of the both materials. All these parameters need to be taken into account for effective SERS performance.

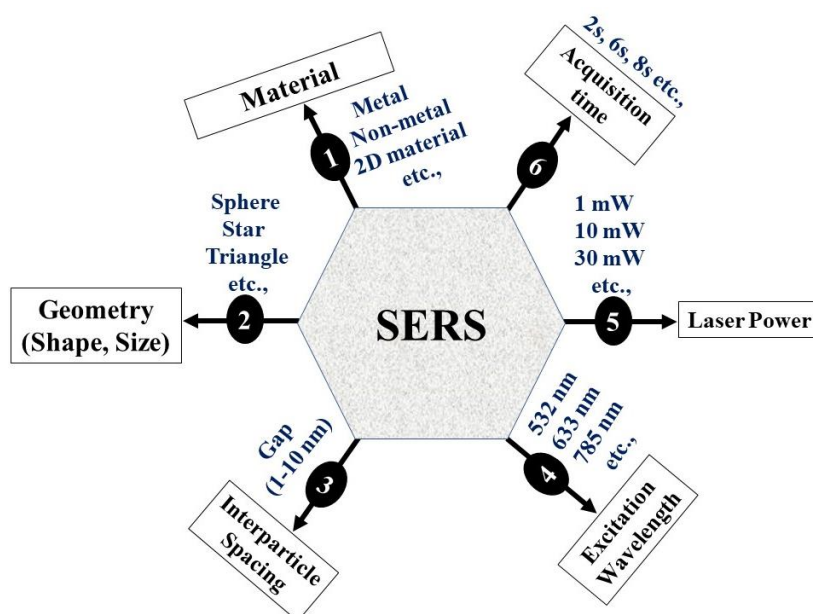


**Figure 2.8.** Schematic representation of the various factors which influence the SERS signal performance.

## 2.2.6 Fabrication methods for SERS

The demand of fabrication techniques is increasing day by day for the improvement in the properties of the SERS substrates, such as the fabricated substrate should be reproducible (Raman signal variation from substrate to substrate), uniform (Raman signal variation from point to point on the same substrate), chemically stable, highly sensitive, and able to show good enhancement factor. Furthermore, the selected fabrication method should be cost-effective,

easy to adapt, and less time-consuming. Over the past few decades, various fabrication methods have been reported to fabricate a variety of nanostructures in order to make effective substrates. These methods can be classified into two categories based on the nanostructure's arrangement: (1) Random morphology SERS substrates (these substrates are easy to make through wet chemical synthesis, spin-coating, drop-casting methods etc.) and (2) Periodic morphology SERS substrates include ordered arrays of nanostructures (these substrates are fabricated by using lithography, sputtering, template-based methods, and related techniques) [39], [63]. Each SERS substrates category is discussed in the following sub-sections.

#### 2.2.6.1 *Random morphology SERS substrates*

Random morphology SERS substrates are characterized as having nonuniform morphology and are often difficult to produce reproducibly. Some of the fabrication methods which provide random morphology are discussed below [64].

2.2.6.1.1. *Wet chemical synthesis:* By using this method, plasmonic nanostructures can be directly synthesized onto the supporting surface via the reduction of metal ions with a reducing agent, during this process surfactant is also added to control the nanostructure morphology [65]. As a result, nanoparticles or continuous film is formed. This method is fast, easy, and able to provide good enhancement factors (due to the formation of a large number of hot spots via NPs aggregation). Therefore, researchers are still involved in colloid-based SERS rather than substrates prepared by sophisticated methods [49].

Despite so many advantages, the metallic nanostructures prepared by using this method are randomly distributed and coated on the supporting substrate. Therefore, the SERS substrate fabricated through a wet chemical route generally suffers from poor uniformity as well as reproducibility (different structures of aggregated clusters) problem every time. This problem can be overcome by immobilizing the NPs onto the pre-functionalized substrate to form an array. This method is called Self-assembly method and is explained below.

2.2.6.1.2. *Drop casting:* It is a commonly used method to fabricate SERS substrates. In this method, the suspension of nanoparticles is drop-casted onto a glass slide and Si etc. and after that the solution is allowed to evaporate [66]. However, with this method, the nanoparticle distribution is not under control, and the reproducibility of the signal is also not guaranteed.

2.2.6.1.3. *Self-assembly method:* As discussed, the wet chemical and drop-casting methods provide a random arrangement of metal nanostructures onto the substrate, which leads to non-uniform and non-reproducible substrates. To arrange nanostructures orderly or ensure their successful adsorption, the self-assembly method can be applied. In this method, before adsorption of nanoparticles onto a substrate, the surface is modified physically or chemically. In this method, a bifunctional molecule is used in order to immobilize the nanostructures in a particular array. One end of the molecule is attached to the substrate

and the other end is free to bind with the NPs. The generally used linkers to functionalize the solid surface are amines and thiols, which are attached to bifunctional silanes. Then a chemically functionalized substrate is immersed in a pre-synthesized colloidal suspension, and along with that a specific number of particles are assembled onto the substrate.

Furthermore, during the immobilization process, parameter optimization such as concentration, nature of the self-assembled molecule, and immersion time of the substrate in suspension can be performed to get a reproducible and uniform substrate. However, by using these techniques the formation of regular arrays is also not guaranteed every time. One literature is briefly explained for a better understanding of the procedure. Sun et al. and his co-workers prepared a flexible SERS substrate by adsorbing Ag nanoparticles onto APTMS (3-aminopropyltriethoxysilane)-modified structured PDMS surface [67]. The Ag NPs bind to the PDMS via the electrostatic interaction, the interaction occurs between the negatively charged Ag NPs and the positively charged amine group on the APTMS. The prepared substrate shows good sensitivity by detecting 4 femto moles of R6G molecule.

The method to assemble nanoparticles via electrostatic interaction is versatile and can be used for the deposition of a variety of nanostructures. The nanostructures can be pre-synthesised by using many methods, and their adsorption can be organized by surface engineering of the supporting film. The advantage of this self-assembly method is that, it is easy, cost-effective, and also large-scale SERS substrates can be easily fabricated.

**2.2.6.1.4. Spin coating:** Spin coating is an effective, easy, and inexpensive method for the preparation of SERS substrates. In this method, the solution of plasmonic nanostructures is drop-casted onto the substrate (Si, glass, PDMS, etc.). After that, the substrate is rotated at a certain speed for a particular time period in order to get a uniform distribution of nanostructures onto the substrate [68]. The advantage of this method is that the morphology (single NPs, aggregated NPs, etc.), thickness of the deposition layer, interparticle spacing between NPs, and coverage area can be easily controlled by varying the spin coating parameters such as concentration of the solution, drop volume, rotation speed, and time.

#### **2.2.6.2 Periodic morphology SERS substrate**

Although metallic colloids are well-known for their high SERS EF and are able to provide high SERS spectra of even a single molecule. However, routinely reproducing such high-performance SERS substrates with uniform, reproducible, and sensitive features is often difficult. To address this problem, various techniques have been introduced for the formation of regular arrays of nanostructures onto substrates. The commonly used techniques for the fabrication of substrates are sputtering, lithography, template-based methods, etc. Lithographic techniques such as nanosphere lithography, electron-beam lithography, focused-ion-beam

lithography, and other photolithographic methods have been widely used for the fabrication of periodic structures [69], [70] and are briefly discussed below.

2.2.6.2.1 *Sputtering*: This method is widely used to fabricate uniform, reproducible, scalable, and controlled-morphology SERS substrates. This method allows the rapid fabrication of films and coatings. The deposition process takes place in a chamber pre-filled with low-pressure argon gas. The film is formed onto a substrate when a DC voltage is applied between the metal target (from where the atoms is to be ejected and deposited onto the substrate surface) and the substrate. The voltage causes the gas to disintegrate into  $\text{Ar}^+$  ions and electrons. Then the positively charged ions accelerate due to the high voltage and strike the target. As a result of collision, the surface atoms are ejected from the target and deposited on the substrate surface in the form of nanostructures or films.

The important thing about this method is, morphology and thickness of the metallic nanostructures/films can be easily altered by varying the deposition parameters such as sputtering voltage, time, and pressure [71]. As discussed, the signal enhancement is inversely proportional to the interparticle spacing (nanogaps  $\leq 10$  nm). Therefore, it is important to fabricate nanostructures with nanogaps for better signal enhancement, which can be easily possible by using this technique. Along with the advantages, this method also has certain disadvantages such as specific equipment, targets, and high vacuum is required, therefore the method is quite expensive which limits its use for many applications.

2.2.6.2.2 *Nanosphere lithography (NSL)*: It is a cost-effective, high-throughput, and easy method to fabricate 2D ordered arrays of nanostructures onto the substrate with controlled size, shape, and spacing [72]. This process starts with the self-assembly of monodisperse polystyrene nanosphere or  $\text{SiO}_2$  nanosphere suspension of the specific diameter onto a precleaned conductive substrate such as indium tin oxide and metal layer over the glass. The suspension can be deposited onto the substrate by spin coating or drop-casting method. As the solvent evaporates, nanospheres get closer due to capillary action and form a periodic mask for metal deposition. Then the metal layer of a specific thickness is deposited onto the mask by electrochemical deposition or magnetron sputtering method. After that, the substrate is sonicated in a solvent to remove nanospheres, which leaves confined metal nanostructures with a triangular footprint behind the surface. By altering the nanosphere size and the thickness of the metal layer deposition, the size, shape, and spacing between nanostructures can be varied to optimize the SERS performance.

2.2.6.2.3 *Electron-beam lithography (EBL)*: It is another method to create a highly reproducible and uniform SERS substrate [73], [74]. It uses a focused electron beam to draw shapes onto a Si wafer covered with an electron-sensitive resist such as polymethyl methacrylate (PMMA). The E-beam alters the solubility of the resist, allowing the removal of the

exposed areas of the resist by submerging the substrate into a developer. Then a thin metal layer is deposited onto a substrate by using a magnetron sputtering and the remaining resist layer is removed by rinsing the substrate with acetone.

Two methods are commonly used to fabricate a variety of nanostructures for SERS substrate, one is the evaporation of Au onto a substrate followed by a lift-off technique. The second method includes reactive ion etching. The key advantage of E-beam lithography over other methods is that it can draw patterns with sub-10 nm resolution due to the shorter wavelength possessed by electron ( $1\text{ \AA}$ ), which is important in the fabrication of SERS substrate. EBL does not require a mask as like photolithography, an image designed on engineering software such as AutoCAD is patterned directly onto a resist through a computer-controlled position of the electron beam. Despite the number of advantages, EBL has certain limitations such as it has a low throughput (takes more than an hour for writing over an area of  $1\text{ mm}^2$ ). The resolution of EBL is good for the preparation of individual particles of various sizes and shapes. Whereas, it is still difficult to fabricate closely spaced nanostructures with a gap of less than 5 nm by using this technique.

**2.2.6.2.4 Focused-Ion beam lithography (FIB):** FIB is better than other nanofabrication methods for many reasons such as 3D nanostructures can be prepared onto a substrate without masks, a single-step is required to fabricate a structured substrate, it requires less fabrication time, and provides a better spatial resolution than EBL (able to write ultra-fine features 15 nm or below). It is generally used in areas where site-specific deposition and ablation at the micro- and nano-scale is required. Currently, its applications have been expanded to many research areas such as nanoscale imaging, material deposition, and removal.

With FIB, complex nanostructures can be fabricated by the removal of the material by ion milling or by deposition caused by the interaction between the gaseous precursor and the ion beam [75]. Most FIB techniques use a liquid metal ion source (LMIS) which is often gallium, placed in contact with a tungsten needle and heated to its melting point. When Ga melts, it wets the tungsten needle and generates a strong electric field in the middle, which ionizes and accelerates the Ga ions. The ions are accelerated through a potential difference of  $\sim 5\text{--}50\text{ keV}$  and focused into a beam onto a sample by an electrostatic lens. When these high-momentum ions strike with the substrate, they knock out atoms from the substrate, which enables fine and detailed patterning of the substrate. Recent FIB systems use a gas-assisted etching through the chemisorption of reactive gasses on the substrate. The generally used gas for this purpose is carbon tetrafluoride ( $\text{CF}_4$ ). It is purged close to the area being sputtered and deposited onto the atoms to be removed. This deposition process

makes the substrate atoms volatile and forces them to evaporate from the surface in a controlled manner.

2.2.6.2.5 *Template-based method:* Lithography techniques are able to provide uniform as well as reproducible substrates. But the use of these techniques is limited due to their cost, complex fabrication methods, and low throughput. In addition to the lithographic methods, template-based methods have also gained attention from the past few decades due to their ease of manipulation and capability to generate periodic nanostructures over a large area [76]. There are numerous templates available such as anodic aluminium oxide (AAO), porous silicon, and titania nanotube-based arrays which are commonly used for sensing applications. As compared to all, AAO is a widely used template due to its fast, simple preparation steps and its ability to provide ordered arrays of nanostructured pores with controlled nanoscale geometry. The geometry of the AAO such as pore diameter, inter-pore distance, and pore length can be modified by adjusting the anodization conditions (concentration, electrolyte type, temperature, voltage, and time). The AAO-based SERS substrates are fabricated by depositing a plasmonic (Ag and Au) metallic layer on the substrate via a sputtering or thermal evaporation system. The thickness and interparticle distance between NPs can be varied by varying the time duration of the deposition process.

#### 2.2.7 *Applications of Surface-enhanced Raman scattering substrates*

As discussed, Raman spectroscopy is able to provide information about the unknown molecule, but due to the weak signal strength its use for an application point of view is limited. The invention of SERS led to a new evolution in Raman spectroscopy, due to its signal amplification ability which has made it possible to detect trace amounts or even single molecules [49]. As like Raman spectroscopy, SERS has been extensively used for the detection of a wide variety of molecules such as environmental pollutants, especially aromatic dyes, pesticide/fertilizer residues, pharmaceutical contaminants, explosives, and biomolecules, etc. There is also a great demand for the detection of trace amounts of harmful chemicals due to their increased risk to food as well as environmental safety. Melamine is a chemical substance which has been used as an additive to raise the protein content in milk and pet food [77], [78]. However, since 2007, melamine along with its contaminant cyanuric acid has become prominent due to the milk controversy.

As a sensitive and specific technique, SERS has been used to identify the presence of melamine content. Furthermore, SERS has been extensively used for bioimaging and bioanalysis, including the identification of biomolecules, cancer diagnosis, detection of urine components, and in vivo molecular probing in live cells, which play an important role in the field of life science for health monitoring or treatment [79], [80], [81], [82], [83], [84]. It has also been used for real-time rapid monitoring of ongoing chemical reactions such as catalytic reactions and

provides an opportunity for the long-distance monitoring of atmospheric airborne species (gases, aerosols, and volatile organic compounds) at the ppb level [85].

#### 2.2.8 *Limitations of Surface-enhanced Raman scattering*

Although SERS has developed as a potential tool for biological and chemical sensing, still it has certain limitations like other techniques. Glass slides and Si substrates are the two most common base substrates used for the formation of SERS active layers. Whereas, these base substrates are brittle and rigid. Other factors which limit the potential of these substrates is that they cannot be applied onto curved surfaces as well as show poor adhesion property upon attachment to the surface. The detection of molecules onto a curved surface with these substrates requires some pre-treatment steps; hence non-invasive detection is impossible.

From the past few years, efforts have been initiated to fabricate flexible SERS substrates. Flexible substrates have advantages over rigid substrates as they can be wrapped onto irregular surfaces (fruit, suitcase, table, bag etc.) and can be cut into different sizes and shapes as per the application demand. Furthermore, non-invasive and in-situ detection can also be possible. The flexible and rigid substrates have their own benefits and drawbacks in their respective fields. The rigid substrates generally show better uniformity, reusability, and high enhancement factor compared to flexible substrates. The molecule collection (substrate is rubbed onto the sample surface) and cost have made a strong impact on the daily usage of this rigid substrate for practical application.

Some flexible materials such as nanocellulose, polymer, paper, and adhesive tape have received great attention to fabricate flexible SERS substrates. Furthermore, these substrates can be combined with handheld Raman spectrometers for on-site detection which can be beneficial in real-world applications for food safety, drugs, explosives, as well as environmental pollutants, etc. The selection of a suitable substrate is extremely essential for effective SERS performance. There are some requirements of effective substrate for real-world applications which are further mentioned such as substrate should be (a) cheap (fabrication method should be cost-effective and easy to use), (b) sensitive (able to detect low concentrations of molecules), (c) uniform (less signal intensity fluctuations over the entire substrate) ( $RSD \leq 20\%$ ), (d) reproducible (less signal intensity fluctuation from substrate to substrate ( $RSD \leq 20\%$ )), (e) reusable (able to reuse by simple cleaning process), (f) stable (signal intensity variation should not vary  $> 50\%$  at least for a couple of weeks), as well as (g) flexible (able to collect samples from irregular surfaces also). Figure 2.9. demonstrates the key factors of SERS substrate requirement.

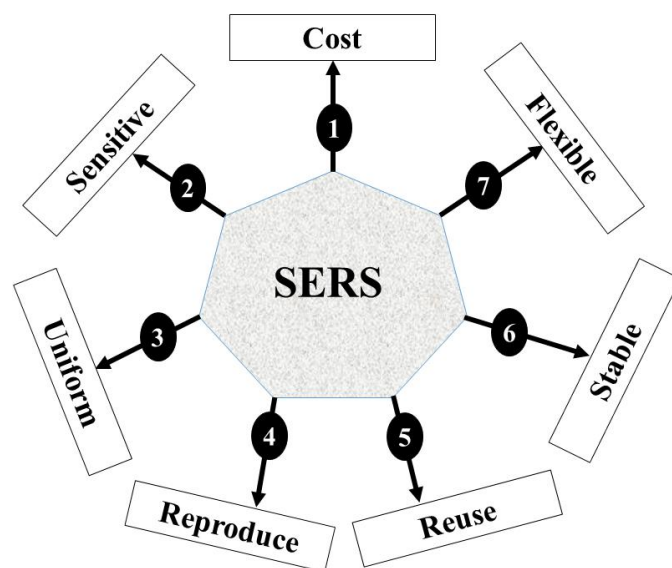


**Figure 2. 9.** The key requirements of SERS substrate is described in this graphic.

In this thesis, both solid as well flexible SERS substrates has been fabricated by the facile and reproducible method. After the fabrication, the effectiveness of both substrates has been tested by detecting the R6G molecule (organic contaminant) and these substrates have also been used to detect urea (fertilizer) for real-world application purposes. The solid substrate is prepared by a cost-effective dealloying method. The  $\text{Ag}_{50}\text{Au}_{50}$  alloy sheet is dealloyed into nitric acid ( $\text{HNO}_3$ ) for a varied time-period from 5-65 minutes with an interval of 5 minutes to determine which dealloying time shows the highest enhancement in the signal. The nitric acid basically etches the Ag and the final structure appears in the form of nanoporous gold (NP-Au) which is SERS active. In addition, the effect of laser power variation from 0.01 to 10 mW (of Raman spectrophotometer laser) onto the morphology and SERS performance of NP-Au is also examined. The flexible substrate is prepared by replicating the pattern of red Rose by using a polymer such as PDMS in order to make a patterned substrate. The nanocasting approach is used to create the inverted texture of Rose and then the textured substrate is made SERS active by the deposition of pre-synthesized Au NPs via the self-assembly approach.

#### 2.2.9 SERS substrates based on rigid substrates

It has been discussed in detail that an increase in SERS signal intensity is observed due to the generation of LSPRs around the nanostructures or the formation of hotspots between the nanostructures. Generally, the colloidal suspensions or films made of silver (Ag) and gold (Au) nanoparticles (NPs) are used as SERS substrates which show remarkable SERS enhancement from “hot spots” generated due to aggregation. It is well known that aggregation is an uncontrolled phenomenon and it is often difficult to get a similar morphology of aggerates (same number of nanoparticles clustering) every time. Therefore, the reproduction of similar-



intensity SERS signals becomes a challenge when using these kinds of substrates [86], [87]. As discussed earlier, the reproducible/uniform SERS substrate can be fabricated by using lithography, sputtering, and template-based methods. However, the use of these methods for making SERS substrates is limited because of their cost, complicated fabrication procedures, and along with that the limited area of the substrate is achieved.

As compared to the earlier discussed techniques, from the recent decades, the dealloying method has been proposed as an alternative technique for the preparation of effective SERS substrates due to its easy, fast, single-step fabrication method and low processing cost [88]. This method does not require specific setup and working conditions such as a clean room, metallic targets, patterned masks, and photoresists, as like the earlier-mentioned techniques and furthermore, highly ordered nanostructures over large areas can be easily fabricated by using these techniques. This method is discussed and used in this thesis for the fabrication of SERS substrates.

#### *2.2.9.1 Nanoporous structured substrate fabrication methods*

Dealloying process provides a bicontinuous porous structure which is made up of nanosized pores and ligaments, the substrates with that kind of morphology are commonly known as porous substrates. This kind of structure is made by the leaching of less noble elements from a precursor alloy by chemical etching. Generally, acids ( $\text{HNO}_3$ ,  $\text{HCl}$ ) or bases ( $\text{NaOH}$ ) are used to dissolve metal elements such as Ag, Cu, and Al from the alloy except Au [89]. These porous films have attracted increasing attention from the past few years due to their distinct advantages such as high surface area, high electrochemical conductivity, and ability to tune the surface features (morphology and volume of pores and ligaments) by varying the parameters i.e., the alloy composition, etching time, and the etching solution concentration [90].

Among the porous films, a gold film made via an AgAu alloy is widely used due to its unique surface chemistry, chemical stability, and homogenous morphology throughout the surface due to the existence of similar lattice parameters as well as a single-phase crystal structure [88]. These films have been used in various fields for example in dye-sensitized solar cells, supercapacitors, electrochemical catalysis, and as a Raman sensor for chemical analysis [89]. In addition to dealloying, these films can also be made by other methods such as templating, self-assembling and dynamic hydrogen bubble templating. Each fabrication method is briefly discussed below.

##### *2.2.9.1.1 Dealloying*

It is a corrosive method of alloy components and involves the selective leaching of the active elements from the alloy as shown in fig. 2.10. It is widely used in the NP-Au formation due to its easy fabrication nature and the availability of commercial high-purity Au-M alloys. These Au-M alloys can also be made by sputter coating, casting, or molecular

beam epitaxy. The ‘M’ word corresponds to less noble elements such as Cu, Zn, Ag etc. The less noble metals should be present in sufficient quantities to attain the partitioning limit of the alloy. The limit is found to be 40% in the case of Au-Cu alloys and 50% for Au-Ag alloys [91]. The dissolution of less noble metals has been studied extensively both theoretically and experimentally[88].

The dealloying method of Au-Ag alloy was first introduced by Erlebacher et al. They have discussed the formation of porosity in Au-Ag alloy occurs due to the chemical-driven aggregation of Au atoms by a phase separation process [92]. The formation of pores during the dealloying process follows two stages. In the first stage, dissolution of the less noble element is observed and in the second stage, diffusion of atoms of stable element starts and causes the morphological change [57]. The diffusion of atoms continues until the alloy is immersed in the electrolyte, which leads to the interconnected pores and ligament coarsening. The surface diffusion of atoms in electrolyte permits atoms to locally reorganize into the porous network. The movement of atoms can be quenched immediately by simply transferring the leaf from the acid to water

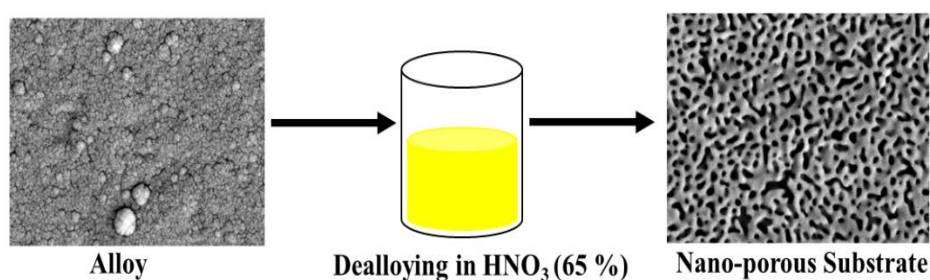


**Figure 2. 10.** Pictorial representation of nano-porous substrate formation from alloy.

The dealloying is further classified into two processes: chemical and electrochemical dealloying.

#### 2.2.9.1.1.1 *Chemical dealloying*

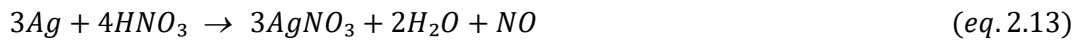
Chemical dealloying is based on the chemical reactivity of the metal and the process is also known as chemical etching. As Au is a chemically stable metal, in contrast to it acids or bases ( $\text{HNO}_3$ ,  $\text{HCl}$ , and  $\text{NaOH}$ ) are commonly used to etch other metal components such as Al, Sn, Ag, and Cu by performing specific chemical reactions between the illuminated metal atom of interest and the solution (acid or base).

In the current work, NP-Au has been fabricated by dealloying of  $\text{Au}_{50}\text{Ag}_{50}$  alloy leaf in  $\text{HNO}_3$ . The mechanism of NP-Au fabrication is multistep: initially, the Ag atoms dissolves, followed by Au atoms filling the vacant sites through substitutable diffusion. Finally, the coarsening of Au atoms leads to the formation of Au islands or ligaments. The schematic which shows about the pore formation mechanism is represented in fig 2.11 and explained

further. The process starts with the dissolution of Ag atoms from the first layer (terrace) of alloy (atoms with closed pack (111) orientation) after immersion in the acid and which leaves behind a terrace vacancy and Au atoms (“adatoms”).

The chemical reaction is mentioned below, which shows the by-products after immersion in  $\text{HNO}_3$ . The atoms coordinating this vacancy have a lesser number of lateral neighbours in the terrace than other Ag atoms and thus are more prone to dissolution [92]. Thus, the whole terrace is etched, leaving behind Au atoms on the terrace with no lateral coordination. Before the second layer is attacked, these Au adatoms diffuse and begin to agglomerate into islands [90]. As a result, instead of the formation of a uniform diffuse layer of Au over the entire terrace, the terrace is composed of two different regions, namely, pure Au clusters that protect the surface locally, and patches of the un-dealloyed sample exposed to an electrolyte. As the Ag atoms from the patches dissolve into  $\text{HNO}_3$  solution, the Au adatoms are simultaneously released onto the terrace. These atoms diffuse to the Au clusters, which are formed by the dissolution of previous layers. Along with that, the etching of un-dealloyed sample continues. During the initial phases, these Au clusters are in the shape of hills that are Au-rich at their peak side and while their bases have an alloy composition. With time as more layers is exposed, these hills get undercut and lead to the formation of ligaments and pores.

The Ag atoms dissolve in  $\text{HNO}_3$  by the following redox reactions [93].



The biproducts from the reaction are  $\text{AgNO}_3$  and  $\text{H}_2\text{O}$  (released in liquid form) and  $\text{NO}_2$  or  $\text{NO}$  (released in gas form) are easily separated from the alloy leaf during immersion in acid.

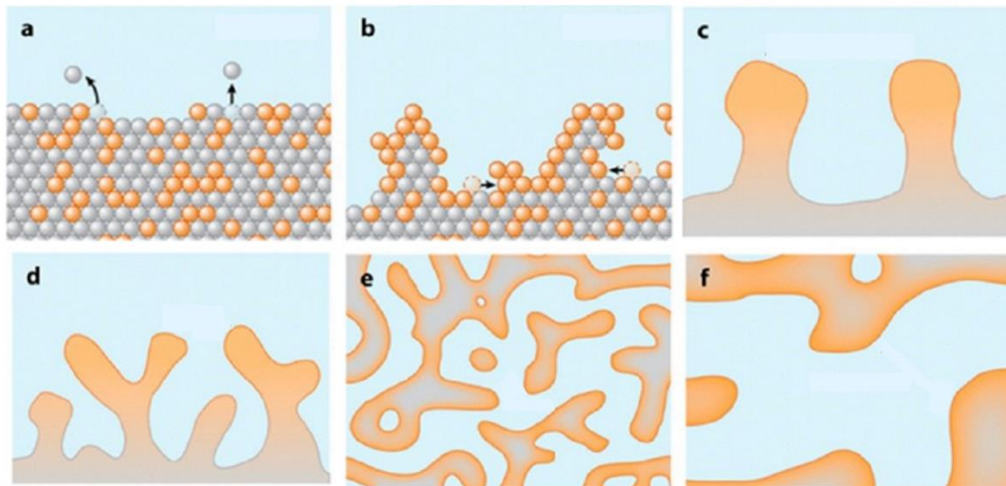


**Figure 2. 11.** represents a step-by-step pore formation mechanism in an Ag-Au alloy (Au (orange) and Ag (grey)). The fig ‘a’ demonstrates the removal of Ag atoms from the terrace and the vacancy

generation, which is later converted into Au clusters by substantial diffusion as can be seen from fig 'b'. As the dissolution processed from layer to layer, coarsening of Au atoms occurs, which leads to the formation of hills-like structure first (fig. d) and then the structure changes to islands with time (fig. e). At the end, the entire surface is made up of pores and islands of Au atoms (fig. f) [89].

Ding et al. examined the effect of dealloying time on the NP-Au morphology. They studied for different periods of time such as for 5 minutes, 15 minutes, 1 hour, or 1 day, and noticed that the immersion of the leaf in acid for different periods of time leads to coarsening and the formation of larger pores [94]. It can be observed from fig. 2.12. that, after 5 minutes small pores were generated and were separated by Au ligaments. The continuous immersion in acid for another 15- and 60-minutes leads to the coarsening of pores and ligaments due to the substitutable diffusion of Au atoms along with the etching of Ag. This dealloyed sample was stable, and no morphological changes were observed even after six months.

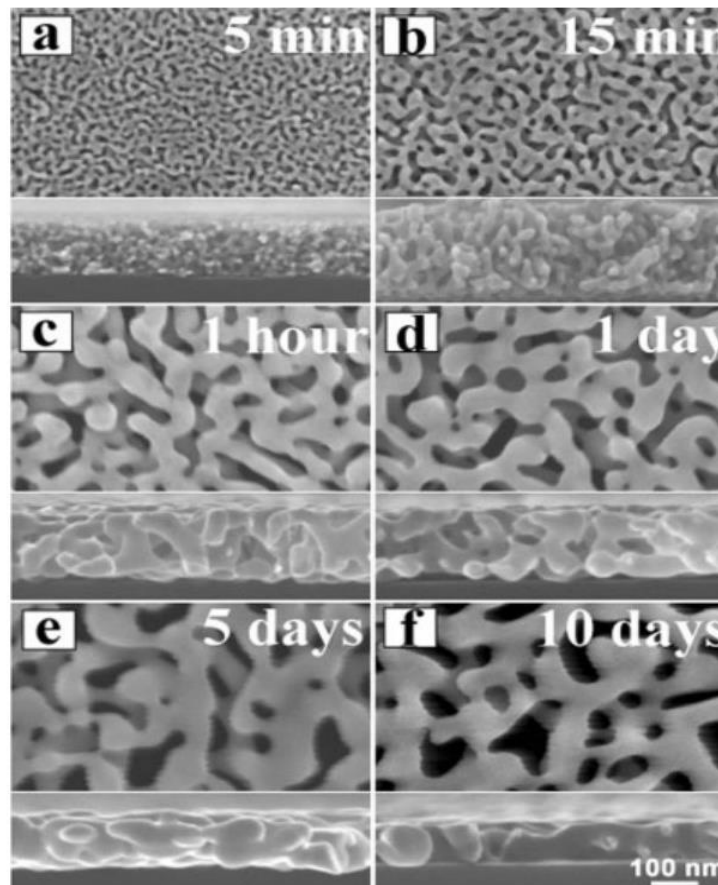


**Figure 2. 12.** Morphological and cross-sectional view of NP-Au substrates show coarsening of ligaments and pores upon continued immersion in acid for varied time period [92].

In another literature, Sun et al. studied the effect of corrosion onto the Au:Cu alloys prepared with different ratios and deposited on Si or glass via the sputtering method[95] . The alloy is dealloyed by the dissolution of Cu in  $\text{HNO}_3$ , which leads to the formation of an NP-Au thin film. The study demonstrated that an Au-Cu film with a higher Au content showed slow kinetics

in NP-Au formation; therefore, dealloying was performed for a longer time to increase the porosity rate. Quian et al. examined the effect of thermal annealing on to the morphology of ~ 55 nm pre-dealloyed NP-Au. They observed that further annealing for 2 h leads to the coarsening of the ligaments with pore sizes ranging from ~90 nm at 200 °C to 700 nm at 700 °C. It has been stated that annealing restarts the diffusion of Au atoms in the sample, which was stopped by immersing it in water [96].

#### 2.2.9.1.1.2 *Electrochemical dealloying*

It is type of dealloying. Here, the electrochemical activities of the metals in the alloy determine the dissolution order [97]. Au is the hardest metal to dissolve electrochemically, therefore it lies at the bottom of the metal element series. By using this method, fabrication factors such as pore dimensions and uniformity of NP-Au can be controlled as well as monitored at higher levels. This method can effectively eliminate the need of the pre-formation of Au-M alloys through an in situ electrochemical alloying or dealloying process. The electrochemical alloying/dealloying method is a one-step method to form NP-Au, in this method, an Au electrode is inserted into a three-electrode cell which contains an electrolyte and metal ions such as Ag, Zn, Cu, etc. Cyclic voltammetry (CV) is scanned over a potential window with a scan rate between 5 and 50 mVs<sup>-1</sup>, which enables the electrochemical alloying and dealloying process [98]. The metal ions are reduced in solution at the Au working electrode side due to cathodic potential and generate an Au-M alloy. The anodic scan oxidizes the alloy and detaches it from the Au electrode, which leaves the surface with pits. By continuing the alloying and dealloying process, the pits become wider and deeper. Hence results in the formation of nano-porous structure. Another type of electrochemical method is the direct oxidation or reduction of Au electrode without the need of a metal ion electrolyte to promote alloying and dealloying.

Sukeri et al. observed the formation of an oxide layer on the Au electrode by immersing it in a 0.5 M H<sub>2</sub>SO<sub>4</sub> solution against the Ag/AgCl reference electrode at ~ 2.0 V potential. The electrode reduction causes the oxide layer pitting, which results in the formation of NP-Au surface [99]. The anodization process is a great example of green chemistry, where fabrication methods are optimized to minimize the number of chemicals consumed. In other literature, it has been stated that porous structures can be formed via the electrochemical deposition method without the use

of alloying and de-alloying methods. In this method, an electrochemical reaction between the Au and HCl in an electrochemical cell happens, where the electro dissolution-disproportion-deposition processes are involved [100]. Firstly, the electro-dissolution of an Au substrate occurs under a diffusion control of HCl, which creates  $\text{AuCl}_2^-$ , after that the  $\text{AuCl}_2^-$  instantly disproportionate into Au atoms; and finally, the Au atoms aggregate and deposit on the Au substrate, providing a porous Au film. One more approach to produce porous Au film is to reduce Au ions from  $\text{HAuCl}_4$ . The Au nanoclusters was formed by applying a constant potential to the substrate which is based on the material, e.g., 0.28 V (vs saturated calomel electrode) on an indium tin oxide electrode, - 0.5 V (vs Ag/AgCl) on a glassy carbon electrode in the presence of lead acetate, and - 0.1 V (vs. Pt) on an Au electrode in the presence of lead (IV) acetate [101], [102]. After the nanocluster formation, they aggregate in the form of a porous Au film on these substrates. This technique is commonly combined with a templating method which is discussed below.

#### 2.2.9.1.2 *Dynamic hydrogen bubble method*

It is another method to produce NP-Au. Metals such as Au, Cu, Ag, Zn, and Sn, have been widely used to generate nanoporous structures via this method. The basic mechanism behind this method is as follows: the electrolyte of a three-electrode cell is made up of a less amount of ammonium and a lower concentration of chloroauric acid (0.1 M), with a Pt as a counter electrode against a Pt or Ti as a working electrode. A potential within the  $\text{H}_2$  evolution regime ( $\sim -4$  to  $-8$  V) is supplied to the working electrode side [103]. Then at the electrode surface,  $\text{H}_2$  evolution and Au ions reduction occur simultaneously. Gas nucleation, coalescence, and desorption at the electrode surface led to the formation of a self-supporting Au thin film, which consists of micrometre pores with nanoporous features. Wei et al. revised the method by repeating the  $\text{H}_2$  evolution/Au oxidation and reduction on the working electrode (Au disk) side by using square wave potential pulse voltammetry and switching the potential between + 0.8 and - 5 V at 50 Hz as shown in fig 2.13. When the potential was maintained at 0.8 V, the gold was oxidized, along with the release of oxygen gas. The produced oxide layer was reduced to gold metal when the potential was changed to - 5 V, and this Au metal was then self-assembled under the action of intense hydrogen bubbles. The 2D and 3D porous structures were formed as the cycle was repeated.

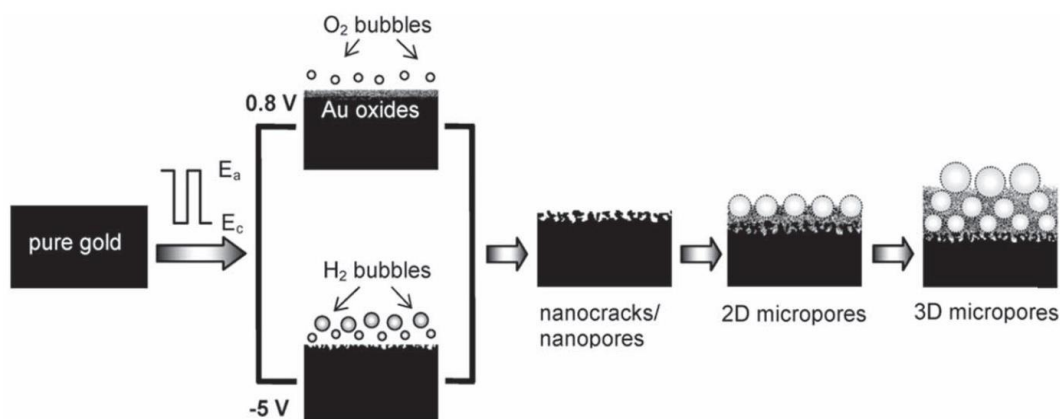


**Figure 2. 13.** Schematic representation of NP-Au template formation by dynamic hydrogen bubble route using square wave potential pulse voltammetry approach [101].

In addition to the above-discussed methods, there are other methods to fabricate porous Au films such as template-based method, self-assembly, and sputtering, etc.

#### 2.2.9.1.3 *Template-based methods*

In this method, a template is first prepared, then Au is deposited onto it, and finally the template is removed [104]. The template can be a layer of assembled particles, an ion-etched substrate, or a biologically generated template [105]. Polystyrene beads or silica particles are generally used to assemble the particles as templates. Then the Au is electrochemically deposited onto the template by electrochemically reducing Au from the  $\text{HAuCl}_4$  solution. There is another method to create a porous gold film in the liquid phase using the droplet condensation of water, where the condensed water droplets produce the pores and Au NPs are deposited at the gap between the droplets [106].

#### 2.2.9.1.4 *Self-assembly method*

It is also used to obtain porous structure. This method does not depend on external assistance as like templating methods, the self-assembly of the Au NPs can directly create the porous structure. The generation of porous structure is based on the coalescence and aggregation of particles. Zhang et al. and his co-workers discussed an evaporation-induced self-assembly approach to form porous Au from colloidal Au solution. The porous Au film fabrication has been done by evaporating the colloidal Au solution [107]. The Au NPs are concentrated at the capillary meniscus and after that, they coalesce into nanowire-like structures. Then their growth is extended to the surface of colloidal Au solution, resulting in a porous Au film. Various morphologies of pores can be generated by varying the evaporation conditions.

#### 2.2.9.1.5 *Sputter deposition method*

In this method, the porous Au film can be formed using templating process alone or by a combination of electrochemical etching and templating methods. Patterned templates for deposition can be formed by photolithography, where the patterning is commonly done by an optical mask. Wi et al. formed a complicated porous gold film, where pores were created in the gold film by a de-alloying technique. First, a porous template was fabricated by lithography, and then by sputtering, an alloy film of Au-Cu was deposited [108]. After that, by dealloying, smaller pores were created with the dissolution of Cu.

As compared to the discussed fabrication methods, dealloying is a simple, fast, and regularly preferred approach for the fabrication of NP-Au from preprepared Au-M alloy leaves, which is extensively available for purchase and cost-effective (Rs 2000, 25 sheets ( $8 \times 8 \text{ cm}^2$ )). As discussed earlier, by using this method bulk scale and large area samples ( $10 \times 10 \text{ cm}^2$ ) of repeatable morphology can be fabricated in a lab without the requirement of specific equipment and clean room facilities, which are generally needed in lithography and sputtering techniques.

#### 2.2.9.2 *Rigid substrate-based SERS sensors*

Due to the distinctive characteristics of NP-Au (chemical stability, high surface area, facile fabrication, tuneable pore/ligament size, and easy surface modification), it has been used for various application purposes, widely as an electrochemical, bio-electrochemical, and optical sensor due to its ability to detect many harmful molecules such as heavy metals, food contaminants, and drugs etc. The detection method of the mentioned sensors is discussed below.

##### 2.2.9.2.1 *NP-Au based electrochemical sensor*

Electrochemical sensors based on NP-Au showed significant attention towards the detection of biomarkers, environmental pollutants, as well as additives and contaminants in food products, etc. due to their high stability and large surface areas.

##### 2.2.9.2.1.1 *Electrochemical sensors for biomolecule detection*

The detection of biomarkers such as dopamine (DA), nitric oxide (NO), glucose (Glu), and ascorbic acid (AA) is required in medicine due to their biological significance. These can be identified by examining the direct oxidation at the electrode surface. DA plays an important role in facilitating the function of the mammalian central nervous system. It is necessary to identify DA for the treatment of cognitive diseases. Xiao et al. prepared a paper-based highly conductive NP-Au film composed of Au NPs placed on top of a matrix of metallic single-walled carbon nanotubes on mixed cellulose ester filter paper [109]. The prepared film was used to detect serotonin and DA by cyclic voltammetry, it showed a linear range from 250 nM to 1 mM with a detection limit of 50 nM for serotonin and from 50 nM to 1 mM with a Limit of detection 10 nM for DA. Other group fabricated a DA



sensor based on a NP-Au microelectrode, where the NP-Au was fabricated by the electrochemical anodization-reduction of Au microelectrode in an  $\text{H}_2\text{SO}_4$  electrolyte. Square wave voltammetry showed a sensitivity of  $1.18 \text{ mA } \mu\text{M}^{-1}\text{cm}^{-2}$  and a detection limit of 30 nM [99].

As like DA, AA plays an important role in the body, as it is a necessary nutrient for humans and animals, which is involved in metabolism. The detection of AA is advantageous for food safety applications and medical diagnostics. Huang et al. demonstrated the Au NPs ( $\sim 2\text{-}5 \text{ nm}$ ) synthesis by anodically suspending a gold wire in an acidic solution containing  $\text{Cl}^-$  and  $\text{SnCl}_2$  [110]. The Au NPs modification onto a glassy carbon electrode led to the formation of a hierarchical NP-Au structure due to the protective residual Sn oxide layer. The prepared NP-Au sensor showed good performance for the amperometric identification of AA and high electrocatalytic activity for AA oxidation with a good sensitivity of  $10^{33} \mu\text{AmM}^{-1}\text{cm}^{-2}$ , and a low detection limit of 0.06  $\mu\text{M}$ . Liu et al. prepared NP-Au via electrochemical dealloying of an Au microwire [111]. The NP-Au exhibited improved electrocatalytic activity for NO oxidation, which is 6.23 times greater than the bare Au microwire electrode, and showed good performance for the identification of NO by differential amperometry and pulse voltammetry. Additionally, the fabricated NP-Au has been tested for the in-situ identification of NO release from numerous cells.

#### 2.2.9.2.1.2 *Electrochemical sensors for food safety*

Food safety has attracted a lot of attention due to the presence of a wide variety of chemical additives and contaminants. Electrochemistry is an effective and easy approach to determine the quality of food as well as its safety, in this kind of method the electrode material plays an important role in the sensor's design. Sensors based on these methods have been widely used for the determination of numerous food additives and contaminants, such as hydrazine ( $\text{N}_2\text{H}_4$ ), bisphenol A (BPA), nitrite ( $\text{NO}_2^-$ ) and sulfite ( $\text{SO}_3^{2-}$ ).

Fang et al. prepared NP-Au via the anodic etching of Au in a mixture of dimethylformamide and hydrofluoric acid [112]. After modification with SWNTs, the fabricated BPA sensor is able to detect a lower limit of  $\sim 100 \text{ nM}$ . Li et al. prepared a dual-signal BPA sensor by self-modification of thiolated beta-cyclodextrin on the NP-Au surface. The particular sensor is able to detect BPA in tap water and milk with a limit of up to  $\sim 60 \text{ nm}$  [113]. Manikandan et al. used an electrochemical dealloying approach to prepare NP-Au and used it for the recognition of  $\text{N}_2\text{H}_4$ ,  $\text{NO}_2$ , and  $\text{SO}_3^{2-}$  by differential pulse voltammetry. The detection limits for  $\text{N}_2\text{H}_4$ ,  $\text{NO}_2$ , and  $\text{SO}_3^{2-}$  are 0.911, 1.44, and 0.337  $\mu\text{M}$ , respectively. Further, the sensor has also been tested for real samples of wine, water, beef, and apple cider beer and showed good accuracy [114].

#### 2.2.9.2.1.3 *Electrochemical sensors for environmental application*

The existence of heavy metals such as  $\text{Hg}^{2+}$ ,  $\text{Ag}^{3+}$ ,  $\text{Pb}^{2+}$ , etc. in the environment leads to serious threats to both animal as well as human health, and natural ecosystems. Therefore, it is required to fabricate an easy and suitable sensor for the detection of these pollutants. The electrochemical method is a reliable approach among different analytical methods. Liu et al. prepared a  $\text{FeOOH}/\text{NP-Au}$  based sensor that was able to detect  $\sim 7.81 \text{ nM}$   $\text{Hg}^{2+}$  ions and showed a linear range of  $0.02 - 2.2 \mu\text{M}$ . The sensor was fabricated by first preparing NP-Au by electrochemical dealloying method, and then  $\text{FeOOH}$  nanoflakes were decorated onto its surface by electrodeposition [115]. Fang et al. fabricated NP-Au by dealloying Au-Zn alloy in  $\text{ZnCl}_2$ -urea deep eutectic solvent [116]. The porous substrate was highly sensitive to recognize nitrobenzene and  $\text{Hg}^{2+}$  ions by cyclic voltammetry.

#### 2.2.9.2.1.4 *Other sensing applications based on electrochemical approach*

NP-Au based films can also act as good sensors for the identification of other molecular species. Cui et al. fabricated a NP-Au@Ni electrode via dealloying of an AuSn film, which was electrodeposited onto a Ni foam. This electrode showed a good detection limit of  $10 \mu\text{M}$  and  $33 \text{ nM}$  for  $\text{H}_2\text{O}_2$  and  $\text{N}_2\text{H}_4$ , respectively [117]. Another group prepared Pt NPs decorated with NP-Au by electrochemical dealloying approach [98]. The mentioned sensor showed good selectivity and sensitivity with a detection limit of  $0.3 \text{ nM}$  for hydrogen peroxide reduction. Hu et al. used an array of NP-Au for the electrochemical sensing of  $\text{O}_2$  in an ionic liquid. The  $\text{O}_2$ -based sensor showed a fast response ( $< 10 \text{ s}$ ) and exhibited a low detection limit [118].

#### 2.2.9.2.2 *Nanoporous gold Based optical sensors*

When metal dimensions are reduced to the nanoscale, NP-Au shows distinct optical characteristics due to LSPR phenomena. This phenomenon makes these substrates suitable for optical sensors when combined with other spectroscopic techniques such as UV-Vis, Raman, or photoluminescence. In the case of NP-Au, the number of peaks and peak position depend on the pore size. Chen et al. demonstrated that NP-Au with pores sizes of 7, 12, and 18 nm represents a single and broad absorbance band, whereas pores with 20, 35, 40, and 140 nm exhibit two peaks, one at 480 and the other at 525 nm as shown in fig 2.14 [119]. The peak at 525 nm, represented by the black solid arrow, shifts toward a longer wavelength with the increment in pore size, as depicted by the red dotted arrow. However, the peak at 480 nm remains constant, as can be seen by a solid arrow.

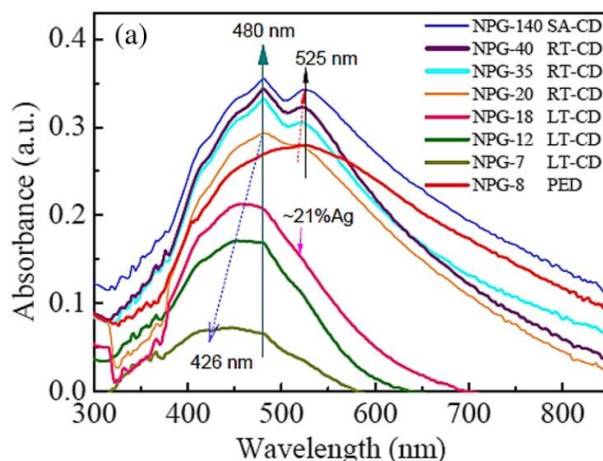


**Figure 2. 14.** UV-vis absorption spectra of NP-Au with different pore sizes [117].

LSPR helps to enhance the signal strength in Raman spectroscopy via the SERS mechanisms. SERS effects caused by NP-Au has been studied by varying the nanopore sizes via different aspects such as by altering the dealloying time, alloy composition, and annealing temperature, etc. The results indicate that the Raman signal intensity increases as the pore size decreases. The reason for the enhancement can be explained by two mechanisms: one is the local field creation around the Au ligaments, and the second is the generation of hot-spots due to the nanosized pores. Moreover, due to its continuous porous structure over a large area, similar intensity signals can be regenerated from any area of the substrate. Qian et al. studied the effect of temperature on the morphology of pre-dealloyed  $\sim 55$  nm NP-Au. They annealed it in air for 2h at a varied temperature range from 200 to 600 °C with 100° intervals [57]. The increment in pore size from 90 to 700 nm, as well as the coarsening of ligaments, is observed with increasing temperature as demonstrated in fig 2.15. (a)-(f). The reason for the variation in morphology was heating, that restarted the diffusion of Au atoms, which was quenched during the time of dealloying by immersing the leaf into water. The substrate was able to sense  $10^{-8}$  M R6G and  $10^{-5}$  M CV and exhibited the strongest enhancement with the smaller pores  $\sim 5 - 10$  nm due to the creation of a large number of hot spots, which was able to separate a large number of adjacent ligaments from each other. Yang et al. fabricated an Ag NPs decorated NP-Au substrate. Due to the excellent plasmonic properties of Ag as compared to other metals, it is widely used after that Au [120]. But due to its oxidation problem, the SERS performance degrades with time. Therefore, the author decorated the Au substrate with Ag to take advantage of both materials. The substrate was able to achieve good enhancement, which was due to the generation of hot spots between the adjacent NPs decorated onto NP-Au or by the LSPR phenomena in NP-Au. The substrate was modified by following a simple method, firstly the dealloyed film was immersed in  $\text{SnCl}_2$  (0.01 M) solution to assemble  $\text{Cl}^-$  ions onto the

NP-Au. After that, the activated substrate was immersed for 48 h in silver nitrate solution and then illuminated with a UV light ( $\lambda = 274$  nm) for the formation of Ag NPs onto their surface. The substrate is able to detect  $10^{-8}$  M R6G molecules by using a 532 nm laser, which is better than the bare NP-Au.

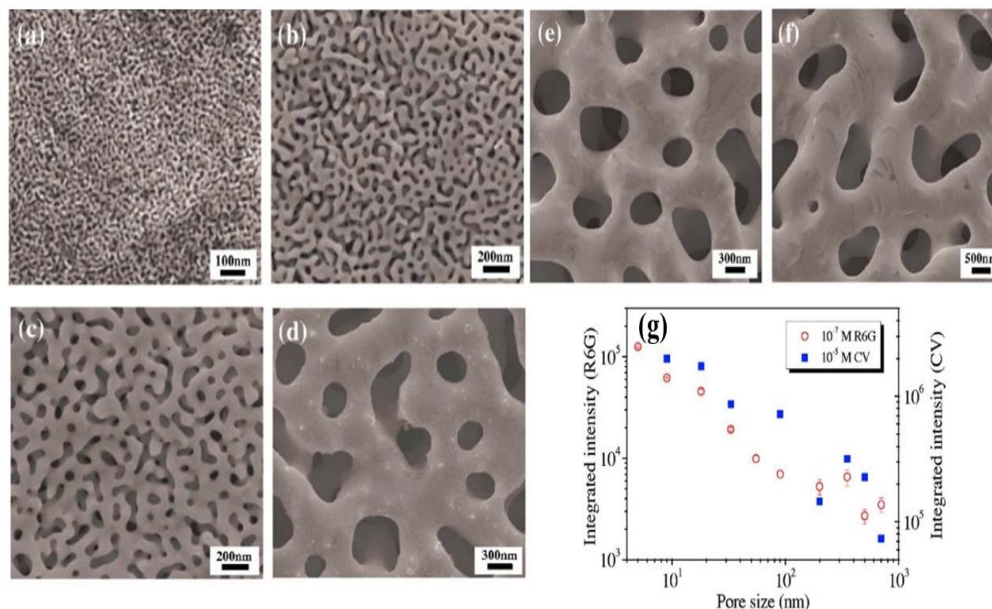


**Figure 2. 15.** Right-hand sand is the morphological view of NP-Au dealloyed for different time periods (a) 5 min; (b) 48 h; sample (b) was further annealed for 2 h at varied temperature range (c) 200 °C; (d) 400 °C; (e) 500 °C; (f) 600 °C; (g) represents intensities of  $10^{-7}$  M R6G at  $1650\text{ cm}^{-1}$  at 514.5 nm laser and  $10^{-5}$  M CV at  $1175\text{ cm}^{-1}$  at 632.8 nm laser [56].

Zhang and his co-workers prepared wrinkled NP-Au by heating NP-Au attached to the polystyrene base at  $160^\circ\text{C}$ , which was above then the PS glass transition temperature and below then the melting point [121]. The thermal contraction resulted in the formation of abundant nanogaps and sharp nanotips through the shrinkage of the polystyrene substrate which was beneficial to provide 100 times greater SERS signal enhancement compared to the planer NP-Au.

In other work, Zhang et al. fabricated a highly sensitive and selective aptamer-based NP-Au as an optical sensor for the detection of  $\text{Hg}^{2+}$  ions [122]. The sensor was able to selectively detect  $\text{Hg}^{2+}$  from the twelve metal ions solution as well as in underground and river water. For the fabrication of this sensor, the NP-Au was modified with an aptamer (-SH moiety at the 50-terminus and Cy5 tag at the 30-end). The aptamer was attached to the NP-Au by the thiol group. The aptamer was the Raman active molecule and its signal was enhanced by the LSPR generated from the NP-Au. The detection of  $\text{Hg}^{2+}$  ions was determined by monitoring the intensity change of the aptamer peak with respect to the metal ion concentration. In the presence of  $\text{Hg}^{2+}$  ions,  $\text{Hg}^{2+}$  was specifically bound between two

thymine's (T) and led to the creation of T-Hg<sup>2+</sup>-T pairs as represented in fig. 2.16. Which changed the structure from single-strand poly-T oligonucleotides to a rigid duplex-like structure. Due to this, Cy5 pulled away from the substrate, and thereby the SERS signal intensity decreased. At low concentration, the SERS signals from Cy5 was partially reduced, because Hg<sup>2+</sup> ions were not sufficient to form a duplex structure and some aptamers were freely laid on the surface. Hence, it can be concluded that there is an inverse relationship between Hg<sup>2+</sup> concentration and Cy5 tags. The decrement in the SERS intensity of the Cy5 tags is observed with the increment in Hg<sup>2+</sup> concentration. The Hg<sup>2+</sup> detection up to pM level is possible by using this substrate, which is several orders of magnitude higher than the maximum limit provided by the European protection agency.

In one literature authors electrodeposited the Au nanostructures onto NP-Au in order to increase its effectiveness. They tested the substrate at different potentials and for different time period [123]. For varied potentials, different structures of Au were formed onto NP-Au such as waxberry-like nanostructure, irregular polyhedral Au nanoparticles, and Au dendritic nanostructures and for increased electrodeposition time, the intensity was increased correspondingly. As compared to all the substrates, the substrate prepared for 3000s at -0.04 V electric potential showed the highest enhancement, due to the achievement of lightning rod effect via the formation of sharp tips onto Au dendritic nanostructures. These structures not only helped to amplify the signal but also improved the substrate uniformity. The substrate is able to detect 10<sup>-6</sup> M R6G, which is better than the planer NP-Au substrate.

Xue et al. fabricated NP-Au from a low-Au content alloy leaf (Au<sub>20</sub>Cu<sub>48</sub>Ag<sub>7</sub>Pd<sub>5</sub>Si<sub>20</sub>) in order to reduce the cost or to achieve a finer morphology. After dealloying, the ligaments with an average size of ~ 50 nm and many of ~ 25 nm were observed in some areas. In order to examine the SERS effectiveness of the substrate, a probe molecule such as 4,4'-bipyridine was used and this substrate was able to detect even 10<sup>-14</sup> M concentration. Here, the enhancement was due to the local field creation around the ligaments because of the resonant condition satisfaction and furthermore, EDS analysis confirmed that the presence of Pd and Ag residues inside the ligaments was also the reason for the signal enhancement [124].

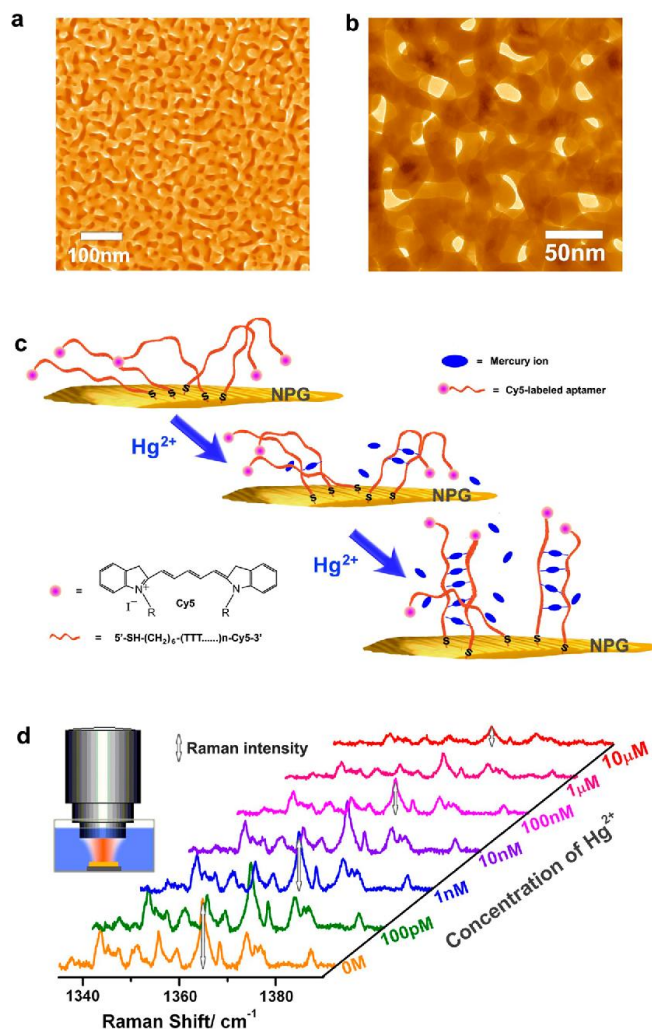


**Figure 2. 16.** Aptamer-modified NP-Au-based SERS sensor: (a) SEM; (b) TEM images of NP-Au. (c) Schematic illustration of protocol used for the sensing of  $\text{Hg}^{2+}$  via the substrate; (d) represents the increase in concentration of  $\text{Hg}^{2+}$  ions lead to the drop in the intensity of Cy5 tag [120].

Hu et al. studied the effect of varied dealloying time on to the morphology of NP-Au substrate. It has been discussed that with the varying dealloying parameters, the distribution density of “hot spots” can be varied which improves the SERS performance. The authors tested for different time period such as for 3, 4, 5, 10, 15, 60, and 120 min, and noticed that smaller-sized pores with an average pore diameter of  $\sim 13$  nm were observed for 3 and 4 min of dealloying and separated from each other due to ligaments [57]. But for extended time periods such as for 5, 10, 15, 60, and 120 min, the morphology changed abruptly, the pores and ligaments began to connect with each other and their size kept on increasing. To check the SERS effectiveness, Rhodamine B was used as the Raman active molecule. As compared to all the dealloying times, 4 and 15 min dealloyed samples showed the highest enhancement. It is well known that; the SERS activity is highly affected by the composition and morphology. With the extending dealloying time,

the size of pores was increasing and the Ag content was also decreasing continuously. The enhancement reason for the 4 min sample was the generation of hot spots and the presence of Ag content, whereas for the 15 min samples, the hot spot generation is larger as compared to other samples.

Zhang et al. has fabricated Au nanocones onto NP-Au by optimizing the concentration of the reactants (tetrachloroauric acid, sodium dodecyl sulfate) and plating time. For 90 minutes of plating, nanocones with an apex of 10-20 nm and an average length of ~ 40 nm were formed and represented as NC1@NP-Au, and when the plating time was extended to 180 minutes, the tip apex was still 10–20 nm in size, but the average length of the nanocones was increased from ~40 nm to ~80 nm, double than the previous plating and represented as NC2@NP-Au. Figure 2.17 shows that both substrates show improved SERS enhancement. The NC2@NP-Au showed a 20-fold enhancement, and the NC1@NP-Au exhibited a 10-fold enhancement compared to the as-prepared NP-Au [125]. The reason for the enhancement in these substrates was the confinement of the electric field (lighting rod effect) due to the sharp corners and edges of nanocones. This substrate was also capable of single-molecule detection.

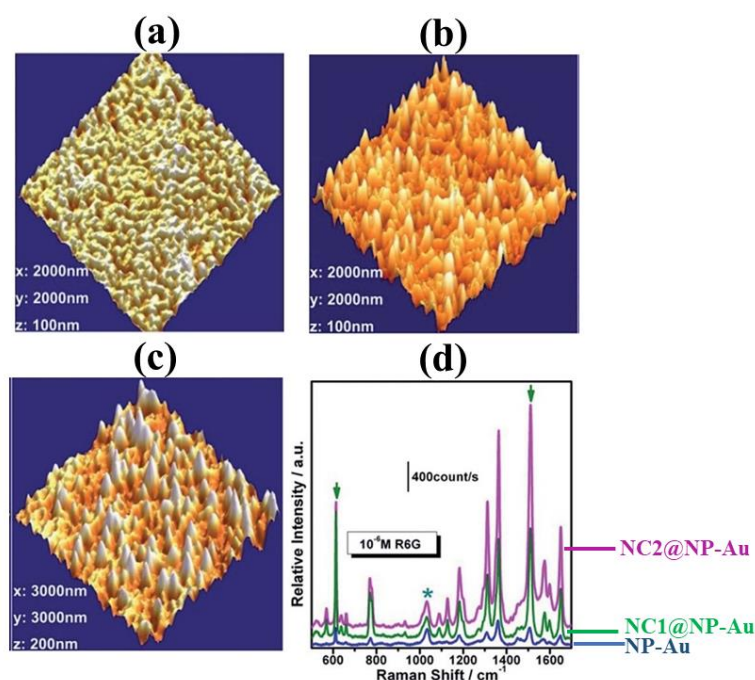


**Figure 2. 17.** AFM image of (a) dealloyed NP-Au; (b) nano-cones on the NP-Au after 90 minutes of plating; and (c) nano-cones on the NP-Au after 180 minutes of plating; (d) SERS spectra of R6G onto NP-Au (blue colour), NC1@NP-Au (green colour), and NC2@NP-Au (pink colour) [127].

In summary, the wide variety of literature on the use of NP-Au as a sensor demonstrates that both its morphological and chemical properties make it a good candidate for sensing applications. Other porous materials such as zeolites and MOFs are also popular for



sensing, but their practical trials are limited and still questioned due to certain challenges such as their costly and difficult fabrication procedures as well as difficulties in reproduction and reusability. However, as discussed dealloyed NP-Au possess excellent characteristics (such as reproducibility, facile fabrication, uniformity, and reusability) which make it suitable for many applications. It is believed that research in this area will continue and increase, with a focus on optimizing fabrication procedures to further improve the targeting of molecules of interest. Since there is still a large gap between these studies and their uses in industry, more effort should be made toward the use of NP-Au based sensors for real-world applications such as for biomarker monitoring, environmental pollutant detection, and food safety.

#### 2.2.10 *SERS substrate based on flexible substrate*

A flexible SERS substrate refers to assembly of plasmonic nanostructures onto a flexible support. These substrates have various advantages over conventional rigid substrates due to their easy usability, non-destructive or invasive method, and cost-effectiveness. These substrates have been used in multiple fields such as for the detection of explosives, pesticides/fertilizer, and chemical pollutants [43]. As compared to the detection of the mentioned molecules, these substrates have been widely used for the analysis of agricultural and food products due to their flexible nature. With conventional Si or glass-based substrates, detection on flat and planer surfaces is possible, whereas on curved and non-planar surfaces the detection is difficult [126]. In order to detect molecules from such kinds of surfaces, a sample is cut into pieces to adjust substrate onto the sample surface; hence nondestructive detection is difficult. Whereas flexible substrates can be cut into any desired shape and size, can be swabbed, and attached or detached on the sample surface to detect the molecule.

From the past few years, researchers have used filter paper, adhesive tape, cotton fabrics, and polymer films as flexible supports to make flexible SERS substrates [12]. As discussed in section '1.2' pesticides and fertilizers are frequently used in agriculture to protect the crops from weeds, insects, and fungi etc. and to increase the growth of crops and plants. However, improper, and excessive use of these can be harmful to human and result in both acute and long-term health problems [127]. Conventionally, high-performance liquid chromatography (HPLC), gas chromatography-mass spectrometry (GC-MS), and liquid chromatography-mass spectrometry (LC-MS) have been used to identify pesticides/fertilizers in food products. Although these methods are precise and effective, but with these techniques the lower limit detection is quite difficult as well as the on-site detection is not possible at all due to the bulky size of the instruments [128]. However, recent advancements in technology made possible the fast, simple, and easy detection of pesticides/fertilizers by using surface-enhanced Raman spectroscopy. This technique has distinct advantages such as no need of sample preparation



(need to drop-cast a few microliters sample onto a substrate), faster detection time, and trace level detection is possible. Furthermore, as well with flexible substrates non-destructive as well as onsite detection is also possible [16]. The first report on pesticide detection based on SERS was reported in 1987 by Alak et al. [129]. They have used an Ag-coated microsphere-based substrate to detect eight organophosphorus pesticides. After that, a large number of papers based on the use of SERS for pesticide detection have been published. Some of them are discussed below.

#### *2.2.10.1 Literature survey on flexible SERS substrates*

Flexible substrates have been used to detect R6G (xanthene dye used in the food industry and textile: as per the material safety data sheet, its overexposure leads to headache, drowsiness, and irritation to the skin, eyes, respiratory tract, etc.), Crystal Violet (non-biodegradable cationic dye used as a food additive and food colouring agent), Thiram (widely used in crops and seeds for fungal diseases protection and it is toxic when come in contact via ingestion or inhalation), Urea (used to increase the crop production as well as to protect the crops from insects and fungus; its high exposure can cause kidney diseases in humans) [130], [131], [132] etc., Some of the detection methods are briefly explained below.

##### *2.2.10.1.1 Paper-based SERS substrate*

Papers have been widely used as a supporting substrate to deposit nanostructures due to their natural hydrophilicity, wide availability, cost-effectiveness, and being made from renewable resources. Cellulose is a naturally abundant biopolymer and is biodegradable. It possesses good hydrophilicity due to the presence of numerous hydroxyl functional groups, which is beneficial to make contact with molecules in solution. The substrates based on cellulose paper have the advantages of easy portability, availability, and environmental friendliness. These substrates can easily collect molecules by soaking, filtering, and wiping, etc. However, the SERS substrate based on cellulose has faced disadvantages such as the loss of incident laser as well as nonuniform distribution of the nanoparticles due to the presence of pits and holes in the paper which leads to the generation of insufficient hot spots. Furthermore, due to the excellent hydrophilicity, sometimes molecules penetrate into the depth of the paper, which causes the uniformity problem. Among the cellulose papers, the filter paper is the first choice due to its high cellulose content and porous nature.

Dong-Jin and his co-workers provided a simple, economical, and environmentally friendly method for the fabrication of filter paper-based SERS substrates [132]. The authors tried to make the substrate hydrophobic in order to improve the SERS performance of the substrate such as uniformity, sensitivity, and reproducibility. The hydrophobic character is introduced by depositing PDMS onto the paper via spin-coating method. The paper is made SERS active by drop-casting an AuNPs@GO solution onto it. The substrate shows good

sensing capability by detecting R6G ( $10^{-9}$  M) and thiram molecule ( $10^{-6}$  M) as shown in fig. 2.18.

Zhu et al. fabricated the SERS substrate and named it Dynamic SERS (D-SERS) It is prepared differently than the traditional substrate preparation method. Ag NPs are synthesized in the presence of filter paper to decorate the paper surface. For the fabrication of this substrate, a piece of filter paper is inserted into an Ag  $(\text{NH}_3)_2\text{OH}$  solution, and then the formaldehyde solution (reducing agent) is added for the generation of Ag NPs. The prepared Ag NPs-decorated filter paper is used to detect pesticide residues via swabbing the substrate across the different fruit surfaces (apples, bananas, and tomatoes). The LOD by using this substrate is  $7.2 \text{ ng/cm}^2$  for thiram and  $0.23 \text{ } \mu\text{g/cm}^2$  for paraoxon, respectively, which is lower than the acceptable limit [131].

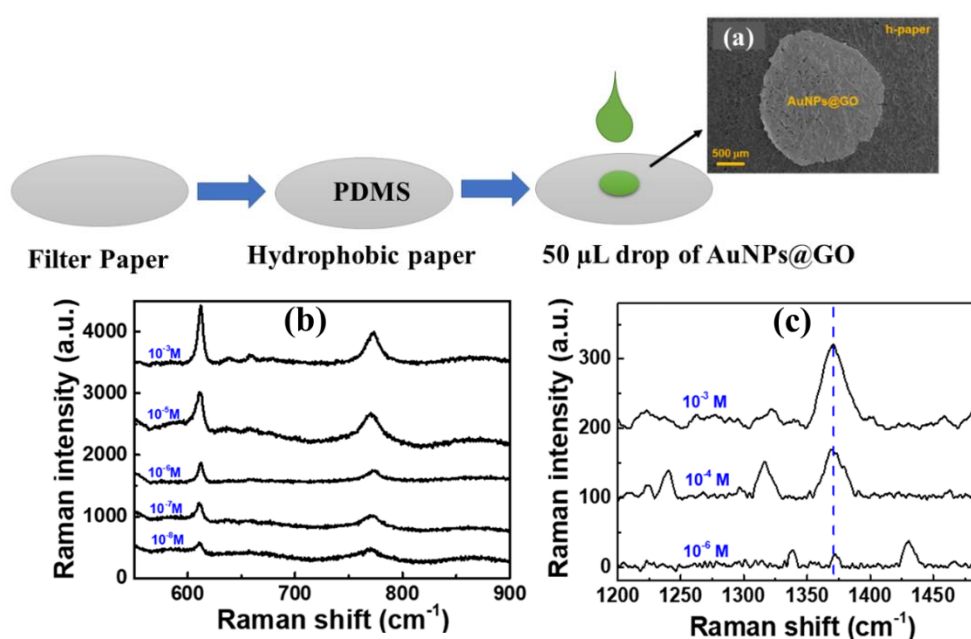


**Figure 2.18.** Schematic representation of the fabrication process for h-paper-based Surface-enhanced Raman scattering (SERS) sensor. (a) SEM image of the Au NPs@GO coated h-paper substrate. SERS spectra of varied concentration of (b) R6G from  $10^{-3}$  to  $10^{-8}$  M and (c) urea from  $10^{-3}$  to  $10^{-6}$  M onto h-paper substrate [129].

Wang et al. used a rapid and simple drop-wipe test method to extract the thiram pesticide residues from the different fruit surfaces [133]. The flexible substrate is prepared by immersing a filter paper in Ag colloid for 24 hours, as shown in fig 2.19. The substrate is able to detect lower limits of thiram such as  $4.62$ ,  $5.18$ , and  $5.70 \text{ ng/cm}^2$ , spiked onto apple, pear, and grape peel fruits. Which is much lower than the national standard of acceptable limit of  $50 \text{ ng/cm}^2$ . The important thing is that only a few minutes is required for sampling as well as for measurement with the substrate via the drop-wipe method.

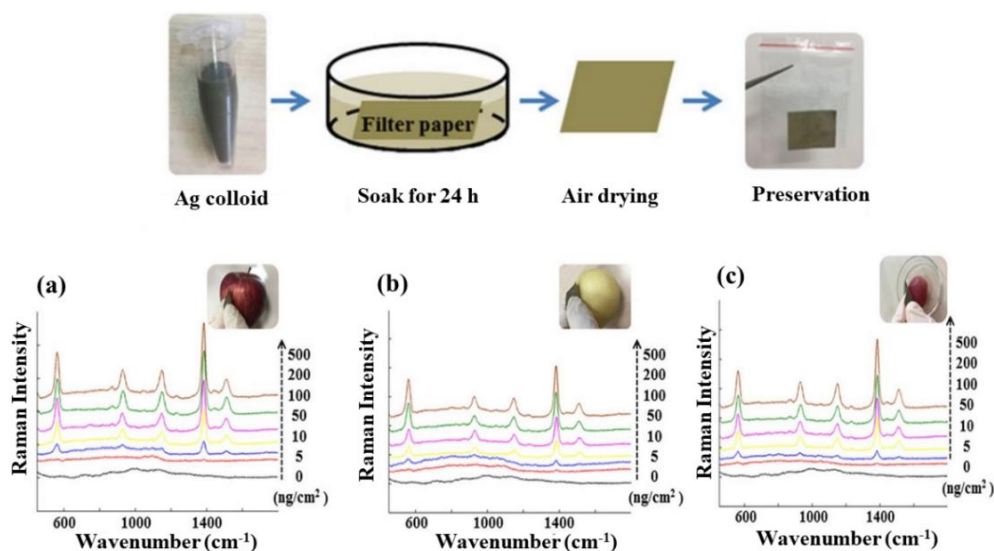


**Figure 2. 19.** Schematic representation of the substrate fabrication process. Below the SERS spectra is shown for the varied concentrations of thiram measured using the prepared substrate on different fruits (a) apple, (b) pear, and (c) grape [132].

#### 2.2.10.1.2 Adhesive tape-based SERS substrate

Commercial adhesive taps are also used as SERS substrates due to their flexible, sticky, cost-effective, as well as transparent nature. The tape is made SERS active by drop-casting or by either pasting nanoparticles onto it. However, most tape-based substrates are thermally unstable and lose their stickiness when exposed to air. Furthermore, some taps show fluorescence when exposed to laser light. Therefore, optimization of instrumental parameters and background subtraction is required before Raman measurement. Jiang et al. used adhesive tape to make a flexible substrate. The substrate is fabricated by transferring the Ag nanorod structures from the Si substrate to the transparent tape via a paste-and peel-off approach [134]. The arrays of Ag nanorod is prepared on Si by the oblique angle deposition method. The transparent substrate is able to rapidly detect  $28.8 \text{ ng.cm}^{-2}$  tetramethyl thiuram disulphide pesticide on the apple surface. Chen et al. prepared a flexible, sticky, and low-cost SERS substrate by drop-casting Au NPs onto the sticky side of the daily-use adhesive tape. The effectiveness of the SERS active tape is tested directly by pasting a tape onto the different surfaces (pre-contaminated with parathion-methyl pesticides) and then peeled off for further detection as shown in fig 2.20. The substrate shows great sensitivity by detecting a lower limit ( $26.3 \text{ ng/cm}^2$ ) of parathion-methyl pesticide [135].

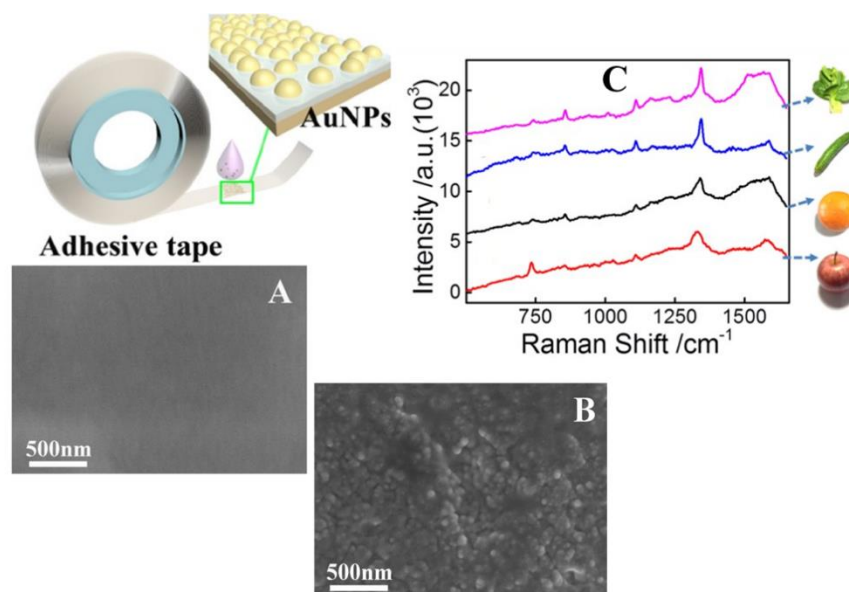


**Figure 2.20.** Schematic demonstration of the fabrication of SERS tape; SEM images of (A) adhesive tape and (B) Au NPs-decorated adhesive tape (C) SERS spectra of parathion-methyl peel off from the surfaces of (a) apples, (b) oranges, (c) cucumbers, and (d) green vegetables using SERS tape [134].

#### 2.2.10.1.3 Polymer based SERS substrate

From the past few years, polymers such as polydimethylsiloxane (PDMS), polyethylene terephthalate (PET), polyvinylidene fluoride (PVDF), and poly (methyl methacrylate) (PMMA) have been widely used as supporting materials to make substrates flexible due to their easy-to- shape, transparent, long-lasting properties, and additionally, these materials do not interfere with molecules signals. Park et al. (2017) fabricated PDMS-based substrates with Au nanostar arrays and demonstrated that the substrate was able to show good sensing capability even after 100 cycles of mechanical deformation of bending, stretching, and twisting [15]. Samir and colleagues have fabricated a flexible and sensitive substrate via embedding Ag nanorods into the PDMS surface [12]. The substrate is prepared by transferring the Ag NRs array from Si to the polymer surface by nano casting approach. The substrate effectiveness is examined by extracting thiram ( $\sim 10^{-9}$  g/cm<sup>2</sup>) on an apple surface via “paste and peel off” method as demonstrated in fig 2.21. Sun et al. prepared a flexible substrate by using PDMS to duplicate the morphology of sandpaper. Then the substrate is modified with 3-aminopropyltrimethoxysilane to assemble Ag NPs onto structured PDMS to make substrate SERS active. The two pesticides triazophos and methyl parathion have been detected onto the surface of tomatoes [136]. Furthermore, the stretching length (at about 58.6 mm) of the substrate is tested, and it is observed that the SERS performance is not affected by the stretching.

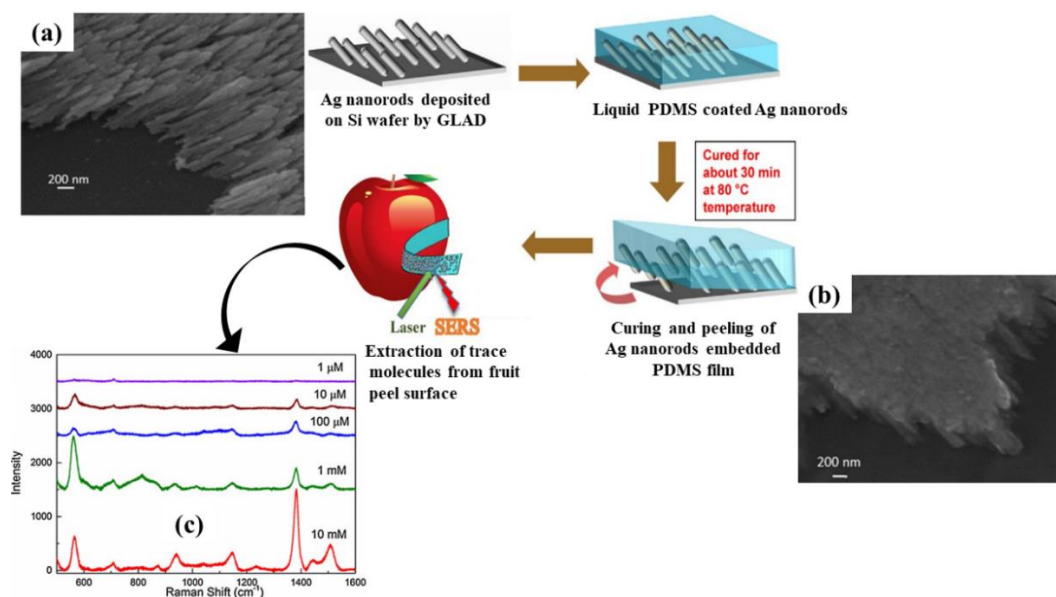


**Figure 2.21.** Schematic demonstration of the substrate fabrication process. The SEM images of (a) Ag nanorod arrays on Si wafer and (b) Ag nanorods embedded in PDMS film. (c) SERS spectra of different concentration of thiram pesticide extracted from apple peel [12].

#### 2.2.10.1.4 Natural artifacts based SERS substrates

As discussed, a variety of substrates (Ag nanorods onto Si) have been used as supporting materials to fabricate flexible substrates. However, the complex fabrication procedure of supporting substrates reduces reproducibility and increases the cost of the substrates. Therefore, from the past few decades, researchers have been trying to find facile, green, and low-cost fabrication methods to make flexible SERS substrates. Recently, SERS substrates based on natural plant leaves such as lotus, rose petals, taro, rice, etc. have been reported for the detection of R6G, crystal violet, and malachite green etc. [137] [138]. These natural plants can be directly used as a substrate as well as a supporting material (the replicates of these structures can be generated by using various polymer films). This approach provides a fast, facile, effective, and economical method for the preparation of flexible substrate which is independent of specialized equipment. Xu and his coworkers developed a SERS substrate via a coating of Ag film onto white rose petals [139]. The presence of submicron grooves, micro-papillae arrays, grating, and silver islands contributes to not only surface hydrophobicity but also significantly enhances signal intensity. The detection limit of substrate is  $10^{-9}$  M for R6G and the enhancement factor corresponds to  $10^8$ . Chou et al. presented an easy and novel method by using rose petals as a supporting substrate. The substrate is made SERS-active by drop-casting Ag NPs suspension onto the petal surface. The hydrophobic effect of the petal leads to the aggregation of the NPs as well as R6G onto their surface as represented in fig 2.22. The SERS performance is examined on both the upper and lower surfaces of the petal. It is

found that lower surface contributes effectively in the signal enhancement due to the uniform distribution of NPs aggregates throughout the surfaces. The LOD of R6G is below  $10^{-15}$  M by using this substrate [9]. Kumar et al. fabricated an Ag-coated structured PDMS substrate by using taro leaf as a supporting material [10]. The substrate is fabricated by casting PDMS onto a taro leaf in order to create the reverse texture of taro leaf. The thin film of Ag is deposited in the microcavities by a thermal evaporation method. The substrate shows good sensitivity ( $\sim 10^{-11}$  M), reproducibility, and good enhancement factor ( $\sim 2.06 \times 10^5$ ) towards the detection of malachite green. They have also checked the effect of substrate bending onto the SERS signal intensity value. The intensity of the signal decreases with decreasing bending angle from  $180^\circ$  to  $100^\circ$ , which is due to an increase in nano spacing between the metallic NPs.

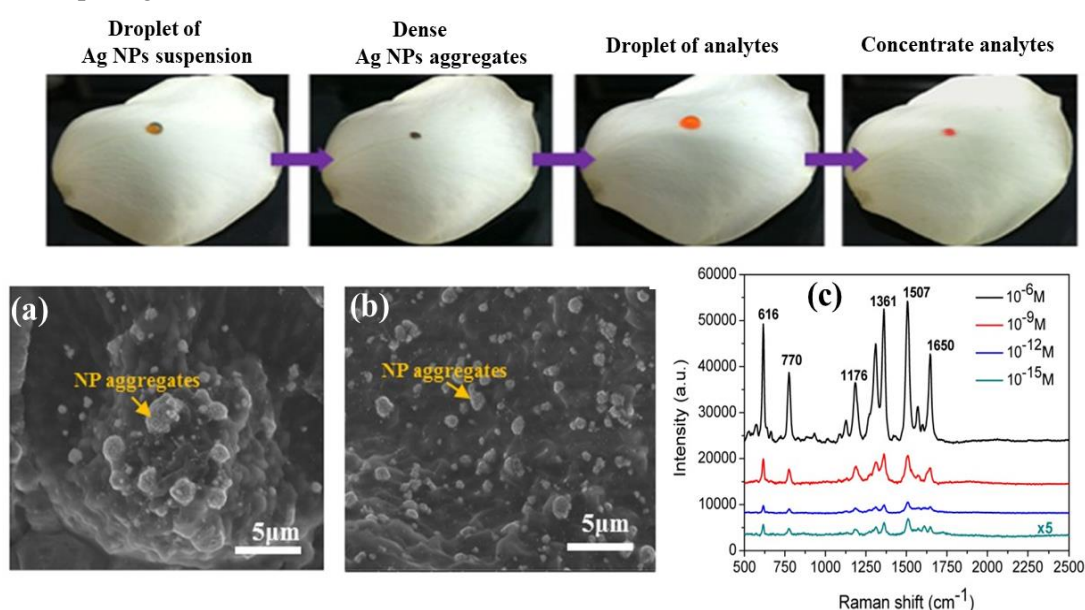


**Figure 2. 22.** Photographic pictures representing the Ag NPs aggregation and R6G accumulation on one area of the rose petal. SEM images (a) upper surface (b) lower surface of rose petal after absorption of R6G. SERS spectra of varied concentration of R6G (c) lower surface of Rose Petal [9].

### ***Chapter 3: Techniques used for the SERS substrate's characterization***

To examine the properties of nanostructures, there is a need to use multiple instruments to characterize them. There are specific techniques to identify the specific properties of the material such as size, shape, absorption, composition etc. Like to study morphology (nanoscale features): field emission scanning electron microscope (FESEM) and scanning electron microscope (SEM) are suitable techniques. This microscopy provides information by detecting emitted electrons, which are ejected when a highly energetic electron beam hits the specimen. The SEM and FESEM follows the same working principle; the difference is that the electron source used in FESEM (field emission gun) is better than SEM (thermionic emission). The source provides a smaller spot size and an extremely focused high-energy beam, which improves resolution and enables imaging to be carried out at higher magnification. A brief explanation about microscopic and spectroscopic techniques is mentioned below. To examine the surface roughness and uniformity of the substrate atomic force microscopy (AFM) is used. A detailed topographical profile of the sample is generated by scanning across the surface. The optical characteristics such as absorption, scattering, and emission are measured with a various spectroscopic technique. The absorption spectrum of the sample is recorded with the help of UV-visible spectroscopy. In order to know the fingerprint of the molecule, the scattered signal is collected by Raman spectroscopy. Photoluminescence spectroscopy is used to collect the emission spectra of the molecule. In short, all the spectroscopic techniques work on the same principle: electromagnetic radiation is incident onto the sample (liquid, solid, or powder) and the spectra is obtained due to the interaction of light with the sample.

#### ***3.1 Techniques based on topography measurement***

##### ***3.1.1 Field-Emission scanning electron microscopy (FESEM)***

FESEM is a commonly used technique for the topological identification of nanostructures. It has a capability to provide images with a resolution of  $\sim 1\text{ nm}$  and magnifications up to 5,000,00 x. An electron beam is generated from a field emission source and accelerated with a high voltage of  $\sim 1\text{ keV}$  to 50 keV. This beam is focused by electromagnetic lenses in a high vacuum column to produce a narrow beam which is incident on the sample. There are certain requirements in order to observe a sample through SEM. Like the sample should be conductive in order to avoid charging effect and to get sharp featured image. To make the sample conductive; an extremely thin layer of gold, carbon, and palladium is coated. After the coating, it is stuck onto a holder with the help of a double-sided carbon tape, and then it is placed in a SEM chamber. When the beam is bombarded onto the sample, variety of electrons (secondary, backscattered, auger, characteristic X-ray, continuous X-ray, and cathodoluminescence etc.,) is ejected from the sample. The electron beam scans the sample in a zig-zag-type pattern (raster scanning) to analyse the surface. The image is formed by



detecting secondary electrons from the sample surface. Furthermore, with the topological view, it can also provide information about the elemental composition and the distribution of the elements in the sample in association with Energy dispersive X-ray spectroscopy (EDS).

### 3.1.2 Atomic force microscopy (AFM)

AFM is used to check the roughness of the sample surface. It provides a 3D topographical image of the sample surface as compared to other electron microscopy techniques. It is a type of scanning probe microscopy in which interactions between a tip and a sample surface is recorded. The tip supported on a flexible cantilever moves across the surface and experiences attractive and repulsive forces as per the surface texture. The movement of the tip is noticed by the deflection of a cantilever, according to Hook's law. The backside of the cantilever has a reflective coating so that it can reflect light like a mirror. A laser beam is incident on the backside of cantilever, and due to the vertical movement in the cantilever position, the angle of reflected light is changed. This reflected light is collected by the arrays of photodetectors, and accordingly a 3D image of the surface is formed.

## 3.2 Techniques based on optical properties measurement

When light interacts with matter, it can be absorbed, scattered, reflected, and transmitted by the matter. To observe these properties, a variety of spectroscopic techniques are used, which are briefly explained below.

### 3.2.1 UV-visible (UV-Vis)

It is used to quantitatively analyse the optical properties of organic and inorganic compounds. The technique operates on the principle of absorption of photons. The absorbance of light causes the transition of electrons in the molecules from the low-energy ground state HOMO (highest occupied molecular orbital) to a higher-energy excited state LUMO (lowest unoccupied molecular orbital). In this spectrophotometer the sample is irradiated with ultraviolet and visible electromagnetic radiation, some part of the light is absorbed and the rest is transmitted through the sample. The final spectrum is obtained as per Beer Lambert law by measuring a comparison between the intensity of incident light on the sample and the intensity of transmitted light from the sample (which decreases as the concentration of the molecule in solution increases) and in the form of absorbance as a function of wavelength. The spectra provide knowledge about plasmon resonance region of the nanostructure, concentration of the solution, chemical composition, particle size, and formation and correspondingly the band will change or shift based on changes in medium, shape, and arrangement.

### 3.2.2 Photoluminescence (PL)

PL is a kind of light emission spectroscopy. UV-visible spectroscopy provides the absorption spectra ( $\lambda_{\text{abs}}$ ) of the molecule. To identify the emission spectra ( $\lambda_{\text{em}}$ ) of the molecule, PL spectroscopy is used. The principle is same as UV-Vis; the only difference is that in which



the emitted photon is detected. The brief explanation about its working is as follows; when the light is directed onto the molecule, it absorbs light and excitation occurs from a lower to a higher energy state. Then the molecule loses some of the energy by the emission of photons and return to the ground state. The emission is of two types: one is radiative and other is non-radiative. PL comes under radiative emission. In radiative emission, excited electron releases a photon during relaxation. Whereas, in non-radiative emission, the energy is lost in the form of heat through atomic collisions or vibrational interactions. PL is of two types: fluorescence and phosphorescence. Fluorescence is a prompt emission observed for a very short time (picoseconds to nanoseconds) after excitation, while phosphorescence continues long even after a light incident (microseconds to thousands of seconds). The resultant spectrum is in the form of intensity of emitted light as a function of wavelength.

### 3.2.3 *Dynamic light scattering (DLS)*

DLS is used to determine the size and size distribution of the particles in the solution typically in the nanometer range. It provides a rough idea about the size by examining the Brownian motion of the particles. The polydispersity index (PDI) parameter describes the variation in the particle size distribution, and it is a dimensionless number. The value of PDI is in the range of 0.01 to 0.7, which indicates particles are of same size. However, a value  $> 0.7$  indicates the wide distribution in the particle size. The particles move randomly in all directions when dispersed in a liquid. As per the principle of Brownian motion, the particles which are dispersed in a solvent, are constantly colliding with the solvent molecules. These collisions induce movement in the particle by transferring a certain amount of energy. The energy transfer is varied as per the particle size. The smaller particles move at a higher speed than the larger particles. By measuring the speed of the particle, the hydrodynamic diameter is determined. If there are aggregates, there is no random movement that would lead to inaccurate results. In this instrument, a single-frequency laser is incident onto the sample containing particles. The light gets scattered in all directions and the scattered light is collected by detector at a certain angle over time, and this signal is used to measure the particle size. The intensity of the scattered signal is fluctuating over time. Smaller particles show faster fluctuations than larger particles due to their fast movement.

### 3.2.4 *Raman spectroscopy*

Raman spectroscopy is a type of vibrational spectroscopy where scattered radiation is used to recognise the vibrational modes of a molecule. These modes are different for different molecules, and by analysing them unknown molecule is easily identified. It is based on the inelastic scattering of light which occurs when a sample is incident with monochromatic light. When light is directed onto the sample, most of the light is elastically scattered known as Rayleigh scattering. Here the emitted photon has the same wavelength as the incident light.

The molecule relaxes to the same vibrational energy state after excitation. Whereas a small portion of the light it can be said that from millions of photons only one photon scatters at a frequency different than that of incident frequency due to molecular vibrations. This scattering is known as inelastic scattering, also known as Raman scattering. Here, the molecule relaxes to a different vibrational energy level either higher or lower than that of its beginning state. The difference between the energy of the scattered photon and incident photon is called the Raman shift. The Raman shift is associated with two kinds of shifts: one is Stokes and the other is anti-Stokes shift. If the scattered photon is of lower energy than that of incident photon, the shift is known as Stoke's shift (photons transfer their energy to molecules) or if the scattered photon is of higher energy than that of incident photon is called anti-Stoke's shift (photons gain energy from the molecules). There are certain conditions for the sample to be analysed by Raman: the molecule should undergo a change in polarizability at a specific vibrational frequency and it is applicable to characterize only those molecules, which have homo-nuclear functional groups such as C-C, C=C, and C≡C bonds. The positions of the peak is observed by determining the vibrational energies, that are related to the bonds in the molecules. Rayleigh scattering is million times more intense than the Raman scattering as discussed from millions of photons only one photon shows Raman scattering. To obtain Raman spectra, there is a need to filter out Rayleigh scattering. The sample preparation is easy, there is a need to just put a droplet of the tested molecule onto a silicon or glass substrate. Some important components of Raman spectrophotometer are the laser's (excitation source), a notch filter (to remove Rayleigh scattering), a dispersion element (grating), and a CCD detector.

## ***Chapter 4. Rigid SERS substrates for urea detection***

### ***Part 4.1: Rigid SERS substrate fabrication***

#### ***4.1.1 Introduction***

Raman spectroscopy is a widely used technique for the identification of various materials owing to its ability to give ‘figure-print’ spectra of the molecules. However, due to the small Raman scattering cross-section of the molecules, generally in the range of  $10^{-30}$ - $10^{-25}$  cm<sup>2</sup>, only highly concentrated or pure molecules can be recognized [121]. In addition, the high inherent fluorescence suppresses the weak Raman signals from the molecules. All these limitations restrict its use in a variety of applications for the identification of many chemicals and molecules. This shortcoming can be effectively overcome by the highly sensitive and selective spectroscopy technique known as surface-enhanced Raman spectroscopy (SERS). It increases the weak Raman signal of molecules by several orders of magnitude [76]. Here, a studied moiety is placed at a close distance to the structured metallic/non-metallic substrates [41]. The SERS enhancement is generally due to the local electromagnetic enhancement around the nanostructure when the incident light frequency is in resonance with the plasmon frequency of the conduction electrons in the nanostructure [140]. The SERS value can be drastically enhanced up to 10 orders of magnitude at ‘hot spots’ (sub-10-nm gaps) where extensive electromagnetic fields are generated due to the electromagnetic coupling between adjacent nanostructures [121].

Various platforms made using materials such as Ag, Au, Al, Cu, Pt, Pd, Fe, Co, C, Ru, and 2D nanomaterials such as graphene, transition metal dichalcogenides (TMDs) are used to make the SERS substrate [55] [7]. Among these materials, Ag and Au are widely used because of their excellent plasmonic properties compared to others and also their localized surface resonance lies in the visible and near-infrared wavelength range, where most Raman measurements occur [56], [141]. It has been demonstrated that the SERS signal is quite delicate to the substrate nature and its performance degrades over time [57]. Therefore, most of the studies on the SERS activity is conducted on the Au due to its comparatively more stable nature than Ag.

Different types of methods have been used to fabricate the SERS substrates that include the chemical synthesis method to prepare different shapes of nanoparticles, an electrochemical method to make roughed metal films, and other methods such as template, self-assembly or sputtering [142]. In recent times, lithographic methods (focused-ion-beam, electron-beam lithography, and nanosphere lithography) have been used to form arrays of nanostructures with defined morphologies and interparticle spacing [143], [144], [145], [146], [147]. However, these methods have limitations, such as complicated/time-consuming, and expensive fabrication approaches, low Raman signal enhancement factor, poor uniformity, stability, and reusability. In recent times, dealloying method has been proposed as an alternative technique

for the preparation of effective SERS substrates due to its easy, fast, single step fabrication method, and low processing cost [88]. This method does not require specific setup and working conditions such as clean room, patterned masks, and photoresists like lithography techniques. It involves the leaching of less noble elements from a precursor alloy by chemical etching. Generally, acids ( $\text{HNO}_3$ ,  $\text{HCl}$ ) or bases ( $\text{NaOH}$ ) are used to dissolve metal elements such as Ag, Cu, and Al from the alloy except the Au [89]. The structure is made of nano-sized pores which are connected with gold ligaments [94]. The pore size, pore volume, pore shape, and inter-pore distance of the structure can be easily varied by adjusting the dealloying parameters i.e., the alloy composition, etching time, and the etching solution concentration [88]. Another advantage of the nano-porous substrate is that spatially independent SERS signals can be regenerated from anywhere over the  $\text{cm}^2$  area of the sample due to its uniform bi-continuous structure from tens of nanometers to centimeters [122]. The SERS performance of nano-porous gold (NP-Au) based systems has been analyzed in recent studies [123], [148], [149]. However, most of the attempts have been devoted towards increasing the enhancement factor and the sensitivity through structural modification [150], [151], [152], [153]. Only a few literature reports have investigated substrate uniformity, with no studies on the reproducibility, reusability, and stability of such substrates [89], [120], [123], [124], [125], [150], [151], [152], [154], [155], [156]. Therefore, it is essential to explore the performance of NP-Au to increase its use for applications.

Further, most of the SERS substrates are prepared by all these fabrication techniques have to be disposed of after the adsorption of analytes onto their surface, which increases the cost, pollution as well as limits its use for practical applications [157], [158]. Therefore, many efforts have been initiated on improving the SERS substrate performance. But still, the challenge remains to prepare a reusable, uniform SERS substrates with enhancement through low-cost fabrication process.

Hence, in the current work, the reusability of the substrate in relation to the SERS enhancement using an interconnected network structure consisting of Au ligaments (NP-Au) is studied. The fabricated SERS substrate is uniform and capable of providing a five-fold of enhancement in Raman signal, which is higher than the earlier reports [96], [125]. Furthermore, all the specific vibrational modes of R6G molecules are clearly identifiable, which are either quite weak or absent in earlier studies [156]. The interconnected network structure-based SERS substrate can be easily cleaned by removing adsorbed analytes via the drop-casting method in ethanol.

#### 4.1.2 *Materials and Methods*

##### 4.1.2.1 *Materials*

Au-Ag alloy leaves (50/50 by weight, ~100 nm thick) were procured from Dukatshop, nitric acid ( $\text{HNO}_3$ {65%}), and R6G were bought from Merck, p-type Silicon wafers with  $\langle 100 \rangle$

orientation, 0.5 mm thickness, and 2 inches in diameter were purchased from Sigma Aldrich, and Deionized (DI) water of 18.2 M $\Omega$  cm resistivity was used during all the experiments, wherever required.

#### *4.1.2.2 Fabrication methods*

##### *4.1.2.2.1 Fabrication of NP-Au substrate*

NP-Au substrate was prepared similarly as reported by Ding et al. with slight modifications [148]. The substrate was fabricated using a low-cost alloy leaf (Au<sub>50</sub>Ag<sub>50</sub>) and the preparation of substrate was done by the dealloying method. The 65% concentrated HNO<sub>3</sub> was used to dealloy the leaf at room temperature for different periods of time as demonstrated in fig. 4.1. First, the leaf was cut to 1.5  $\times$  1.5 cm<sup>2</sup> in size similar to the silicon (Si) substrate size, so that it completely covered the substrate surface. After that, the leaf piece was carefully placed on the corner of the microscopic glass edge with the help of a tweezer, and the slide corner was slowly immersed into a beaker containing the HNO<sub>3</sub>. As the leaf started floating on the HNO<sub>3</sub> surface, the slide was gently removed from the acid beaker. The leaf colour was altered immediately from the silver colour to a copper tone, which is an indication of the Ag dissolution from the alloy had started. The leaf was kept in acid for different etching times of 5–65 min. After the desired time, the dealloying was rapidly quenched by carefully transferring the leaf to a beaker of DI water. It was left in the beaker for 10 min and again transferred to another beaker of DI water to make the leaf free from acid. This rinsing step was repeated 2 to 3 times. Finally, the fabricated NP-Au film was removed from the beaker using precleaned Si substrate as a base material and kept to dry at room temperature for 6 h. The Si substrates were pre-treated with piranha solution to remove the atmospheric oxide layer onto the surface, in order to avoid any kind of hindrance from the oxides during the measurements.

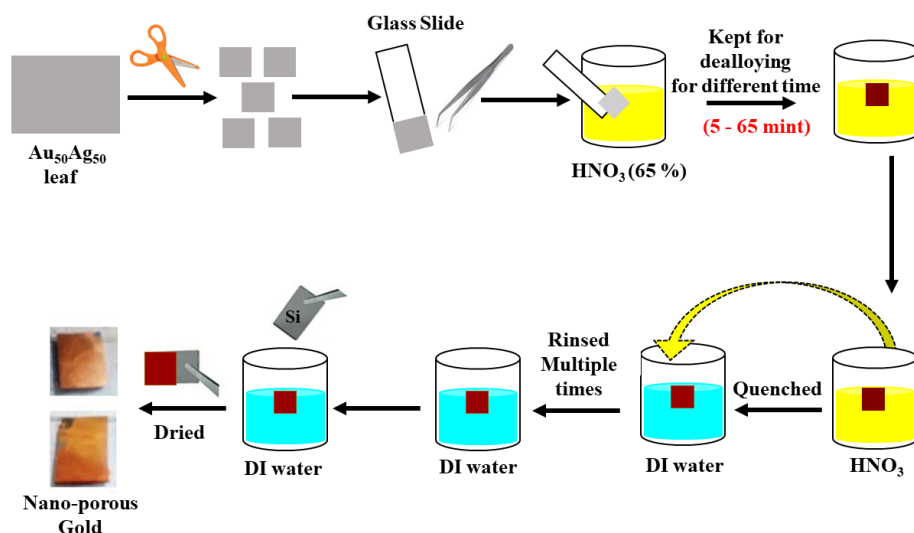


**Figure 4. 2.** Schematic representation of step-by-step fabrication of NP-Au from an alloy leaf by the chemical dealloying method.

#### 4.1.2.2.2 Fabrication of NP-Au based SERS sensor

The most common probe molecule, R6G, was used to examine the SERS activities of the NP-Au substrates. The R6G molecules possess well characterized Raman bands. In a typical procedure, 10  $\mu\text{l}$  of  $10^{-3}$  M R6G ethanol solution was drop-casted onto the NP-Au ( $1 \times 1 \text{ cm}^2$ ) which was dried at room temperature for 30 min in the dark. The substrate preparation procedure is represented in fig. 4.2. Also, the equivalent volume of  $10^{-3}$  M R6G solution was dropped onto the Si substrate, which was used as a reference sample and as a base material (mentioned earlier) to coat NPAu onto it. After drying, the substrates were stored under vacuum conditions for further analysis. The reason for the selection of Si as a reference and a base material is that its Raman peaks and bands are well known at 521 and 935–990  $\text{cm}^{-1}$ . The Raman spectra of R6G has been widely reported, but the spectra of NP-Au has not been shown in the literature. Therefore, it has been chosen to know about the NP-Au peaks. So that if peaks appear in the spectra, the NP-Au peaks can be easily distinguished from the Si peaks.

The SERS performance of the substrates was examined using a Horiba Raman spectrophotometer (LabRam HR Evolution, Horiba Scientific) equipped with a 532 nm Ar ion laser source. The Rayleigh scattering was rejected using a notch filter with a blocking region of  $532 \pm 8 \text{ nm}$ . The excitation beam was focused on the sample using a 50X microscope objective and the scattered Raman light was collected using the same objective. All the measurements were recorded at 23  $^{\circ}\text{C}$ . The laser beam power was varied from 0.1 mW to 10 mW in order to optimize the results. The integration time was 2 s with two accumulations for a better signal-to-noise ratio, and the grating of 600 grooves/mm was

used. The diameter of the laser spot was  $\sim 1.3 \mu\text{m}$  and each of the spectra which were shown in the study was the average of seven spectra's recorded by selecting seven spatial positions on each sample. The characteristic Raman peak of a Si substrate at  $520 \text{ cm}^{-1}$  was used to calibrate the spectrometer.

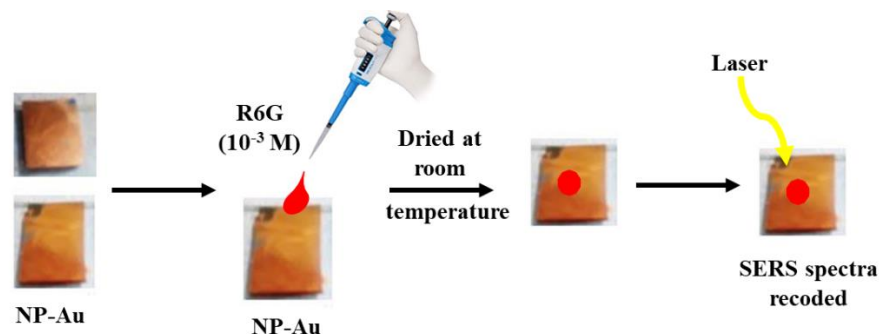


**Figure 4. 3.** Pictorial representation of the fabrication of NP-Au as a SERS sensor.

#### 4.1.2.2.3 *SERS substrate (NP-Au) characterization*

The absorption maxima of R6G and NP-Au substrate is measured using the UV–visible spectrophotometer (UV–Vis lambda 950, PerkinElmer). The surface morphology of the film before and after de-alloying is studied using field emission scanning electron microscopy (Carl Zeiss, supra-55) and the Everhart–Thornley detector is used to collect the emitted secondary electrons from the sample surface. The content variance of the dealloyed samples have been evaluated by an energy dispersive X-ray spectrometer (EDS) connected with SEM (Jeol, JSM6610LB). The average pore size is calculated by using an image J software by counting  $\sim 150$  pores and ligaments from the FE-SEM images.

### 4.1.3 *Result and Discussion*

#### 4.1.3.1 *Absorption peak determination*

In order to select the optimal laser excitation source for Raman measurement, the absorption spectra of R6G and dealloyed substrates for different time were recorded as shown in fig. 4.3. It has been stated that enhancement in the SERS signal can be improved by two resonance effects: (a) if the excitation wavelength is in resonance with the surface plasmon resonance (SPR) of nanostructured materials (the plasmon resonance peak i.e  $\lambda_{\text{max}}$  of the nanostructured materials) and (b) if the Raman active molecule is in resonance (absorption wavelength i.e.,  $\lambda_{\text{abs}}$ ) with both the excitation wavelength and the SPR of nanostructured materials [62]. Fig. 4.3 (a) illustrates the absorption and emission spectra of ethanolic solution of R6G and fig. 4.3 (b) shows the absorption spectra of NP-Au substrates dealloyed for different times. As depicted from fig. 4.3 (a) the absorption peaks of R6G ranges between 440 nm and 570 nm, with the maximum  $\lambda_{\text{ab}}$  peak at  $\sim 532 \text{ nm}$  and a vibronic shoulder of around  $\sim 470 - 495 \text{ nm}$ . One peak is due to the monomer absorption band at  $\sim 532 \text{ nm}$  (much more pronounced as well as a

characteristic peak) and a minor shoulder at  $\sim 492$  nm is due to the dimer [158]. Similarly, the emission spectrum varies from about 510 nm to around 710 nm with the maximum peak at  $\sim 550$  nm depending on the solvent and the dye concentration. Fig. 4.3 (b) represents NP-Au substrates represent  $\lambda_{\text{max}}$  peak at around 515 nm, which is due to the resonant excitation of plasma oscillations. The common laser excitation wavelengths used in the Raman spectrometer are 532, 633 and 785 nm and the peak of both the spectrums are very close to the 532 nm laser of the Raman spectrometer. Therefore, the 532 nm laser has been used as the excitation source which is beneficial for the formation of localized surface plasmon resonance (LSPR) in the NP-Au and also in resonance with the R6G. The  $532 \pm 8$  nm notch filter has been used to block the Rayleigh line. The filter blocking wavelength range is from 523.5 nm to 540.5 nm, thus it cannot affect or cut off the R6G peaks as they fall far beyond this range. The below mentioned table represents the peak values of R6G taken directly from the literature [159], the values have been converted from the wave number to wavelength as shown in table 4.1. It can be seen that none of the peaks of R6G falls into the notch filter blocking range.

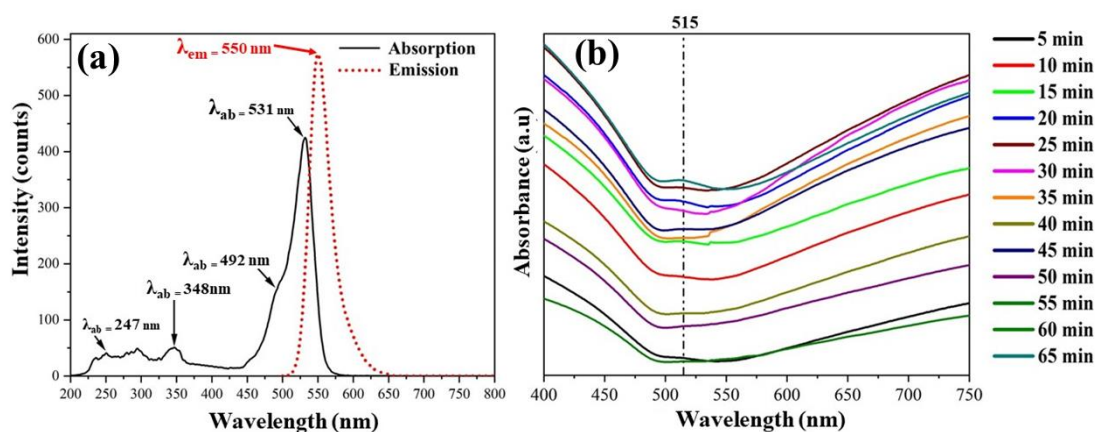


**Figure 4. 4.** (a) Absorption and emission spectrum of ethanolic solution of R6G and (b) absorption spectrum of NP-Au substrates dealloyed for different time.

**Table 4. 1.** Conversion of R6G characteristic peaks from wavenumber to wavelength.

S.No.	Peak value in terms of wavenumber ( $\text{cm}^{-1}$ )	Peak value in terms of wavelength (nm)
1.	611	16366
2.	771	12970
3.	1185	8439
4.	1360	7453
5.	1505	6644
6.	1570	6369
7.	1648	6067



#### 4.1.4 SERS effectiveness testing of NP-Au

To examine the SERS performance of NP-Au substrates, the measured Raman spectrum of three samples as shown in fig. 4.4 for SERS substrate (NP-Au coated on Si (black colour)), R6G adsorbed on SERS (blue colour) and for the bare Si substrate (red colour). Here, the sample dealloyed for 65 min is only considered as it has been reported that the content of Ag decreases with the increase of etching time, which is an advantage for the SERS performance. The spontaneous oxidation of Ag causes the reduction in the SERS intensity that also leads to the difficulty of reproducible SERS signals [57]. Therefore, in order to avoid much contribution from Ag, this etching time is selected for the initial studies. Fig. 4.4 (a) shows the measured Raman signal from the R6G on a Si substrate that exhibits broad spectral features due to the strong background fluorescence of R6G that overwhelms its Raman signal [160]. However, the fluorescence of R6G is quenched on NP-Au as can be seen from fig. 4.4 (b). In addition, all the characteristics Raman vibrational bands of R6G at 611, 771, 1185, 1360, 1369, 1505, 1570, and  $1648\text{ cm}^{-1}$  are obtained, which are well-matched with the previous reports on R6G [159], [161]. It has been reported that, if the detected molecule is present in or close to the hot spot or the LSPR region, the fluorescence is quenched and the characteristic signals of the molecule is observable [162]. The propagation length of the plasmonic resonance of NP-Au is  $\sim 4\text{--}5\text{ }\mu\text{m}$ , which is quite larger than the detection area as well as the laser spot size [163]. Therefore, it can be said that the detection of molecule over the substrate has an appropriate contribution from plasmonic. The right-hand spectra is the magnified view of fig. 4.4 (b) & (c). It can be clearly noticed that the Raman peaks of R6G on NP-Au are very intense and well resolved. However, the bare SERS substrate is not showing any peaks, which means that it only plays a role in maximally amplify the SERS signal.

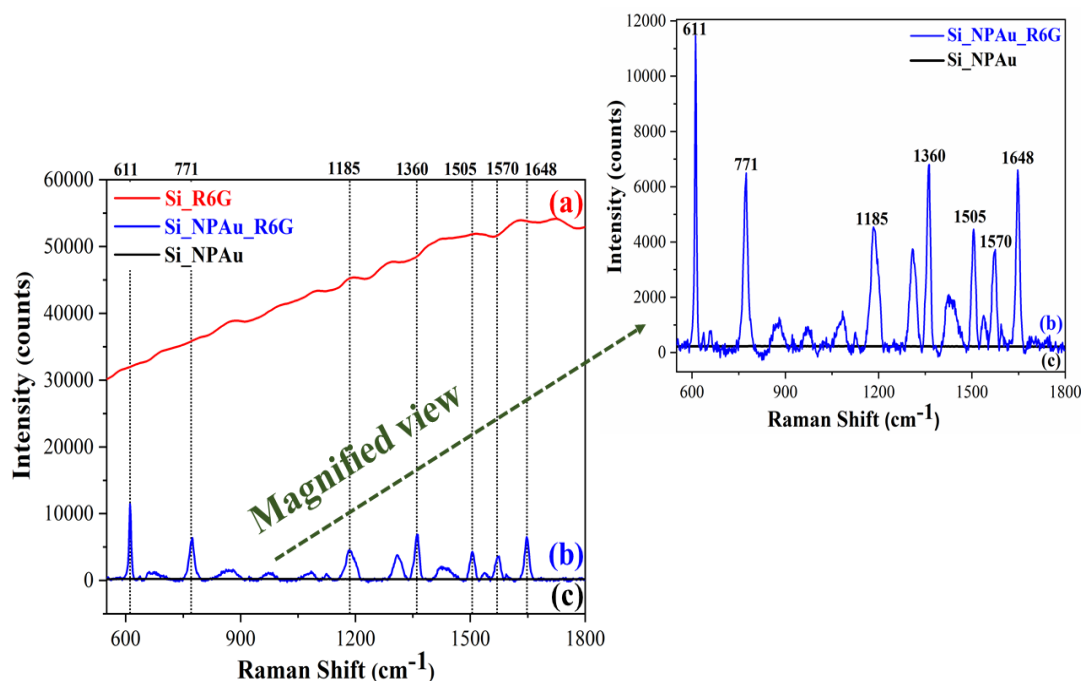


**Figure 4. 5.** Raman spectra of R6G adsorption on different substrates recorded at 10 mW laser power (a) bare Si substrate; (b) SERS substrate (NP–Au coated on Si); (c) Raman spectrum of SERS substrate without adsorption of R6G molecule. Right-hand side is the enlarging view of (b) and (c) spectrum clearly indicating that the bare SERS substrate does not show its own peaks.

#### 4.1.3.1.1 Optimization of SERS parameters

Most of the reported literature did not report the characteristic Raman bands of R6G on bare Si substrate due to the strong fluorescence background which results in the broad spectrum [164]. On the other hand, it has also been demonstrated that R6G is a Raman active molecule, and thus shows some of its characteristics peak on Si with very low-intensity values [165], [166]. Hence, the Raman peak intensity of R6G on Si is used to optimize the required excitation laser power in the subsequent experiments. The results presented in fig. 4.4 is obtained with 10 mW laser power and that shown in fig. 4.5 is measured using 0.1 mW of excitation laser power. The power of the laser is reduced by using a Neutral Density (ND) filter. The 532 nm laser used for the experiment has a maximum power value of 100 mW. All other parameters such as the concentration and volume of R6G, wavelength, and laser spot size are kept the same. It is clear from fig. 4.5 (a) that the R6G shows signals on Si substrate but with poor intensity values and some of the signals corresponding to 1505, 1570, and 1648  $\text{cm}^{-1}$  are not clearly observable, which merged into noise. However, on NP-Au the R6G Raman intensity of signals is quite high with all the fingerprints of Raman peaks associated with R6G. These results indicate that the pump power also affects the signal strength of R6G, so with the selection of laser

wavelength, laser power also matters for optimum SERS performance. Hence, 0.1 mW laser power has been used in the following discussions.

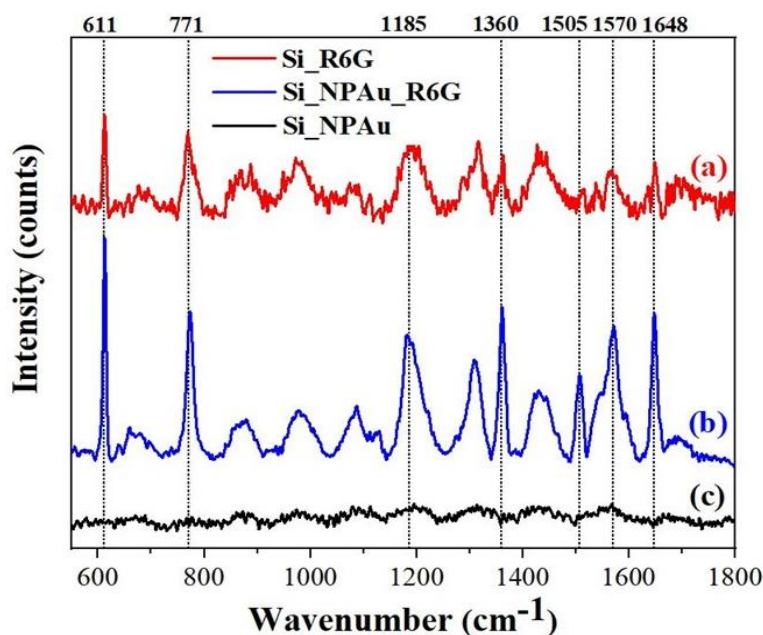


**Figure 4. 6.** Raman spectrum of R6G adsorbed on substrates corresponding to 0.1 mW laser power (a) bare Si substrate; (b) SERS substrate; (c) Raman spectrum of SERS substrate without adsorption of R6G molecule.

#### 4.1.3.1.2 *Enhancement factor calculation*

After the optimization of the experimental parameters and analysis of the SERS spectrum of R6G on the 65 min dealloyed NP-Au, a study on the rest of the dealloyed samples is elaborated to check which dealloying time shows the highest signal enhancement as depicted in fig. 4.6. The abbreviations of the samples used in the current study are summarized in table 4.2 with  $S_0$  corresponds to bare Si substrate. Fig. 4.6 shows the measured Raman spectra for different dealloyed samples. The measured spectra shown in fig. 4.6 is obtained by averaging the data collected from seven spatial regions on the sample. It is clearly noticed that the dealloyed samples show a similar kind of spectrum with a quite variation in the intensities of the SERS signal. Therefore, to evaluate how much the intensity of SERS signals varied against the dealloying time, the intensity of all the characteristic peaks of R6G is measured and represented in the histogram with 3% error bars in fig. 4.7. The obtained results indicate that samples  $S_6$  and  $S_9$  possesses the highest enhancement in SERS intensity for all the peaks of R6G.

**Table 4. 2.** Representation of substrate names with abbreviations

S. No.	Substrate Name	Abbreviation
1.	Bare Si	S <sub>0</sub>
2.	5 min etched NP-Au	S <sub>1</sub>
3.	10 min etched NP-Au	S <sub>2</sub>
4.	15 min etched NP-Au	S <sub>3</sub>
5.	20 min etched NP-Au	S <sub>4</sub>
6.	25 min etched NP-Au	S <sub>5</sub>
7.	30 min etched NP-Au	S <sub>6</sub>
8.	35 min etched NP-Au	S <sub>7</sub>
9.	40 min etched NP-Au	S <sub>8</sub>
10.	45 min etched NP-Au	S <sub>9</sub>
11.	50 min etched NP-Au	S <sub>10</sub>
12.	55 min etched NP-Au	S <sub>11</sub>
13.	60 min etched NP-Au	S <sub>12</sub>
14.	65 min etched NP-Au	S <sub>13</sub>

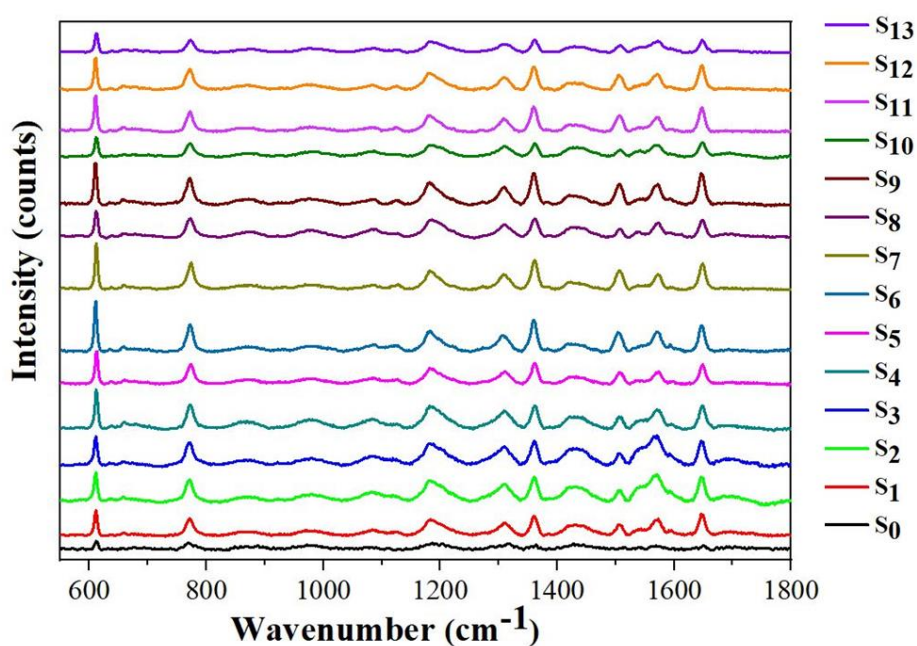


**Figure 4. 7.** SERS spectrum of  $10^{-3}$  M R6G on the samples dealloyed for different time

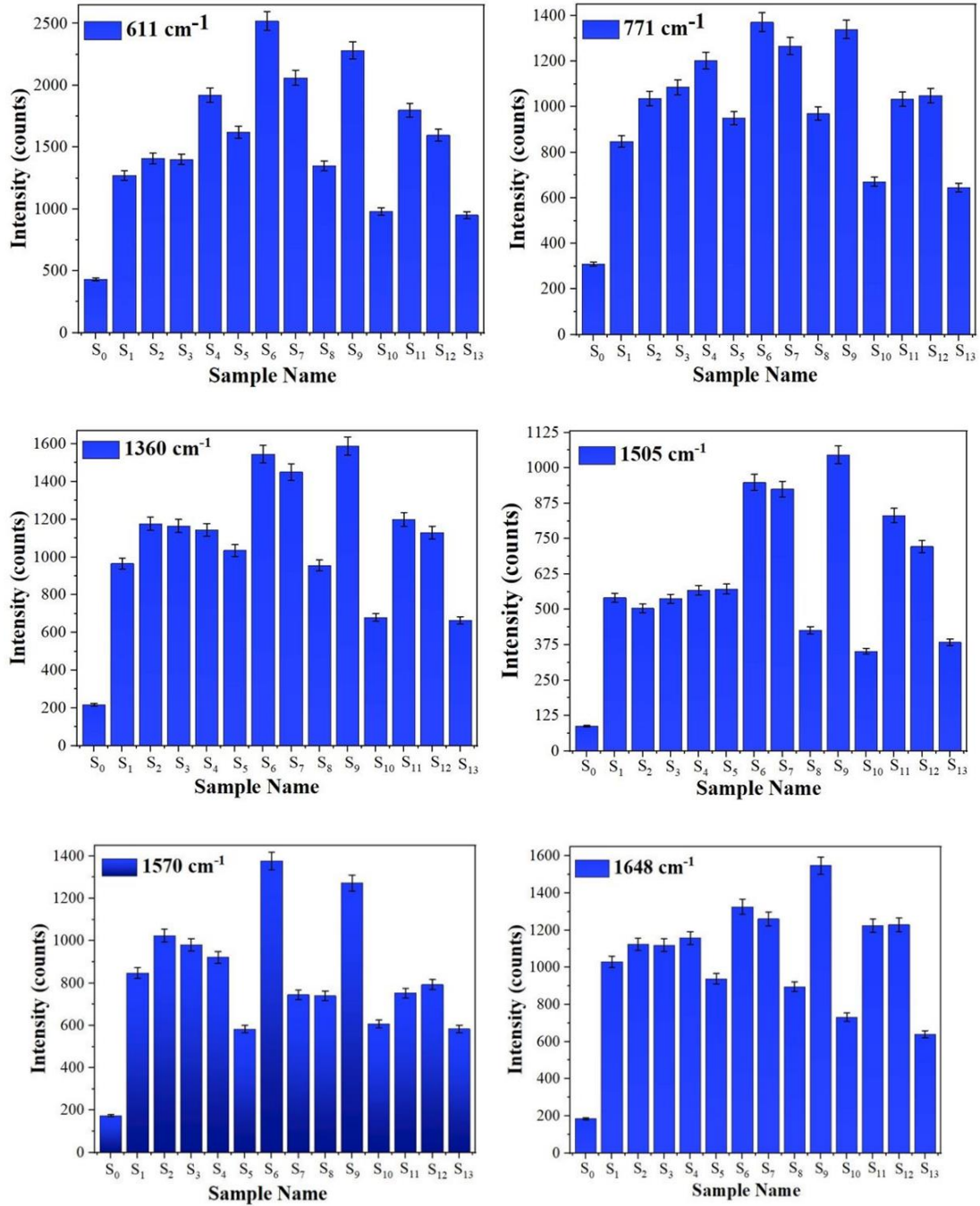


**Figure 4. 8.** Intensities of the characteristic peaks of R6G measured from fig. 4.6.

To examine the Raman signal enhancement of S<sub>6</sub> and S<sub>9</sub> samples, the enhancement factor (EF) is calculated using the formula as discussed in section 2.2.3.3 in equation ‘2.11’ [138]:

$$EF = \frac{I_{SERS} \cdot C_{Raman}}{I_{Raman} \cdot C_{SERS}} \quad (eq. 2.11)$$

Where  $I_{SERS}$  and  $I_{normal}$  corresponds to the Raman intensities of R6G on S<sub>6</sub> or S<sub>9</sub> and S<sub>0</sub>, respectively.  $C_{normal}$  and  $C_{SERS}$  represent the molar concentration of R6G on S<sub>0</sub> and S<sub>6</sub>/S<sub>9</sub> respectively. In this study, similar concentration ( $10^{-3}$  M) and equal volume (10  $\mu$ l) of R6G is

applied to both substrates, so the values of  $C_{\text{normal}}$  and  $C_{\text{SERS}}$  cancel each other. The values of  $I_{\text{SERS}}$  and  $I_{\text{normal}}$  are taken directly from the measured Raman spectra. The EF values of both the samples corresponding to all the bands are given in table 4.3. It can be clearly recognized that the intensity at the  $1505\text{ cm}^{-1}$  band is enhanced more than nine-fold and in-fact this Raman peak of R6G is not seen on the Si substrate. This confirms that the NP-Au is an effective SERS substrate. The average EF values are also calculated for both substrates; it is above  $\sim$  fivefold. The important point about this substrate is, it provides five-fold enhancement without any kind of further improvement onto the morphology and which is higher than the earlier reports [43], [96], [157]. The other reason for less signal enhancement is the use of low laser power to avoid fluorescence from the molecule. It is well known that; with increasing laser power, intense light is produced due to the generation of a greater number of photons. These photons come in contact with the sample as well as the molecules in that particular area. Correspondingly, the localized field gets intensified as the laser power increases. The adsorbed molecules feel an enhanced electromagnetic field and emit intensified Raman signals.

**Table 4. 3.** Calculation of SERS EF for the  $S_6$  &  $S_9$  samples.

S. No.	Peak Position ( $\text{cm}^{-1}$ )	EF_ $S_6$	Average EF	EF_ $S_9$	Average EF
1.	611	5.83	5.55	4.79	5.69
2.	771	3.81		3.72	
3.	1185	3.06		3.35	
4.	1360	6.05		6.04	
5.	1505	9.69		10.42	
6.	1570	4.82		4.96	
7.	1648	5.59		6.61	

#### 4.1.5 Morphology examination

As shown in fig. 4.8 (b), the  $S_6$  and  $S_9$  samples show the highest Raman signal enhancement. So, to understand the reason behind the enhancement, morphology evaluation of the samples is performed. Figure. 4.8 represents the top-view FE-SEM images of the commercial alloy leaf and the dealloyed samples ( $S_6$  &  $S_9$ ). The 5 kV operating beam voltage is used to analyze the morphology of all the samples and to prevent the sample from damage. Fig. 4.8 (a) shows that alloy has a granular kind of structure without pores, whereas it becomes porous after dealloying as demonstrated in fig. 4.8 (b) and (c). After chemical dealloying, a metal-void phase is obtained throughout the samples. The microstructure of both the dealloyed samples consists of a pore and a network of gold ligaments. No cracks or other defects are seen in these structures, which represents the excellent structural uniformity of these NP-Au over a large area. In the  $S_6$  sample,



ligaments are separated with very small pores (represented by a yellow arrow). The average size of the pores and ligaments are  $\sim 13 \pm 0.43$  &  $\sim 81 \pm 1.6$  nm. There could be two mechanisms that are responsible for the SERS enhancement in NP-Au samples. One could be the plasmon excitation in the nano-sized ligaments by an incident laser that induces local electromagnetic field enhancement around the ligaments. The second mechanism could be the electromagnetic coupling between the adjacent Au ligaments that further increases the localized field intensity, leading to a further improvement in the SERS enhancement. The morphology of the  $S_9$  sample is quite different from the  $S_6$  sample. Immersion in acid for another 15 min causes the coarsening (diffusion of Au atoms at the surface of ligaments) of the ligament and the pores. The interconnected network of ligaments is separated by pores with an average size of the pores are  $3.7 \pm 0.9$  nm. The Raman signal enhancement arises here due to the creation of hot spots between the neighbouring ligaments separated by nanosized pores (shown by a yellow circle) and the creation of local electromagnetic fields around ligaments. These results suggest that, for these etching times, the maximum number of nanopores, nanosized ligaments, and hotspots are obtained as compared to the rest of the dealloying time.

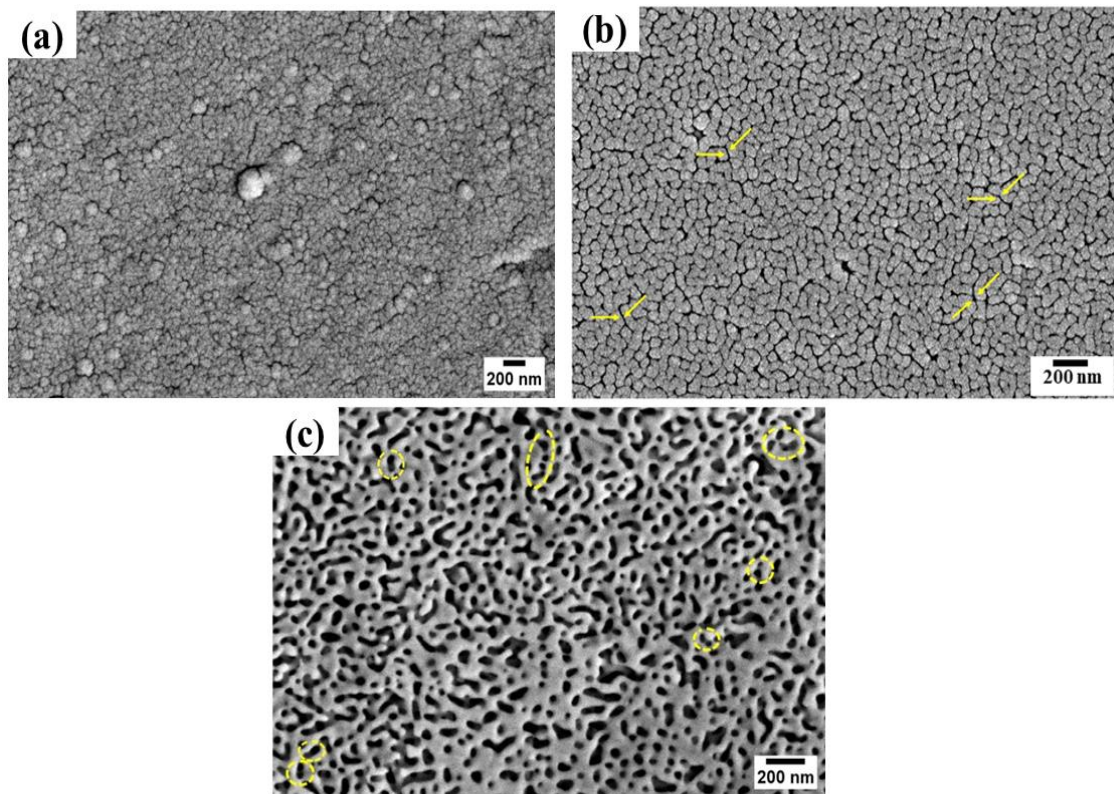


**Figure 4. 9.** FESEM images of (a)  $Au_{50}Ag_{50}$  alloy leaf, (b)  $S_6$  and (c)  $S_9$  samples. The magnification of all the shown images is 75 K.

To check the surface area, roughness, and uniformity of the structures in the alloy and dealloyed samples (30 & 45 min), the 2D and 3D AFM topographical images is captured in contact mode as shown in fig. 4.9 and 4.10. The alphabetical letter (a, b, c) without symbol dash (') represents the 2D image and with symbol (') represents the 3D image of substrates. The morphological view of the alloy leaf shows that it has a non-uniform microstructure pattern (fig. 4.9 (a)). Most part of the alloy is filled with the varied size of humps as can be clearly seen from fig. 4.9 (a'). The statistical parameters of the alloy such as root mean square (R.M.S.) roughness of the alloy is  $\sim 12.2$  nm, height is  $\sim 43.7$  nm, and the surface area are  $9.62 \mu\text{m}^2$  respectively is mentioned in table 4.4. Figure. 4.10 ((b), (b'), (c), and (c')) represent the morphology of the dealloyed samples. It can be seen from the 2D image of both the samples that the topography is completely changed and the formation of Au ligaments separated by nanopores is clearly visible and matched with the FESEM images. The nanostructures formed on the substrate are uniform after dealloying. The 3D image of fig. 4.10 (b') and 4.10 (c') shows that most of the area of the substrate is filled with nano-ligaments.

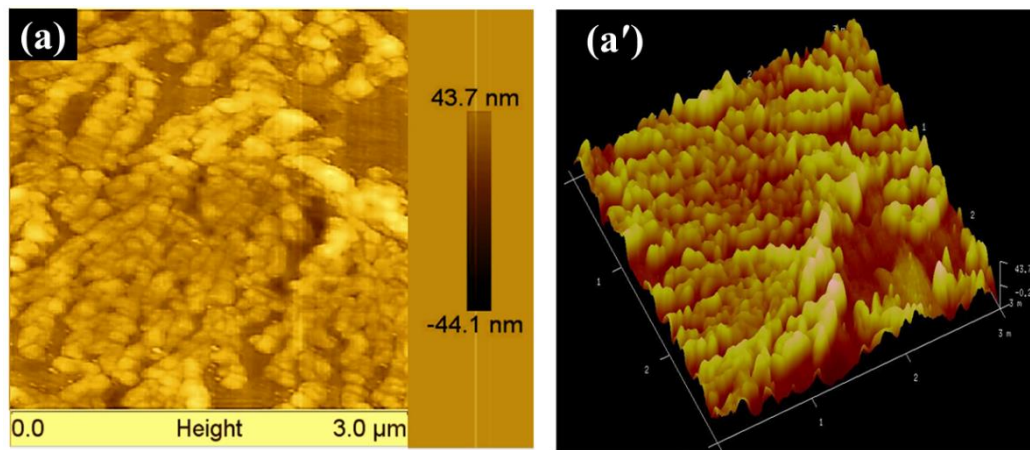


**Figure 4. 10.** AFM analysis of Alloy leaf (a) represents the 2D image and (a') shows the 3D view of surface. The size of both image is  $3 \mu\text{m} \times 3 \mu\text{m}$ . The height scales are shown in the right side of 2D image.



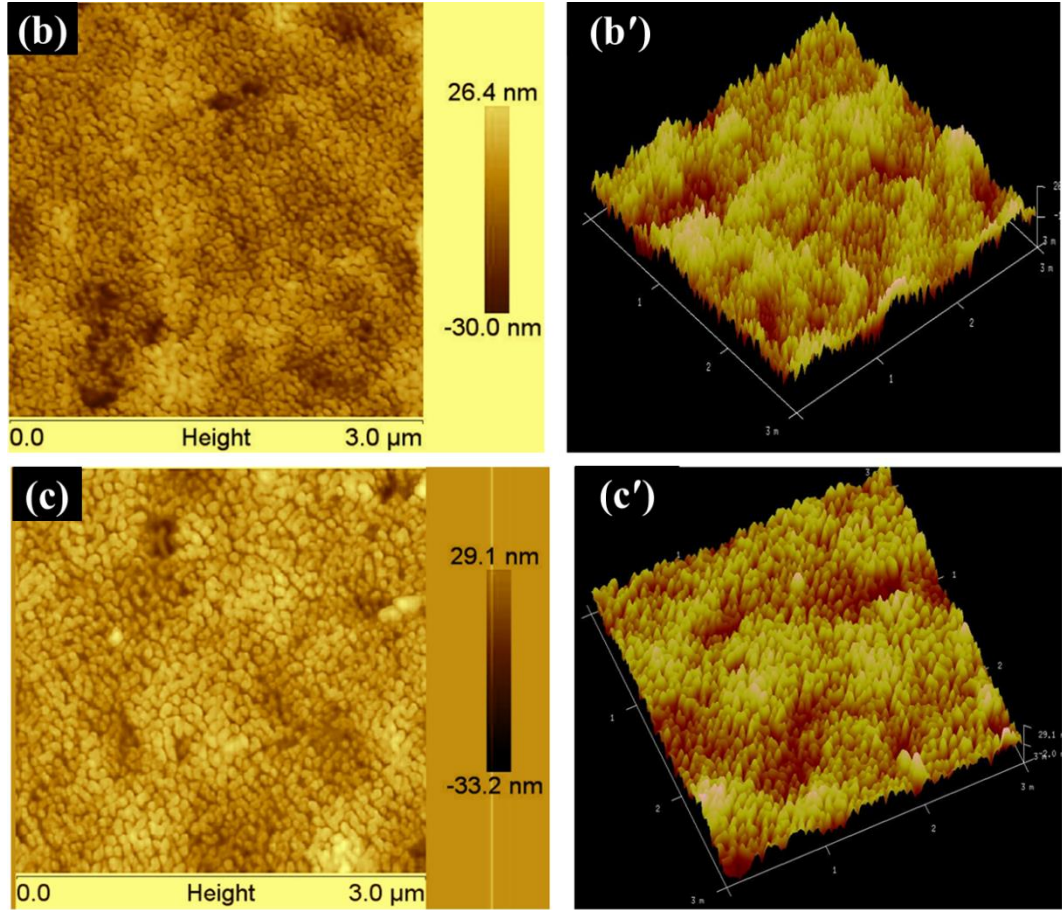


**Figure 4. 11.** AFM analysis of dealloyed samples such as (b) and (b') represents the sample dealloyed for 30 minutes and (c) and (c') represents the sample dealloyed for 45 minutes. The surface morphology shifts from a nonuniform substrate to uniformly nano-structured surface with dealloying. The left-hand side is the 2D view and the Right-hand side is the 3D view of the substrate. The size of each image is  $3\ \mu\text{m} \times 3\ \mu\text{m}$ . The height scales are shown in the right side of 2D image.

The parameter values of the dealloyed samples increase with increasing dealloying time as shown in table 4.4. The roughness and height values increase due to the coarsening of the ligaments, which cause the Au ligament to interconnect with each other, that correspondingly makes the substrate more roughened with increasing dealloying time. On the other hand, if the parameter values are compared with alloy, the surface area is higher for the dealloyed samples because of the formation of nanostructures such as nanopores and nano-ligaments. Subsequently, the roughness and height values of the alloy are higher than dealloyed samples, due to the lack of uniformity in microstructures.

**Table 4. 4.** Represents the statistical parameters of the samples such as surface area, roughness, and height of the structures.

S. No.	Sample Name	Surface Area ( $\mu\text{m}^2$ )	Roughness (nm)	Average height (nm)
1.	Alloy ( $\text{Au}_{50}\text{Ag}_{50}$ )	9.62	~12.2	43.7
2.	Dealloyed sample (30 min)	9.83	~7.77	26.4
3.	Dealloyed sample (45 min)	9.96	~ 8.77	29.1

#### 4.1.6 Composition determination

The composition analysis of the dealloyed samples is also performed using the measured EDS spectra as represented in fig. 4.11. These studies assume importance as it suggests the beginning of etching as well as the saturation of Ag removal during the dealloying of the samples. As discussed earlier, Ag is readily oxidized and leads to inhomogeneous results. Saturation in the element's content after a particular time raises the possibility of reproducible signals. It can be noticed that from fig. 4.11 (a-n), the signals of Au and Ag are clearly present in the alloy, whereas in the dealloyed samples, signals of Au are present, and the absence of Ag peak indicates the dissolution of Ag from the leaf. However, there is a content variation of Au and Ag with the dealloying time which is not observable with these spectra. Therefore, to measure the actual content variation the graph is plotted between the variation in composition with respect to the samples shown in fig. 4.11 (o). For ease of comparison, the signal from Si substrate is eliminated (used as a base material) in the dealloyed samples. The Au and Ag content in the commercial alloy is ~48:52 at% while after dealloying the sample is composed mainly of Au with residues of Ag. The  $S_1$  sample possesses less than ~5 at% of Ag, and with further increase in the dealloying time, the Ag content is continuously reduced down to ~0.5 at % for the  $S_{10}$  sample. The Ag content is zero for the  $S_{11}$  sample which indicates the total dissolution of Ag from the leaf which is confirmed up to the  $S_{13}$  sample.

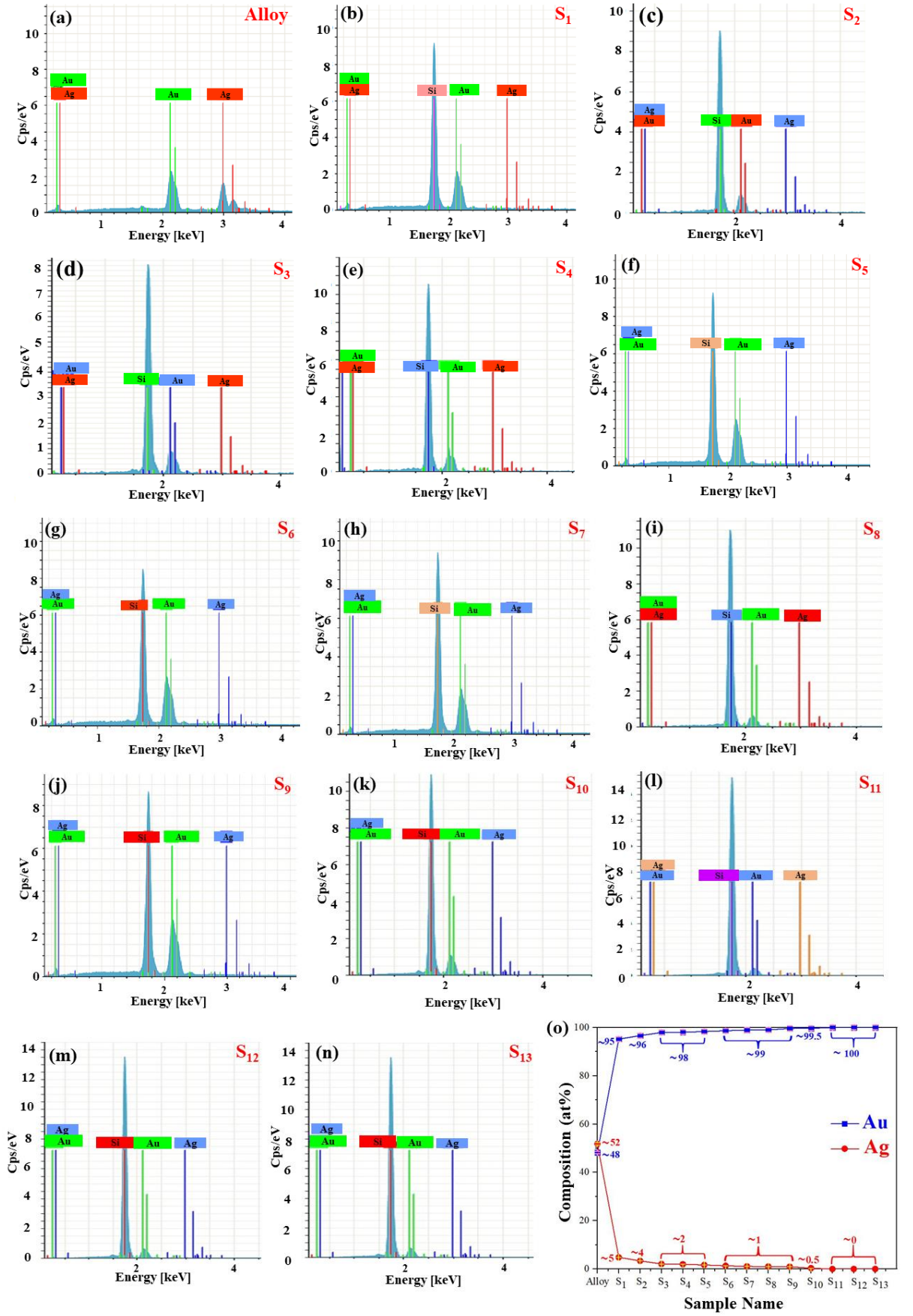


**Figure 4. 12.** EDS spectra (a) commercial alloy, (b)-(n) dealloyed samples, and (o) the composition variance of Au and Ag with respect to samples.

#### 4.1.7 SERS parameter determination

##### 4.1.3.1.3 Substrate uniformity testing

The practical applications of SERS are significantly affected by the uniformity of the substrate (intensity variation across the substrate). Hence, to determine whether our proposed SERS substrates can reproduce the signals across the whole substrate, seven different locations on the highest enhancement samples ( $S_6$  and  $S_9$ ) are randomly selected which are displayed in fig. 4.12. All the spectra are similar in shape with peaks appearing at similar frequencies with a minimal intensity variation of the SERS signal. The exact intensity variation is confirmed through the estimation of Relative standard deviation (RSD) values corresponding to all the characteristic peaks of R6G for both the dealloying time are calculated as represented in table 4.5. The RSD values for both the samples is less than 20%, which represents the excellent homogenous nature of the samples over the whole area.

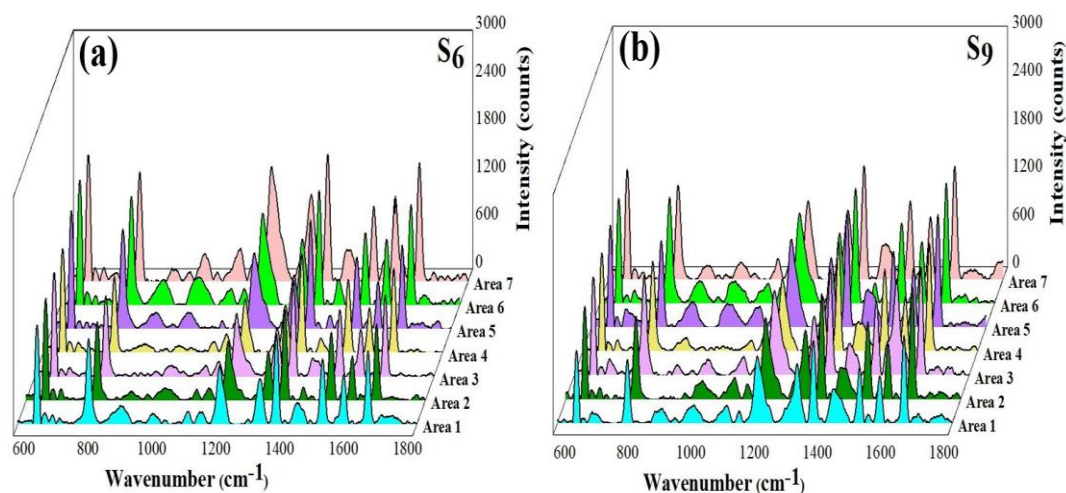


Figure 4. 13. SERS spectrum of  $10^{-3}$  M R6G obtained at seven areas selected randomly on the same NP-Au substrate (A)  $S_6$  and (B)  $S_9$ .

**Table 4. 5.** RSD values of samples  $S_6$  &  $S_9$  corresponds to the characteristic peaks of the R6G

Sample Name	Peak position (cm <sup>-1</sup> )	611	771	1360	1505	1570	1648
$S_6$	RSD value (%)	10.52	13.79	11.59	7.47	17.79	17.41
$S_9$	RSD value (%)	11.15	12.41	8.89	11.61	18.62	7.42

##### 4.1.3.1.4 Substrate reusability testing

The reusability of the SERS substrate is an interesting point to be addressed with any kind of SERS substrate. The reusability of substrate reduces the cost as well as fabrication time. Several methods such as heating, acid cleaning, and photocatalytic degradation have been

developed for the removal of the analytes to prepare substrates for its reuse for SERS measurement [158]. Inspired by these considerations, the reusability of the  $S_6$  sample has been studied. The  $S_6$  sample possesses the microstructural features such as nanopores and ligaments which are continuous throughout the sample in comparison to the  $S_9$  sample. Reusability was tested by following a simple method, slowly dropping 3 mL of ethanol onto a substrate kept at  $45^\circ$ , so that all R6G could be rinsed off with ethanol. Four cycles of washing and re-adsorbing the R6G on the same substrate was performed. After each washing and re-adsorption, the Raman spectrum was recorded as represented in fig. 4.13 (a).

The cycle began with attaining the spectra of  $S_6$  sample without the adsorption of R6G, then the SERS spectrum of the  $S_6$  with R6G is recorded. After that, the used NP-Au is cleaned with ethanol. The removal of the analyte is confirmed again by spectroscopic measurement. No trace of R6G is detected in the Raman spectra after washing indicating the complete removal of the analyte molecule. Then the R6G is re-adsorbed on the cleaned substrate which shows all the characteristic bands, but the intensity is little suppressed as compared to the fresh sample. These washing and re-adsorption steps are repeated two times more. The intensities of the characteristic bands of R6G after each recycles is depicted in the histogram with 3% error bars in fig. 4.13 (b).

To evaluate the intensity fluctuation, the RSD values related to all the peaks of R6G are calculated as mentioned in table 4.6. The RSD values for the recycled samples are calculated with respect to the fresh sample. It can be seen that for three cycles the average RSD values are less than 20% indicating not much signal loss in the signal intensity variation, which is considered to be a satisfactory degree of SERS signal fluctuation [157]. For the fourth measurement, the RSD values are greater than 20%, but the peaks of R6G are sharp, intensified, and clearly identifiable, which indicates that the substrate can be reused at least 4 times.



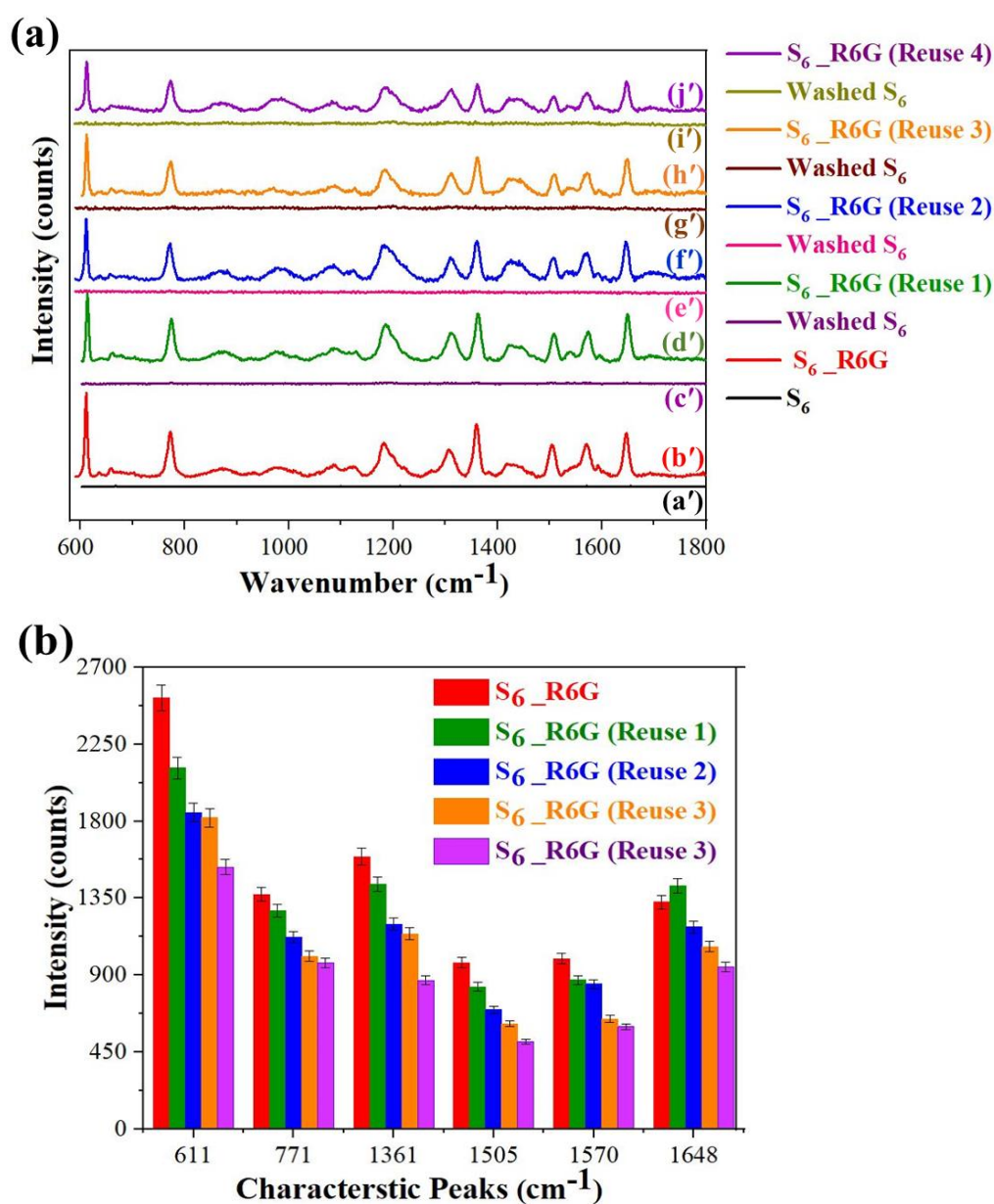


**Figure 4. 14.** (a) Reusability test, spectra (a') (c') (e') (g') (i') related to  $\text{S}_6$  sample and (b') (d') (f') (h') (j') related to R6G adsorbed on  $\text{S}_6$  sample; (b) Histogram shows variation in the intensities of the characteristic peaks of R6G after four cycles.

#### 4.1.3.1.5 Cost calculation of the substrate

The NP-Au substrate cost is ~3855 /- when the Si substrate is used as base substrate. However, when the glass is used as a base substrate instead of Si than the cost is only ~250 /- for a  $1.5 \times 1.5 \text{ cm}^2$  substrate. The below mentioned table 4.6. shows the cost of each material, which is required for the fabrication of the NP-Au substrate.

**Table 4. 6.** represents the material which is required for the fabrication (alloy leaf, HNO<sub>3</sub>, glass slides, two beakers (one for HNO<sub>3</sub> and other for DI water) with cost.

S.No.	Material	Available Quantity	Cost	Required quantity	Cost
1.	Au <sub>50</sub> Ag <sub>50</sub> Leaf	1 Pack (25 sheets- 8×8 cm <sup>2</sup> )	~2000/-	1×1 cm <sup>2</sup>	~10/-
2.	HNO <sub>3</sub>	2.5 L (69 %)	~500/-	~20 mL	~5/-
3.	Deionized Water	1L	75/-	3L	~225/-
4.	Silicon (Si)	8×8 cm <sup>2</sup> (p-type with <100> orientation	~19,280/-	1.5×1.5 cm <sup>2</sup>	~3615/-
<b>Total (Including Silicon) =</b>					<b>Rs= ~3855/-</b>
5.	Glass	1 Pack (50 slides)	~330/-	1.5×1.5 cm <sup>2</sup>	~ 10/-
<b>Total (Glass replaced with Silicon) =</b>					<b>Rs= ~250/-</b>

#### *Conclusion of part 4.1*

The uniform and reusable NP-Au as a SERS substrate has been fabricated by varying the dealloying time. The 30- and 45-min dealloyed samples exhibited the highest SERS enhancement in comparison to other samples. Morphological study confirmed that the Raman enhancement of these is due to the combination of localized field enhancement around the nanopores, gold ligaments, as well as electromagnetic coupling effect between adjacent ligaments. The composition study revealed that the content of Ag in 30- and 45-min samples is ~1 at% which is beneficial for enhancing the stability of the SERS signal. The SERS substrate exhibit good uniformity and showed reusability capability by representing an RSD value of less than 20% which is important for practical applications. Hence the proposed interconnected metal network structure could be used as a promising SERS substrate. It can help to reduce the cost of the fabrication process, pollution after disposal of the substrate, and enhance its utilization for many applications. The substrate can be used for the detection of pathogens (bacteria and viruses etc.), food contaminants (pesticides {chlorpyrifos, methyl parathion, and thiram which are generally used to kill pests and protect the crop from fungal disease}), and also can be used for narcotics (cocaine, heroin, morphine, and codeine, etc.) and environment pollutants (heavy metals {As, Pb, and Cd, etc.}) detection.

#### ***Part 4.2: Tuning the structure of NP-Au substrate by Raman spectrometer ‘Argon’ ion laser to improve SERS performance.***

The easy, fast, and reproducible laser annealing method has been used to tune the morphology of the substrate in order to improve the SERS performance. For this study, a pre-dealloyed 30-minute NP-Au has been selected for further treatment due to its high enhancement factor and uniform nature. In the earlier discussion, all SERS measurements such as enhancement factor calculation, uniformity, and reusability have been recorded only with the 0.1 mW laser power of the Raman system. The effect of laser power variation from 0.01 to 10 mW of a 532 nm laser has not been tested in the earlier study. Furthermore, certain other parameters examination such as sensitivity, stability, and testing of substrate for containment detection have not been investigated.

In the above-discussed work, the laser power of Raman spectrophotometer laser has been varied from 0.01 to 10 mW to examine its effect on the SERS enhancement. The Raman results have shown a good linear relationship with the laser power increment up to 3.2 mW and after that, the signal becomes saturated for a further increment in the power. In order to know the reason for SERS enhancement with power increment, morphological identification has been done and it reveals that the different sizes and shapes of the pores (open, diffused, and interlinked) are responsible for the SERS signal enhancement. Furthermore, the substrate showed good limit of detection (LOD) by detecting nanomolar range of R6G, the value is comparable with the substrates prepared by expensive techniques. The applicability of the substrate has been tested by detecting small cross-sectional urea molecules and it is able to enhance the signal up-to 16-fold. Other than this, the substrate shows good stability property by representing all characteristic peaks of R6G even after ageing for 2 years.

##### ***4.2.1 Introduction***

It has been earlier discussed that the SERS enhancement commonly depends on the nanoscale features such as surface morphology (shape, size) and the arrangement of plasmonic structures onto the substrates [167] [168]. Thus, fabrication of the optimized SERS substrate is important for signal enhancement. Processes such as laser and thermal annealing methods have also been used instead of the above-mentioned time-consuming and costly methods to fabricate and modify SERS substrates, but these are less known by researchers due to the availability of limited reports based on their use for SERS [169], [170], [171].

From the past few years, most of the research focused on the fabrication of ordered substrates in order to obtain a large enhancement factor and reproducible substrate, while other SERS parameters such as facile fabrication, cost-effectiveness, and most importantly substrate fabrication over a large area is usually neglected. The important thing about these annealing methods is that, these methods involve a single-step process to fabricate substrate over a large area and require a smaller number of sophisticated equipment compared to previously discussed



techniques. Furthermore, the substrate morphology such as size, shape, and arrangement of plasmonic nanostructures can be easily altered by optimizing the parameters during the annealing process [86], [155], [172], [173]. It has been reported that laser-induced annealing is more favourable to cause structural alteration in substrates as compared to thermal annealing [172], [174], [175]. The thermal approach requires a long annealing time and high temperature to restructure the plasmonic nanostructures.

Another advantage of laser annealing is that it is able to produce substrates with repeatable structural morphology. It has been stated that due to laser exposure, two things can happen: the first is the burning as well as tuning of the morphology of the substrate and the second is desorption, detachment, and degradation of the detected molecule can also occur [172]. Due to these two conditions, changes in SERS response mean either increment, decrement, appearance, or disappearance of peaks, as well as a shift in peak position can be observed [171]. From these points, it can be concluded that, along with the fabrication method, instrumental parameters such as laser wavelength and laser power need to be used carefully. These parameters can cause changes in the substrate as well as in the molecule.

#### 4.2.2 *Materials and Methods*

##### 4.2.2.1 *Materials*

All the chemicals (Au-Ag alloy leaves, R6G, P-type Silicon wafers, and solvents (Nitric acid) used for this study are the same as those discussed in earlier work. Only urea (fertilizer) was the new chemical used and was procured from the local market of Rupnagar.

##### 4.2.2.2 *Morphology tuning approach of NP-Au substrate*

First the NP-Au substrate was prepared similarly by the dealloying method as discussed earlier. The 30-minute dealloyed sample is selected for laser treatment as compared to other dealloyed samples due to their homogenous morphology and good SERS signal enhancement capability. After fabrication, the 30-minute dealloyed sample was exposed under varied laser power of Raman spectrometer as depicted from fig 4.14. For different laser powers, a different 30-minute dealloyed sample was used. The 20  $\mu\text{L}$  droplet of  $10^{-3}$  M R6G molecule was pre-adsorbed on all substrates prior to laser treatment.

##### 4.2.2.3 *Instrumentation*

Instrumentation used for the characterization of the substrate properties was also same as previous. The FE-SEM (Carl Zeiss, supra-55) was used to observe the change in surface morphology of the sample after laser power treatment. All the images were captured at 10 kV voltage. The parameters of the prepared substrates such as roughness and uniformity were determined by atomic force microscopy (AFM). Contact-mode AFM imaging was performed on a Bruker Instruments multimode microscope controlled by Nano scope V apparatus. A standard silicon nitride cantilever tip from budget sensors was used. The scan rate was 1–1.5

Hz. All AFM images were acquired at room temperature under ambient conditions. SERS measurements were conducted on a Horiba Raman spectrophotometer (LabRam HR Evolution, Horiba Scientific) equipped with an Ar ion laser source (532 nm). All other optical parameters such as objective lens (50 X), grating (600 grooves/mm), accumulation time (3) and integration time (2s) were used same as in the earlier study. Only laser beam power was varied from 0.1 mW to 10 mW in order to check the thermal effect onto the substrate as well onto the adsorbed molecule.

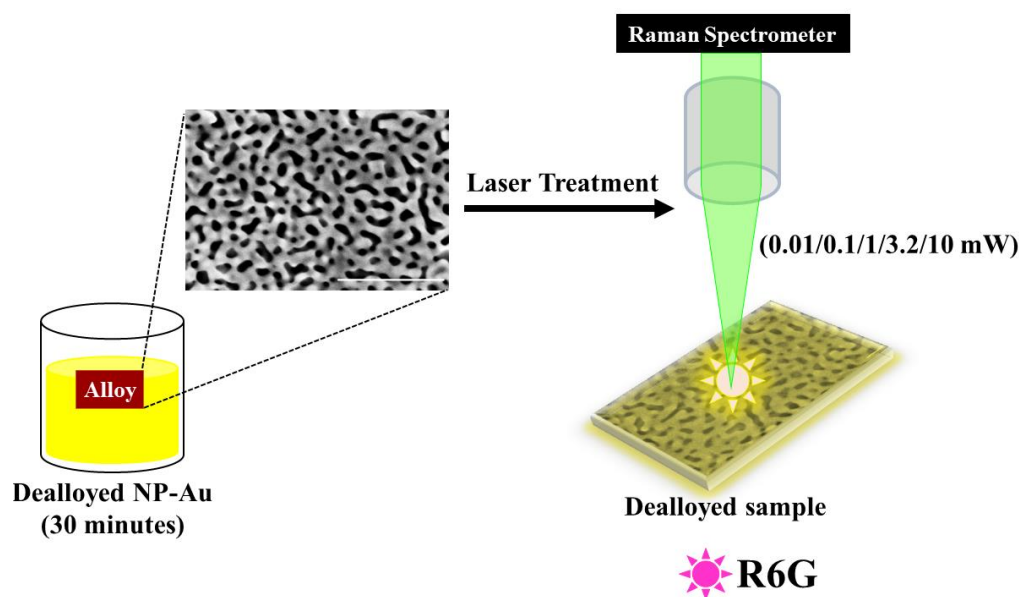


**Figure 4. 15.** Pictorial illustration of the NP-Au treatment process via different laser power of Raman system.

#### 4.2.3 Result and Discussion

##### 4.2.3.1 Laser power-dependent SERS intensities of NP-Au

To examine the thermal stability as well as the saturation point in the signal intensity of the substrate, the substrate is exposed with varying laser power from 0.1 to 10 mW as represented in fig. 4.15. Figure 4.15 (a) shows that peak positions of R6G adsorbed on NP-Au is not shifted with increasing laser power. All the peaks appeared at their reported positions. And also, the appearance and disappearance of any band is not observed during power variation. However, the intensities of all R6G bands increase dramatically as the laser power rises. To know the actual variation in the signal intensity, the spectrum is plotted between the intensity and laser power as represented in fig. 4.15 (b). The highest intensity band at  $611\text{ cm}^{-1}$  is used to measure the SERS enhancement of the substrate. It can be seen from fig. 4.15 (b) that SERS spectra of R6G adsorbed on NPAu increase fastly with increasing laser power up to 3.2 mW. This response is weaker for higher powers such as for 5 and 10 mW. Only a minor increment is observed in the SERS intensities above 3.2 mW as seen from table 4.6.

From these results, it can be stated that the performance of the substrate is also affected by the laser power. Figure 4.15 (b) (red dotted line) shows the behaviour of the molecule. The data have been fitted to the equation  $[I = I_{sat} (P/(P+P_{sat}))]$ , here,  $I_{sat}$  is the saturation count rate,  $P_{sat}$  is the saturation power of the detected molecule, and  $P$  is the applied laser power. The spectrum shape indicates that the SERS signal saturates at 3.2 mW with the saturation intensity of  $I_{sat} = \sim 16000$  counts. For the estimation of SERS enhancement factor, the enhancement of  $611\text{ cm}^{-1}$  peak corresponding to all laser power is calculated with respect to 0.01 mW power as shown in table 4.6. According to the data,  $\sim 10$ -fold enhancement is obtained at 0.1 mW, whereas for 1 mW, the SERS signal increases by about  $\sim 50$ -fold. The enhancement is further amplified by  $10^2$ -fold for 3.2 mW and it remains  $\sim 10^2$ -fold for a further increment in power (5 and 10 mW). Hence any power increment above 3.2 mW provides only a minor increase in the SERS intensities. Therefore, the study has only been done up to 10 mW power. No further increment in power is examined.

One more experiment is performed, in order to compare the SERS performance of the laser treated NP-Au substrate (green) with respect to untreated NP-Au (red) and bare substrate (black) as represented in fig. 4.15 (c). The treated NP-Au substrate is exposed with the 0.1 mW laser power of 532 nm laser before the R6G adsorption, to check the laser treatment effect. It can be clearly seen from the fig. 4.15 that the treated and untreated NP-Au samples are able to increase the signals as compared to Si due to the plasmonic enhancement. However, compared to the untreated sample, the treated sample exhibits a slight enhancement in signal, it might be due to the morphological changes which occur by exposing the same substrate with the laser multiple times. From these tests, it can be concluded that exposure of the sample multiple times with the same laser power may lead to the enhancement in signal slightly and slowly, while laser power increments such as from 0.01 to 3.2 mW can result in a rapid signal enhancement due to effective morphological changes.

As discussed earlier the increment or loss in the proportionality of SERS intensity with laser power is related to either degradation of the probe molecule or the change of morphology as well as burning of the substrate due to the raising of the power. The degradation of the molecule may not be happened in our case, because peaks are stable at its position. If degradation happens then peak shifting, the disappearance of the peaks or the reduction in peak intensity must be observed. But this is not the case, the intensity of the signal increases with laser power. Therefore, it can be said that an increment in laser power causes the change in morphology of the substrate which leads to an enhancement in the SERS signal. The higher laser power does not further increase the SERS intensity, the SERS signal becomes saturated. This saturation might result of the saturation in the structural morphology of the NP-Au substrate.

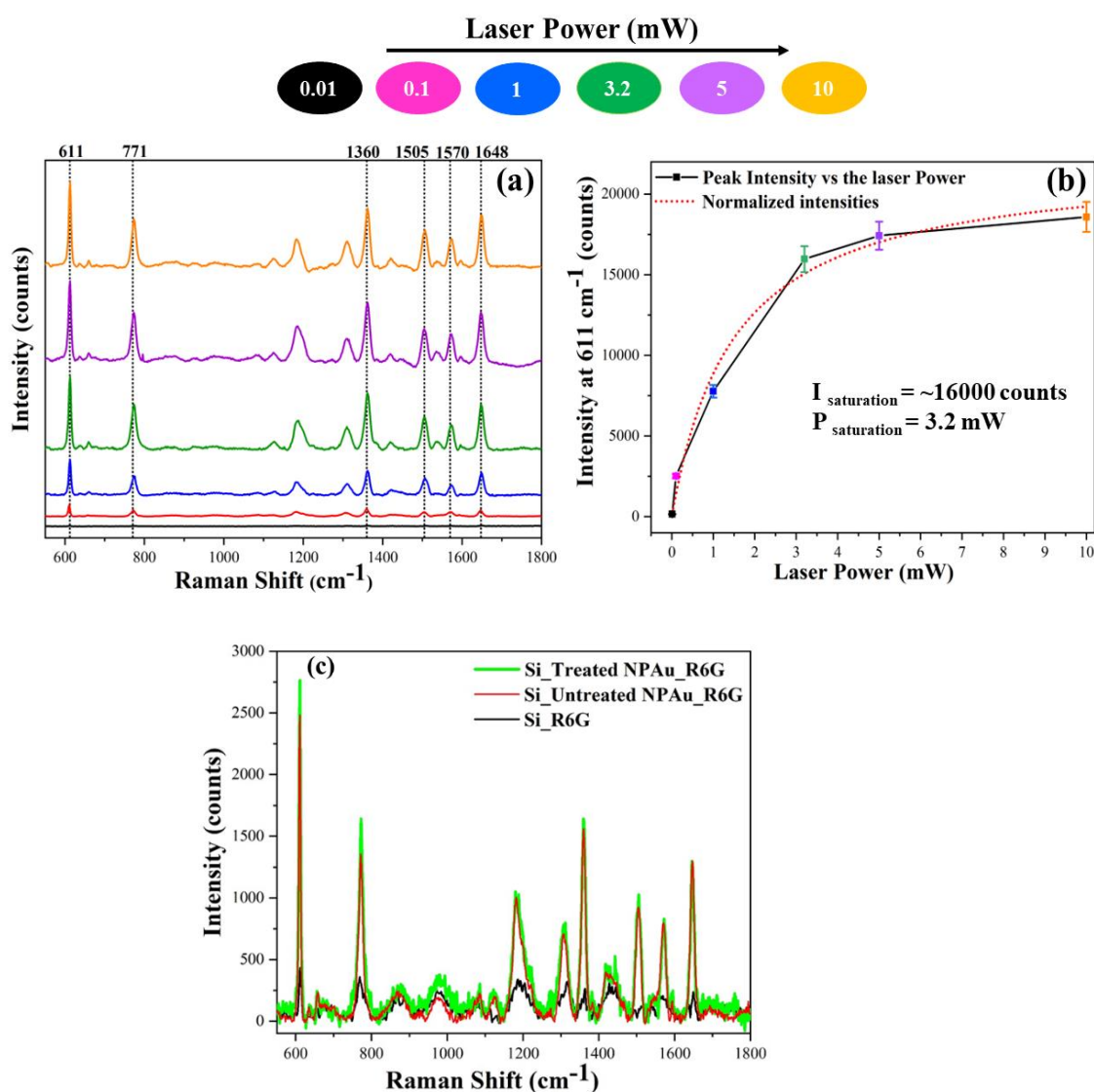


**Figure 4. 16.** (a) SERS spectra of R6G on NP-Au excited with different laser power (0.01, 0.1, 1, 3.2, 5, and 10 mW); (b) Relationship between the intensity of the 611 cm<sup>-1</sup> peaks under a varied laser power (black line) and fitted with a polynomial fitting (red line). The exposure time for each spectrum was 2s. The signals collected at each power is represented in different colours; (c) Comparison SERS spectrum of R6G adsorbed on different substrates (laser treated NP-Au (green), untreated NP-Au (red) and Si (black)) recorded at lower laser power (0.1 mW).

**Table 4. 7.** SERS enhancement factor calculation corresponding to different laser power. In the formula,  $I_n$  represents the intensity counts related to 0.1, 1, 3.2, 5 and 10 mW power and  $I_{0.01}$  corresponds to counts of 0.01 mW.

Sample No.	Laser Power (mW)	Intensity (counts)	Enhancement ( $I_n/I_{0.01}$ )	Fold
1.	0.01	159.14	-	-
2.	0.1	2520.07	15.84	~ 10
3.	1	7778.02	48.88	~ 50

4.	3.2	15974.33	100.38	$\sim 10^2$
5.	5	17422.75	109.48	$\sim 10^2$
6.	10	18584.31	116.78	$\sim 10^2$

#### 4.2.3.2 Morphological characterization

As per the SERS analysis, the intensity of the signal is increased with the laser power increment. Therefore, to know the actual reason/mechanism behind the SERS enhancement, the topological investigation of the substrates such as alloy, untreated NP-Au and laser-treated NP-Au (0.1, 1, 3.2, and 10 mW) is performed. It can be seen from fig. 4.16 (a) that the alloy has a granular type of features without pores; whereas after dealloying the sample is made up of a pore and a network of gold ligaments (fig. 4.16 (b)). The average size of the pores is  $\sim 31 \pm 1.15$  nm. However, from the fig. 4.16 ((c), (d), (e) and (f)) it can be seen that the morphology of the samples is affected with the laser power variation. The structural features of the substrate are different for different laser power such as substrate exposed with 0.1 mW laser power (fig. 4.16 (c)) consists of open channels of pores as well as interlinked pores, as depicted by yellow dotted circles. The average size of the pores is  $\sim 111 \pm 5.5$  nm and the interpore spacing between the pores is  $\sim 27 \pm 5.8$  nm. The average size of the pores is calculated with the help of Image J software. In contrast, the NP-Au exposed with 1 mW laser power (fig. 4.16 (d)) shows a noticeable change in surface morphology (porosity) relative to sample '4.16 (c)'. The fractions of the smaller sizes of pores are decreased here and correspondingly, the interconnection of multiple pores with a size of  $\sim 144 \pm 16$  nm is observed. The interpore spacing between the pores is almost similar as previous samples  $\sim 27 \pm 6.4$  nm.

However, it is interesting to observe that along with the open and interconnected pores, the appearance of diffused (filled) pores is also seen in some places as demonstrated by red dotted circles. The interconnection, as well as the diffusion of the pores, can be defined by the thermally activated mechanism which occurs due to the laser exposure. It is well known that thermally driven coarsening (surface diffusion of Au atoms caused by the heating) is observed in NP-Au, which is generally expressed as a continuous increase in the pore and ligament size. This approach is also applicable in our case, it can be said that the exposure of laser on the substrate resumes the surface diffusion of gold atoms, which has been quenched by immersing the NP-Au substrate into the water during the preparation step.

As long as the laser is incident on the sample for 1s, 2s, or longer, the gold atoms continue to diffuse, due to that the pores keep on interlinking and the size of the pore changes accordingly. The interlinking of the pores depends on the interpore distance, it can be seen from the fig. that not all the pores are connected. Only a few are connected which have  $\sim$  nanogap between them. The phenomenon can be correlated to the change in morphology of Au nanoparticles (NPs) in

the presence of external force. It has been reported that the shape of Au nanoparticles is changed from spherical to dumbbell, chains, and ellipsoid when certain kind of external force such as heating, mechanical compression, and e-beam exposure is applied. The conversion into different shapes is dependent on the interparticle distance [176], [177], [178]. Therefore, particles prefer to connect with the particles which are in a close proximity. As discussed, in some areas of the sample '4.16 (d)' diffused pores are also observed. The filling of the pores can be explained by the transportation of the atoms from the nearby gold ligament. As the laser is incident on the sample, atoms from the nearby ligament begin to transport into the pores and correspondingly convert the open pores into diffused pores. The topography of NP-Au incident with 3.2 and 10 mW (fig. 4.16 ((e) and (f))) is quite different relative to the sample '(c)' and '(d)'. It is interesting to see that the observation of the number of diffused pores is greater here with the smaller size of interconnected pores and ligaments. It has been observed in one of the literatures that during the in-situ HRTEM analysis, the NP-Au disintegrated in the presence of methane pyrolysis, which led to the release of a large number of Au atoms [179]. It is also well explained in the same report that the change in the morphology of NP-Au and the transportation of Au atoms from the NP-Au surface occurred due to the methane pyrolysis, not caused due to the electron beam bombardment as in the case of Au NPs (transform into different shapes during beam exposure). As per the state of the art, the minimum e-beam exposure to transport Au atoms is  $\sim 407$  keV, and in our case, a much lower energy  $\sim 9.9$  keV has been used. Therefore, it can be said that the morphology changes in NP-Au occurred due to thermal heating generated due to the laser exposure and not because of electron beam exposure.

From these results, it can be concluded that the high-power exposure enhanced and fasten the diffusion of gold atoms from the nearby ligaments and due to that pores filled with Au atoms are observed with the open as well as interconnected pores in the respective samples. The diameter of the pores is smaller  $\sim 93 \pm 3.4$  nm than that of the samples treated with lower laser power, the reason is the same as explained earlier, the release of Au atoms from the ligament surface gradually fills the pores. Therefore, a reduction in pore size is observed and also the number of smaller pores is less as compared to the lower laser power treated sample. Furthermore, the interpore distance is  $\sim 34 \pm 13.4$  nm which is larger than the previous results because at some places the Au atoms have completely filled the pores, and due to that the pore looks like a ligament. Based on these observations, it can be said that with the laser power increment, the density distribution of the gold atoms is increased because the Au atoms are released from the adjacent ligaments. However, this point is also advantageous in terms of providing more adsorption sites to the molecule on a rough Au surface.

As discussed earlier, two factors one is the generation of a local electromagnetic field and other is the formation of hot spots is necessary for SERS enhancement. In our case, the hot spot

formation is not the reason because the interpore gap is greater than 10 nm. The generation of a local electromagnetic field around the ligament has made an impact on the signal intensity. It is well known that; with increasing laser power, a higher energy photon, as well as a greater number of photons is generated. These photons come in contact with the ligaments as well as diffused pores in that particular area which led to the generation of a localized electromagnetic field, the adsorbed molecules feel this localized electromagnetic field and emit a highly intensified Raman signal.

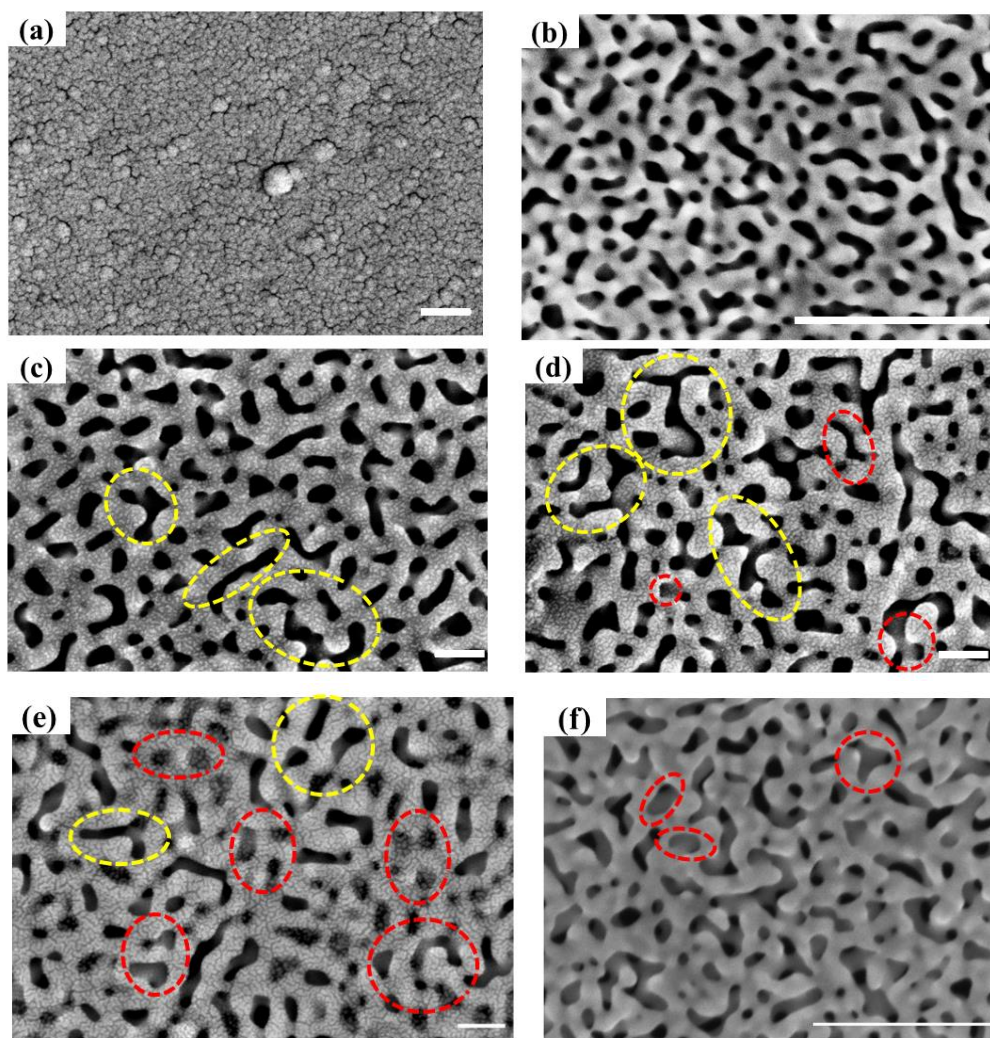


**Figure 4. 17.** Microstructure revelation of the (a) alloy; (b) NP-Au; NP-Au incident with varied laser power (c) 0.1 mW; (d) 1 mW; (e) 3.2 mW and (f) 10 mW. The different shapes of pores such as open, diffused as well as interconnected is observed in the samples exposed with different power. The interconnected pores are represented by the yellow circle and the red circle is used to depict diffused pores. All the shown images are at the same magnification (120 K); the single scale bar shown in the fig. corresponds to 400 nm applied to each image.

For more clarification about the change in structural morphology of the substrates, whether it is being affected by laser power increment or with the electron beam exposure, AFM analysis



has been performed only after laser treatment and before the FESEM measurement as shown in fig. 4.17 and 4.18. This analysis proved that the change in morphology is caused by the laser power treatment which can be clearly seen from the 2D images of the samples. The important statistical parameters such as roughness and uniformity of the samples (alloy, NP-Au before and after laser treatment) is determined by capturing the 3D images of substrates in contact mode. The sample's name is represented with an abbreviation is represented in table 4.7; 'a' letter corresponds to alloy and 'b' corresponds to untreated NP-Au. The alphabetical letters (a, b, c, d, e, and f) without dash represent the 2D image and with dash represents the 3D image of substrates. From fig. 4.17 it can be seen that the alloy (labelled as 'a' and 'a') is not consisting any kind of structure on its surface, the presence of dot-shaped particles may be due to the presence of certain kinds of impurities. The surface roughness as well as height value is  $\sim 5$  and  $\sim 21$  nm respectively. After dealloying, the morphology of the sample (labelled as 'b' and 'b') is changed and a bi-continuous structure is formed. From the 3D view, it can be seen that the nanostructures formed on the substrate are quite uniform. The roughness and height values are increased of the sample due to the creation of ligaments and pores as represented in fig. 4.19. With the laser treatment, the morphology of NP-Au is affected as can be seen from fig. 4.18 and the treatment leads to the joining of the pores (indicated by a white dotted circle (2D view) and arrows (3D view)). With power increment, an increased density of interconnected pores is observed throughout the substrate, similarly as observed in the FESEM images up to sample 'd'. The 3D images of samples 'c' and 'd' show that most of the area of the substrate is filled with nano-ligaments (golden colour); whereas in some area's humps (darker colour) are also present which corresponds to interconnected pores.

Further, incident with higher laser power ('e' and 'f') leads to a reduction in the number of interconnected pores, while smaller size pores and ligaments is observed throughout, due to the diffusion of gold atoms through adjacent ligaments. The diffusion of gold atoms cannot be observed in these images due to the low resolving power of AFM. The surface roughness and height of the structures increase with the laser power increment as like SERS measurement up to 'd' sample and after that both the parameters become approximately saturated demonstrated in the plot 'g' and 'h' of fig. 4.19. The roughness and height values increase after laser treatment due to the creation of interconnected as well as diffused pores, which makes the substrate rougher than the untreated sample.

**Table 4. 8.** Representation of substrate names with abbreviations

S. No.	Sample Name	Abbreviation
1.	Alloy	a
2.	NP-Au	b



3.	NP-Au@ 0.1 mW	c
4.	NP-Au@1 mW	d
5.	NP-Au@ 3.2 mW	e
6.	NP-Au@10 mW	f

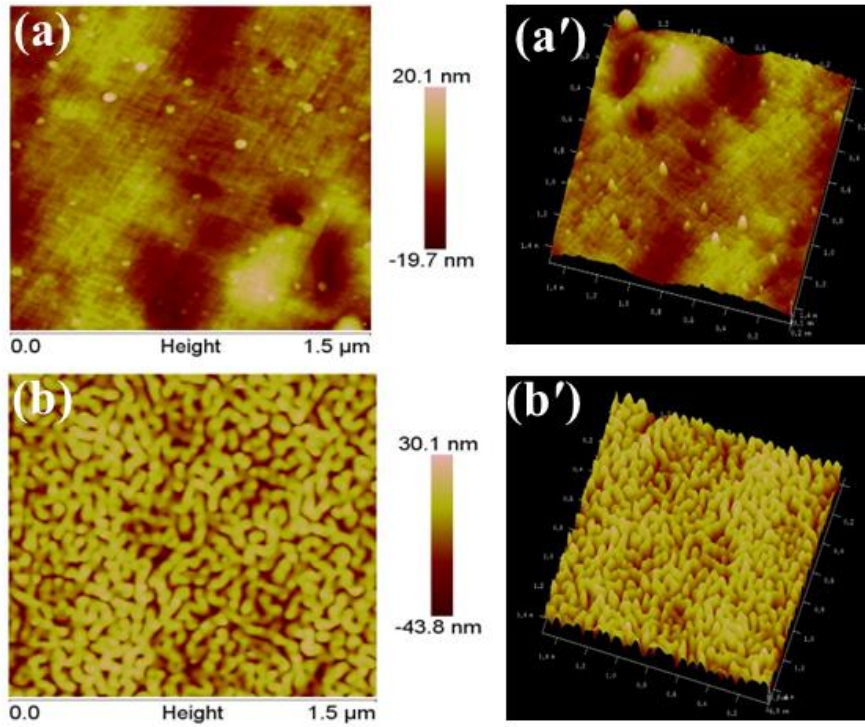


**Figure 4. 18.** AFM analysis of alloy leaf: (a) 2D image, (a') 3D image; and Bare NP-Au sample without laser treatment (b) 2D image, (b') 3D image. The size of each image corresponds to  $1.5 \times 1.5 \mu\text{m}$ . The height scales are demonstrated in the right side of the 2D.

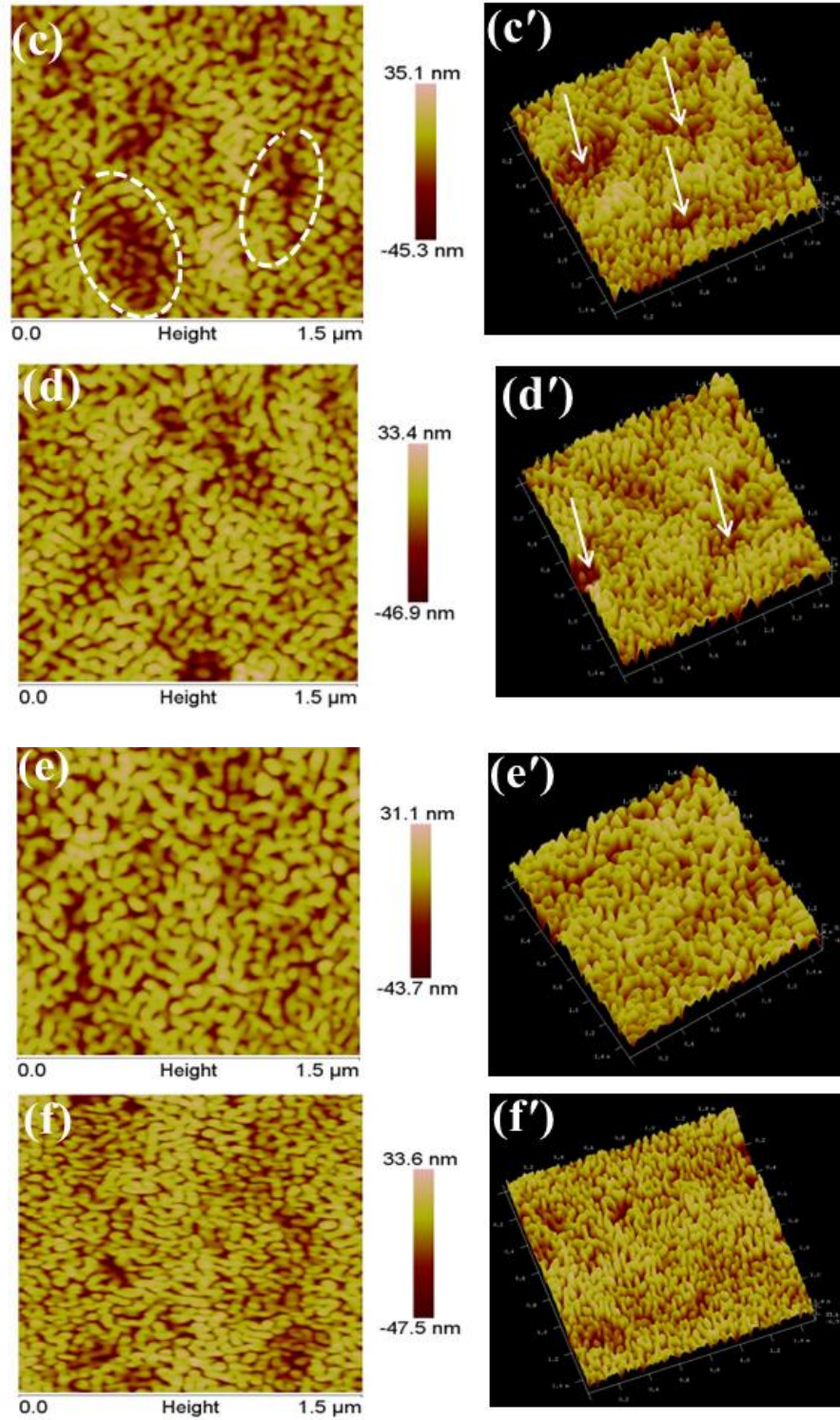


**Figure 4. 19.** AFM analysis of laser treated sample (c, d, e, and f). The left-hand side shows the 2D view and the right-hand side represents the 3D view of the samples. The size of each image corresponds to  $1.5 \times 1.5 \mu\text{m}$ . The height scales are demonstrated in the right side of the 2D.

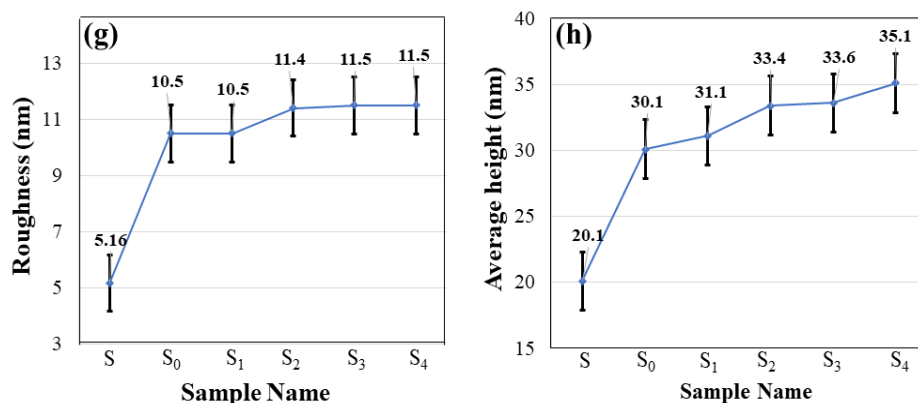


**Figure 4. 20.** The plots (g) and (h) corresponds to the roughness and height of the structures.

#### 4.2.3.3 SERS parameters examination

##### 4.2.3.3.1 Sensitivity of NP-Au substrates

In the SERS field; sensitivity is the major concern for any kind of substrate. In order to examine the LOD, the substrate is treated with varied concentration of R6G as shown in fig. 4.20. The Raman spectra of R6G with a concentration varying from  $\sim 10^{-3}$  to  $\sim 10^{-11}$  M on the NP-Au substrate is measured and are represented in fig. 4.20 (a). For this study, a lower laser power such as 0.1 mW is used in order to check the substrate efficacy. It can be seen from fig. 4.20 (a) that, all the characteristic peaks is still clearly identifiable even when the concentration is  $10^{-9}$  M which indicates the good contribution of the purposed substrate towards sensitivity [180]. The intensities of the signals is enhanced linearly with the increase of the R6G concentration. When the concentration is  $10^{-11}$  M, the signals is still observed, but the intensity of the signals is quite weak (only  $\sim 53$  intensity counts of R6G is observed at  $611\text{ cm}^{-1}$  peak) as represented in fig. 4.20 (c). Thus, it can be said that this substrate shows good sensitivity and able to sense the  $\sim 10^{-9}$  M concentration. Furthermore, fig. 4.20. (b) shows the calibration curves, which correspond to the signal intensity at  $611\text{ cm}^{-1}$  vs the varied concentrations of R6G on the logarithmic scale, representing a good linear relationship between the concentration and intensity. Each point in the graph corresponds to the average value of intensity taken from seven randomly selected areas, and the error bar represents the standard deviation. The linear equation is  $I = 310.25 [\log (C)] + 3480.8$  for  $611\text{ cm}^{-1}$  peak, where C and I represent the concentration and intensity of R6G. The value of the coefficient of determination ( $R^2$ ) is 0.996 suggesting the good linearity of the calibration curve.

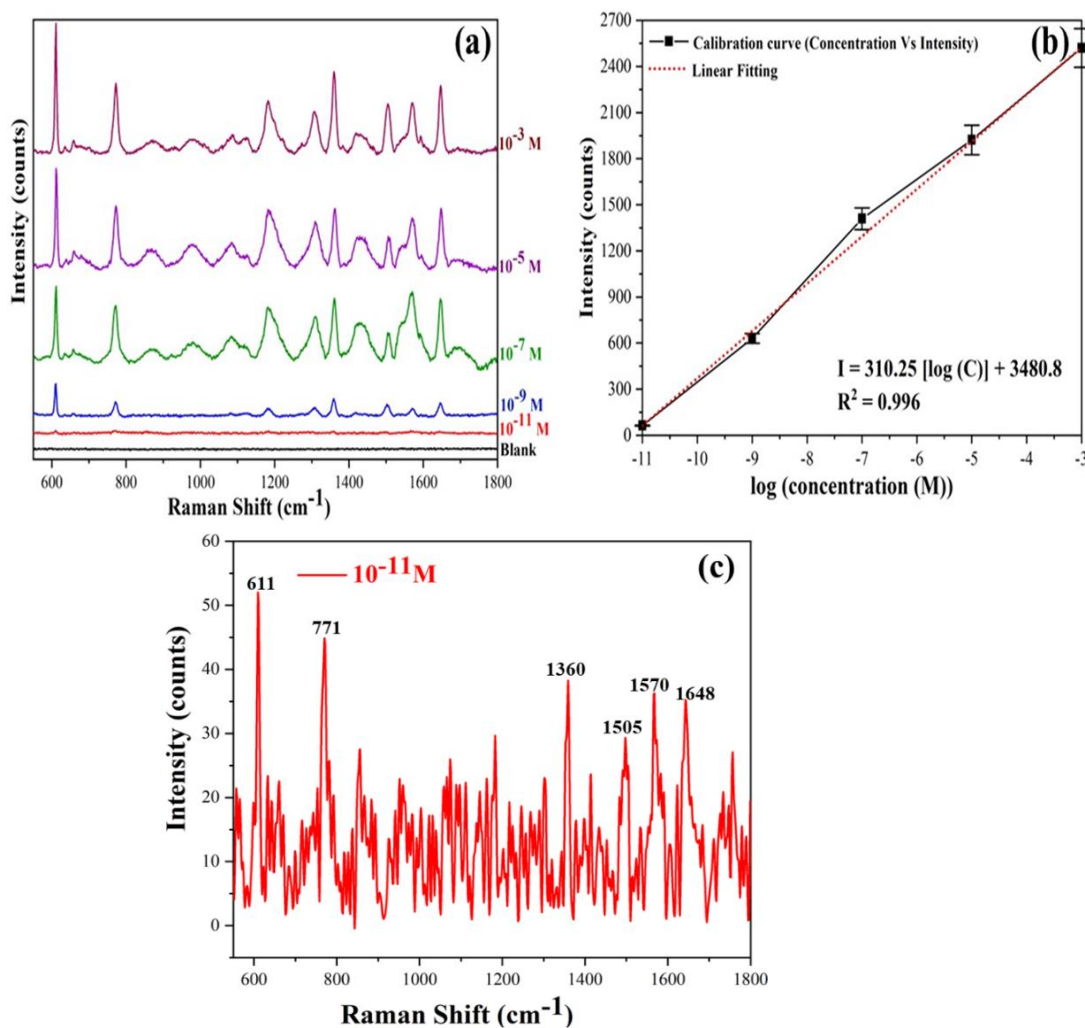


**Figure 4. 21.** (a) SERS spectra of R6G at a concentration range from  $10^{-3}$  M to  $10^{-11}$  M on NP-Au. The blank is the spectrum of NP-Au; (b) The calibration curve produced by logarithmic linear trend between the  $611 \text{ cm}^{-1}$  peak intensity and the R6G concentration (the x-axis is expressed in logarithmic scale and y axis is not converted to logarithmic scale for the readers better understanding); (c) Enlarged view of  $10^{-11}$  M R6G concentration on NP-Au.

In order to confirm that the concentration of the molecule in solution or after drop-casting/drying on to the sample is the same, concentration values have been calculated from the linear regression plot (fig. 4.20 (b)). As it is well known that Raman spectrum provides the Intensity values with the help of that unknown sample name as well as concentration can be measured by inserting slope and intercept values. The slope and intercept values has been calculated from the linear regression plot as illustrated in fig 4.20 (b). The slope value corresponds to 310.25 and intercept value equals to 3480.8. The formula for concentration calculation is mentioned in *eq. 2.12*. For the calculation of concentration values there is a requirement of three values such as Intensity (I), Intercept, and slope values. The intensity values is provided by the spectrum. Table 4.9. represents the intensities values (highlighted with blue colour on the spectrum) recorded during analysis.

$$\text{Concentration (mM)} = \frac{I - \text{Intercept Value}}{\text{Slope Value}} \quad (\text{eq. 2.12})$$

**Table 4. 9.** Represents the concentration values obtained after inserting the slope, intercept, and intensities values collected from spectrum.

S. No.	Slope	Intercept	Intensity	Concentration (mM)
1.	310.25	3480.8	2520	-3
2.			1922	-5
3.			1409	-7
4.			630	-9
5.			63	-11

#### 4.2.3.3.2 Uniformity of NP-Au substrates

To examine the substrate uniformity, the substrate treated with  $10^{-9}$  M concentration of R6G is selected, because all the peaks are well recognised even at this lower concentration and lower laser power (0.1 mW); as can be clearly seen from fig. 4.21. Therefore, to know the homogenous nature of the substrate, the laser is randomly incident on the seven points of the same substrate (substrate size:  $1 \times 1 \text{ cm}^2$ ) as shown in fig. 4.21. It can be observed from the fig. 4.21 that all the peaks are its well-defined position, there is neither any kind of frequency shift nor significant intensity change. The distribution of the peak intensity of the band at  $611 \text{ cm}^{-1}$  is represented as a histogram in fig. 4.21. where the black horizontal dotted line demonstrates the average intensity of the  $611 \text{ cm}^{-1}$  peak for the seven areas, and the grey rectangular box indicates the fluctuation in the signal intensity. For more confirmation regarding the intensity fluctuation from area to area, the RSD value has been calculated for all the peaks on the respective exposed areas as represented in table 7. The values for all the peaks is less than 20 % which confirms that the substrate has good uniformity over the whole area [157] .



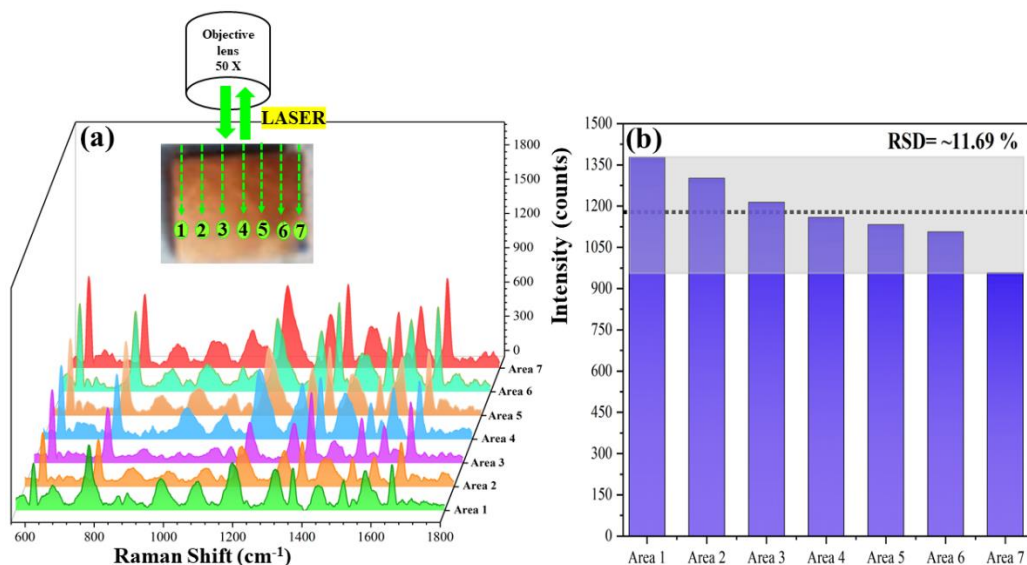


**Figure 4. 22.** (a) Raman spectra of the  $10^{-9}$  M R6G measured from seven random spots; (b) The intensity variation of  $611 \text{ cm}^{-1}$  peak obtained from spectra (a).

**Table 4. 10.** RSD values of substrate corresponds to the characteristic peaks of the R6G.

Peak Position ( $\text{cm}^{-1}$ )	611	771	1360	1505	1648
RSD Value (%)	11.62	9.69	11.87	14.47	10.54

#### 4.2.3.3.3 Stability of NP-Au

Stability of the signal is the key requirement for a SERS substrate performance for routine analysis. Figure 4.22 shows the comparison in the intensity variation of the SERS peaks of freshly prepared NP-Au and after its storage in a desiccator for 2 years, respectively. Prior to SERS measurement of the stored substrate (R6G deposited onto NP-Au), the substrate was washed by drop-casting method as discussed in our previous work to remove any kind of impurities and dust particles from its surface. Along with that, the deposited R6G was also drained out from the substrate. Then, after drying the freshly prepared R6G was drop-casted onto old as well as new NP-Au in order to compare the performance. It can be seen from fig. 4.22. that the stored sample is able to show all the characteristic peaks of R6G with  $\sim 50\%$  reduction in the intensity compared to the fresh sample. The  $50\%$  intensity is maintained because the ligaments are made up of Au and it is well-known that Au shows good resistance to oxidation.

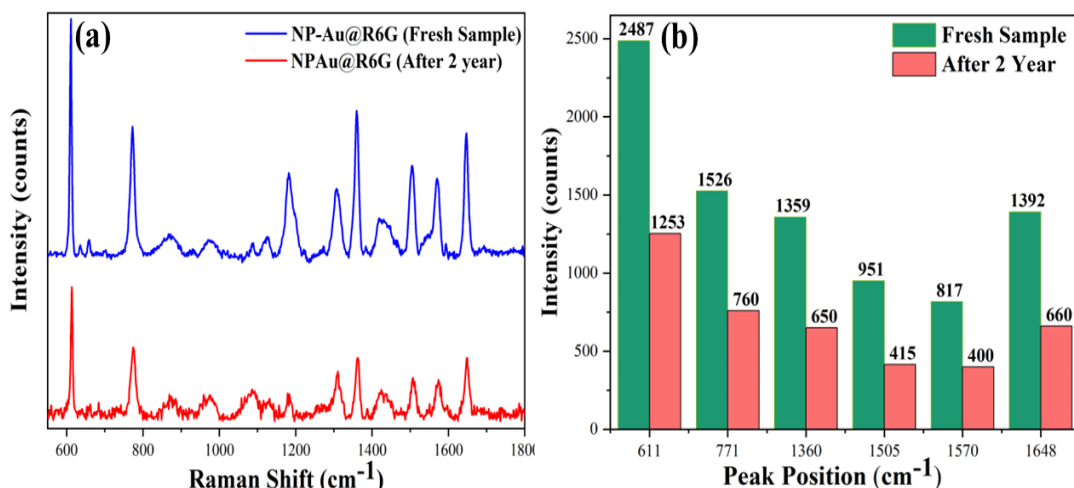


**Figure 4. 23.** (a) SERS spectra of the freshly prepared NP-Au and after 2 years storage of the same substrate; (b) Histogram represents the reduced intensity value of the stored sample with respect to the fresh sample.

To know the reason behind the signal intensity reduction; the morphological analysis has been performed. It has been reported [181] that the rough morphology as well as number of hot spots are the important factors for SERS performance. It can be observed from fig. 4.23. that the density of nanosize pores is less in the old samples (labelled as 'b') compared to the new sample (labelled as 'a') due to the laser treatment of the old sample multiple times, hence the reduction in number of Hot spots leads to reduction in signal intensity. A few literature [182], [183], [184] have reported the presence of dust as one key reason, but on analysing the SEM images, our stored samples are found to be free from any kind of dust particles. Furthermore, EDX analysis of the fresh and stored sample is recorded in order to get rough idea about the elemental composition of the freshly prepared sample as well to know any composition variation in stored sample. From the fig 4.23 (a') and (b') it can be seen that both samples exhibit almost similar content of Au and Ag elements.

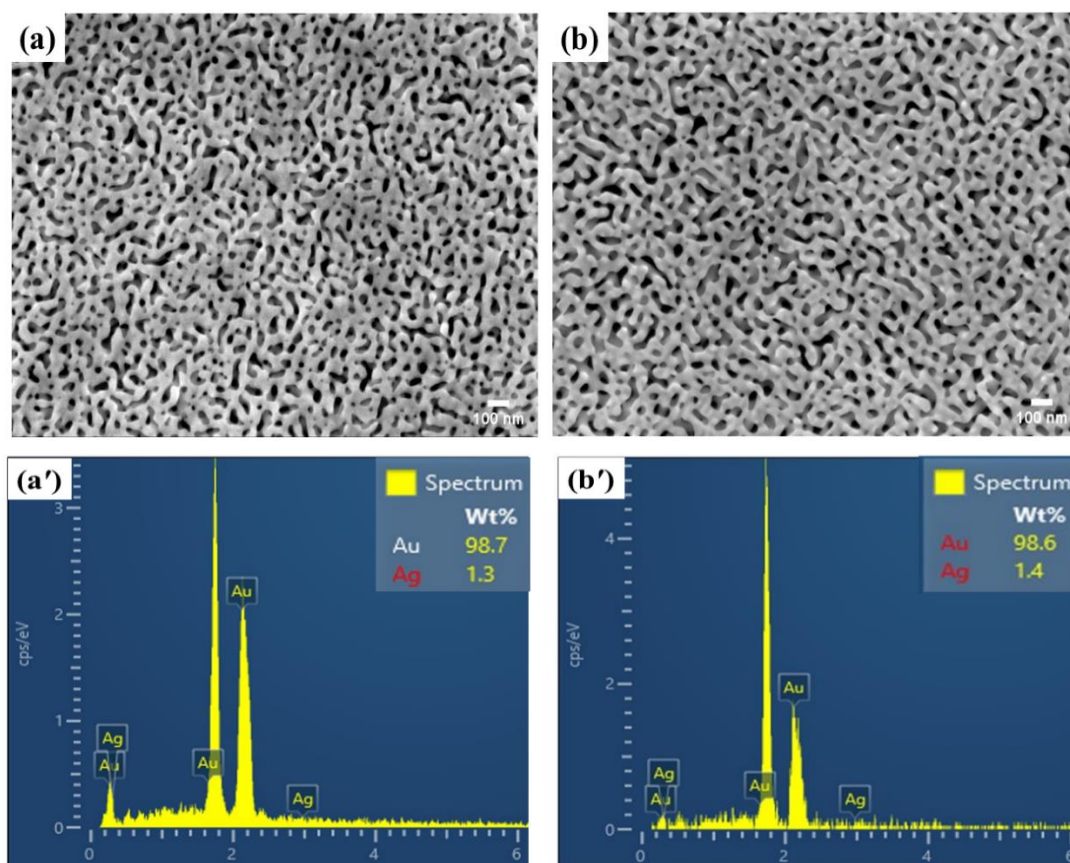


**Figure 4. 24.** FESEM images of NP-Au (a) freshly prepared; (b) '2' years stored sample. The stored sample is consisting larger and interconnected pores due to multiple time laser treatment. The figure (a') and (b') represents the composition analysis of freshly and stored NP-Au samples.

X-ray photoelectron spectroscopy (XPS) has been used to examine the surface composition of NP-Au in terms of the elements present and their oxidation states. The complete XPS spectrum of NP-Au is shown in fig. 4.24 with Au, Ag, O and C peaks identifiable. The doublet peaks correspond to Au 4f at around ~87.44 and 83.73 eV confirms the presence of Au in NP-Au in a zero-valent oxidation state. Further the two weak binding energy peaks at 373.5 and 367.74 eV corresponding to Ag 3d depicts the presence of Ag in the substrate. The peak at 533 eV corresponds to O 1s is the indicative of  $\text{Ag}_2\text{O}$  and the peak at ~284 eV corresponds to C 1s as double-sided carbon tape has been used to stack the substrate with the sample holder. The XPS data for the fresh as well as stored sample are tabulated in table 4.11.



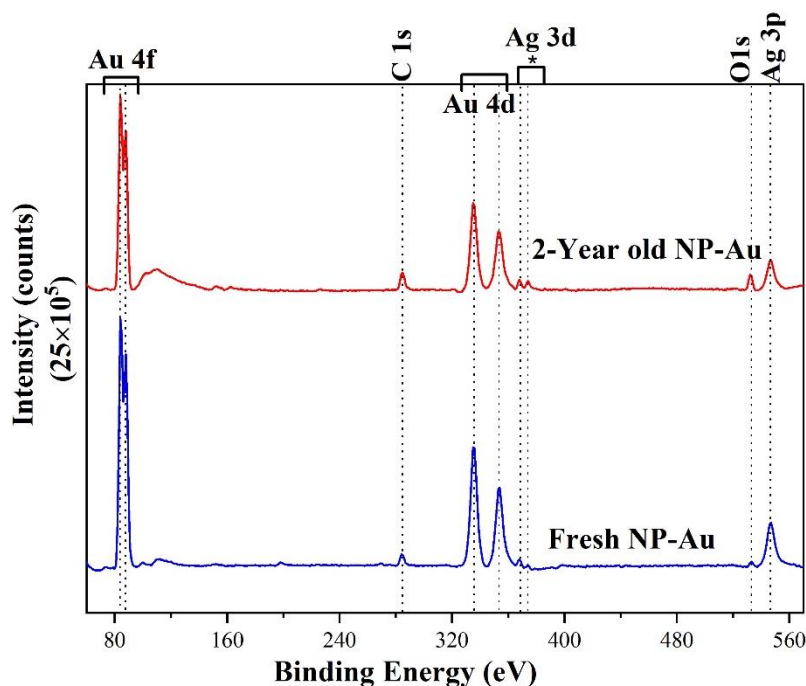


**Figure 4. 25.** XPS analysis of NP-Au (blue spectra corresponds to fresh sample of NP-Au and red spectra corresponds to NP-Au sample stored for two years).

**Table 4. 11.** XPS spectral data represents the compositional variation of fresh and stored NP-Au substrate.

S. No.	Element Name	Weight (%) (Fresh Sample)	Weight (%) (2-year-old sample)
1.	Au	93.25	85.29
2.	Ag	1.71	3.89
3.	O	0.80	3.52
4.	C	4.24	7.29

#### *Conclusion of part 4.2*

In the present work, the effect of laser power variation onto the structural morphology as well as on the SERS performance of NP-Au has been studied. It is found that morphological features alter and the SERS performance improves with increasing laser power. Different shapes of pores such as open, diffused, and interconnected pores are observed with laser power variation and also the filling factor of pores as well as the distribution density of the Au atoms is increased with increasing the laser power. The intensity of the SERS signal increase linearly with the laser power up to 3.2 mW, after that no noticeable change is observed for further higher powers.

The substrate is able to enhance the signal up to 10-fold with lower laser power (0.1 mW), which is beneficial for those practical applications where commonly low laser power is required. The important point about this method is that just by varying the laser parameters, the structural features can be altered for sufficient signal enhancement as per the requirement. The substrate exhibits good detection ability for R6G ( $\text{LOD}=10^{-9}$  M) with excellent uniformity (average RSD = ~ 12%) throughout the substrate. However, the substrate is able to show all the characteristic peaks of R6G even after ageing for 2 years, which indicates the good stability property of the NP-Au substrate.

### ***Part 4.3: Testing of NP-Au substrate for urea detection***

#### ***4.3.1 Introduction***

In agriculture, pesticides/fertilizers are widely used to increase the crop production and to protect the crops from various kinds of insects, fungi, weeds, and other pests [185]. However, their excessive use and residues on food and agricultural products are toxic to humans and can cause acute and chronic health effects in humans. Therefore, to prevent humans from the adverse effects of pesticides/fertilizers, WHO has recommended a maximum permissible limit for each pesticide/fertilizer, beyond that limit these are considered toxic. Regularly used fertilizer such as urea is a multi-purpose fertilizer which is generally preferred by farmers worldwide to stimulate the growth of crops or plants by mixing the beads of urea into the soil or by spraying the urea solution onto crops and plants. The acceptable limit of urea is 2.5-6.7 mM, higher than that can cause kidney diseases in humans [186]. The main issue with urea is that its excessive and frequent use leads to environmental pollution (urea beads break down into ammonia and nitrate, and then evaporate or dissolve into water sources and cause air and water pollution).

On the other hand, not only in agricultural science but also in clinical analysis the monitoring of urea is important as it is an important biomarker for various renal diseases. As discussed in section 2.2.11, various methods such as GC-MS, HPLC, and LC-MS etc is used to detect fertilizer residues in food products. These techniques are effective and accurate, but rather than that the sample preparation is difficult, time-consuming, and lower limit detection is not possible [187]. Therefore, research on finding a reliable, fast, easy, and highly sensitive method to detect fertilizers is in current demand. As compared to the existing and currently used methods, Surface-enhanced Raman scattering (SERS) is suitable and well fits on the above-mentioned characteristics due to its simplicity, fast nature, and ability to detect lower concentration of inorganic and organic contaminants such as pathogens, pesticides, fertilizers, and environmental pollutants [188]. Therefore, the capability of NP-Au substrate has been tested further for the sensing of urea as it has shown a good detection limit for R6G.

#### 4.3.2 NP-Au sensor fabrication

To test the NP-Au substrate performance for real-world application purposes,  $10^{-3}$  M aqueous urea solution was prepared from the nano urea beads purchased from the Ropar local market. The reason for the selection of  $10^{-3}$  M concentration was, it is an acceptable limit, beyond that can cause serious health issues. The sensor was fabricated by drop-casting 40  $\mu$ L urea solution onto NP-Au substrate and after 20 min of drying at room temperature the Raman spectrum was recorded.

#### 4.3.3 NP-Au sensor testing for urea detection

Urea is a molecule which has a small Raman scattering cross-section. The high laser power and long accumulation time is required for the analysis of urea [189]. Therefore, in order to detect it on the reference (Si) as well as on the SERS substrate, the parameters were again optimized and the characteristic Raman band of urea at  $1011\text{ cm}^{-1}$  was used to finalize the parameters. The integration time was 6s and accumulation was set to 6. The laser beam power was optimized at 10 mW. The other instrumental optics setting such as the objective lens and gratings were kept the same as in the case of R6G. It can be seen from the fig. 4.25, the NP-Au is able to identify as well as to enhance the urea signal. However, some of the peaks ( $1538$  and  $1648\text{ cm}^{-1}$ ) which are not detected on the Si, are clearly identifiable on NP-Au. The effectiveness of the substrate has been tested by comparing the  $1011\text{ cm}^{-1}$  peak intensity of urea on NP-Au with the signal intensity on Si. The substrate is able to provide a 16-fold enhancement, which is comparable with the previous literature where the substrate is fabricated by expensive techniques [190], [191]. The same formula which is mentioned in eq 2.11. has been used to calculate the enhancement factor. Similarly,  $I_{\text{SERS}}$  and  $I_{\text{Raman}}$  correspond to the peak intensity at  $1011\text{ cm}^{-1}$  on NP-Au and Si. Whereas  $C_{\text{SERS}}$  and  $C_{\text{normal}}$  represent the molar concentration of urea on NP-Au and Si respectively. From these results, it can be said that the fabricated substrate can be used for the of analysis urea.

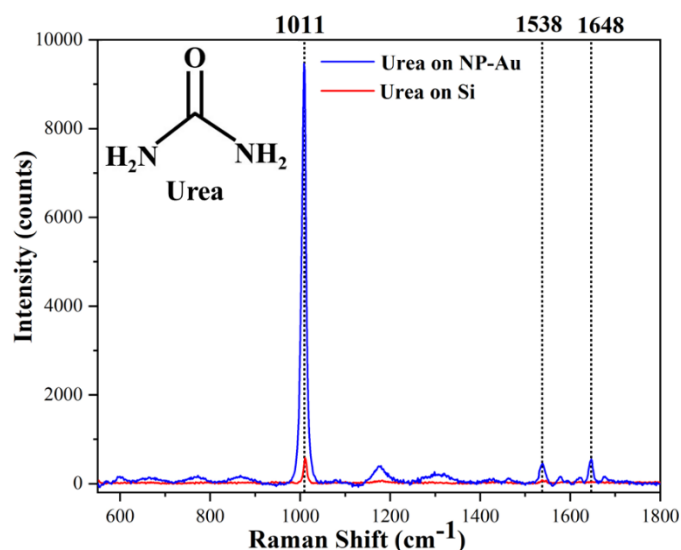


**Figure 4. 26.** Raman spectrum of  $10^{-3}$  M urea on NP-Au and on Si substrate.

#### 4.3.3.1 Sensitivity testing of NP-Au sensor

In order to measure the LOD capability of NP-Au, different concentrations of urea ranging from  $10^{-3}$  to  $10^{-9}$  M were drop-casted onto the substrate, and after drying their SERS measurement were recorded as represented in fig. 4.26. The lower concentrations of urea solution such as  $10^{-5}$ ,  $10^{-7}$ , and  $10^{-9}$  M were prepared from a  $10^{-3}$  M stock solution. It can be seen that even at a concentration of  $10^{-9}$  M, the peak of urea is clearly identifiable. Based on these studies, it can be said that the LOD of the substrate is  $10^{-9}$  M for urea molecule, which is also a competitive LOD in comparison to other SERS-based sensors prepared from expensive techniques for urea detection [190], [191]. Moreover, to determine the good linear relationship between the concentration and the intensity, the calibration curve of the signal intensity at  $1011\text{ cm}^{-1}$  vs the varied concentration of urea on the logarithmic scale is plotted as shown in fig. 4.26 (b). Each point represents the average value of Raman intensities collected from seven different areas of the same substrate. The linear equation is  $I = 1507.2 [\log (C)] + 13903$ , where C and I represents the concentration and Raman intensity of urea. The correlation coefficient ( $R^2$ ) value is  $\sim 0.998$ , representing a good linear relation. Furthermore, it can be clearly seen from the fig 4.26 (b) that with increasing the concentration of urea molecule, the intensity of the characteristic peaks of urea molecule is increased. And this is because as the concentration increases, a greater number of urea molecules are excited by a laser, due to that greater number of photons are emitted from the molecule, which helps to make the signals stronger and strengthen.

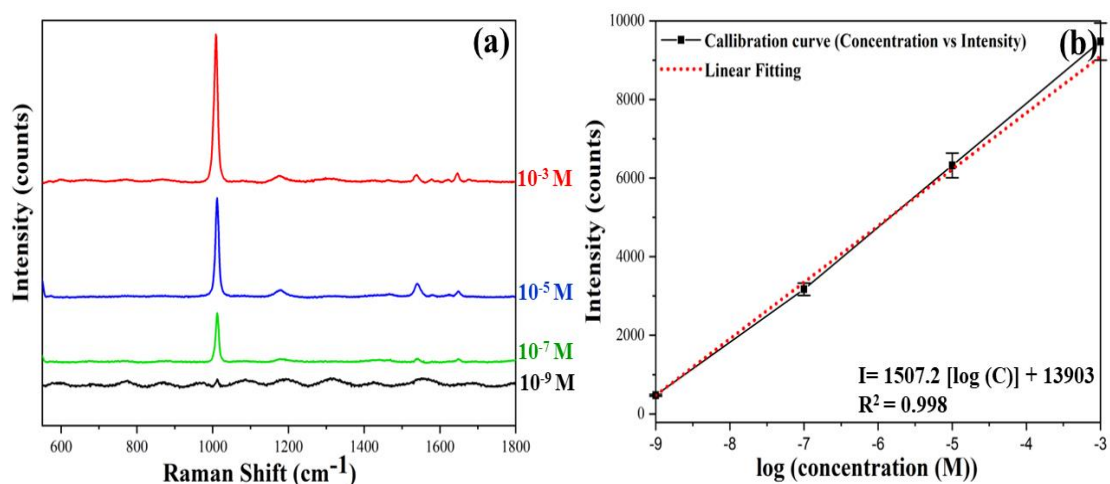


**Figure 4. 27.** (a) Raman spectra of urea under different concentrations. (b) The calibration curve of the intensity vs different concentrations of urea. The x-axis is converted to a logarithmic scale and the y-axis is mentioned as it (intensity counts) for better understanding of the reader.

#### *Conclusions of part 4.3*

The applicability of the NP-Au substrate has been examined by detecting the environmental contaminant as well as biomolecules such as urea. The substrate is able to show an intensified signal of urea with  $\sim 16$ -fold enhancement. The important thing about this substrate is that it shows good sensing capability for urea molecules in the nanomolar range by representing a good correlation coefficient value ( $R^2 = \sim 0.998$ ). Therefore, it can be said that the NP-Au substrate can also be used for the recognition of other contaminants (fertilizers and pesticides etc.,) as well as low-cross-section molecules.

## ***Chapter 5. Flexible SERS substrate for urea detection***

### ***5.1 Introduction***

As discussed extensively, in SERS field, for strong signal enhancement, the structural morphology of SERS substrates matters most and to fabricate effective morphology substrates some fabrication methods such as chemical etching, self-assembly, sputtering, electron beam, focused ion beam, nanoimprint lithography, and photolithography etc. is commonly used [139], [192]. Although substrates prepared by these methods are able to show strong enhancement, but along with that the optimized conditions and specific expensive setups are essential for many of these techniques [14]. Furthermore, these techniques involve time-consuming, complex, and low-throughput fabrication procedures, which limit the use of these substrates for various applications. Colloquially, most of the literature has focused on the fabrication of SERS substrates based on solid substrates such as silicon, glass, quartz, and alumina [134]. These substrates are advantageous for various sensing applications. However, with these substrates, the detection of molecules only on planar or flat objects is possible, whereas on non-planar, uneven, and on curved objects, non-destructive detection is difficult [126]. This factor limits its use for real-world sensing applications such as on-field pesticides, fertilizers, pathogens, and trace chemical detection. Therefore, a SERS substrate which can adjust on any kind of surface (irregular as well as planar surface) to detect the unknown molecules is in great need [16].

From the past few years, the demand of SERS substrates for daily-life sensing applications has enforced the development of flexible SERS substrates [12]. Flexibility offers an integration of SERS substrate onto various non-planar surfaces as well as it can be easily cut into various sizes and shapes as per the application demand [137]. As discussed, numerous techniques are used to fabricate different kinds of SERS substrates. But the complexity, limited spatial range, and high cost of the fabrication procedures made these substrates unaffordable to lower-end users. Recently researchers have paid attention to provide a “cost-down” method for the development of facile, green, and low-cost fabrication procedures for effective SERS substrates based on natural plant leaves such as lotus, rose petals, taro, and rice etc. for the detection of R6G, crystal violet, and malachite green etc. [12], [138]. It has been widely stated that natural artifacts generally possess homogenous micro-nano structural morphology in a wide scale range. These natural artifacts can be directly used as a substrate as well as by nano-casting method the replicates of these structures can be generated by using various polymer films to make the substrate flexible [193]. This approach provides a fast, facile, effective, and economical method for the preparation of flexible substrate which is independent of specialized equipment.

Several flexible SERS substrates have been reported based on the method of immobilization and coating of coinage metallic (Ag, Au) nanostructures onto the flexible substrates such as polymer film (polydimethylsiloxane), Scotch tape, and filter/sandpaper [12], [126], [194]. These paper and

tape-based substrates have attracted great attention due to the advantages of facile fabrication, environmentally friendly, economical viable, and disposable nature. But one factor which limits the use of these substrates; is their weak adhesion property with the contaminated surfaces. However, polymer such as polydimethylsiloxane (PDMS) has shown good adhesion property and are also able to maintain adhesiveness for a quite longer time. It can be pasted multiple times after peeling off from the substrate as Scotch tape cannot be reapplied [14] . Other characteristics such as chemical stability, cheap nature, flexibility, and non-toxicity make it a more effective and valuable material for molding and stamping as compared to others.

With this aim in the current study, PDMS as a polymeric material is selected for replicating the micro/nanostructure for suitable SERS substrate and rose petal as a template. The rose petal is known to possess the uniform and ordered nano/micro scale bumped morphology [14]. After that, self-modification of Au NPs onto structured PDMS is performed to make the substrate SERS active. R6G is used as a Raman reporter molecule to check the effectiveness of the substrate and a small Raman scattering cross-section molecule such as urea is detected to examine its efficacy for an application point of view.

To our amazement, a reproducible pattern by using PDMS as a polymeric material and rose petal as a template has been created and also has been used for optoelectronic (photoelectric properties) and biomedical (Capture and Release of Tumor Cells) applications [14], [193] . But the potential of these cost-effective and easily prepared reproducible patterns has not been tested for the detection of low cross-sectional urea molecules. Therefore, for the first time, Au-coated flexible structured substrates fabricated from rose petals is used for the urea detection. The experimental process is easy, reproducible, and can occur without expensive lab equipment. The natural artifacts-based SERS substrates may open a door for both easy preparation and the broad application of SERS technique in a wide range of routine analysis (chemical, pollutant, and pathogen detection).

## 5.2 Material and Methods

### 5.2.1 Materials

Poly (dimethylsiloxane) (Sylgard-184, PDMS kit) was procured from Sigma-Aldrich and used as an elastomer to replicate the surface structure of rose petals. Hydrofluoric (HF), Sulfuric ( $\text{H}_2\text{SO}_4$ ) acids, (3-aminopropyl) triethoxysilane (APTMS) and rhodamine 6G with 99 % were bought from Merck, P-type Silicon wafers with  $\langle 100 \rangle$  orientation were procured from Sigma Aldrich. The de-ionized (DI) water with  $\sim 18.2 \text{ M}\Omega \text{ cm}^{-1}$  resistivity was used during all the experiments, wherever required. Red Roses were plucked from the IIT Ropar garden. Urea was procured from local market of Ropar.

### 5.2.2 Fabrication processes

#### 5.2.2.1 Fabrication of flexible structured substrate

The petals of fresh Rose were cut into small pieces ( $1.5 \times 1.5 \text{ cm}^2$ ) and fixed onto Silicon ( $2 \times 2 \text{ cm}^2$ ) substrate by an ultrathin double-sided adhesive tape. The elastomer base and curing agent were mixed in a weight ratio of 10:1 for  $\sim 2$  min to make a homogeneous slurry and then degassed in a desiccator in a vacuum to remove air bubbles. Thereafter, the  $250 \mu\text{L}$  PDMS mixture was poured onto the petal and spin-coated for 1 min (rotation speed 900 rpm, acceleration 30 s). Then as prepared substrate was again degassed in a vacuum for 1 min to get rid of the bubbles. After that the substrate was cured at  $50^\circ\text{C}$  for 4 h. Here, the low temperature is used to cure the substrate in order to prevent the loss of structural features of the petal due to heating. After curing, the PDMS film ( $\sim 0.5 \text{ mm}$  thick) with the negative surface structure of rose petal was gently peeled off from the rose petal as shown in fig 5.1 and cut into many small pieces  $\sim 0.5 \times 0.5 \text{ cm}^2$  dimension. Further, the pieces of structured PDMS were placed onto the backside of Si wafer to avoid any kind of reflections during microscopic and spectroscopic measurements.

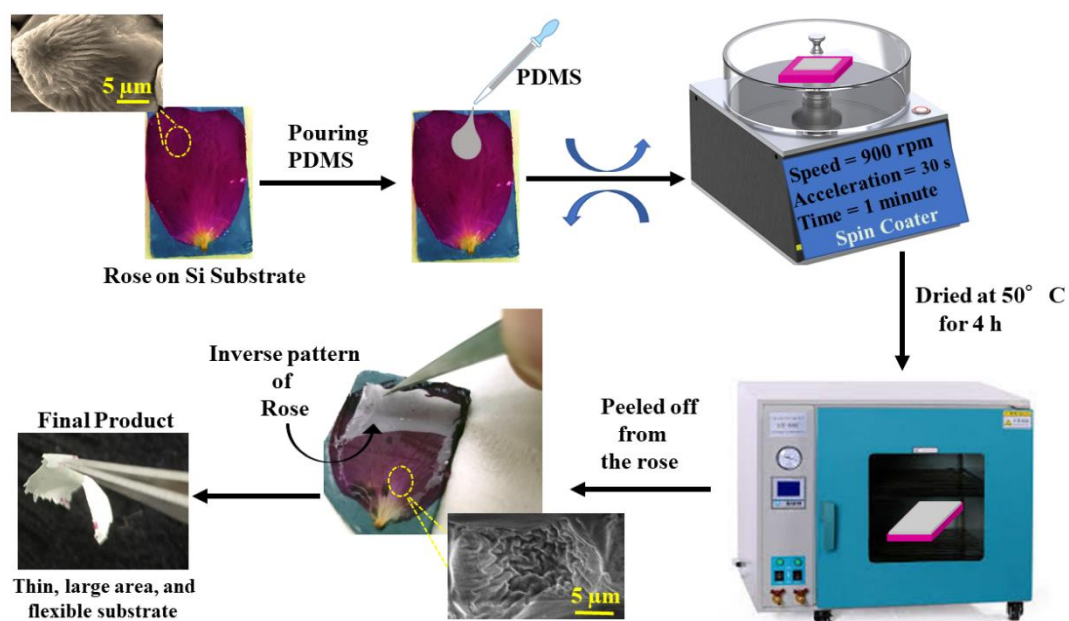


**Figure 5. 1.** Schematic representation of the fabrication process to create inverse replicas of the rose petal by using PDMS.

#### 5.2.2.2 Au NPs immobilized flexible structured substrate

The immobilization of the Au NPs onto the substrates is performed by linking the negatively charged Au NPs with the positively charged amino terminated APTMS as shown in fig. 5.2. For this, first the flexible structured substrate was immersed into a piranha solution ( $\text{H}_2\text{SO}_4$ :  $\text{H}_2\text{O}_2$  (3:1)) for 2 min to hydroxylate the substrate, which was used to link the functional



siloxane molecules in the next step. After rinsing 3 to 4 times with water, the substrate was immersed in freshly prepared APTMS aqueous solution (5 wt%) and incubated at 70 °C for 2 h to immobilize the amino groups. The amino groups on the APTMS were used further to immobilize the Au NPs onto the structured substrate due to the electrostatic binding ability of the amino group to the gold NPs. Then the siloxane-functionalized PDMS film was rinsed three times in water to remove the unbounded siloxane molecules. Then the modified film was kept in oven at 70 °C for 1 h to complete the Si-O bond formation. Thereafter, freshly prepared APTMS-modified flexible substrate was immersed for 6 h into the pre-synthesized Au NPs solution. The Au NPs were synthesized by the well-known Turkevich method [178]. Finally, the Au-decorated structured PDMS film was removed from the solution, followed by rinsing with water 3 to 4 times, dried at room temperature, and kept for storage for further use. In order to compare the effect of structuring onto the substrate with respect to the unstructured substrate, in a similar way unstructured/planar PDMS substrate (directly pouring PDMS onto polished Si substrate) was prepared. After drying of the substrates, the colour change of both the structured and unstructured PDMS substrates is observed from white to lustrous golden depicts the deposition of the Au NPs onto the substrates.

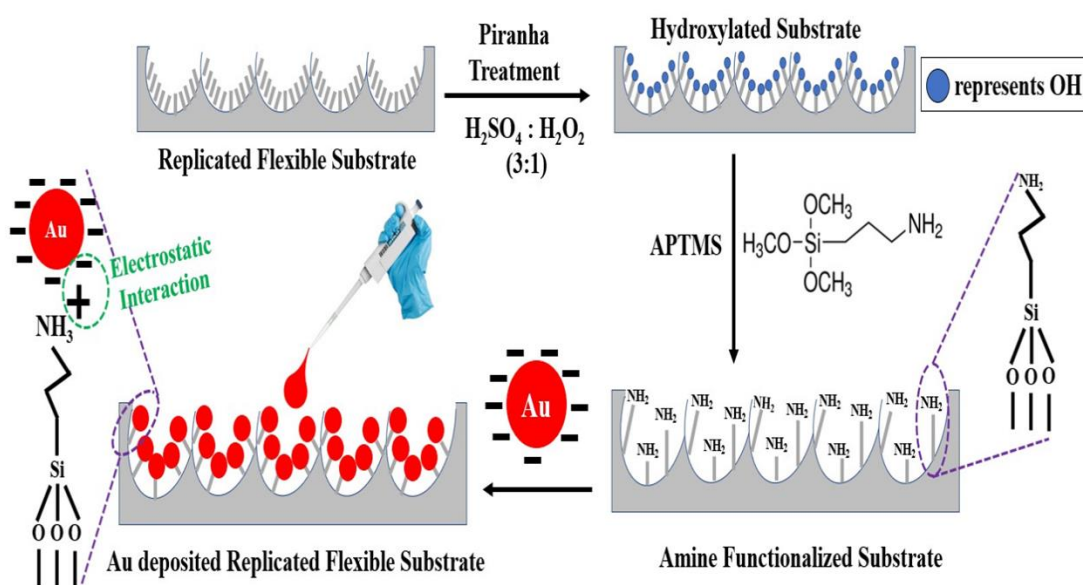


**Figure 5. 2.** A step-by-step pictorial illustration of the process for the deposition of Au NPs onto the APTMS functionalized Rose replicated substrate. The purple colour dotted lines show the enlarged view of the region, representing the presence of functional groups and bond formation between the molecules.

### 5.2.2.3 Fabrication of SERS sensor

To check the effectiveness of SERS substrate, two molecules: R6G (organic pollutant) and Urea (fertilizer) have been chosen. The reason for the selection of R6G, is its well-reported Raman bands, which has been used to optimize the instrumental parameters for a substrate such as laser

power, accumulation time, and acquisition time, etc. as well as urea is selected due to its regular use as a fertilizer. The sensor fabrication procedure was simple, the 15  $\mu\text{l}$  of  $10^{-5}$  M of the R6G and  $10^{-3}$  M of urea aqueous solution was drop-casted onto the planar as well as structured flexible substrates. After drying, the Raman spectra of both samples were recorded.

### 5.2.3 SERS Substrate characterization

Optical morphology of the as-prepared substrates is determined by the confocal microscope, surface topographies of the samples is examined by scanning electron microscopy (SEM) (Jeol, JSM6610LB) and field emission scanning electron microscopy (Carl Zeiss, supra-55). The spectroscopy measurements such as absorption maxima of colloidal solution of Au NPs and after its immobilization on to flexible unstructured and structured substrate is measured using the UV-visible spectrophotometer (UV-Vis lambda 950, Perkin Elmer) and the SERS effectiveness of the flexible substrate was tested by using a Horiba Raman spectrophotometer (LabRam HR Evolution, Horiba Scientific). A 532 nm Ar ion laser source was used as an excitation source. The characteristic Raman bands of R6G and urea are used to optimize the instrumental parameters. Parameters such as high laser power (5 mW), objective lens (50 X), grating (600 grooves/mm), long accumulation (6s), and acquisition time (2s) were finalized to detect R6G. In the case of urea, the parameter optimization was again performed due to its small Raman scattering cross-section of the molecule [189]. In this case, only the acquisition time (6s) value needs to be changed for a better signal-to-noise ratio, rest all the instrumental parameters were similar as used for R6G detection. All the measurements were recorded at room temperature and the characteristic peak at  $520\text{ cm}^{-1}$  of a Si substrate was used for spectrometer calibration. The laser spot diameter was  $\sim 1.3\text{ }\mu\text{m}$  and all the spectra were recorded over the range of  $500 - 1800\text{ cm}^{-1}$ . Each spectrum which was shown in the paper was the average of seven spectra recorded by randomly selected spots across the substrate.

## 5.3 Results and Discussion

### 5.3.1 Absorption spectra determination

For the confirmation of the immobilization of Au NPs onto the unstructured and structured PDMS the UV-vis absorption spectroscopy is performed. Figure 5.3. shows the absorption spectra of Au NPs suspension (a), Au coated onto unstructured (b), and structured PDMS (c). The plasmon absorption band of Au NPs is observed at  $\sim 525\text{ nm}$  (because in a liquid solution, Au NPs are at a distance from each other due to the strong electrostatic repulsion) which is in good agreement with the previous literature [195] and after the assembly of particles onto the unstructured as well as structured PDMS ‘bimodal bands’ is observed. One band which is at  $525\text{ nm}$  in the case of colloidal Au NPs, is slightly red-shifted to  $\sim 538\text{ nm}$ . The shift in SPRs peaks depends on the morphology (shape, size) and arrangement (interparticle spacing) of the

nanoparticles [196]. The peak shift, in this case, can be correlated to the reduction in interparticle gap due to the immobilization of Au NPs onto the substrates. The appearance of a second band at  $\sim 578$  nm which is redshifted by 23 nm with respect to the colloidal Au NPs. This red shift depicts that the greater number of Au NPs has come closer to each other due to the immobilization which indicates the formation of a closed packed array of Au NPs onto both substrates.

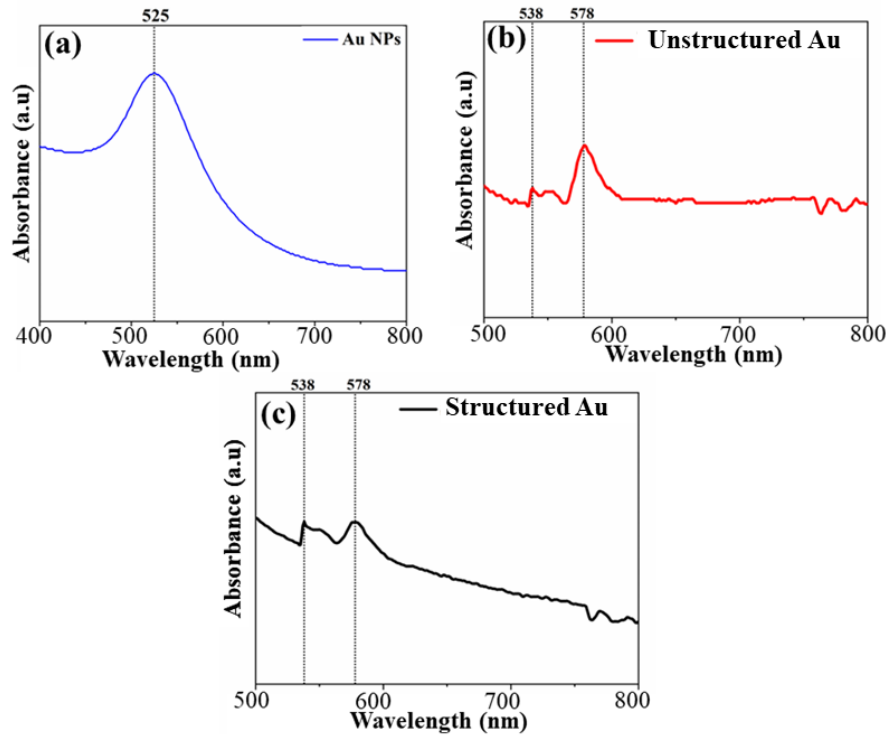


**Figure 5. 3.** Absorption spectra of (a) Au NPs suspension in water; self-assembled Au NPs onto (b) unstructured and (c) structured substrate.

### 5.3.2 Morphological Identification of flexible substrates

#### 5.3.2.1 Optical microscopy examination

In order to confirm the structure formation onto the PDMS, an optical image of the sample has been taken after peeling off the PDMS from the rose template and is shown in fig 5.4. Optical image can give a rough idea about the formation of the pattern onto the substrate as per its resolution. It can be seen from the optical image that the replicated sample surface is completely covered with lots of micropapilla, which indicates the successful formation of the replicated patterned substrate.

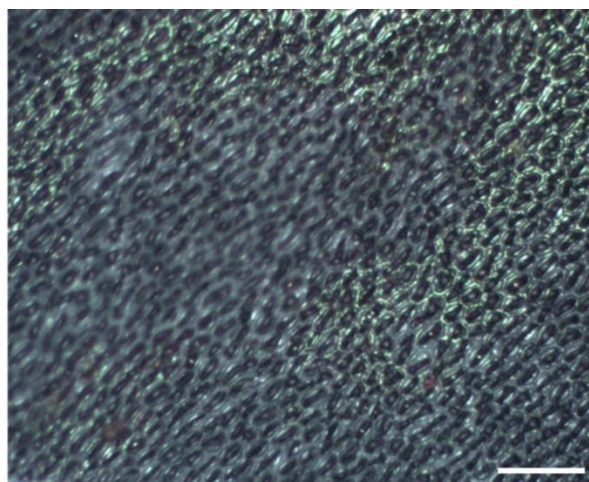
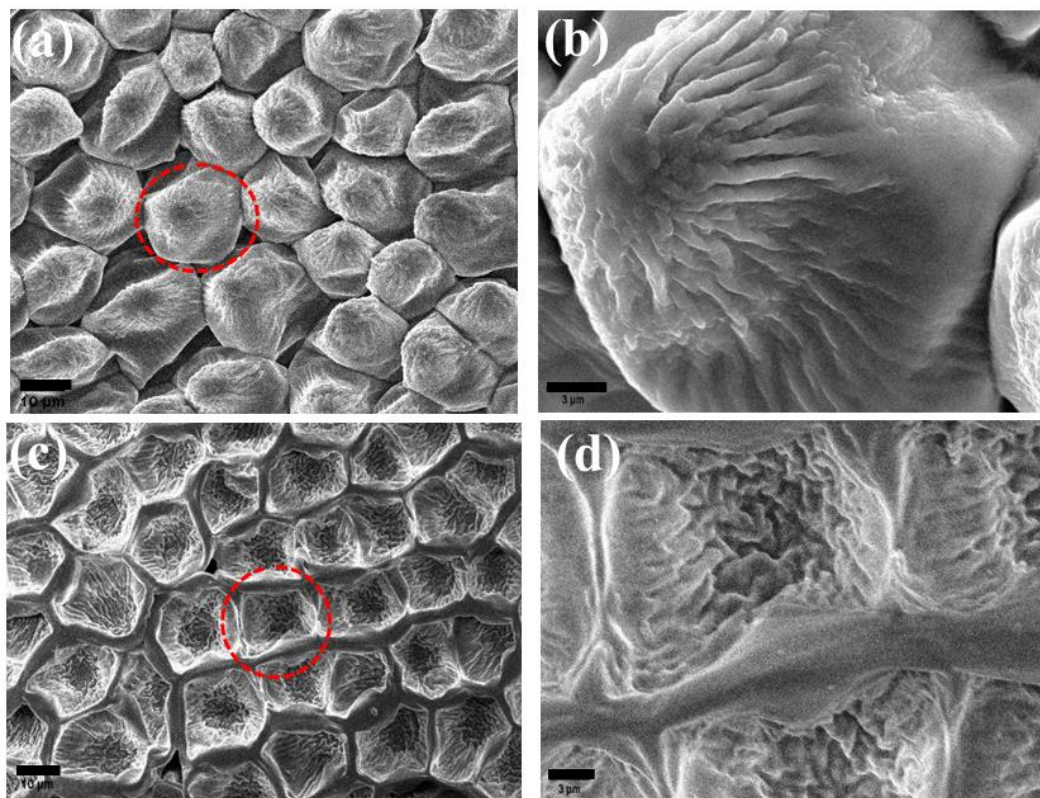


**Figure 5. 4.** Optical image of the replicated structured PDMS prepared from the rose. The scale bar corresponds to 4  $\mu\text{m}$ .

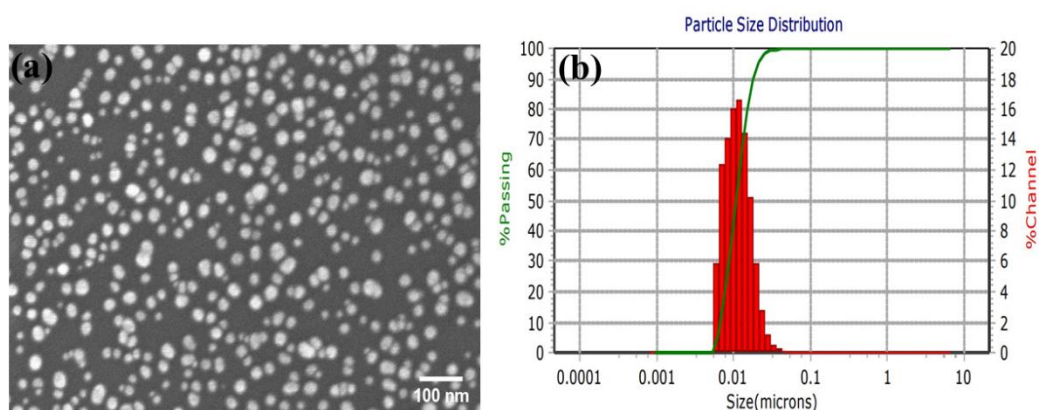
#### 5.3.2.2 *Electron microscopy examination*

Figure 5.5 represents the scanning electron microscopy (SEM) images of natural red rose petal, PDMS replicas of rose petal; and Figure 5.6 (a) and 5.7 represents the field emission scanning electron microscopy (FE-SEM) images of self-assembly of Au NPs on flat PDMS, and on replicated PDMS substrates. Figure 5.5 (a) and (b) shows the morphology of fresh red rose petal and fig. 5.5 (c) and (d) demonstrates the topological view of PDMS replicas of rose. It can be seen from fig. 5.5 (a) that the petal surface is covered by micropapillae. The diameter of a single papilla is  $\sim 20 \mu\text{m}$ . Figure. 5.5 (b) demonstrates the high magnification image of fig. 5.5 (a), it can be seen that single micropapillae contain nano grooves. Figure 5.5 (c) illustrates the SEM image of PDMS replicas; it can be clearly visible that replicas contained the negative structure of Rose petals and the surface is fully covered with microcavities of a diameter ranging from  $\sim 20 \mu\text{m}$ . Right-hand side is the magnified SEM image; multiple folds can be seen in the single cavity. The SEM results show that the surface topographic structure of micro-cavities on PDMS replicas is complementary with the micropapillae on the natural rose petal. Before the immobilization of Au NPs onto different substrates, the morphological evaluation of the particles has been done after synthesis as represented in fig. 5.6. Figure 5.6 (a) shows that the particles are quite stable in solution, not in the form of aggregated state and the average size of the particle is  $\sim 18 \text{ nm}$  calculated by Image J software and fig. 5.6 (b) represents the DLS measurement for the particle size distribution in the solution. The average size of synthesized Au NPs is  $\sim 25 \text{ nm}$  with PDI 0.435 nm, respectively. Figure 5.7 (e), (f), (g), and (h) represents the Au NPs has been successfully self-assembled onto the replicated pattern ((e) and (g)) as well as onto the flat flexible substrate ((f) and (h)). Figure 5.7 (e) and (f) shows the high density of Au NPs is assembled on both substrates. It may be notified that from fig. 5.7 (e) the deposition of Au NPs does not show any obvious changes in the morphology of the replicated

samples. The magnified images of the single pores ( $g'$ ,  $g''$ , and  $g'''$ ) represent that the NPs are spherical in shape, densely packed, continuous, and well-distributed from the top to bottom. It can be seen from the image 'h' (magnified version of 'f'), flat PDMS is also covered with spherical Au NPs and are almost forming a continuous film throughout the substrate. The scale bar of fig. ((a), (c), (e), and (f)) corresponds to 10  $\mu\text{m}$ , fig (b), (d) and (g) related to 3  $\mu\text{m}$ , and fig ( $g'$ ,  $g''$ ,  $g'''$  and h) corresponds to 100 nm.



**Figure 5.5.** SEM images of (a)-(d) prior to Au decoration, (a) natural rose petal; (b) magnified view of the single rose petal; (c) negative structured PDMS replica of rose petal; (d) magnified image of the single replicated structure.



**Figure 5.6.** (a) Histogram represents the NPs size distribution measured from DLS spectra. (b) FESEM observations of Au NPs.



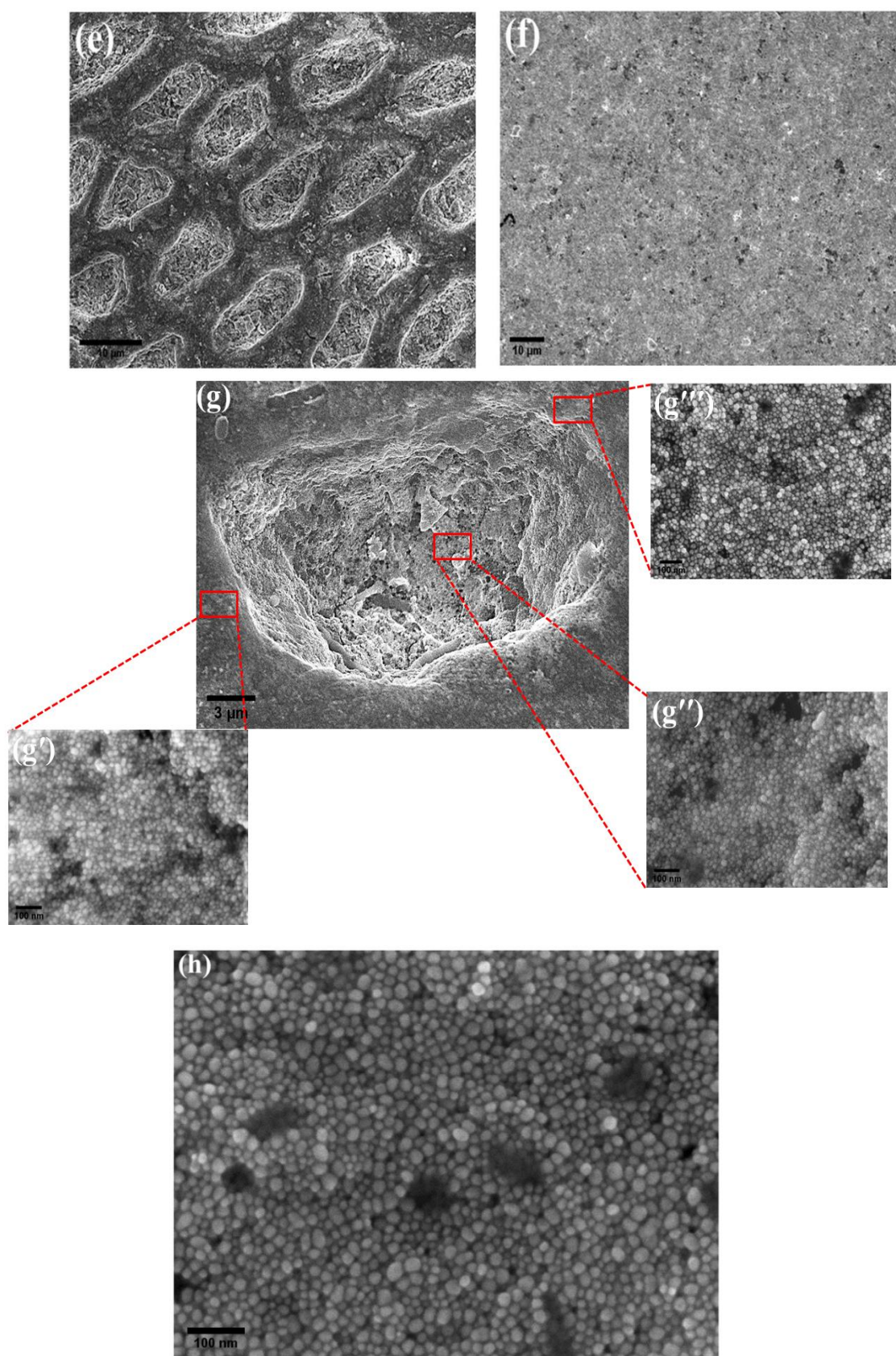


**Figure 5. 7.** Images (e) and (f) are the FESEM images represents the post -Au decoration onto PDMS replica of rose petal (e) and flat PDMS (f), correspondingly (g) and (h) are the magnified view of image

(e) and (f) respectively. Figure (g'), (g'') and (g''') are the images captured from different areas of a single pore.

### 5.3.3 SERS performance determination

In order to check the substrate effectiveness and enhancement factor, the prepared structured substrate performance is compared with the unstructured (flexible) and silicon (solid) substrates. The same volume (15  $\mu\text{L}$ ) and concentration ( $10^{-5}$  M) of the R6G was drop-casted onto all substrates and after drying the Raman measurement was recorded. It can be seen from fig 5.8 the R6G on Si substrate is able to show some characteristic peaks, but the intensity of the peaks is quite low and also some of the peaks is not identifiable. Whereas on Au-coated unstructured and structured flexible substrate, the signals are quite sharp and all the signals are clearly identifiable, which indicates good SERS enhancement due to the presence of SERS active material. As can be seen from the morphological images of the replicated templates, the Au NPs are densely packed. The reason for the enhancement can be co-relate to the generation of an electromagnetic field around the NPs as the size of the particle is smaller than the wavelength of light and due to the formation of hot spots between nanogaps as NPs are in the form of a closed-packed array. It can be observed that the signals on to the structured substrate show higher enhancement as compared to the unstructured (flat) substrate. Because in the case of structured substrate, the detected molecules are getting more adsorption sites for deposition due to the presence of multiple folding as compared to the planar flexible substrate, which helps in enhancing the signal.

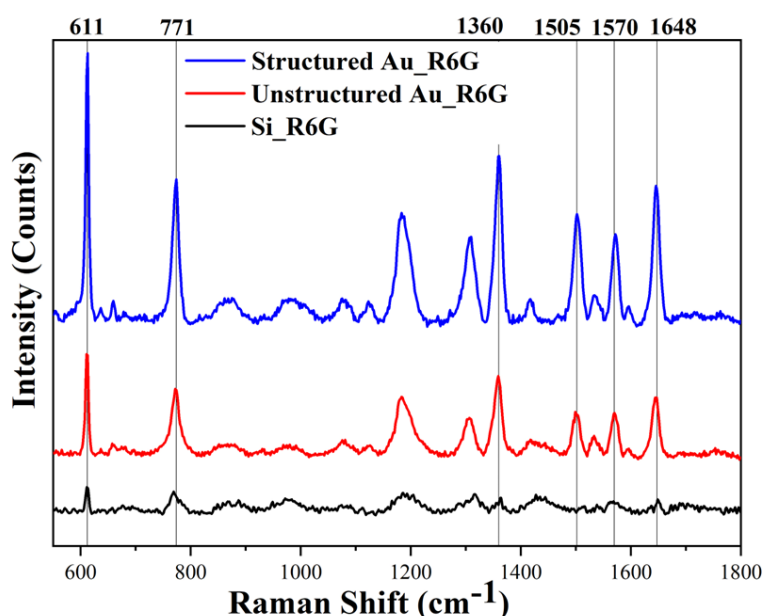


**Figure 5. 8.** SERS spectra of R6G on the different substrates- Si Substrate (black line); NPs decorated onto the unstructured/flat flexible (red line) as well as onto the structured flexible (blue line).

### 5.3.3.1 Enhancement factor determination

In order to quantify the enhancement factor of substrates, the formula mentioned in equation ‘2.11’ in section 2.2.3.3. is used. The enhancement factor is calculated by comparing the intensities of R6G molecules at 611  $\text{cm}^{-1}$  and the concentration of the molecule on different substrates (structured, unstructured/planer, and Si substrate). The figure mentioning the intensity counts is represented in 5.9.

$$EF = \frac{I_{SERS} \cdot C_{Raman}}{I_{Raman} \cdot C_{SERS}} \quad (\text{eq. 2.13})$$

Here ‘I’ term corresponds to intensity and the ‘C’ term is relative to the concentration of the molecule. In the study, a similar concentration ( $10^{-5}$  M) and equal volume (15  $\mu\text{l}$ ) of R6G is drop-casted on all the substrates, therefore the values of  $C_{Raman}$  and  $C_{SERS}$  directly cancel each other. The enhancement factor is calculated by comparing the intensities of structured substrate with respect to the unstructured substrate (flexible) or as well as with the Si substrate (solid). The structured substrate is able to provide ~10-fold enhancement with respect to Si substrate and ~3-fold with respect to the flat substrate, which is higher than the previous substrates based on solid substrates [125], [156] as well as flexible substrates [130].

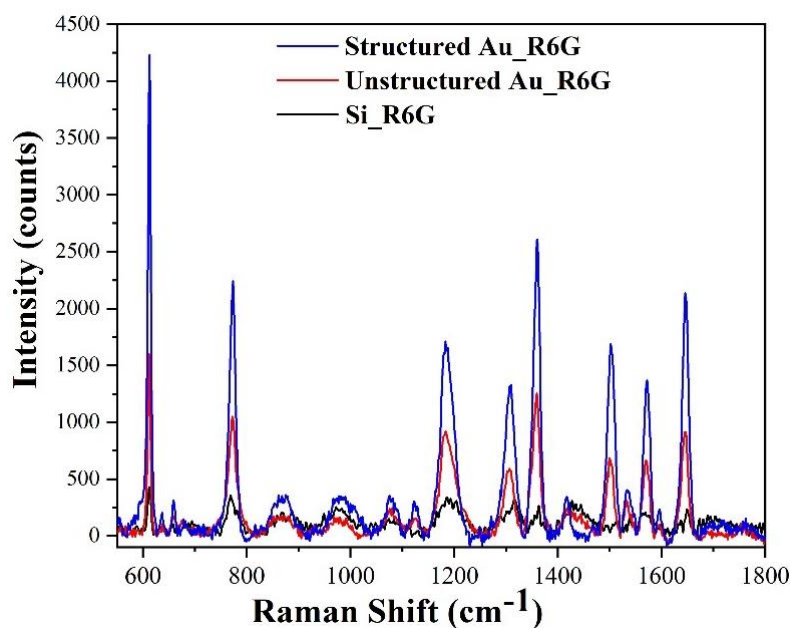


**Figure 5. 9.** SERS spectra of R6G on different substrates, clearly represents the intensity counts of structured substrate is higher than the unstructured and Si substrate.

### 5.3.3.2 Flexible substrate testing for fertilizer detection

For this examination,  $10^{-3}$  M urea aqueous solution is used which is lower than the acceptable limit [186]. Figure 5.10 represents the SERS spectra of urea on substrates. It can be clearly seen that the structured substrate is able to enhance the signal as well as able to clearly identify some peaks at 1538 and 1648  $\text{cm}^{-1}$  which are not detected on the Si substrate. The



effectiveness of the substrate has been tested by comparing the intensity of the  $1011\text{ cm}^{-1}$  peak of urea on the structured with respect to the signal intensity on the unstructured and Si substrate respectively. The substrate is able to provide 23-fold enhancement when the intensity is compared with the Si and 3-fold enhancement when compared with the unstructured substrate. The enhancement is better than the previous literature where the substrate has been fabricated by expensive techniques [190], [191]. The enhancement factor is calculated by the equation mentioned in section 2.2.4. The figure mentioning the intensity counts is represented in 5.11. From these results, it can be said that the fabricated substrate can be used for the of analysis urea.

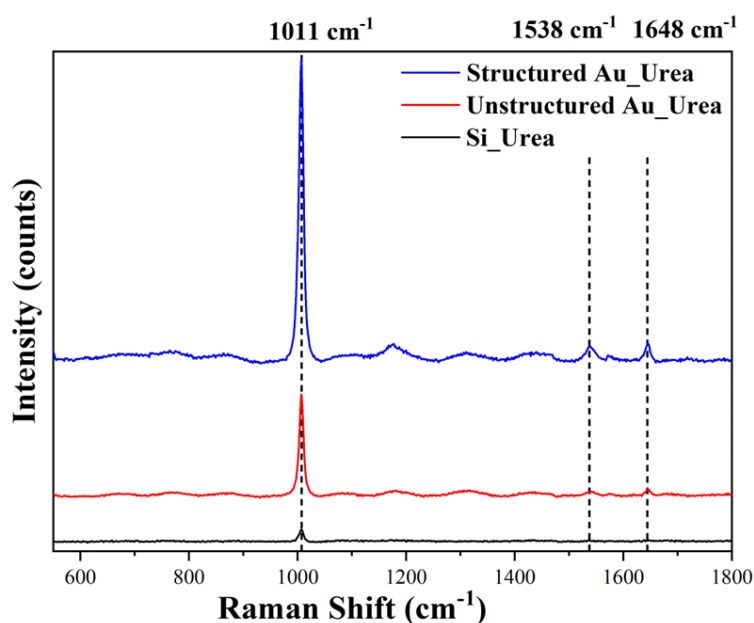


**Figure 5. 10.** SERS spectrum of  $10^{-3}$  M urea on different substrates- Si substrate (black line), NPs assembled onto structured (red line) and unstructured (blue line) substrate.

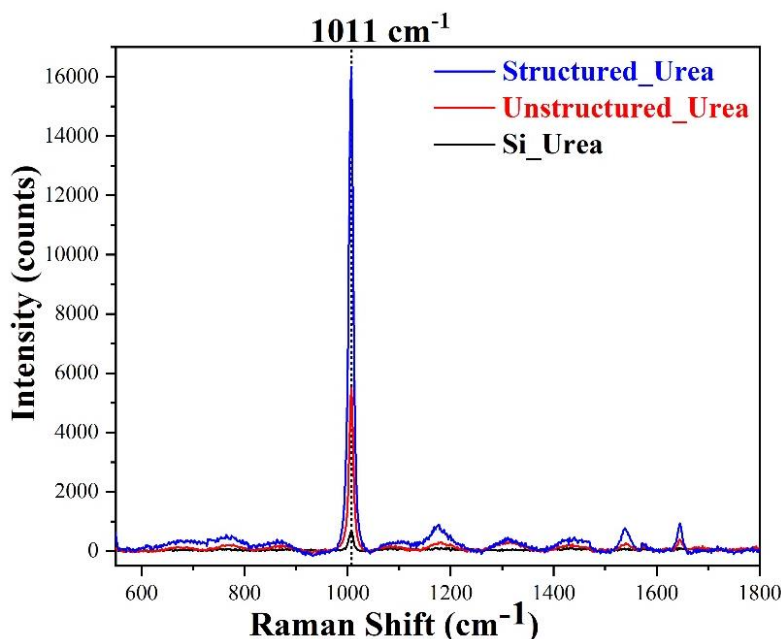


**Figure 5.11.** SERS spectra of urea on different substrates clearly represent structured substrate is able to enhance the signal compared to the unstructured and flat substrate.

#### 5.3.3.3 Substrate sensitivity determination

As discussed in the SERS field; sensitivity is the major concern for any kind of substrate. In order to examine the LOD, the substrate has been treated with varied concentrations of urea as demonstrated in fig 5.12. The Raman spectra of urea with a concentration varying from  $\sim 10^{-3}$  to  $\sim 10^{-11}$  M on the structured substrate has been measured and are represented in fig 5.12 (a). The intensities of the signals is enhanced linearly with the increase of the urea concentration. It can be seen from fig 5.12 (a) that, even at a concentration of  $10^{-11}$  M, the substrate is able to detect as well as to provide  $\sim 3$ -fold enhancement in comparison with silicon ( $10^{-3}$  M). Which indicates the good contribution of the purposed substrate towards sensitivity. When the concentration is  $10^{-13}$  M, the signal is still observed, but the intensity of the signals is weak (only  $\sim 900$  counts is observed) as depicted from fig 5.13. Thus, it can be said that this substrate shows good sensitivity and able to sense till the  $\sim 10^{-11}$  M concentration, which is much lower than the acceptable limit and indicates the lower limit detection capability of such substrate. Furthermore, fig 5.12 (b) shows the calibration curves, which correspond to the signal intensity at  $1011\text{ cm}^{-1}$  vs the varied concentrations of urea on the logarithmic scale, representing a good linear relationship between the concentration and intensity. Each point in the graph corresponds to the average value of intensity taken from seven randomly selected areas, and the error bar represents the standard deviation. The linear equation is  $I = 1894 [\log (C)] + 22732$ , where C and I correspond to the concentration and Raman intensity of urea. The correlation coefficient ( $R^2$ ) value is  $\sim 0.99$ , representing a good linear relation.

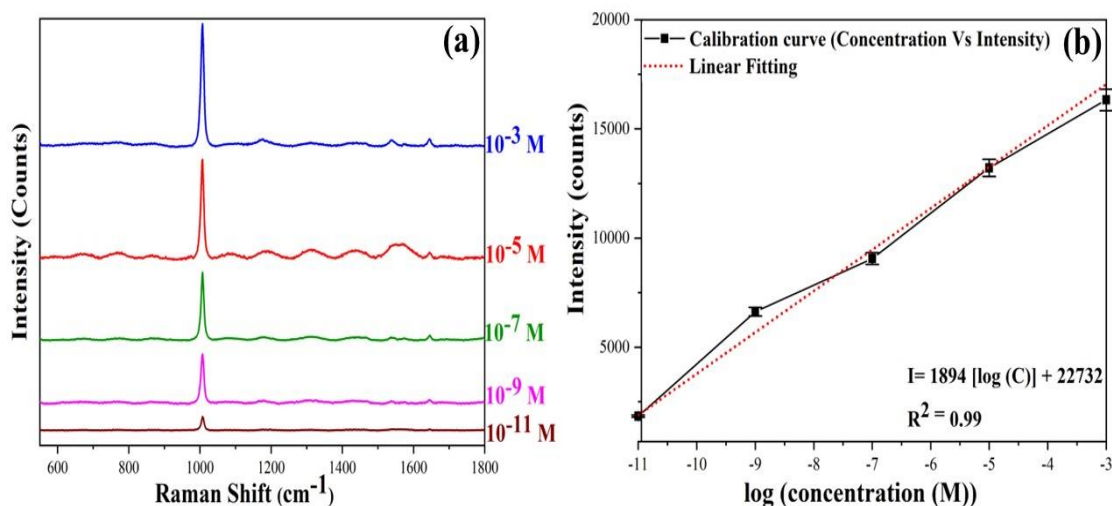


**Figure 5. 12** (a) Raman spectra of urea under different concentrations. (b) The calibration curve of the intensity vs different concentrations of urea. The x-axis is converted to a logarithmic scale and the y-axis is mentioned as it (intensity counts) for better understanding.

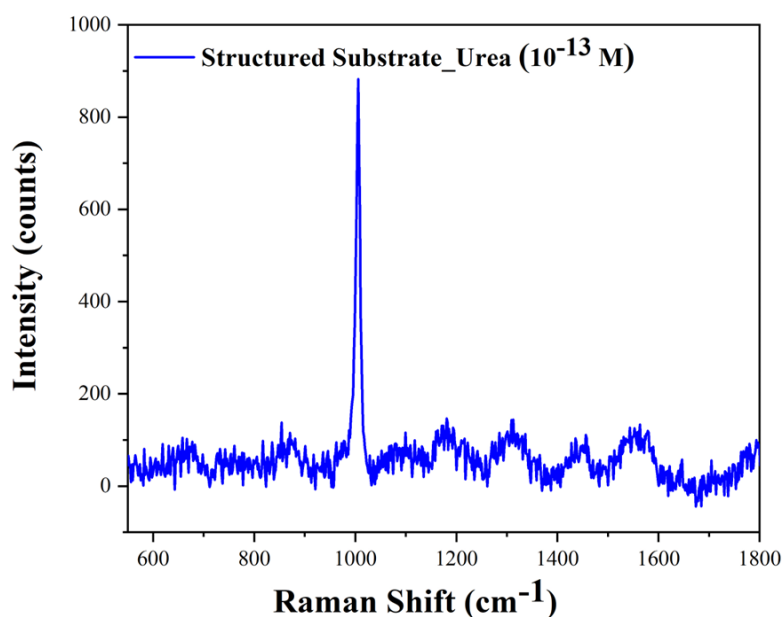


**Figure 5. 13.** Detection of  $10^{-13}$  M urea concentration on the structured substrate.

#### 5.3.3.4 Stability and reusability examination of substrate

Stability of the signal is the key requirement for a SERS substrate performance for routine analysis. Fig. 5.14 shows a comparative study of the SERS spectra of the substrate after one day of fabrication and after its storage in a desiccator for about four months. Prior to SERS measurement of the stored substrate, the substrate is washed by drop-casting method to drain out the adsorbed urea from the substrate as shown in fig. 5.14 (a). In order to confirm the urea removal, Raman spectra has been recorded and shown in fig. 5.14 (b). It can be seen that the washed substrate represented as (b') in fig. 5.14 (b) is not showing any kind of peak which

means the substrate is free from urea molecules and ready to reuse. After that for the stability testing of the stored substrate, freshly prepared ( $10^{-3}$  M) urea solution was re-adsorbed onto the cleaned substrate and allowed to dry for  $\sim 15$  min in order to collect the SERS spectra. It can be clearly seen that the reused substrate labelled as (c') in fig. 5.14 (b) is able to represent the characteristic bands of urea. The bands are clearly observable and well-intensified. For the better understanding of the intensity fluctuation after  $\sim 120$  days, the spectra has been plotted against time versus intensity as depicted in fig. 5.14 (c). The intensity counts of the  $\sim 120$ -day-old substrate is almost similar to one day-stored substrate. The signal intensity fluctuation corresponding to  $1011\text{ cm}^{-1}$  peak has also been calculated and it varies only about  $\sim 2\%$  with respect to one day stored sample. These results indicate the good durability of the prepared substrate. The overlapped stability spectra of the 1-day and 120-day older sample (represents the intensity counts) is shown in fig. 5.15.

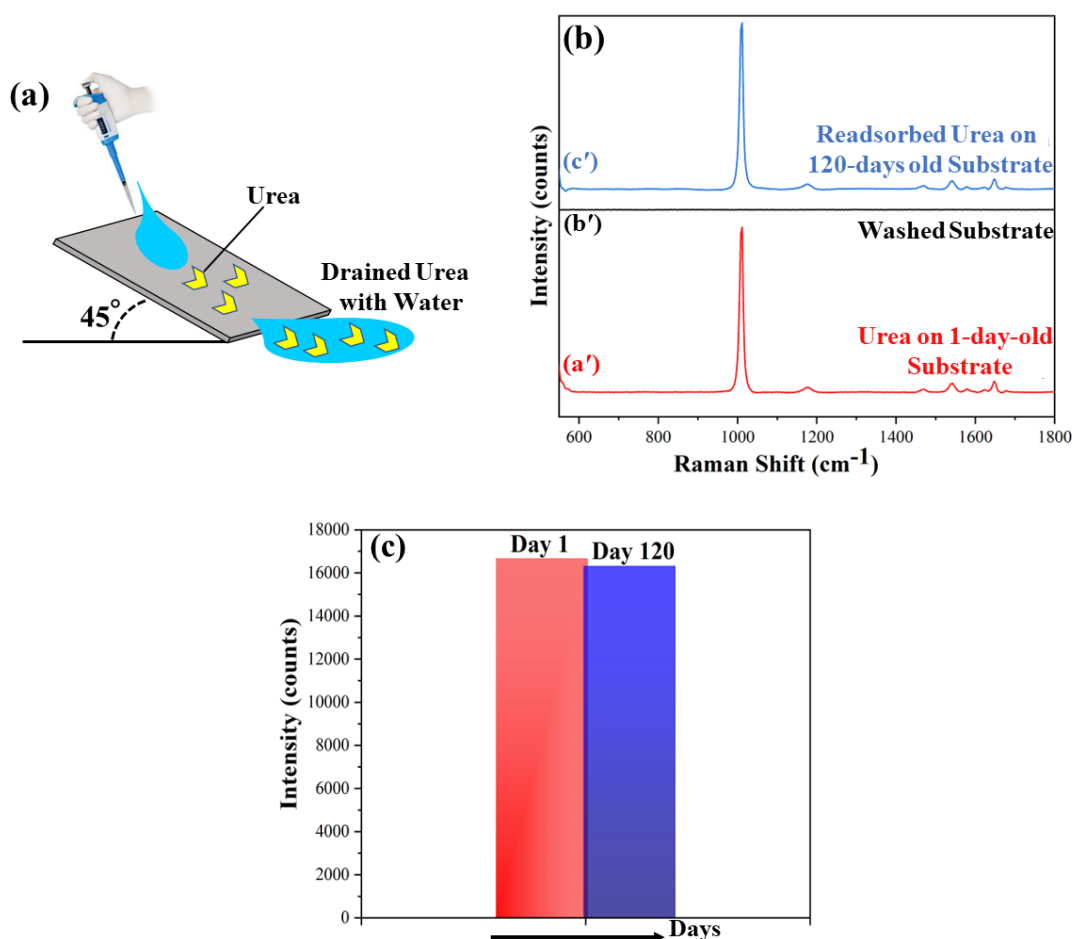


**Figure 5. 14.** (a) Represents the washing method to reuse the substrate; (b) reusability test spectra of urea absorbed on substrate after (a') '1' day and (c') '120' days and (b') corresponds to washed substrate; (c) histogram shows variation in the intensities of the characteristic peak of urea of the 120 days old sample with respect to one-day old sample.

#### 5.3.3.5 Testing of substrate effectiveness for real-world application

It has been discussed that the flexible substrates have the advantage over solid substrates due to their ability to attach onto the curved surface as well as extraction of contaminants directly from the surfaces. Urea fertilizer is not only used to stimulate the growth of crops or plants by just mixing it to the soil, but it is also used in the spray form to increase the growth of crops and plants. In this work, the flexible substrate has been tested for the detection of urea from the curved surface of tomato via paste and peel-off approach. The tomatoes were purchased from the local market of Ropar.

##### 5.3.3.5.1 Method of sensor fabrication

First, the Tomato surface was washed with D.I. water to remove any kind of impurities from the surface and dried at room temperature. Next, the  $10^{-5}$  M concentration of urea aqueous solution was sprayed over the tomato surface which is below the maximum permissible limit as discussed in the introduction part and allowed to dry for ~ 1 h at room temperature as shown in fig. 5.15. Then the flexible structured substrate (replica of Rose petal) was pasted onto the white spots (indicates the residues of urea) over the tomato surface. After that, the pasted substrate was swabbed gently for ~1 min along the white spot's areas and finally, it was peeled off from the tomato surface and placed onto the Si substrate for SERS measurement.

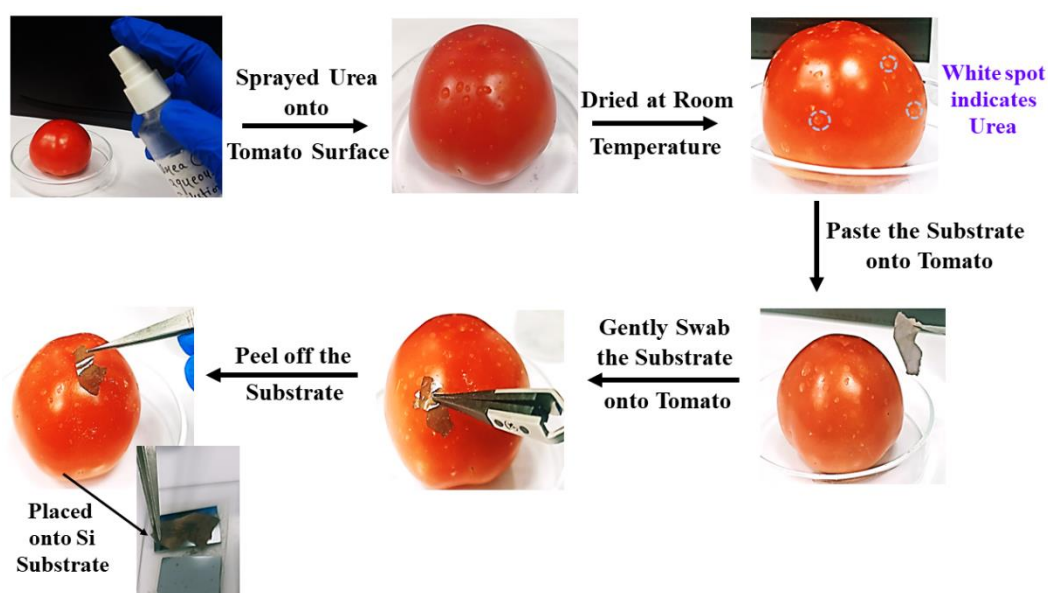


**Figure 5. 15.** Pictorial representation of procedure used for detecting urea on the Tomato surface.

##### 5.3.3.5.2 Testing of sensor

The urea-contaminated flexible substrate was placed inside the Raman spectrometer for measurement. All the instrumental parameters were similar as described earlier in section '5.2.3' for urea (laser (532 nm), high laser power (5 mW), objective lens (50 X), grating (600 grooves/mm), long accumulation (6 s), and acquisition time (2 s)). The spectra shown

in fig. 5.16 is the average spectra taken from seven different spots on the substrate. It can be clearly seen from the spectra that the characteristic Raman band of urea ( $1011\text{ cm}^{-1}$ ) with  $\sim 12,000$  counts is well appeared on the substrate, which has been directly peeled off from the tomato surface. These results clearly validated the applicability of the prepared flexible substrate for the real-world detection of fertilizer. These substrates can further be used for the detection of other contaminants such as explosives, drugs, biomolecules etc.

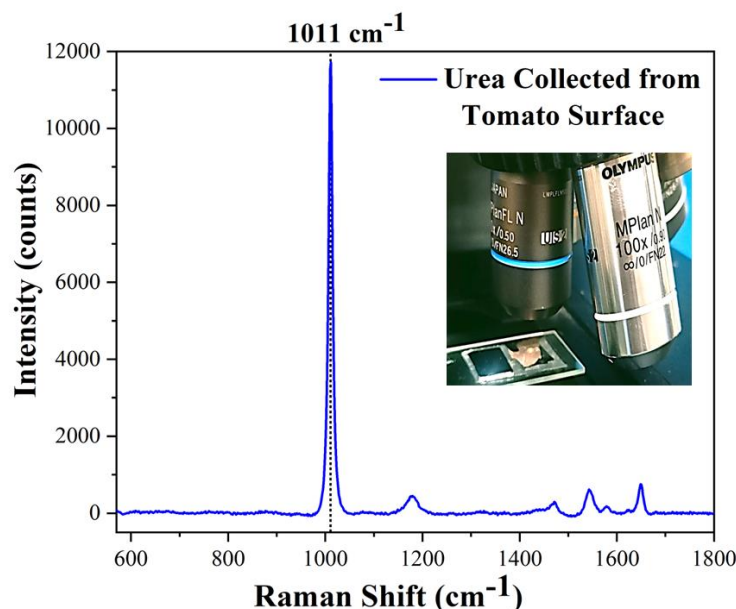


**Figure 5. 16.** SERS spectra of substrate contaminated with urea residues directly peeled from the tomato surface.

#### 5.3.3.6 Cost calculation of substrate

The Flexible structured substrate cost is Rs= $\sim 4566/-$ , when the Si is used as base substrate. However, when the glass is used as a base substrate than the cost is only  $\sim 961$   $-/$  for  $1.5 \times 1.5\text{ cm}^2$  substrate. The below mentioned table shows the cost of each material, which is required for the fabrication of the flexible substrate.

**Table 4. 12.** demonstrates the fabrication material with cost which is required for second substrate (a rose petal as a template, PDMS as a surface texturing agent, Silicon substrate,  $\text{H}_2\text{O}_2$ , and HF).

S.No.	Material	Available Quantity	Cost	Required quantity	Cost
1.	Rose flower	1 Rose flower	$\sim 25/-$	1 petal	$\sim 25/-$
2.	3-Aminopropyl triethoxysilane	500 mL (69 %)	$\sim 2178/-$	$\sim 10\text{ mL}$	$\sim 45/-$

3.	Deionized Water	1L	75/-	5L	~375/-
4.	Silicon (Si)	8×8 cm <sup>2</sup> (p-type with <100> orientation)	~19,280/-	1.5×1.5 cm <sup>2</sup>	~3615/-
5.	Hydrofluoric (HF),	500 mL	~530/-	~5 mL	~5/-
6.	Hydrogen Peroxide (H <sub>2</sub> O <sub>2</sub> )	500 mL	~500/-	~5 mL	~5/-
7.	Tetrachloroauric (III) acid trihydrate	1G	~21,889/-	~16 mg	~350/-
8.	Sulfuric (H <sub>2</sub> SO <sub>4</sub> ) acids,	2.5L	~990/-	~10 mL	~5/-
9.	Sylgard-184, PDMS kit	1L	~14,175/-		~141/-
<b>Total (Including Silicon) =</b>					<b>Rs= ~4566/-</b>
10.	Glass	1 Pack (50 slides)	~330/-	1.5×1.5 cm <sup>2</sup>	~10
<b>Total (Glass replaced with Silicon) =</b>					<b>Rs= ~961/-</b>

### *Conclusion of chapter 5*

A scalable, effective, and economical method to fabricate SERS substrates for the detection of urea fertilizer as an environment contaminant is discussed. The substrate is prepared via a self-assembly deposition of colloidal Au NPs onto the microcavities of replicated template created through rose petals. The NPs are uniformly distributed throughout the substrate as well as closely packed from top to bottom throughout the substrate or on the edges as well, as demonstrated from topographical view. The beneficial point about the substrate is that, the microcavities covered with Au NPs provide more adsorption sites to the molecules, which results in highly intensive SERS spectra of low cross-sectional urea as well as offers a good enhancement factor upto 23-fold. The enhancement in signals arises due to the generation of a local field around the NPs and the plasmonic coupling between the adjacent NPs. The substrate has been applied to determine urea sprayed on the tomato surface by paste and peel off method.

Moreover, substrate has shown good analytical performance in terms of sensitivity, stability, and reusability. At the end, it can be said that substrate prepared by replicating the structure of natural artifacts can help to reduce the fabrication cost by reducing the use of expensive preparation techniques (lithography, sputtering, etc.), as well as help to construct the flexible and nanostructured substrate via an easy and bulk scale method.



## ***Chapter 6. Summary and future perspectives***

### ***6.1 Summary***

In this thesis, rigid and flexible SERS substrates have been fabricated by an easy, reproducible, and low-cost fabrication method. The solid substrate is fabricated by the dealloying method. This is a single-step method and does not require specific setup and working conditions such as a clean room, patterned masks, photoresists, and metallic targets like lithography and sputtering techniques. It involves the leaching of less noble elements from a precursor alloy. For the fabrication of substrate, alloy leaf such as Au<sub>50</sub>Ag<sub>50</sub> was immersed in nitric acid for varied periods of time in order to check the effect of dealloying time onto the morphology as well as onto the SERS performance of substrate. After the optimized dealloying time, the obtained substrate consisted of a porous kind of morphology (gold ligaments separated by nanopores) named as NP-Au, which was effective for improving the SERS performance ~ 10-fold; through generating the localized surface plasmons resonance around the gold ligaments as well via hot spots formation between adjacent ligaments (which were separated by nanopores).

Furthermore, the effect of laser power variation of Raman spectrophotometer laser onto the SERS performance of substrate has also been examined. It has been noticed that with the laser power variation the morphology of NP-Au substrate has been affected and due to that the change in SERS performance is observed. The laser power treatment resumes the surface diffusion of Au atoms which has been quenched during the dealloying process; due to that pores keep on interlinking and the size of pore changes accordingly. The substrate durability has also examined, it was stable even after storage of ~ 2 years in a desiccator as well as uniform due to the homogenous morphology throughout the substrate (similar intensity signals were observed from randomly selected seven areas of the same substrate) and most importantly it was reusable at least four times via applying simple drop-casting method. The applicability of the prepared substrate has been tested by detecting the fertilizer such as Urea. Urea is a multi-purpose fertilizer, which is used worldwide to increase the crop production as well as to protect the crops from insects and fungus. The substrate has shown good sensing capability by detecting urea in the nanomolar range which is much lower than the maximum permissible limit.

The flexible substrate was prepared by using rose petal as a template, PDMS as an elastomer, and nano casting approach was used to create the inverted texture of rose. After that the Au nanoparticles (~ 19 nm in size) were deposited via a self-assembly approach onto the flexible substrate (consisting inverted texture of rose) to make the substrate SERS active. The effectiveness of the substrate was tested by detecting rhodamine 6G (organic pollutant) and urea (fertilizer) molecules and the substrate shows the good LOD (~ 10<sup>-9</sup> M) for both contaminants. Moreover, the substrate has shown good analytical performance in terms of sensitivity, stability, and reusability. The substrate has been used to collect urea residues on the tomato surface by a

paste and peel-off method. At the end it can be said that the flexible structured substrates prepared from natural artefacts may open a new door in the field of facile and fast synthesis of substrates. Furthermore, these methods can help to reduce the fabrication cost by reducing the use of expensive preparation techniques (lithography, sputtering, etc.) and also bulk scale synthesis is possible by using nanotexturing method which is difficult with the earlier mentioned methods. The cost of both the fabricated substrates is lower than the substrates which are generally purchased by the researchers from the different companies in order to detect various contaminants. On the other hand, the detection area of the fabricated substrates is greater than the company-made substrates as represented in Table 3. Furthermore, the substrates made by the companies are also not reusable, the use of new substrates for the testing of other molecules also increases the cost.

**Table 4. 13:** Cost comparison with company made substrates.

S.No	Company Name	Substrate Material	Substrate Name	Area (cm)	Cost	Ref.
1.	Klarite	Au thin film on Si nanopyramids	Klarite™ 302 SERS substrates	0.02	~8,288.20/-	1
2.	Ocen	Au nanoparticle	RAM-SERS-AU-5 SERS Substrates	0.05	~6,962.09/-	2
3.	SILMECO	Au coated on Nanostructured Si	SERStrate	0.1	~31,435.3/-	3
5.	-	Au <sub>50</sub> Ag <sub>50</sub> leaf	NP-Au	1	~3855/-	<b>Our Substrate</b>
6.	-	Au NPs on to flexible structured substrate	Flexible Structured Substrate	1.5	~4566/-	

## 6.2 Future perspectives

These substrates can be used for the detection of other contaminants such as pathogens, environmental pollutants, narcotics and to identify other food contaminants such as pesticides/fertilizers, which are used regularly to kill pests and protect the crop from fungal diseases.

The flexible substrates can be used for the onsite detection (real-world application) of contaminants (pesticides, fertilizers, biomolecules, and environmental pollutants etc.) on other vegetables and fruits surfaces and can also be used for other applications such as optoelectronic (photoelectric properties) and biomedical (capture and release of tumor cells) instead of SERS.

## References

- [1] G. V. Pavan. Kumar, “Plasmonic nano-architectures for surface enhanced Raman scattering: a review,” *J. Nanophotonics*, vol. 6, pp. 064503, 2012, doi: 10.1117/1.jnp.6.064503.
- [2] E. C. Le Ru, E. Blackie, M. Meyer, and P. G. Etchegoint, “Surface enhanced raman scattering enhancement factors: A comprehensive study,” *J. Phys. Chem. C*, vol. 111, pp. 13794–13803, 2007, doi: 10.1021/jp0687908.
- [3] Ram. P. Gandhiraman, D. Nordlund, V. Jayan, M. Meyyappan, and J. E. Koehne, “Scalable low-cost fabrication of disposable paper sensors for DNA detection,” *ACS Appl Mater Interfaces*, vol. 6, pp. 22751–22760, 2014, doi: 10.1021/am5069003.
- [4] Anna. Huefner, W. L. Kuan, R. A. Barker, and S. Mahajan, “Intracellular SERS nanoprobe for distinction of different neuronal cell types,” *Nano Lett*, vol. 13, pp. 2463–2470, 2013, doi: 10.1021/nl400448n.
- [5] Steven. E. J. Bell and N. M. S. Sirimuthu, “Surface-enhanced Raman spectroscopy (SERS) for sub-micromolar detection of DNA/RNA mononucleotides,” *J Am Chem Soc*, vol. 128, pp. 15580–15581, 2006, doi: 10.1021/ja066263w.
- [6] Huigao. Duan, H. Hu, K. Kumar, Z. Shen, and J. K. W. Yang, “Direct and reliable patterning of plasmonic nanostructures with sub-10-nm gaps,” *ACS Nano*, vol. 5, pp. 7593–7600, 2011, doi: 10.1021/nn2025868.
- [7] Chao Zhang, Ji. Chang, Yu. Jing, Li. Zhen, Li. Zhaoxiang, Li. Chonghui, Xu. Shicai, Li. Weifeng, Man. Baoyuan, Zhao. Xiaofei, “MoS<sub>2</sub>-based multiple surface plasmonic coupling for enhanced surface-enhanced Raman scattering and photoelectrocatalytic performance utilizing the size effect,” *Opt Express*, vol. 29, pp. 38768–38780, 2021, doi: 10.1364/OE.441176.
- [8] Chang. Ji, J. Lu, B. Shan, F. Li, X. Zhao, J. Yu, S. Xu, B. Man, C. Zhang, Z. Li, “The Origin of MO<sub>2</sub>C Films for Surface-Enhanced Raman Scattering Analysis: Electromagnetic or Chemical Enhancement,” *J Phys Chem Lett*, vol. 13, pp. 8864–8871, doi:10.1021/acs.jpcllett.2c02392.
- [9] Sin-Yi. Chou, C. C. Yu, Y. T. Yen, K. Te Lin, H. L. Chen, and W. F. Su, “Romantic Story or Raman Scattering? Rose Petals as Ecofriendly, Low-Cost Substrates for Ultrasensitive Surface-Enhanced Raman Scattering,” *Anal Chem*, vol. 87, pp. 6017–6024, 2015, doi: 10.1021/acs.analchem.5b00551.

- [10] Pawan. Kumar, R. Khosla, M. Soni, D. Deva, and S. K. Sharma, “A highly sensitive, flexible SERS sensor for malachite green detection based on Ag decorated microstructured PDMS substrate fabricated from Taro leaf as template,” *Sens Actuators B Chem*, vol. 246, pp. 477–486, 2017, doi: 10.1016/j.snb.2017.01.202.
- [11] Chao. Zhang, Zh. Li, Si. Qiu, W. Lu, M. Shao, C. Ji, G. Wang, X. Zhao, J. Yu, and Z. Li, “Highly ordered arrays of hat-shaped hierarchical nanostructures with different curvatures for sensitive SERS and plasmon-driven catalysis,” *Nanophotonics*, vol. 11, pp. 33–44, 2022, doi: 10.1515/nanoph-2021-0476.
- [12] Samir. Kumar, P. Goel, and J. P. Singh, “Flexible and robust SERS active substrates for conformal rapid detection of pesticide residues from fruits,” *Sens Actuators B Chem*, vol. 241, pp. 577–583, 2017, doi: 10.1016/j.snb.2016.10.106.
- [13] Yue. Li, Z. Hao, H. Cao, S. Wei, T. Jiao, and M. Wang, “Study on annealed graphene oxide nano-sheets for improving the surface enhanced fluorescence of silver nanoparticles,” *Opt Laser Technol*, vol. 160, pp. 109054, 2023, doi: 10.1016/j.optlastec.2022.109054.
- [14] Xiaoci. Dou., P. Li, S. Jiang, H. Bayat, H. Schonherr, “Bioinspired Hierarchically Structured Surfaces for Efficient Capture and Release of Circulating Tumor Cells,” *ACS Appl Mater Interfaces*, vol. 9, pp. 8508–8518, 2017, doi:10.1021/acsami.6b16202
- [15] Seungyoung. Park, J. Lee, and H. Ko, “Transparent and Flexible Surface-Enhanced Raman Scattering (SERS) Sensors Based on Gold Nanostar Arrays Embedded in Silicon Rubber Film,” *ACS Appl Mater Interfaces*, vol. 9, pp. 44088–44095, 2017, doi: 10.1021/acsami.7b14022.
- [16] Xinglin. Wen, G. Li, J. Zhang, Q. Zhang, B. Peng, L.M. Wong, S. Wang, O. Xiong, “Transparent free-standing metamaterials and their applications in surface-enhanced Raman scattering,” *Nanoscale*, vol. 6, pp. 132–139, 2014, doi: 10.1039/c3nr04012g.
- [17] Maria. Knauer, N.P. Ivleva, X. Liu, R. Niessner, and C. Haisch, “Surface-enhanced raman scattering-based label-free microarray readout for the detection of microorganisms,” *Anal Chem*, vol. 82, pp. 2766–2772, 2010, doi: 10.1021/ac902696y.
- [18] Chandrasekhara Venkata. Raman, “A new radiation,” *Indian J. Phys*, vol. 74, pp. 387–398, 1928, <https://www.jstor.org/stable/24101519>.
- [19] Chandrasekhara Venkata. Raman, K. Krishnan, “A new type of secondary radiation,” *Nature*, vol. 121, pp. 501–502, 1928, <https://doi.org/10.1038/121501c0>.

- [20] Xiaoqin. Zhu, Xu Tao, Lin Qingyu, and Duan and yixiang, “Technical Development of Raman Spectroscopy : From Instrumental to Advanced Combined Technologies,” *Appl Spectrosc Rev*, vol. 49, pp. 64–82, 2014, doi: 10.1080/05704928.2013.798801.
- [21] Gurvinder Singh. Bumbrah, R.M. Sharma, “Raman spectroscopy – Basic principle, instrumentation and selected applications for the characterization of drugs of abuse,” *Egypt J Forensic Sci*, vol. 6, pp. 209–215, 2016, <https://doi.org/10.1016/j.ejfs.2015.06.001>.
- [22] Eric Le Ru, Pablo Etchegoin, “*Principles of Surface-Enhanced Raman Spectroscopy and related plasmonic effects*,” 1st Edition. Elsevier Science, 2009, doi: <https://doi.org/10.1016/B978-0-444-52779-0.X0001-3>.
- [23] Andera. Orlando, F. Franceschini, C. Muscas, S. Pidkova, M. Bartoli, M. Rovere, A. Tagliaferro, “A Comprehensive Review on Raman Spectroscopy Applications,” *Chemosensors*, vol. 9, pp. 262, 2021. <https://doi.org/10.3390/chemosensors9090262>.
- [24] Robert W. Boyd, “*Nonlinear Optics*,” Sixth. 2020, ISBN 978-0-12-811002-7, [doi.org/10.1016/C2015-0-05510-1](https://doi.org/10.1016/C2015-0-05510-1).
- [25] Song-Yuan Ding, E.M. You, Z.Q. Tian, M. Moskovits, “Electromagnetic theories of surface-enhanced Raman spectroscopy,” *Chem. Soc. Rev.*, vol. 46, pp. 4042–4076, 2017, <https://doi.org/10.1039/C7CS00238F>.
- [26] Laura T. Kerr, K. Domijan, I. Cullen, B.M. Hennelly, “Applications of Raman spectroscopy to the urinary bladder for cancer diagnostics,” *Photonics Lasers Med*, vol. 3, pp. 2193–064, 2014, <https://doi.org/10.1515/plm-2014-0004>.
- [27] Tony Lam, “A New Era in Affordable Raman Spectroscopy,” *30 Raman Technology For Today’s Spectroscopists*, 2004.
- [28] Eric Le. Ru, Pablo Etchegoin, “Principles of Surface-Enhanced Raman Spectroscopy and Related Plasmonic Effects,” *Elsevier Science*, pp. 688, 2008, ISBN: 978-0444527790.
- [29] Bumbrah Gurvinder Singh, S. R. Mohan, “Raman spectroscopy – Basic principle, instrumentation and selected applications for the characterization of drugs of abuse,” *Egypt J Forensic Sci*, vol. 6, pp. 209–215, 2016.
- [30] Matthew J Baker, C.S. Hughes, K.A. Hollywood, “Raman spectroscopy,” *Institute of Physics*, pp. 1–13, 2016, ISBN: 978-1-6817-4071-3.

- [31] Mildred S. Dresselhaus, A. Jorio, M. Hofmann, G. Dresselhaus, and R. Saito, "Perspectives on Carbon Nanotubes and Graphene Raman Spectroscopy," *Nano Lett*, vol. 10, pp. 751–758, 2010, doi: 10.1021/nl904286r.
- [32] L.M. Malarda, M.A. Pimenta, G. Dresselhaus, M.S. Dresselhaus, "Raman spectroscopy in graphene," *Phys Rep*, vol. 473, pp. 51–87, 2009, doi.org/10.1016/j.physrep.2009.02.003
- [33] Yanping Liu, Z. Liu, W.S. Lew, and Qi. J. Wang, "Temperature dependence of the electrical transport properties in few-layer graphene interconnects," *Nanoscale Res Lett*, vol. 8, pp. 335, 2013, <https://doi.org/10.1186/1556-276X-8-335>.
- [34] Anna Dychalska, P. Popielarski, W. Frankow, K. Fabisiak, K. Paprock, and M. Szybowicz, "Study of CVD diamond layers with amorphous carbon admixture by Raman scattering spectroscopy," *MATERIALS SCIENCE-POLAND*, vol. 33, pp. 799–805, 2015, doi:10.1515/msp-2015-0067.
- [35] Robin J.H. Clark, "Pigment identification by spectroscopic means: an arts/science interface," *C. R. Chimie*, vol. 5, pp. 7–20, 2002, [https://doi.org/10.1016/S1631-0748\(02\)01341-3](https://doi.org/10.1016/S1631-0748(02)01341-3).
- [36] Nikki Kuhar, S. Sil, T. Verma, and S. Umapathy, "Challenges in application of Raman spectroscopy to biology and materials," *RSC Adv*, vol. 8, pp. 25888–25908, 2018, doi: 10.1039/C8RA04491K.
- [37] Yang Danting, Y. Yibin, "Applications of Raman Spectroscopy in Agricultural Products and Food Analysis: A Review," *Appl Spectrosc Rev*, vol. 46, pp. 539–560, 2011, doi: 10.1080/05704928.2011.593216.
- [38] Xiinying. Gong, M. Tang, Z. Gong, Z. Qiu, D. Wang, and M. Fan, "Screening pesticide residues on fruit peels using portable Raman spectrometer combined with adhesive tape sampling," *Food Chem*, vol. 295, pp. 254–258, 2019, doi: 10.1016/j.foodchem.2019.05.127.
- [39] Shelby R. Khandasammy, M.A Fikiet, E. Mistek, A. Yasmine, L. Halamkova, J. Bueno, I.K. Lednev "Bloodstains, paintings, and drugs: Raman spectroscopy applications in forensic science," *Forensic Chemistry*, vol. 8, pp. 111–113, 2018, <https://doi.org/10.1016/j.forc.2018.02.002>.
- [40] Robin R Jones, D.C. Hooper, L. Zhang, D. Wolverson, V.K Valev, "Raman Techniques: Fundamentals and Frontiers," *Nanoscale Res Lett*, vol. 14, pp. 231, 2019. <https://doi.org/10.1186/s11671-019-3039-2>.

- [41] Alessia Polemi, S. M. Wells, N. V. Lavrik, M. J. Sepaniak, K. L. Shuford, “Local Field Enhancement of Pillar Nanosurfaces for SERS,” *J. Phys. Chem. C*, 114, vol. 42, pp. 18096–18102, 2010, <https://doi.org/10.1021/jp106540q>.
- [42] Yuxuan Qiu, Cuifang Kuang, Xu Liu, and Longhua Tang, “Single-Molecule Surface-Enhanced Raman Spectroscopy,” *Sensors*, vol. 22, pp. 4889, 2022, <https://doi.org/10.3390/s22134889>.
- [43] Moram Sree Satya Bharati, V.R. Soma, “Flexible SERS substrates for hazardous materials detection: recent advances,” *Opto-Electronic Advances*, vol. 4, pp. 210048, 2021, doi: 10.29026/oea.2021.210048.
- [44] P. Mandal and B.S. Tewari, “Progress in surface enhanced Raman scattering molecular sensing: A review,” *Surfaces and Interfaces*, vol. 28, pp. 101655, 2022, [doi.org/10.1016/j.surfin.2021.101655](https://doi.org/10.1016/j.surfin.2021.101655).
- [45] M. Fleischmann, P.J. Hendra, and A.J. Mc. Quillan, “Raman spectra of pyridine adsorbed at a silver electrode,” *Chem Phys Lett*, vol. 26, pp. 163–166, 1974, doi: [https://doi.org/10.1016/0009-2614\(74\)85388-1](https://doi.org/10.1016/0009-2614(74)85388-1).
- [46] David L. Jeanmaire. R. P. V. Duyne, “Surface raman spectroelectro chemistry: Part I. Heterocyclic, aromatic, and aliphatic amines adsorbed on the anodized silver electrode,” *J Electroanal Chem Interfacial Electrochem*, vol. 1–20, pp. 1–20, 1977, [https://doi.org/10.1016/S0022-0728\(77\)80224-6](https://doi.org/10.1016/S0022-0728(77)80224-6).
- [47] M. Grant Albrecht, J. A. Creighton, “Anomalously intense Raman spectra of pyridine at a silver electrode,” *J Am Chem Soc*, vol. 99, pp. 5215–5217, 1977. <https://doi.org/10.1021/ja00457a071>.
- [48] Kahrizi Mojtaba, P.A. Sohi, *Recent Advances in Nanophotonics: Fundamentals and Applications*. IntechOpen, 2020, ISBN:978-1-83962-844-3.
- [49] Nie Shuming, S. Emory, Probing Single Molecules and Single Nanoparticles by Surface-Enhanced Raman Scattering, *SCIENCE*, vol. 275, pp. 1102–1106, 1997, DOI: 10.1126/science.275.5303.1102
- [50] Katherine A. Willets, R.P. Van. Duyne, “Localized surface plasmon resonance spectroscopy and sensing,” *Annu Rev Phys Chem*, vol. 58, pp. 267–297, 2007, doi: 10.1146/annurev.physchem.58.032806.104607.
- [51] V.A.G. Rivera, Ferri F.A., and Jr. E. Marega, *Localized Surface Plasmon Resonances: Noble Metal Nanoparticle Interaction with Rare-Earth Ions*. IntechOpen, 2012, doi: 10.5772/50753.



- [52] Eleonora Petryayeva, U.J. Krull, “Localized surface plasmon resonance: nanostructures, bioassays and biosensing--a review,” *Anal Chim Acta*, vol. 706, pp. 8–24, 2011, doi.org/10.1016/j.aca.2011.08.020.
- [53] Alan Campion, P. Kambhampati, “Surface-enhanced Raman scattering,” *Chem Soc Rev*, vol. 27, pp. 241–250, 1998, <https://doi.org/10.1039/A827241Z>.
- [54] Pablo A. Mercadal, J.C. Fraire, E.A. Coronado, “Simple Approach to Assess the Maximum Hot Spot SERS Enhancement Factors in Colloidal Dispersions of Gold Nanoparticle Aggregates,” *J. Phys. Chem. C*, vol. 126, pp. 10524–10533, 2022, doi.org/10.1021/acs.jpcc.2c02299.
- [55] Ujjal Kumar Sur, “Surface-enhanced Raman spectroscopy,” *Resonance*, vol. 15, pp. 154–164, 2010, doi: 10.1007/s12045-010-0016-6.
- [56] Roberto Pilot, Raffaella Signorini, Christian Durante, Laura Orian, Manjari Bhamidipati, and Laura Fabris, “A review on surface-enhanced Raman scattering,” *Biosensors (Basel)*, vol. 9, p. 57, 2019, doi: 10.3390/bios9020057.
- [57] Li-Wei Hua, X. Liu, G.M. Leb, J.F. Lib, F.S. Qub, S.Y. Luc, Li. Qi, Morphology evolution and SERS activity of the nanoporous Au prepared by dealloying sputtered Au-Ag film,” *Physica B Condens Matter*, vol. 558, pp. 49–53, 2019, doi.org/10.1016/.physb.2019.01.019.
- [58] Pamela A. Mosier-Boss, “Review of SERS Substrates for Chemical Sensing,” *Nanomaterials*, vol. 6, pp. 142, 2017, doi: 10.3390/nano7060142.
- [59] Wenying. Ma, H. Yang, J. P. Hilton, Q. Lin, J.Y Liu, L.X Huang, J. Yao “A numerical investigation of the effect of vertex geometry on localized surface plasmon resonance of nanostructures,” *Optics Express*, vol. 18, pp. 843–53, 2010, doi: 10.1364/OE.18.000843.
- [60] Furong Tian, Franck Bonnier, Alan Casey, Anne E. Shanahan, and Hugh J. Byrne, “Surface enhanced Raman scattering with gold nanoparticles: effect of particle shape,” *Analytical Methods*, vol. 6, pp. 9116–9123, 2014, doi: 10.1039/x0xx00000x.
- [61] Tae Yoon Jeon, D.J. Kim, S.G. Park, S.H. Kim, D.Ho. Kim, “Nanostructured plasmonic substrates for use as SERS sensors,” *Nano Conver*, vol. 3, pp. 8, 2016. doi: 10.1186/s40580-016-0078-6.
- [62] Xing You Lang, L. Chen, P. Guan, T. Fujita, M.W. Chen, “Geometric effect on surface enhanced Raman scattering of nanoporous gold: Improving Raman scattering by tailoring ligament and nanopore ratios,” *Appl. Phys. Lett*, vol. 94, pp. 213109, 2009, <https://doi.org/10.1063/1.3143628>.

- [63] Samir Kumar, Prabhat Kumar, Anamika Das, Chandra Shakher Pathak, *Surface-Enhanced Raman Scattering: Introduction and Applications Recent Advances in Nanophotonics - Fundamentals and Applications*. IntechOpen, 2020, doi:10.5772/intechopen.92614.
- [64] Deepak Bhandari, "Surface-Enhanced Raman Scattering: Substrate Development and Applications in Analytical Detection," University of Tennessee, Knoxville, 2011.
- [65] Carla Daruich De Souza, B.R. Nogueira, M. E. C. M. Rostelato, "Review of the methodologies used in the synthesis gold nanoparticles by chemical reduction," *Journal of Alloys and Compounds*, vol. 798, pp. 714–740, 2019, doi: 10.1016/j.jallcom.2019.05.153.
- [66] Gour Mohan Das, S. Managò, M. Mangini, A. C. De Luca, "Biosensing using sers active gold nanostructures," *Nanomaterials*, vol. 11, pp. 10, Nanomaterials (Basel), 2021. doi: 10.3390/nano11102679.
- [67] Zhuoyao Li, X. Huang, G. Lu, "Recent developments of flexible and transparent SERS substrates," *J. Mater. Chem. C*, vol. 8, pp. 3956–3969, 2020. doi: 10.1039/d0tc00002g.
- [68] Imran Shaikh, M.A. Haque, H. Pathan, S. Sartale, "Spin-Coated Ag NPs SERS Substrate: Role of Electromagnetic and Chemical Enhancement in Trace Detection of Methylene Blue and Congo Red," *Plasmonics*, vol. 17, pp. 1889–1900, 2022, doi: 10.1007/s11468-022-01671-2.
- [69] George C. Schatz, M.A. Young, R.P. V. Duyne, "*Electromagnetic mechanism of SERS. In Surface-Enhanced Raman Scattering: Physics and Applications*," vol. 103. Springer, 2006, ISBN: 978-3-540-33566-5, [https://doi.org/10.1007/3-540-33567-6\\_2](https://doi.org/10.1007/3-540-33567-6_2).
- [70] Jenny M. Oran, R.J. Hinde, N.A. Hatab, S.T. Retterer, M.J. Sepaniak "Nanofabricated periodic arrays of silver elliptical discs as SERS substrates," *Journal of Raman Spectroscopy*, vol. 39, pp. 1811–1820, 2008, <https://doi.org/10.1002/jrs.2044>.
- [71] Kun Ge, Yuling Hu, Gongke Li, "Recent Progress on Solid Substrates for Surface-Enhanced Raman Spectroscopy Analysis," *Biosensors*, vol. 12, Nov. 01, 2022. doi: 10.3390/bios12110941.
- [72] John C. Hulteen, Richard P. V. Duyne, "Nanosphere lithography: A materials general fabrication process for periodic particle array surfaces," *Journal of Vacuum Science & Technology A: Vacuum, Surfaces, and Films*, vol. 13, pp. 1553–1558, 1995, doi: 10.1116/1.579726.

- [73] H. Wang, G. M. Laws, S. Milicic, P. Boland, A. Handugan, M. Pratt, T. Eschrich, S. Myhajlenkoa, “Low temperature ZEP-520A development process for enhanced critical dimension realization in reactive ion etched polysilicon,” *Journal of Vacuum Science & Technology B: Microelectronics and Nanometer Structures*, vol. 25, p. 102, 2007, doi: 10.1116/1.2426976.
- [74] Yao Nan, W. Zh. Lin, *Handbook of Microscopy for Nanotechnology*. Springer New York, NY, 2005.
- [75] Mariachiara Manoccio, M. Esposito, A. Passaseo, M. Cuscunà, and V. Tasco, “Focused Ion Beam Processing for 3D Chiral Photonics Nanostructures,” *micromachines*, 2021, vol. 12, pp. 6, 2020, doi: 10.3390/mi1201.
- [76] Heena. Sammi, R. V. Nair, and N. Sardana, “Recent advances in nanoporous AAO based substrates for surface-enhanced raman scattering,” in *Materials Today: Proceedings*, Elsevier Ltd, 2020, pp. 843–850. doi: 10.1016/j.matpr.2020.09.233.
- [77] Andrea Mario Giovannozzi, F. Rolle, M. Sega, M. C. Abete, D. Marchis, and A. M. Rossi, “Rapid and sensitive detection of melamine in milk with gold nanoparticles by Surface Enhanced Raman Scattering,” *Food Chem*, vol. 159, pp. 250–256, Sep. 2014, doi: 10.1016/j.foodchem.2014.03.013.
- [78] Xiaobing Du, H. Chu, Y. Huang, Y. Zhao, “Qualitative and Quantitative Determination of Melamine by Surface-Enhanced Raman Spectroscopy Using Silver Nanorod Array Substrates,” *Appl Spectrosc*, vol. 64, pp. 781–785, 2010, doi: 10.1366/000370210791666426
- [79] Juanita Hughes, E.L. Izake, W.B. Lott, G.A. Ayoko, M. Sillence “Ultra-sensitive label free surface enhanced Raman spectroscopy method for the detection of biomolecules,” *Talanta*, vol. 130, pp. 20–25, 2014, doi: 10.1016/j.talanta.2014.06.012.
- [80] Jichun Zhu, J. Zhou, J. Guo, W. Cai, B. Liu, Z. Wang, Z. Sun “Surface-enhanced Raman spectroscopy investigation on human breast cancer cells,” *Chem Cent J*, vol. 7, pp. 37, 2013, doi: 10.1186/1752-153X-7-37.
- [81] Ronglu. Dong, S. Weng, L. Yang, and J. Liu, “Detection and direct readout of drugs in human urine using dynamic surface-enhanced Raman spectroscopy and support vector machines,” *Anal Chem*, vol. 87, pp. 2937–2944, 2015, doi: 10.1021/acs.analchem.5b00137.

- [82] Javier E. L. Villa, and R. J. Poppi, “A portable SERS method for the determination of uric acid using a paper-based substrate and multivariate curve resolution,” *Analyst*, vol. 141, pp. 1966–1972, 2016, doi: 10.1039/c5an02398j.
- [83] Katherine A Willets, “Surface-enhanced Raman scattering (SERS) for probing internal cellular structure and dynamics,” *Analytical and Bioanalytical Chemistry*, vol. 394, pp. 85–94, 2009. doi: 10.1007/s00216-009-2682-3.
- [84] Darya. Radziuk, H. Moehwald, “Prospects for plasmonic hot spots in single molecule SERS towards the chemical imaging of live cells,” *Physical Chemistry Chemical Physics*, vol. 17, pp. 21072–21093, *Royal Society of Chemistry*, 2015, doi: 10.1039/c4cp04946b.
- [85] Weiqing. Xiong, X. Wang, H. Liu, Y. Zhang, “Metal-organic frameworks: opportunities and challenges for surface-enhanced Raman scattering-a review,” *Journal of Materials Chemistry C*, vol. 8, pp. 2952–2963, *Royal Society of Chemistry*, 2020. doi: 10.1039/d0tc00040j.
- [86] R. Griffith Freeman, K.C Grabar, K.J Allison, R.M Bright, J.A Davis, A.P Guthrie, M.B Hommer, M.A Jackson, P.C Smith, D.G Walter, M.J Natan, “Self-Assembled Metal Colloid Monolayers: An Approach to SERS Substrates,” *Science (1979)*, Vol. 267, pp. 1629-1632, 1995, doi: 10.1126/science.267.5204.1629.
- [87] Katrin Kneipp, Y. Wang, H. Kneipp, L.T. Perelman, I. Itzkan, R.R. Dasari, and M.S. Feld, “Single Molecule Detection Using Surface-Enhanced Raman Scattering (SERS),” 1997, doi:10.1103/PhysRevLett.78.1667.
- [88] Joshua Van der Zalm, Sh. Chen, W. Huang, A. Chen, “Review—Recent Advances in the Development of Nanoporous Au for Sensing Applications,” *J Electrochem Soc*, vol. 167, pp. 037532, 2020, doi: 10.1149/1945-7111/ab64c0.
- [89] Renyun Zhang, Hakan Olin, “Porous gold films-a short review on recent progress,” *Materials*, vol. 7, pp. 3834–3854, 2014, doi: 10.3390/ma7053834.
- [90] Gabriele Scandura, P. Kumari, G. Palmisano, G. Karanikolos, J. Orwa, L.F. Dumée, “Nanoporous Dealloyed Metal Materials Processing and Applications-A Review,” *Ind Eng Chem*, vol. 62, pp. 1736–1763, 2023, doi: 10.3390/ma7053834.
- [91] Abdel-Aziz EI Mell, F. B-Hacene, L.M. Luna, N. Bouts, A.C.D. Thiry, E.G.N. Gautier, P.Y.Tessier, “Unusual dealloying effect in gold/copper alloy thin films: The role of defects and column boundaries in the formation of nanoporous gold,” *ACS Appl Mater Interfaces*, vol. 7, pp. 2310–2321, 2015, doi: 10.1021/am5065816.

- [92] Jonah Erlebacher, J.A. Michael, A. Karma, N. Dimitrov, K. Sieradzki, "Evolution of nanoporosity in dealloying," *Nature*, vol. 410, pp. 450–453, 2001, doi.org/10.1038/35068529.
- [93] O. Zinchenko, H.A. De Raedt, E. Detsi, P.R. Onck, and J.T.M. De Hosson, "Nanoporous gold formation by dealloying: A Metropolis Monte Carlo study," *Comput Phys Commun*, vol. 184, pp. 1562–1569, 2013, doi: 10.1016/j.cpc.2013.02.004.
- [94] Y. Ding, Yong Ju Kim, J. Erlebacher J, "Nanoporous Gold Leaf: 'Ancient Technology'/Advanced Material," *Advanced Materials*, vol. 16, pp. 1897–1900, 2004. doi: 10.1002/adma.200400792.
- [95] Shaofeng Sun, X. Chen, N. Badwe, and K. Sieradzki, "Potential-dependent dynamic fracture of nanoporous gold," *Nat Mater*, vol. 14, pp. 894–898, 2015, doi: 10.1038/nmat4335.
- [96] Lihua Qian, X.Q. Yan, T. Fujita, A. Inoue, M. W. Chen, "Surface enhanced Raman scattering of nanoporous gold: Smaller pore sizes stronger enhancements," *Appl Phys Lett*, vol. 90, no. 15, 2007, doi: 10.1063/1.2722199.
- [97] Zhen Qi, Jorg Weissmüller, "A Hierarchical Nested Network Nanostructure by Dealloying.," *ACS Nano*, vol. 7, pp. 5948–5954, 2013, doi: 10.1021/nn4021345.
- [98] Chong Xiao, Y. L. Liu, J. Q. Xu, S. W. Lv, S. Guo, and W. H. Huang, "Real-time monitoring of H<sub>2</sub>O<sub>2</sub> release from single cells using nanoporous gold microelectrodes decorated with platinum nanoparticles," *Analyst*, vol. 140, pp. 3753–3758, 2015, doi: 10.1039/c4an02056a.
- [99] Henry Steven Catota Saenz, L. P. Hernandez-Saravia, J. S. G. Selva, A. Sukeri, P. J. Espinoza-Montero, and M. Bertotti, "Electrochemical dopamine sensor using a nanoporous gold microelectrode: a proof-of-concept study for the detection of dopamine release by scanning electrochemical microscopy," *Microchimica Acta*, vol. 185, pp. 367, 2018, doi: 10.1007/s00604-018-2898-z.
- [100] Yanping. Deng, W. Huang, X. Chen, and Z. Li, "Facile fabrication of nanoporous gold film electrodes," *Electrochem commun*, vol. 10, pp. 810–813, 2008, doi: 10.1016/j.elecom.2008.03.003.
- [101] Zhaopeng Chen, J. Jiang, G. Shen, and R. Yu, "Impedance immunosensor based on receptor protein adsorbed directly on porous gold film," *Anal Chim Acta*, vol. 553, pp. 190–195, 2005, doi: 10.1016/j.aca.2005.08.014.

- [102] Yu. Bai, W. Yang, Y. Sun, and C. Sun, "Enzyme-free glucose sensor based on a three-dimensional gold film electrode," *Sens Actuators B Chem*, vol. 134, pp. 471–476, 2008, doi: 10.1016/j.snb.2008.05.028.
- [103] Huang Wei, W. Minghua, Z. Jufang, Li. Zelin, "Facile Fabrication of Multifunctional Three-Dimensional Hierarchical Porous Gold Films via Surface Rebuilding," *The Journal of Physical Chemistry C*, vol. 113, pp. 1641–2033, 2009, <https://doi.org/10.1021/jp8095693>.
- [104] PS. Shah, M. B. Jr. Sigman, C. A. Stowell, K. P. Johnston, and B. A. Korgel, "Single-Step Self-Organization of Ordered Macroporous Nanocrystal Thin Films," *Advanced Materials*, vol. 15, pp. 12, 2003, <https://doi.org/10.1002/adma.200304903>.
- [105] Bo. Zhao, M. M. Collinson, "Hierarchical porous gold electrodes: Preparation, characterization, and electrochemical behavior," *Journal of Electroanalytical Chemistry*, vol. 684, pp. 53–59, 2012, doi: 10.1016/j.jelechem.2012.08.025.
- [106] Jay Patel, L. Radhakrishnan, B. Zhao, B. Uppalapati, R.C. Danies, K.R. Ward, M.M. Collinson, "Electrochemical properties of nanostructured porous gold electrodes in biofouling solutions," *Anal Chem*, vol. 85, pp. 11610–11618, 2013, doi: 10.1021/ac403013r.
- [107] Renyun. Zhang, M. Hummelgrd, H. Olin, "Single layer porous gold films grown at different temperatures," *Physica B Condens Matter*, vol. 405, pp. 4517–4522, 2010, doi: 10.1016/j.physb.2010.08.029.
- [108] Jung. Sub. Wi, S. Tominaka, K. Uosaki, and T. Nagao, "Porous gold nanodisks with multiple internal hot spots," *Physical Chemistry Chemical Physics*, vol. 14, pp. 9131–9136, 2012, doi: 10.1039/c2cp40578d.
- [109] Bhargav Guntupalli, P. Liang, J.H. Lee, Y. Yang, H. Yu, J. Canoura, J. He, W. Li, Y. Weizmann, Y. Xiao, "Ambient Filtration Method To Rapidly Prepare Highly Conductive, Paper-Based Porous Gold Films for Electrochemical Biosensing," *ACS Appl Mater Interfaces*, vol. 7, pp. 27049–27058, 2015, <https://doi.org/10.1021/acsami.5b09612>.
- [110] Peng Li, H. Zhang, D. Lai, S. Xu, Y. Xia, Z. Li, W. Huang, "Facile Preparation of Gold Nanoparticles via Simultaneous Electrodissolution/Chemical Reduction Processes for the Electrochemical Oxidation and Sensing of Ascorbic Acid," *J Electrochem Soc*, vol. 164, pp. 14, 2017, doi: 10.1149/2.0721714jes.

- [111] Liu Zhonggang, Bakk Ashley Nemec, Khaper Neelam, and Chen Aicheng, “Sensitive Electrochemical Detection of Nitric Oxide Release from Cardiac and Cancer Cells via a Hierarchical Nanoporous Gold Microelectrode,” *American Chemical Society*, vol. 89, pp. 8036–8043, 2017, doi: 10.1021/acs.analchem.7b01430.
- [112] Cheng. Fang, N. M. Bandaru, A. V. Ellis, and N. H. Voelcker, “Electrochemical fabrication of nanoporous gold,” *J Mater Chem*, vol. 22, no. 7, pp. 2952–2957, <https://doi.org/10.1039/C2JM14889G>.
- [113] Ruye. Zhang, Y. Zhang, X. Deng, S. Sun, and Y. Li, “A novel dual-signal electrochemical sensor for bisphenol A determination by coupling nanoporous gold leaf and self-assembled cyclodextrin,” *Electrochim Acta*, vol. 271, pp. 417–424, 2018, doi: 10.1016/j.electacta.2018.03.113.
- [114] Venkatesh. Subramanian. Manikandan, Z. Liu, and A. Chen, “Simultaneous detection of hydrazine, sulfite, and nitrite based on a nanoporous gold microelectrode,” *Journal of Electroanalytical Chemistry*, vol. 819, pp. 524–532, Jun. 2018, doi: 10.1016/j.jelechem.2018.02.004.
- [115] Zhong. Gang Liu, E. Puumala, and A. Chen, “Sensitive electrochemical detection of Hg(II) via a FeOOH modified nanoporous gold microelectrode,” *Sens Actuators B Chem*, vol. 287, pp. 517–525, 2019, doi: 10.1016/j.snb.2019.02.080.
- [116] Kai. Rong, L. Huang, H. Zhang, J. Zhai, Y. Fang, and S. Dong, “Electrochemical fabrication of nanoporous gold electrodes in a deep eutectic solvent for electrochemical detections,” *Chemical Communications*, vol. 54, pp. 8853–8856, 2018, doi: 10.1039/c8cc04454f.
- [117] Xi. Ke, Z. Li, L. Gan, J. Zhao, G. Cui, W. Kellogg, D. Matera, D. Higgins, G. Wu, “Three-dimensional nanoporous Au films as high-efficiency enzyme-free electrochemical sensors,” *Electrochim Acta*, vol. 170, pp. 337–342, 2015, doi: 10.1016/j.electacta.2015.04.144.
- [118] Hu Chengguo, B. Xiaoyun, W. Yingkai, J. Wei, Zh. Xuan, Hu. Shengshui, “Inkjet Printing of Nanoporous Gold Electrode Arrays on Cellulose Membranes for High-Sensitive Paper-Like Electrochemical Oxygen Sensors Using Ionic Liquid Electrolytes,” *Anal Chem*, vol. 84, pp. 3745–3750, 2012, <https://doi.org/10.1021/ac3003243>.

- [119] AY Chen, S.S. Shi, Y.D. Qiu, X.F. Xie, H.H. Ruan, J.F. Gu, D. Pan, “Pore-size tuning and optical performances of nanoporous gold films,” *Microporous and Mesoporous Materials*, vol. 202, pp. 50–56, 2015, doi: 10.1016/j.micromeso.2014.09.048.
- [120] Min Yang, L. Zhang, B. Chen, Z. Wang, C. Chen, and H. Zeng, “Silver nanoparticles decorated nanoporous gold for surface-enhanced Raman scattering,” *Nanotechnology*, vol. 28, 2017, doi: 10.1088/1361-6528/28/5/055301.
- [121] Ling Zhang, L. Xingyou, H. Akihiko, Ch. Mingwei, “Wrinkled Nanoporous Gold Films with Ultrahigh Surface-Enhanced Raman Scattering Enhancement,” *American Chemical Society*, vol. 5, pp. 4407–4413, 2011, doi.org:10.1021/nn201443p.
- [122] Zhang Ling, Ch. Haixin, H. Akihiko, Wu. Hongkai, X. Qi. Kun, Ch. Mingwei, “Nanoporous Gold Based Optical Sensor for Sub-ppt Detection of Mercury Ions,” *American Chemical Society*, vol. 7, pp. 4595–4600, 2013, doi: 10.1021/nn4013737.
- [123] Yanpeng Xue, F. Scaglione, F. Celegato, P. Denis, H.J. Fecht, P. Rizzi, L. Battezzati, “Shape controlled gold nanostructures on de-alloyed nanoporous gold with excellent SERS performance,” *Chem Phys Lett*, vol. 709, pp. 46–51, 2018, doi: 10.1016/j.cplett.2018.08.044.
- [124] Yanpeng. Xue, F. Scaglione, E. M. Paschalidou, P. Rizzi, and L. Battezzati, “Excellent surface enhanced Raman scattering obtained with nanoporous gold fabricated by chemical de-alloying,” *Chem Phys Lett*, vol. 665, pp. 6–9, 2016, doi: 10.1016/j.cplett.2016.10.046.
- [125] Ling. Zhang, H. Liu, L. Chen, P. Guan, B. Chen, T. Fujita, Y. Yamaguchi, H. Iwasaki, Q.K. Xue, M. Chen “Large-scale growth of sharp gold nano-cones for single-molecule SERS detection,” *RSC Adv*, vol. 6, pp. 2882–2887, 2016, doi: 10.1039/c5ra22321k.
- [126] Yu Guo, J. Yu, C. Li, Z. Li, J. Pan, A. Liu, B. Man, T. Wu, X. Xiu, C. Zhang “SERS substrate based on the flexible hybrid of polydimethylsiloxane and silver colloid decorated with silver nanoparticles,” *Optics Express*, vol. 26, pp. 21784–21796, 2018, doi:10.1364/OE.26.021784.
- [127] Jiaolai Jiang, Sumeng Zou, Lingwei Ma, Shaofei Wang, Junsheng Liao, and Zhengjun Zhang, “Surface-Enhanced Raman Scattering Detection of Pesticide Residues Using Transparent Adhesive Tapes and Coated Silver Nanorods,” *American Chemical Society*, vol. 10, pp. 9129–9135, 2018, <https://doi.org/10.1021/acsami.7b18039>.



- [128] Daorui Zhang, H. Pu, L. Huang, D.W. Sun, “Advances in flexible surface-enhanced Raman scattering (SERS) substrates for nondestructive food detection: Fundamentals and recent applications,” *Trends in Food Science and Technology*, vol. 109, pp. 690–701, 2021. doi: 10.1016/j.tifs.2021.01.058.
- [129] Ala. M. Alak, T. V. Dinh, “Surface-Enhanced Raman Spectrometry of Organophosphorus Chemical Agents,” *Anal. Chem*, vol. 59, pp. 2149–2153, 1987, <https://doi.org/10.1021/ac00144a030>.
- [130] Dong. Jin. Lee, D. Y. Kim, “Hydrophobic paper-based SERS sensor using gold nanoparticles arranged on graphene oxide flakes,” *Sensors*, vol. 19, pp. 5471, 2019, doi: 10.3390/s19245471.
- [131] Yiqun Zhu, M. Li, D. Yu, L. Yang, “A novel paper rag as ‘D-SERS’ substrate for detection of pesticide residues at various peels,” *Talanta*, vol. 128, pp. 117–124, 2014, doi: 10.1016/j.talanta.2014.04.066.
- [132] Guochao Shi, M. Wang, Y. Zhu, Y. Wang, H. Xu, “A novel natural SERS system for crystal violet detection based on graphene oxide wrapped Ag micro-islands substrate fabricated from Lotus leaf as a template,” *Appl Surf Sci*, vol. 459, pp. 802–811, 2018, doi: 10.1016/j.apsusc.2018.08.065.
- [133] Kehui Wang, M. Huang, J. Chen, L. Lin, L. Kong, X. Liu, H. Wang, M. Lin, “A ‘drop-wipe-test’ SERS method for rapid detection of pesticide residues in fruits,” *Journal of Raman Spectroscopy*, vol. 49, pp. 493–498, 2017, doi:10.1002/jrs.5308.
- [134] Jiaolai Jiang, S. Zou, Y. Li, F. Zhao, J. Chen, S. Wang, H. Wu, J. Xu, M. Chu, J. Liao, Z. Zhang, “Flexible and adhesive tape decorated with silver nanorods for in-situ analysis of pesticides residues and colorants,” *Microchimica Acta*, vol. 186, 2019, doi: 10.1007/s00604-019-3695-z.
- [135] Jiaming Chen, Y. Huang, P. Kannan, L. Zhang, Z. Lin, J. Zhang, T. Chen, L. Guo, “Flexible and Adhesive Surface Enhance Raman Scattering Active Tape for Rapid Detection of Pesticide Residues in Fruits and Vegetables,” *Anal Chem*, vol. 88, pp. 2149–2155, 2016, doi: 10.1021/acs.analchem.5b03735.
- [136] Ji. Sun, L. Gong, Z. Gong, D. Wang, X. Yin, and M. Fan, “Facile fabrication of a large-area and cost-effective PDMS-SERS substrate by sandpaper template-assisted lithography,” *Analytical Methods*, vol. 11, pp. 4917–4922, 2019, doi: 10.1039/c9ay01494b.

- [137] Lakshminarayana Polavarapu, L. M. Liz-Marzan, “Towards low-cost flexible substrates for nanoplasmonic sensing,” *Physical Chemistry Chemical Physics*, vol. 15, pp. 5288–5300, 2013. doi: 10.1039/c2cp43642f.
- [138] Ling. Yao, P. Dai, L. Ouyang, and L. Zhu, “A sensitive and reproducible SERS sensor based on natural lotus leaf for paraquat detection,” *Microchemical Journal*, vol. 160, 2021, doi: 10.1016/j.microc.2020.105728.
- [139] Bin-Bin Xu, Y.L. Zhang, W.Y. Zhang, X.Q. Liu, J.N. Wang, X.L. Zhang, D.D. Zhang, H.B. Jiang, R. Zhang, H.B. Sun, “SERS Substrates: Silver-Coated Rose Petal: Green, Facile, Low-Cost and Sustainable Fabrication of a SERS Substrate with Unique Superhydrophobicity and High Efficiency,” *Adv Opt Mater*, vol. 1, pp. 55, 2013, <https://doi.org/10.1002/adom.201370007>.
- [140] Sasani Jayawardhana, L. Rosa, S. Juodkazis, and P. R. Stoddart, “Additional enhancement of electric field in surface-enhanced raman scattering due to fresnel mechanism,” *Sci Rep*, vol. 3, 2013, doi: 10.1038/srep02335.
- [141] Nathan D. Israelsen, C. Hanson, and E. Vargis, “Nanoparticle properties and synthesis effects on surface-enhanced Raman scattering enhancement factor: An introduction,” *Scientific World Journal*, vol. 2015. Hindawi Publishing Corporation, 2015, doi: 10.1155/2015/124582.
- [142] Jinglin Huang, Z. He, X. He, Y. Liu, T. Wang, G. Chen, C. Tang, R. Jia, L. Liu, L. Zhang, J. Wang, X. Ai, S. Sun, X. Xu, K. Du “Island-like Nanoporous Gold: Smaller Island Generates Stronger Surface-Enhanced Raman Scattering,” *ACS Appl Mater Interfaces*, vol. 9, pp. 28902–28910, 2017, doi: 10.1021/acsami.7b08013.
- [143] Chengpeng Zhang, P. Yi, L. Peng, X. Lai, J. Chen, M. Huang, J. Ni, “Continuous fabrication of nanostructure arrays for flexible surface enhanced Raman scattering substrate,” *Sci Rep*, vol. 7, 2017, doi: 10.1038/srep39814.
- [144] Kundan Sivashanmugan, J. D. Liao, J. W. You, C. L. Wu, “Focused-ion-beam-fabricated Au/Ag multilayered nanorod array as SERS-active substrate for virus strain detection,” *Sens Actuators B Chem*, vol. 181, pp. 361–367, 2013, doi: 10.1016/j.snb.2013.01.035.
- [145] Yue Bing Zheng, B. Kiraly, S. Cheunkar, T. J. Huang, and P. S. Weiss, “Incident-angle-modulated molecular plasmonic switches: A case of weak exciton-plasmon coupling,” *Nano Lett*, vol. 11, pp. 2061–2065, 2011, doi: 10.1021/nl200524b.

- [146] Tahir Iqbal, Z. Ashfaq, S. Afsheen, M. Ijaz, M.Y. Khan, M. Rafique, G. Nabi “Surface-Enhanced Raman Scattering (SERS) on 1D Nano-gratings,” *Plasmonics*, vol. 15, pp. 1053–1059, 2020, doi: 10.1007/s11468-019-01114-5/Published.
- [147] Ijaz Mohsin, A. Muhammad, A. Sumera, I. Tahir, “Novel Au nano-grating for detection of water in various electrolytes,” *Applied Nanoscience*, vol. 10, pp. 4029–4036, 2020, doi:10.1007/s13204-020-01520-w.
- [148] Li Wei, M. Chao, Z. Ling, C. Bin, C. Luyang, Z. Heping, “Tuning Localized Surface Plasmon Resonance of Nanoporous Gold with a Silica Shell for Surface Enhanced Raman Scattering,” *Nanomaterials*, vol. 9, pp. 251, 2019, doi:10.3390/nano9020251.
- [149] Alemayehu Nana Koya, X. Zhu, N. Ohannesian, A. Ali. Yanik, A. Alabastri, R.P. Zaccaria, R. Krahne, W.Ch. Shih, D. Garoli “Nanoporous Metals: From Plasmonic Properties to Applications in Enhanced Spectroscopy and Photocatalysis,” *ACS Nano*, vol. 15, pp. 6038–6060, 2021, doi: 10.1021/acsnano.0c10945.
- [150] Bo. Kai Chao, Y. Xu, H. Ch. Ho, P. Yiu, Y. C. Lai, C.H. Shek, C.H. Hsueh “Gold-rich ligament nanostructure by dealloying Au-based metallic glass ribbon for surface-enhanced Raman scattering,” *Sci Rep*, vol. 7, pp. 7458, 2017, doi: 10.1038/s41598-017-08033-7.
- [151] Yang. Jiao, J. D. Ryckman, P. N. Ciesielski, C. A. Escobar, G. K. Jennings, and S. M. Weiss, “Patterned nanoporous gold as an effective SERS template,” *Nanotechnology*, vol. 22, pp. 29, 2011, doi: 10.1088/0957-4484/22/29/295302.
- [152] Hong Ying Fu, X.Y. Lang, C. Hou, Zi. Wen, Y.Fu. Zhu, M. Zhao, J.C. Li, W.T. Zheng, Y.B. Liu, Q. Jiang, “Nanoporous Au/SnO/Ag heterogeneous films for ultrahigh and uniform surface-enhanced Raman scattering,” *J Mater Chem C Mater*, vol. 2, pp. 7216–7222, 2014, doi: 10.1039/c4tc00603h.
- [153] Cao Qipu, Feng Jijun, Lu Hongliang, Zhang Hui, Zhang Fuling, Zeng Heping, “Surface-enhanced Raman scattering using nanoporous gold on suspended silicon nitride waveguides,” *Opt Express*, vol. 26, pp. 24614-24620., 2018, doi: 10.1364/OE.26.024614. PMID: 30469574.
- [154] Jinglin Huang, Y. Liu, X. He, C. Tang, K. Du, and Z. He, “Gradient nanoporous gold: a novel surface-enhanced Raman scattering substrate,” *RSC Adv*, vol. 7, pp. 15747–15753, 2017, doi: 10.1039/c6ra28591k.

- [155] Sergei O. Kucheyev, J. R. Hayes, J. Biener, T. Huser, C. E. Talley, and A. V. Hamza, “Surface-enhanced Raman scattering on nanoporous Au,” *Appl Phys Lett*, vol. 89, 2006, doi: 10.1063/1.2260828.
- [156] Lihua Qian, A. Inoue, M. W. Chen, “Large surface enhanced Raman scattering enhancements from fracture surfaces of nanoporous gold,” *Appl Phys Lett*, vol. 92, pp. 9, 2008, doi: 10.1063/1.2890164.
- [157] Huanyu Chi, C. Wang, Z. Wang, H. Zhu, V. St. D. Mesias, X. Dai, Q. Chen, W. Liu, J. Huang, “Highly reusable nanoporous silver sheet for sensitive SERS detection of pesticides,” *Analyst*, vol. 145, pp. 5158–5165, 2020, doi: 10.1039/d3an90017g.
- [158] Shi. Bai, Y. Du, C. Wang, J. Wu, K. Sugioka, “Reusable surface-enhanced raman spectroscopy substrates made of silicon nanowire array coated with silver nanoparticles fabricated by metal-assisted chemical etching and photonic reduction,” *Nanomaterials*, vol. 9, pp. 11, 2019, doi: 10.3390/nano9111531.
- [159] Liping Hou, M. Shao, Z. Li, X. Zhao, A. Liu, C. Zhang, X.W. Xiu, J. Yu, Z. Li, “Elevating the density and intensity of hot spots by repeated annealing for high-efficiency SERS,” *Opt Express*, vol. 28, pp. 29357, 2020, doi: 10.1364/oe.403940.
- [160] Vladimir Halouzka, P. Jakubec, L. Kvitek, V. Likodimos, A.G. Kontos, K. Papadopoulos, P. Falaras, J. Hrbac, “Deposition of Nanostructured Ag Films on Silicon Wafers by Electrochemical/Electrophoretic Deposition for Electrochemical and SERS Sensing,” *J Electrochem Soc*, vol. 160, pp. B54–B59, 2013, doi: 10.1149/2.003306jes.
- [161] Haiyan. Qi, H. Chen, Y. Wang, and L. Jiang, “Detection of ethyl carbamate in liquors using surface-enhanced Raman spectroscopy,” *R Soc Open Sci*, vol. 5, pp. 181539, 2018, doi: 10.1098/rsos.181539.
- [162] Ana. Isabel. Perez. Jimenez, D. Lyu, Z. Lu, G. Liu, and B. Ren, “Surface-enhanced Raman spectroscopy: Benefits, trade-offs and future developments,” *Chemical Science, Royal Society of Chemistry*, vol. 11, pp. 4563–4577, 2020, doi: 10.1039/d0sc00809e.
- [163] Neha. Sardana, T. Birr, S. Schlenker, C. Reinhardt, and J. Schilling, “Surface plasmons on ordered and bi-continuous spongy nanoporous gold,” *New J Phys*, vol. 16, pp. 063053, 2014, doi: 10.1088/1367-2630/16/6/063053.
- [164] Huajun. Zheng, D. Ni, Z. Yu, and P. Liang, “Preparation of SERS-active substrates based on graphene oxide/silver nanocomposites for rapid detection of L-Theanine,” *Food Chem*, vol. 217, pp. 511–516, 2017, doi: 10.1016/j.foodchem.2016.09.010.

- [165] Chuncai. Kong, S. Sun, X. Zhang, X. Song, and Z. Yang, "Nanoparticle-aggregated hollow copper microcages and their surface-enhanced Raman scattering activity," *CrystEngComm*, vol. 15, pp. 6136, 2013, doi: 10.1039/c3ce40703a.
- [166] Kais. Daoudi, M. Gaidi, and S. Columbus, "Silver nanoprisms/graphene oxide/silicon nanowires composites for r6g surface-enhanced raman spectroscopy sensor," *Biointerface Res Appl Chem*, vol. 10, pp. 5670–5674, 2020, doi: 10.33263/BRIAC103.670674.
- [167] Yuting Jing, R. Wang, Q. Wang, Z. Xiang, Z. Li, H. Gu, X. Wang, "An overview of surface-enhanced Raman scattering substrates by pulsed laser deposition technique: fundamentals and applications," *Advanced Composites and Hybrid Materials*, vol. 4, pp. 885–905, 2021, doi: 10.1007/s42114-021-00330-0.
- [168] P. Pal, A. Bonyar, M. Veres, L. Himics, L. Balazs, L. Juhasz, I. Csarnovics, "A generalized exponential relationship between the surface-enhanced Raman scattering (SERS) efficiency of gold/silver nanoisland arrangements and their non-dimensional interparticle distance/particle diameter ratio," *Sens Actuators A Phys*, vol. 314, pp. 112225, 2020, doi: 10.1016/j.sna.2020.112225.
- [169] N. T. Panagiotopoulos, N. Kalfagiannis, K.C. Vasilopoulos, N. Pliatsikas, S. Kassavetis, G. Vourlias, M. A. Karakassides, P. Patsalas, "Self-assembled plasmonic templates produced by microwave annealing: Applications to surface-enhanced Raman scattering," *Nanotechnology*, vol. 26, pp. 205603, 2015, doi: 10.1088/0957-4484/26/20/205603.
- [170] Lihua Qian, M. W. Chen, "Ultrafine nanoporous gold by low-temperature dealloying and kinetics of nanopore formation," *Appl Phys Lett*, vol. 91, pp. 083105-083105-3, 2007, doi: 10.1063/1.2773757.
- [171] Chaoxiong Ma, K. Fu, M. J. Trujillo, X. Gu, N. Baig, P. W. Bohn, J. P. Camden, "In Situ Probing of Laser Annealing of Plasmonic Substrates with Surface-Enhanced Raman Spectroscopy," *The Journal of Physical Chemistry C*, vol. 122, pp. 11031–11037, 2018, <https://doi.org/10.1021/acs.jpcc.8b01443>.
- [172] Carmen Viets, W. Hill, "Laser power effects in SERS spectroscopy at thin metal films," *Journal of Physical Chemistry B*, vol. 105, pp. 6330–6336, Jul. 2001, doi: 10.1021/jp004315c.

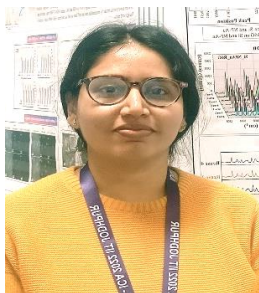
- [173] Md Masud Parvez Arnob, F. Zhao, J. Zeng, G. M. Santos, M. Li, and W. C. Shih, “Laser rapid thermal annealing enables tunable plasmonics in nanoporous gold nanoparticles,” *Nanoscale*, vol. 6, pp. 12470–12475, 2014, doi: 10.1039/c4nr03672g.
- [174] Bolun Cao, Yunyun Mu, Xinping Zhang, “Direct Laser Annealing of Surface-Enhanced Raman Scattering Substrates,” *Adv Eng Mater*, vol. 21, pp. 1900779, 2019, doi:10.1002/adem.201900779.
- [175] N Pliatsikas, N. Kalfagiannis, J. Arvanitidis, D. Christofilos, D.C. Koutsogeorgis, A. Kagkoura, K. Sefiane, V. Koutsos, P. Patsalas, “Edge-engineered self-assembled hierarchical plasmonic SERS templates,” *Applied Surface Science Advances*, vol. 6, pp. 100186, 2021, doi: 10.1016/j.apsadv.2021.100186.
- [176] Liu Guangyang, L. Meng, H. Xiaodong, Li. Tengfei, Xu. Donghui, “Application of Gold-Nanoparticle Colorimetric Sensing to Rapid Food Safety Screening,” *Sensors*, vol. 18, pp. 4166, 2018, doi: 10.3390/s18124166.
- [177] Prashant. K. Jain and M. A. El-Sayed, “Plasmonic coupling in noble metal nanostructures,” *Chem Phys Lett*, vol. 487, pp. 153–164, 2010, doi: 10.1016/j.cplett.2010.01.062.
- [178] Liang. Cheng, X. Zhu, and J. Su, “Coalescence between Au nanoparticles as induced by nanocurvature effect and electron beam athermal activation effect,” *Nanoscale*, vol. 10, pp. 7978–7983, 2018, doi: 10.1039/c7nr09710g.
- [179] Wei Xi, K. Wang, Y. Shen, M. Ge, Z. Deng, Y. Zhao, Q. Cao, Yi. Ding, G. Hu, J. Luo, “Dynamic co-catalysis of Au single atoms and nanoporous Au for methane pyrolysis,” *Nat Commun*, vol. 11, pp. 2020, doi: 10.1038/s41467-020-15806-8.
- [180] Runcheng Liu, Z. Zha, C. Li, M. Shafi, Q. Peng, M. Liu, C. Zhang, X. Du, S. Jiang, “Coupling of multiple plasma polarization modes in particles-multilayer film system for surface-enhanced Raman scattering,” *APL Photonics*, vol. 6, pp. 036104, 2021, doi: 10.1063/5.0042808.
- [181] Li Fei, L. Silang, Q. Fengsheng, W. Dou, L. Chao, L. Xue, “Electrochemical Dealloying Preparation and Morphology Evolution of Nanoporous Au with Enhanced SERS Activity,” *Coatings*, vol. 13, pp. 489, 2023, doi.org/10.3390/coatings 13030489.
- [182] Torun Neslihan, T. Ilker, S. Menekse, K. Mustafa, O. M. Serdar, “Physically Unclonable Surfaces via Dewetting of Polymer Thin Films,” *ACS Applied Material Interfaces*, vol. 13, pp. 11247–11259, 2021, doi: 10.1021/acsami.0c16846.

- [183] Agnieszka Kamińska, I. Dziecielewski, J.L. Weyher, J. Waluk, S. Gawinkowski, V. Sashuk, M. Fiałkowski, M. Sawicka, T. Suski, S. Porowski, R. Hołyst, “Highly reproducible, stable and multiply regenerated surface-enhanced Raman scattering substrate for biomedical applications,” *J Mater Chem*, vol. 21, pp. 8662–8669, 2011, doi: 10.1039/c0jm03336g.
- [184] Kaiqiang Wang, D. W. Sun, H. Pu, Q. Wei, and L. Huang, “Stable, Flexible, and High-Performance SERS Chip Enabled by a Ternary Film-Packaged Plasmonic Nanoparticle Array,” *ACS Appl Mater Interfaces*, vol. 11, pp. 29177–29186, 2019, doi: 10.1021/acsami.9b09746.
- [185] K. Singh Pannu, “JOURNALISM OF COURAGE”. Available: <https://indianexpress.com/article/india/kahan-singh-pannu-raising-awareness-compliance-were-key-to-reducing-pesticide-use-6113572>.
- [186] Quan Doan Mai, H. A. Nguyen, T. L. H. Phung, N.X. Dinh, Q.H. Tran, T.Q. Doan, A. T. Pham, A.T. Le, “Photoinduced Enhanced Raman Spectroscopy for the Ultrasensitive Detection of a Low-Cross-Section Chemical, Urea, Using Silver–Titanium Dioxide Nanostructures,” *ACS Applied Nanomaterials*, vol. 5, pp. 15518–15530, 2022, <https://doi.org/10.1021/acsanm.2c03524>.
- [187] Manvi. Tak, V. Gupta, M. Tomar, “A highly efficient urea detection using flower-like zinc oxide nanostructures,” *Materials Science and Engineering C*, vol. 57, pp. 38–48, 2015, doi: 10.1016/j.msec.2015.06.052.
- [188] Kun. Chen, X. Zhang, D. R. MacFarlane, “Ultrasensitive surface-enhanced Raman scattering detection of urea by highly ordered Au/Cu hybrid nanostructure arrays,” *Chemical Communications*, vol. 53, pp. 7949–7952, 2017, doi: 10.1039/c7cc03523c.
- [189] Yun ah. Han, J. Ju, Y. Yoon, S.M. Kim, “Analysis of Urea in Human Serum using an Oblique Angle Deposited Ag Nanorod Surface Enhanced Raman Scattering Substrate,” 12<sup>th</sup> IEEE International Conference on Nanotechnology (IEEE-NANO), Birmingham, pp.1-4, 2012, doi: 10.1109/NANO.2012.6321979.
- [190] Wen Jin, F. Song, Y. Du, Y. Wang, R. Qiang, “Dendritic Silver Microstructures as Highly Sensitive SERS Platform for the Detection of Trace Urea,” in *IOP Conference Series: Materials Science and Engineering*, Institute of Physics Publishing, vol. 688, pp. 033040, 2019, doi: 10.1088/1757-899X/688/3/033040.
- [191] P. Susthitha Menon, F. A. Said, G. S. Mei, D. D. Berhanuddin, A. A. Umar, S. Shaari, B. Y. Majlis, “Urea and creatinine detection on nanolaminated gold thin film using

- Kretschmann-based surface plasmon resonance biosensor,” *PLoS One*, vol. 13, pp. e0201228, 2018, doi: 10.1371/journal.pone.0201228.
- [192] Xinlong Xu, P. Bo, L. Dehui, Z. Jun, M.W. Lai, Z. Qing, W. Shijie, X. Qihua, “Flexible Visible–Infrared Metamaterials and Their Applications in Highly Sensitive Chemical and Biological Sensing,” *Nano Lett*, vol. 11, pp. 3051–3512, 2011, <https://doi.org/10.1021/nl2014982>
- [193] Shuxi. Dai, Y. Zhu, Y. Gu, Z. Du, “Biomimetic fabrication and photoelectric properties of superhydrophobic ZnO nanostructures on flexible PDMS substrates replicated from rose petal,” *Appl Phys A Mater Sci Process*, vol. 125, pp. 138, 2019, doi: 10.1007/s00339-019-2438-7.
- [194] Luisa. Mandrile, A. M. Giovannozzi, A. Sacco, G. Martra, A. M. Rossi, “Flexible and transparent substrates based on gold nanoparticles and TiO<sub>2</sub> for in situ bioanalysis by surface-enhanced raman spectroscopy,” *Biosensors (Basel)*, vol. 9, pp. 145, 2019, doi: 10.3390/bios9040145.
- [195] Theresa Bartschmid, A. Farhadi, M. E. Musso, E. S. A. Goerlitzer, N. Vogel, and G. R. Bourret, “Self-Assembled Au Nanoparticle Monolayers on Silicon in Two- and Three-Dimensions for Surface-Enhanced Raman Scattering Sensing,” *ACS Appl Nano Mater*, vol. 5, pp. 11839–11851, 2022, doi: 10.1021/acsanm.2c01904.
- [196] Tran Thi Quyen Bich, W.N. Su, K.J. Chen, C.J. Pan, J. Rick, C.C. Chang, B.J. Hwang, “Au@SiO<sub>2</sub> core/shell nanoparticle assemblage used for highly sensitive SERS-based determination of glucose and uric acid,” *Journal of Raman Spectroscopy*, vol. 44, pp. 1671–1677, 2013, doi: 10.1002/jrs.4400.



# Curriculum Vitae



**Heena Sammi**

**PhD scholar (Jan 2019- Jan 2024)**

Indian Institute of Technology, Ropar, Bara Phool, Birla seed farms,  
Rupnagar, 140001, India

**Contact: 7307377623**

**Email id:** [heenasammi5@gmail.com](mailto:heenasammi5@gmail.com), [2018msz0003@iitrpr.ac.in](mailto:2018msz0003@iitrpr.ac.in)

## **Professional Summary**

- Passionate, focused, and self-motivated researcher in multiple fields such as Nanotechnology, Chemistry, and Physics with ~ 5 years of experience.
- Good hand in experiments as well as on instrument handling spectroscopy (UV-Visible, FTIR, DLS, PL, XRD, and optical microscopy) and electron microscopy (SEM and AFM) techniques.
- Rich experience in the synthesis as well as in the analysis of nano-structured materials and the fabrication of thin film (~ nm range) by various characterization techniques.

## **Employment History**

✚ **PhD Scholar** – IIT Ropar, Department of Metallurgical and Materials Engineering  
January 2019- Present

✚ **Junior Research Fellow**-Institute of Nanoscience and technology, Mohali  
December 2017- January 2019

### **❖ Projects Responsibilities**

#### Industry

- Development of the prototype to obtain useful products from the waste (tin can (waste) to FeOOH (product) chemical salt)
- Development of a low-cost water purification cartridge-based system for the removal of heavy metal ions from ground water.

#### Institute

- Synthesis of Single sheet of graphene from coconut fibers by thermal annealing method
- Synthesis of FeOOH by hydrothermal method for heavy metal ions detection

## Education

- ✚ **Post-Graduation/Graduation-** M. Tech Nanotechnology Integrated 5 Year (B. Tech + M. Tech), Sri Guru Granth Sahib World University, Sirhind., Fatehgarh sahib (July 2011-September 2017), C.G.P. A= 8.0  
Activities: Provided a Helping Hand to juniors regarding research skills (Experiments, Analyst, and Report writing)
- ✚ **Senior Secondary:** Govt Girls Senior Secondary school (PSEB), Sirhind, Fatehgarh Sahib, (2011), Marks= 70 %
- ✚ **Matriculation:** Maha Rishi Dayanand High School (PSEB), Sirhind, Fatehgarh Sahib, (2009), Marks= 75 %

## Skills

- ✚ Microsoft Office Word
- ✚ Microsoft Excel
- ✚ Microsoft PowerPoint
- ✚ Gwyddion/Image J/Origin- Software

## Internships

- ✚ **Modeling and Simulation of Nanoscale System**, National Institute of Technical Teachers Training & Research, Chandigarh, Duration: May 2013-July 2013
- ✚ **Decoration of Carbon Nanotubes with Graphene quantum dots.** Centre for Nanoscience and Nanotechnology, Punjab University, Chandigarh, Duration: May 2015- July 2015
- ✚ **Synthesis of Graphene Quantum Dots- Metal Organic framework composite for pollutant detection**, Sri Guru Granth Sahib World University, Fatehgarh Sahib, Duration: April 2017-September 2017

## Publications

### List of papers published in Journals, in year wise descending order

S. No.	Authors	Title	Journal	Year	Volume	Page
1.	Heena Sammi, Rajesh V Nair, Neha Sardana	Fabrication of SERS substrates by laser restructuring of interconnected Au nanostructures for urea detection	Optical Materials	2023	146	114539
2.	Heena Sammi, Rajesh V Nair, Neha Sardana	Reusable SERS substrate based on interconnected metal network structure	Materials Chemistry and Physics	2023	293	126894
3.	Heena Sammi, Neha Sardana	Reusable, flexible, facile, and economical SERS substrates based on rose petal replicas for pesticide detection	<i>Sensors and Actuators: A. Physical,</i>	2023	362	114638
4.	Heena Sammi, Manish Mohanta, Bhagwati Sharma, and Neha Sardana	Coalescence of Au Nanoparticles in Silica Aerogel under Electron Beam Irradiation	Current Nanoscience	2022	19	1573-4137

5.	Krishna K Yadav, Harish Singh, Supriya Rana, <b>Heena Sammi</b> , ST Nishanthi, Ritika Wadhwa, Nausad Khan, Menaka Jha,	Utilization of waste coir fibre architecture to synthesize porous graphene oxide and their derivatives: An efficient energy storage material	Journal of Cleaner Production	2020	276	124240
6.	Jagpreet Singh, Preeti Kukkar, <b>Heena Sammi</b> , Mohit Rawat, Gurjinder Singh, Deepak Kukkar	Enhanced catalytic reduction of 4-nitrophenol and congo red dye By silver nanoparticles prepared from <i>Azadirachta indica</i> leaf extract under direct sunlight exposure,	Particulate Science and Technology	2019	37	434-443
7.	<b>Heena Sammi</b> , Deepak Kukkar, Jaskaran Singh, Preeti Kukkar, Rajwinder Kaur, Harmanpreet Kaur, Mohit Rawat, Gurjinder Singh, Ki-Hyun Kim	Serendipity in solution-GQDs zeolitic imidazole frameworks nanocomposites for highly sensitive detection of sulfide ions	Sensors and Actuators B: Chemical	2018	255	3047-3056
8.	Preeti Kukkar, Deepak Kukkar, <b>Heena Sammi</b> , Karanveer Singh, Mohit Rawat, Pritpal Singh, Soumen Basu, Ki-Hyun Kim	A facile means for the improvement of sensing properties of metal-organic frameworks through control on the key synthesis variables	Sensors and Actuators B: Chemical	2018	271	157-163

#### List of papers published in conferences, in year wise descending order

S. No.	Authors	Title	Journal	Year	Volume	Page
1.	<b>Heena Sammi</b> , Rajesh V Nair, Neha Sardana	Recent advances in nanoporous AAO based substrates for surface-enhanced raman scattering	Materials Today: Proceedings	2021	41	843-850
2.	Preeti Kukkar, <b>Heena Sammi</b> , Mohit Rawat, Pritpal Singh, Soumen Basu, Deepak Kukkar	Bioconjugation of luminescent Eu-BDC-NH <sub>2</sub> MOFs for highly efficient sensing of BSA	AIP Conference Proceedings	2018	1953	030203

## Participation

### Conference

- International Union of Materials Research society: International conference in Asia (19-23<sup>th</sup> December), IIT Jodhpur.
- International Conference on Emerging materials for sustainable development (9-11<sup>th</sup> Oct, 2022), CSIR-CSIO Chandigarh.

- Advancements and futuristic trends in mechanical and materials Engineering (5-7<sup>th</sup> Dec, 2019), IIT Ropar.

#### **Volunteer**

- Advancements and futuristic trends in mechanical and materials Engineering (5-7<sup>th</sup> Dec, 2019), IIT Ropar.
- International Day for Women and Girls in Science, 10th Feb, 2023, IIT Ropar.

### **Other Contact Details**

- Research Gate: <https://www.researchgate.net/profile/Heena-Sammi>
- Google scholar: <https://scholar.google.com/citations?user=00X1vM4AAAAJ&hl=hi>
- LinkedIn: <https://www.linkedin.com/in/heena-sammi-0a85086a/>

### **References**

-  Dr. Neha Saradana  
Assistant Professor  
IIT Ropar  
Email.id: nsardana@iitrpr.ac.in
-  Dr. Rajesh V. Nair  
Associate Professor  
IIT Ropar  
Email.id: rvnair@iitrpr.ac.in
-  Dr. Manaka Jha  
Scientist C  
Institute of Nanoscience and Technology, Mohali  
Email.id: menaka@inst.ac.in
-  Dr. Deepak Kukkar  
Assistant Processor  
Chandigarh University, Landran  
Email.id: deepakukkar@gmail.com